**Title**

Iron Cycling and Redox Evolution in the Precambrian

**Author**

Planavsky, Noah John

**Publication Date**

2012

UNIVERSITY OF CALIFORNIA
RIVERSIDE

# Iron Cycling and Redox Evolution in the Precambrian

A Dissertation submitted in partial satisfaction
of the requirements for the degree of

Doctor of Philosophy

in

Geological Sciences

by

Noah John Planavsky

June 2012

Dissertation Committee:
Dr. Timothy W. Lyons, Chairperson
Dr. Gordon Love,
Dr. Mary L. Droser

The Dissertation of Noah John Planavsky is approved:

_______________________________________

_______________________________________

_______________________________________

Committee Chairperson

University of California, Riverside

# ABSTRACT OF THE DISSERTATION

## Iron Cycling and Redox Evolution in the Precambrian

by

Noah John Planavsky

Doctor of Philosophy, Graduate Program in Geological Sciences
University of California, Riverside, June 2012
Dr. Timothy W. Lyons, Chairperson

The chemical composition of the ocean changed dramatically with the oxidation of the Earth's surface, and this process has profoundly influenced the evolutionary and ecological history of life. The early Earth is generally thought to have been characterized by a reducing ocean-atmosphere system, while the Phanerozoic Eon (<542 million years ago) is known for a stably oxygenated biosphere conducive to the radiation of animals. However, the exact redox landscape of the Earth's oceans is poorly constrained. Similarly, the redox characteristics of surface environments during Earth's middle age (1.8 to 1 billion years ago) are poorly known. I will provide several lines of evidence that even the mixed layer of the surfical ocean was anoxic in the Archean. Oxygen must have been restricted to very localized regions of the regions—'oxygen oases'. Further, I will present evidence that anoxic and Fe(II)-rich conditions were both spatially and temporally extensive across diverse paleogeographic settings in the mid-Proterozoic ocean. This is a new view of Proterozoic redox conditions; it has been commonly assumed for the last decades that the mid-Proterozoic was home to a globally sulfidic (euxinic) or oxic deep ocean. Lastly, I will explore the underlying controls behind the transition from the reducing state that characterized most of the Precambrian to the oxidized state typical of the Phanerozoic. More specifically, I propose based, on a new record of how marine phosphate concentrations have changed through time, that a spike in phosphate levels in the ocean in late Precambrian was key in causing the switch to a more oxidizing ocean atmosphere system.

Table of Contents

# List of Figures

Introduction

Chapter 1

Chapter 2

Chapter 3

Chapter 4

## List of Tables

Chapter 1

Chapter 2

Chapter 3

Chapter 4

## Introduction

The chemical composition of the ocean has changed dramatically with the gradual oxidation of the Earth's surface. The early Earth was characterized by a reducing ocean-atmosphere system, in contrast to the stable and oxygenated biosphere of today. Undoubtedly the single most important event in Earth's progressive oxygenation was the development of oxygenic photosynthesis. Oxygenic photosynthesis relies only on the ubiquitous molecules carbon dioxide and water, and allowed organisms to pioneer essentially every part of the Earth reached by sunlight. The success of this metabolism is reflected in the abundance of its waste product—molecular oxygen. Oxygen went from less than one part per million in the atmosphere to being a major component—approximately 21% of the current atmosphere (Fig. I.1). This singular biochemical process underpins the texture of every major biogeochemical cycle on the modern Earth. Further, the evolution and development of complex multicellular life was ultimately driven by the rise of oxygenic photosynthesis. Despite its importance for our understanding of life's history and decades of intensive investigation, there is not a strong consensus on when oxygenic photosynthesis evolved. Further, there is no consensus on the tempo and mode with which this biochemical development reshaped the Earth's surface chemistry.

There is still intense debate about the timing of the evolution of oxygenic photosynthesis, with common estimates spanning more than a quarter of Earth's history from prior to the appearance of the earliest known sedimentary rocks to the very end of the Archean.

Geochemical traces and fossils have been used to suggest that oxygenic photosynthesis is as ancient as the Earth's sedimentary rock record. For instance, light organic carbon isotopes values in 3.8 Gry sedimentary rocks have been linked to oxygenic photosynthesizers and there are microbial fossils, proposed to be oxygenic photosynthesizers, as early as 3.4 billion years ago. However, previous evidence for an early rise of oxygenic photosynthesis is far from definitive (Rasmussen et al., 2008). Numerous inorganic and wide range of microbial metabolisms can produce organic matter with light carbon isotope values. Microbial fossils have very simple morphologies and it is therefore difficult to link them to specific metabolisms. Molecular fossils (biomarkers) have been central to the debate about the timing of the rise of oxygenic photosynthesis, and have been used to suggest that cyanobacteria and algae evolved before 2.7 Ga. However, since all known Archean rocks are much more thermally mature than the peak of the oil window, diagnostic biomarker abundances should be so low that these studies have been, and will likely to continue to be, controversial (Rasmussen et al., 2008).

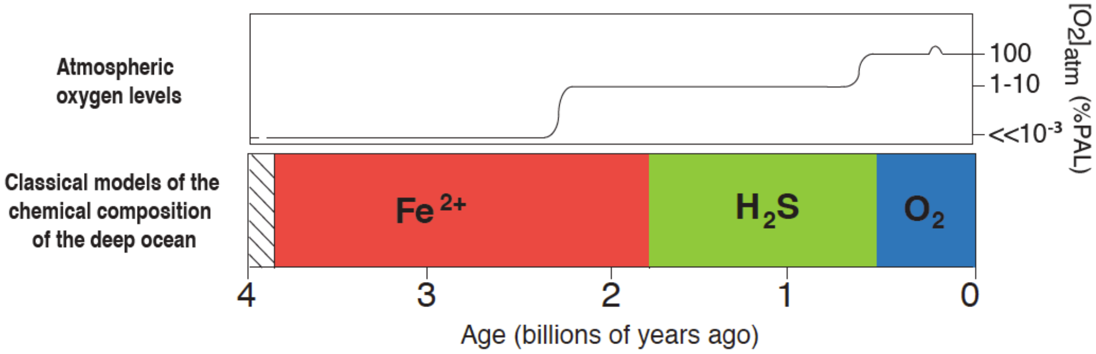

Figure I.1. Overview of the classical model for the Earth's oxygenation. The black line represents the most widely accepted oxygenation model. Estimates for the origin of oxygenic photosynthesis range from >3.8 Ga to 2.4 Ga, but most current evidence prior to the 2.5-2.4 Ga is controversial. Multiple lines of evidence point to a rise in atmospheric oxygen levels and oxygenation of the surface oceans from 2.5-2.4 Gyr. The deep ocean in the mid-Proterzoic (1.8-.55 Ga) is commonly assumed to have been euxinic but there is little empirical evidence for this model. Based on Canfield (2005).

While many typically used lines of evidence for oxygen production in the Archean are controversial, numerous lines of evidence indicate very low levels of oxygen in the early Earth history. Prebiotic oxygen levels, based on atmospheric modeling, are assumed to have been around $10^{-12}$ times that of present atmospheric levels (PAL) (Kasting, 1987). The relatively common occurrence of detrital uraninite, siderite, and pyrite prior to 2.4 Ga is also thought to indicate very low levels of atmospheric oxygen (from $\sim 10^{-12}$ to $\sim 10^{-4}$ PAL) (Holland, 2006). The large range of uncertainty in these calculations is linked to the various estimates of atmospheric exposure times during sediment transport and use of different oxidation rate laws. More recently, the use of rare sulfur isotopes has become central in efforts aimed at constraining Archean atmospheric oxygen partial pressures (Farquhar et al., 2007; Farquhar et al., 2011).

With low levels of atmospheric oxygen, volcanic sulfur dioxide will undergo isotopic fractionation during UV photolysis, not following the typical terrestrial fractionation line (in $^{32}S$-$^{33}S$-$^{34}S$-$^{36}S$ isotope space). This produces what is commonly referred to as a mass independent fractionation (MIF). A coupled MIF generation-preservation model suggests that atmospheric oxygen levels were below $10^{-5}$ PAL whenever a S-MIF signal was recorded in sedimentary rocks (Pavlov and Kasting, 2002). There is a S-MIF signal until around 2.4 Ga, the same time the last detrital pyrite beds are observed. Thus there is almost unanimous acceptance that, until 2.5 Ga - 2.4 Ga, atmospheric oxygen levels were below $10^{-5}$ PAL. It has been commonly proposed that this switch to more oxidizing conditions marks the evolution of oxygenic photosynthesizers, and that this evolutionary event set in place rapid and dramatic shifts in the Earth's global biogeochemical cycles. However, basic mass balance models suggest it is possible to have oxygen production without having any oxygen accumulate in the atmosphere. Consistent with the framework, it is possible that there were local 'oxygen oases' in the Archean in marine or freshwater settings.

Tracking localized oxygen production and the presence of 'oxygen oases' in the Archean with geochemical tracers has been hindered by the difficulties in differentiating between oxic and anoxic oxidation mechanisms (Sverjensky and Lee, 2010). Iron formations provide the foremost example of this quandary. Iron formation deposition is tied to the oxidation of iron in seawater from a soluble reduced state [Fe(II)] to insoluble ferric [Fe(III)] phases. The prevailing view for many years was that large iron formations provided the earliest evidence for microbial oxygen production in the shallow oceans (Cloud, 1973). It has, however, become increasingly clear that other processes (e.g., UV-induced oxidation and anoxygenic photosynthesis) can lead to the formation of iron oxide-rich sediments under completely anoxic conditions. Anoxic oxidation mechanisms, or oxidation induced by ferric iron, could potentially explain other signals of early oxidative processes, such as positive sedimentary N isotope values (Bekker et al., 2010; Sverjensky and Lee, 2010). Additionally, many of the classic geochemical lines of evidence for ‘oxygen oases’’ in the Archean, foremost negative Ce anomalies, have been attributed post-depositional alteration (Bekker et al., 2010; Sverjensky and Lee, 2010). In order to move forward our understanding of the Earth’s early redox evolution we need we need better estimates of the timing of the emergence of oxygenic photosynthesis and the redox landscape of the Earth’s early ocean.

Redox evolution in the time after earliest rise of atmospheric oxygen and before the establishment of a well-oxygenated ocean-atmosphere system teaming with complex life is poorly known. There are very few constraints on mid-Proterozoic atmospheric oxygen levels. After the GOE at ~2.32 Ga, iron is retained in soils, red-beds are common, and there is a marked absence of detrital pyrite beds, all indicating oxidative processes in terrestrial environments (Rye and Holland, 1998). However, these observations provide only a very crude lower estimate on atmospheric $O_2$ of ~1% PAL (Holland, 2006; Rye and Holland, 1998). The most widely accepted upper limit on mid-Proterozoic atmospheric $O_2$, ~40% PAL, is derived from the inferred temporal and spatial extent of anoxia in the Proterozoic ocean (Kump, 2008). However, estimates of anoxia in the deep ocean are often based on inferences about atmospheric oxygen (e.g., Canfield, 1998) and diverse data that leave the door open for wide-ranging possibilities for mid-Proterozoic marine redox state (reviewed in (Canfield, 1998; Lyons et al., 2009a; Lyons et al., 2009b). Another fundamental problem is that ocean anoxia, although strongly tied to atmospheric oxygen levels, is also heavily influenced by, among other factors, temperature, the nutrient status of the deep ocean, and particle sinking rates (Meyer and Kump, 2008).

With current approaches, our best estimates for oxygen levels in the mid-Proterozoic range widely and allow for dramatically different redox landscapes, with markedly contrasting implications for the evolution and ecology of early eukaryotic life.

Numerous research groups have proposed a causal link between a late Proterozoic atmospheric oxygen rise and metazoan evolution and diversification (e.g., Canfield and Teske, 1996; Frei et al., 2009; Love et al., 2008; Lyons et al., 2009b). However, as outlined above, solid constraints on oxygen levels in the ocean and atmosphere during this period are lacking, and it remains debated if oxygen levels in the mid- Proterozoic were low enough to preclude the evolution and ecological expansion of metazoan life (Butterfield, 2009).

The rise of oxygen at the Earth's surface is thought to have proceeding in two major steps. It is commonly assumed that there was a second significant rise to near modern atmospheric oxygen levels, at the end of the Proterozoic (Canfield, 2005; Holland, 1984; Knoll and Carroll, 1999). The timing and magnitude of this second oxygenation event, however, have been difficult to pinpoint. The appearance of metazoan fossils provides a minimum estimate for the timing of the Neoproterozoic oxygenation event. Given most animal's high respiratory requirements, it has been commonly proposed that an oxygenation event, potentially following the extensive Marinoan (ca. 635 Ma) glaciation, triggered early metazoan diversification (Hoffman and Schrag, 2002). Molecular clock estimates place the origin of crown-group animals and crown-group bilaterian animals in the Cryogenian Period (ca. 750 Ma) (Erwin, 2011). There is a well-established Cryogenian sponge biomarker record (Love et al., 2008). Similarly, there are numerous claims of sponge-like fossils in Crygenian or older rocks (Brain, 2012; Maloof, 2010; Neuweiler et al., 2009), but these fossils are controversial (Planavsky, 2009). The first widely accepted complex macroscopic metazoan fossils appear immediately above Marinoan-age glacial deposits in South China (Yin et al., 2007; Yuan et al., 2011). Additionally there is a diversification in marine algae following the Marinoan glaciation, which has been proposed to reflect a major ecosystem change driven by the initial diversification of predatory metazoans (Peterson and Butterfield, 2005). However, there is no direct geochemical evidence for an increase in ocean oxygenation in the immediate aftermath of the Marinoan glaciation. The predominance of existing geochemical evidence for Neoproterozoic redox shift is from much younger (< 580 Ma) sedimentary units. However, existing geochemical records of Neoproterozoic redox shift are controversial, or record a local shift in redox conditions that may not be globally representative (Butterfield, 2009; Canfield et al., 2007; Fike et al., 2006; Li et al., 2010; Scott et al., 2008). Therefore, despite extensive work on the evolution of Earth surface processes in the terminal Proterozoic over the past decade, we still have no consistent well-established view of the timing or dynamics of the rise to Phanerozoic-like oxygen levels.

In this thesis, I explore the major questions about the Earth's redox transformations outlined above. Specifically, in the first two chapters I explore the iron cycle and oxygen levels in the surficial ocean in the Archean with rare earth element and iron isotope systematics in iron formations. To compliment the iron formation rare earth element work, I have also examined rare earth element patterns in a set of Archean carbonates. In the third chapter, I explore the redox landscape of the mid-Proterozoic ocean. Specifically, I used a calibrated sequential iron speciation method to determine local redox conditions and provide insights into the local iron cycle in a temporally and spatially diverse set of fine-grained silicaclastic rocks. Lastly, in the finial chapter I explore the effect of an iron-rich ocean on marine phosphate concentrations. I use compilations of phosphorous and iron data in iron oxide-rich rocks to track have marine phosphate concentrations have changed through time. Thus the work presented in this thesis centers on how iron cycling and redox conditions at the Earth's surface have changed through time. The chapters are presented in manuscript form, with the first two chapters formatted for the journal *Geochimica et Cosmochimica Acta* and the second two chapters formatted for the journal *Nature*.

## References

Bekker, A., Slack, J., Planavsky, N., Krapež, B., Hofmann, A., Konhauser, K.O., Rouxel, O.J., 2010. Iron Formation: The Sedimentary Product of a Complex Interplay Among Mantle, Tectonic, Oceanic, and Biospheric Processes. Economic Geology 105, 467-508.

Brain, C.K.B., Prave, A.R., Hoffmann, K.-H., Fallick, A.E., Botha, A., Herd, D.A., Sturrock, C., Young, I., Condon, D.J., Allison, S.G., 2012. The first animals: ca. 760-million-year-old sponge-like fossils from Namibia. South African Journal of Geology 108, 1-8.

Butterfield, N.J., 2009. Oxygen, animals and oceanic ventilation: an alternative view. Geobiology 7, 1.

Canfield, D., Poulton, S., Narbonne, G., 2007. Late-Neoproterozoic deep-ocean oxygenation and the rise of animal life. Science 315, 92-95.

Canfield, D.E., 1998. A new model for Proterozoic ocean chemistry. Nature 396, 450-453.

Canfield, D.E., 2005. The early history of atmospheric oxygen: Homage to Robert A. Garrels. Annual Review of Earth and Planetary Sciences 33, 1-36.

Canfield, D.E., Teske, A., 1996. Late Proterozoic rise in atmospheric oxygen concentration inferred from phylogenetic and sulphur-isotope studies. Nature 382, 127-132.

Cloud, P., 1973. Paleoecological Significance of Banded Iron-Formation. Economic Geology 68, 1135-1143.

Erwin, D.H., Laflamme, M., Tweedt, S.M., Sperling, E.A., Pisani, D., Peterson, K.J.,, 2011. The Cambrian conundrum: Early divergence and later ecological success in the early history of animals. Science 334, 1091-1097.

Farquhar, J., Peters, M., Johnston, D.T., Strauss, H., Masterson, A., Wiechert, U., Kaufman, A.J., 2007. Isotopic evidence for Mesoarchaean anoxia and changing atmospheric sulphur chemistry. Nature 449, 706-705.

Farquhar, J., Zerkle, A.L., Bekker, A., 2011. Geological constraints on the origin of oxygenic photosynthesis. Photosynthesis Research 107, 11-36.

Fike, D.A., Gortzinger, J.P., Pratt, L.M., Summons, R.E., 2006. Oxidation of the Ediacaran Ocean. Nature 444, 744-747.

Frei, R., Gaucher, C., Poulton, S.W., Canfield, D.E., 2009. Fluctuations in Precambrian atmospheric oxygenation recorded by chromium isotopes. Nature 461, 250-225.

Hoffman, P.F., Schrag, D.P., 2002. The Snowball Earth hypothesis: Testing the limits of global change. Terra Nova 14, 129-155.

Holland, H.D., 1984. The Chemical Evolution of the Atmosphere and Oceans Princeton University Press, Princeton, NJ.

Holland, H.D., 2006. The oxygenation of the atmosphere and oceans. Philosophical Transactions of the Royal Society B-Biological Sciences 361, 903-915.

Kasting, J.F., 1987. Theoretical constraints on oxygen and carbon dioxide concentrations in the Precambrian atmosphere. Precambrain Research 34, 205-229.

Knoll, A.H., Carroll, S.B., 1999. Early animal evolution: emerging views from comparative biology and geology. Science 284, 2129-2137.

Kump, L., 2008. The rise of atmospheric oxygen. Nature 451, 277-278.

Li, C., Love, G.D., Lyons, T.W., Fike, D.A., Sessions, A.L., Chu, X.L., 2010. A Stratified Redox Model for the Ediacaran Ocean. Science 328, 80-83.

Love, G.D., Grosjean, E., Stalvies, C., Fike, D.A., Grotzinger, J.P., A.S., B., Kelly, A.E., Bhatia, M., W., M., Snape, C.E., Bowring, S.A., D.J., C., R.E., S., 2008. Fossil steroids record the appearance of Demospongiae during the Cryogenian period. Nature 457, 718-721.

Lyons, T.W., Anbar, A.D., Severmann, S., Scott, C., Gill, B., 2009a. Tracking euxinia in the ancient ocean: a multiproxy perspective and Proterozoic case study. Annual Review of Earth and Planetary Sciences 37:, 507-534.

Lyons, T.W., Reinhard, C.T., Scott, C., 2009b. Redox Redux. Geobiology 7, 489-494.

Maloof, A.C., Rose, C.V., Beach, R., Samuels, B.M., Calmet, C.C., Erwin, D.H., Poirier, G.R., Yao, N., Simons, F.J., , 2010. Possible animal-body fossils in pre-Marinoan limestones from South Australia. Nature Geoscience 3, 653-659.

Meyer, K.M., Kump, L.R., 2008. Oceanic euxinia in Earth history: Causes and consequences. Annual Review of Earth and Planetary Sciences 36, 251-288.

Neuweiler, F., Turner, E.C., Burdige, D.J., 2009. Early Neoproterozoic origin of the metazoan clade recorded in carbonate rock texture. Geology 37, 475–478.

Pavlov, A.A., Kasting, J.F., 2002. Mass-independent fractionation of sulfur isotopes in Archean sediments: Strong evidence for an anoxic Archean atmosphere. Astrobiology 2, 27-41.
Peterson, K.J., Butterfield, N.J., 2005 Origin of the Eumetazoa: Testing ecological predictions of molecular clocks against the Proterozoic fossil record. Proceeding of the National Academy of Sciences 102, 9547–9552.

Planavsky, N., 2009. Early Neoproterozoic origin of the metazoan clade recorded in carbonate rock texture: Comment. Geology 37, 195.

Rasmussen, B., Fletcher, I.R., Brocks, J.J., Kilburn, M.R., 2008. Reassessing the first appearance of eukaryotes and cyanobacteria. Nature 455, 1101-U1109.

Rye, R., Holland, H.D., 1998. Paleosols and the evolution of atmospheric oxygen: A critical review. American Journal of Science 298, 621-672.

Scott, C., Lyons, T.W., Bekker, A., Shen, Y., Poulton, S.W., Chu, X., Anbar, A.D., 2008. Tracing the stepwise oxygenation of the Proterozoic ocean. Nature 452, 456-U455.
Sverjensky, D.A., Lee, N., 2010. The Great Oxidation Event and Mineral Diversification. Elements 6, 31-36.

Yin, L., Zhu, M., Knoll, A.H., Yuan, X., Zhang, J., Hu, J., 2007. Doushantuo embryos preserved inside diapause egg cysts. Nature 446, 661-663.

Yuan, X. Chen, Z., Xiao, S., Zhou, C., Hua, H., 2011, An early Ediacaran assemblage of macroscopic and morphologically differentiated eukaryotes. Nature 470, 390-393.

# Chapter 1: Rare Earth Element and Yttrium Compositions of Archean and Paleoproterozoic Fe Formations Revisited: New Perspectives on the Significance and Mechanisms of Deposition

## Abstract

The ocean and atmosphere were largely anoxic in the early Precambrian, resulting in an Fe cycle that was dramatically different than today's. Extremely Fe-rich sedimentary deposits—i.e., Fe formations—are the most conspicuous manifestation of this distinct Fe cycle. Rare Earth Element (REE) systematics have long been used as a tool to understand the origin of Fe formations and the corresponding chemistry of the ancient ocean. However, many earlier REE studies of Fe formations have drawn ambiguous conclusions, partially due to analytical limitations and sampling from severely altered units. Here, I present new chemical analyses of Fe formation samples from 18 units, ranging in age from ca. 3.0 to 1.8 billion years old (Ga), which allow a reevaluation of the depositional mechanisms and significance of Precambrian Fe formations. There are several temporal trends in our REE and Y dataset that reflect shifts in marine redox conditions. In general, Archean Fe formations do not display significant shale-normalized negative Ce anomalies, and only Fe formations younger than 1.9 Ga display prominent positive Ce anomalies. Low Y/Ho ratios and high shale-normalized light to heavy REE (LREE/HREE) ratios are also present in ca. 1.9 Ga and younger Fe formations but are essentially absent in their Archean counterparts. These marked differences in Paleoproterozoic versus Archean REE+Y patterns can be explained in terms of varying REE cycling in the water column.

Similar to modern redox-stratified basins, the REE+Y patterns in late Paleoproterozoic Fe formations record evidence of a shuttle of metal and Ce oxides across the redoxcline from oxic shallow seawater to deeper anoxic waters. Oxide dissolution—mainly of Mn oxides—in an anoxic water column lowers the dissolved Y/Ho ratio, raises the light to heavy REE ratio, and increases the concentration of Ce relative to the neighboring REE (La and Pr). Fe oxides precipitating at or near the chemocline will capture these REE anomalies and thus evidence for this oxide shuttle. In contrast, Archean Fe formations do not display REE+Y patterns indicative of an oxide shuttle, which implies an absence of a distinct Mn redoxcline prior to the rise of atmospheric oxygen in the early Paleoproterozoic. As further evidence for reducing conditions in shallow-water environments of the Archean ocean, REE data for carbonates deposited on shallow-water Archean carbonate platforms that stratigraphically underlie Fe formations also lack negative Ce anomalies. These results question classical models for deposition of Archean Fe formations that invoke oxidation by free oxygen at or above a redoxcline. In contrast, I add to growing evidence that metabolic Fe oxidation is a more likely oxidative mechanism for these Fe formations, implying that the Fe distribution in Archean oceans could have been controlled by microbial Fe uptake rather than the oxidative potential of shallow-marine environments.

## Introduction

Fe formations are extensively studied, but still poorly understood, sedimentary rocks composed predominantly of authigenic iron-bearing carbonates, silicates, and oxides in a siliceous matrix. These marine chemical precipitates are often characterized by alternating Fe-rich and Fe-poor layers and therefore are commonly referred to as banded Fe formations (BIFs;(Holland, 2005; Klein, 2005). Fe formations host the majority of the world's economic Fe ore, which has fostered extensive research on their origin, depositional setting, and spatial and temporal distribution. There have been several recent reviews on Fe formations (Beukes and Gutzmer, 2008; Klein, 2005; Ohmoto et al., 2006).

The basic conditions leading to deposition of Fe formations in ancient oceans are generally agreed upon (Holland, 2005). Fe formations appear to be deposited either in close association with volcanic activity (Algoma-type Fe formations) or on submerged platforms on continental shelves more distal to submarine volcanic activity (Superior-type Fe formations) (Beukes and Gutzmer, 2008; Klein, 2005). The precursor particles to both types of Fe formations precipitated from seawater containing micromolar levels of dissolved ferrous Fe (Holland, 1973). A substantial marine ferrous Fe reservoir was possible due to: (1) a reducing atmosphere or one with a low oxidizing potential (Bekker et al., 2004; Holland, 1984), (2) low marine sulfate and sulfide concentrations (Canfield and Teske, 1996; Habicht et al., 2002), and (3) a high hydrothermal Fe flux (Kump and Seyfried, 2005). These conditions persisted, at least episodically, until the late Paleoproterozoic around 1.8 Ga (Holland, 1984; Poulton et al., 2004; Slack et al., 2007). Deposition of Fe formations appears to have been pulsed; the most significant periods occurred during emplacement of large igneous provinces, which enhanced hydrothermal Fe discharge (Barley et al., 1997; Isley and Abbott, 1999).

In contrast, detailed mechanisms involved in the deposition of Fe formations remain poorly resolved despite more than a century of investigation (Beukes and Gutzmer, 2008; Klein, 2005; Ohmoto et al., 2006). The classical and most widely accepted model for Fe formation deposition invokes ambient free oxygen induced ferrous Fe oxygenation. This model, championed by Preston Cloud (Cloud, 1965), suggests that deposition of Fe formation occurred at the interface between oxygenated shallow waters and upwelling Fe-rich reduced waters. The oxidizing shallow waters have been linked to prolific communities of oxygenic photosynthesizers (Cloud, 1973; Cloud, 1965).

Metabolic ferrous Fe oxidation was also proposed as a mechanism for Fe formation deposition. The potential importance of microaerophilic microbial Fe oxidation has been recognized for almost a century (Harder, 1919). Anoxygenic photosynthetic oxidation, photoferrotrophy, is another metabolic Fe oxidation pathway linked to Fe formation deposition by Garrels and Perry (Garrels and Perry, 1974) almost twenty years before organisms capable of this type of metabolism were cultured (Widdel et al., 1993). More recently, organisms able to metabolically couple Fe oxidation to nitrate reduction have been discovered (e.g. (Edwards et al., 2003), providing another possible microbially mediated mechanism for deposition of Fe formations.

It was also proposed that Fe formations may be purely abiogenic products. Many Fe formations are composed predominantly of Fe carbonates or Fe silicates suggested to be abiotic marine precipitates (e.g., (Ohmoto et al., 2004; Sumner, 1997). However, siderite in most Fe formations shows highly negative carbon isotope values, consistent with dissimilatory Fe reduction and formation of siderite during early diagenesis (Kaufman et al., 1990; Walker, 1984). Fe isotopes also appear to provide a signature for diagenetic siderite formation (Johnson et al., 2008; Johnson et al., 2004).

UV-induced ferrous Fe oxidation has also been advanced as an important mechanism (Anbar and Holland, 1992; Braterman et al., 1983), but the efficiency of UV-dependent oxidation in complex seawater solutions has been questioned (Konhauser et al., 2007). Ferrous Fe oxidation in hydrothermal fluids due to phase separation is yet another possible mechanism for Algoma-type Fe formation deposition (Foustoukos and Bekker, 2008), but this process cannot explain Superior-type Fe formations deposited on stable continental shelves away from submarine volcanic activity.

I have conducted a geochemical study on bulk samples from 18 different Fe formations ranging in age from the Archean to the Paleoproterozoic, bracketing the rise of atmospheric oxygen at ca. 2.4 Ga (Bekker et al., 2004), with the goal of better defining the mechanisms behind Fe formation deposition through time. Our study focuses on Rare Earth Element (REE) and yttrium (Y) concentrations in Fe formations, but I also present data for microbialite-dominated marine carbonates deposited on a shallow-water Archean carbonate platform. Both Fe formations and microbially mediated carbonates, as chemical precipitates, are well suited to trace element studies. These lithologies appear to be robust proxies for seawater composition, as long as contamination by clastic sediment and late-stage metamorphism/alteration are well understood (Bau and Dulski, 1996; Kamber and Webb, 2001; Slack et al., 2007; Webb and Kamber, 2000). By examining both shallow (carbonate) and deepwater (Fe formation) depositional environments it is possible to get a complete view of the ocean redox structure. An understanding of water-column redox structure is necessary to distinguish among competing models for the origin of Fe formations. Since Y is geochemically similar to the heavy REE Ho but displays different complexion properties in marine systems (Ho is scavenged on particulate matter two times faster than Y; (Nozaki et al., 1997)), I also use Y/REE ratios to elucidate paleooceanographic processes.

Although REEs have long been used to elucidate mechanisms of Fe formation genesis, the conclusions of many previous studies are compromised by inaccurate or incomplete REE analyses and by a limited number of measurements, as discussed by (Bau and Dulski, 1996). Earlier studies focused mainly on Ce and Eu anomalies as proxies for ocean redox state and hydrothermal flux, respectively. Our study differs from previous work by focusing on evidence for an oxide shuttle from shallow oxic to deeper anoxic waters in late Paleoproterozoic oceans and in highlighting that this process appears to have been absent in the Archean and early Paleoproterozoic.

## Materials and Methods

### *Sample description*

I are using a definition for Fe formation that differs slightly from that of Klein (2005).

For our purposes, siliceous and Fe-rich sedimentary chemical precipitates with low levels of detrital siliciclastic or volcaniclastic material (< 1% $Al_2O_3$) and greater than 10% total Fe are considered to be Fe formations, regardless of whether Fe is associated with a carbonate or oxide phase. This composition-based definition of Fe formation encompasses both granular and banded Fe formations as well as ferruginous cherts (e.g., distal hydrothermal jaspers). For comparison, I also present data for ferruginous shales associated with Fe formations to demonstrate the effect of siliciclastic material on REE patterns. Basic sample information, mineralogy, as well as major and trace element compositions are presented in Appendix Tables 1 and 2.

I also investigated the Mosher carbonates of the ca. 2.9 Ga Steep Rock Group from the Superior Province. The Mosher carbonates offer insight into shallow-water marine conditions; these carbonates are composed of seafloor precipitates that span a significant bathymetric gradient (Fralick et al., 2008; Kusky and Hudleston, 1999). Past work has confirmed that authigenic carbonate precipitates are well suited to reconstructing basin-scale changes in seawater composition (e.g., REEs, Fe, Mn; see(Kamber and Webb, 2001; Sumner and Grotzinger, 2004).

### *Methods*

Clean rocks were crushed between two plexiglass discs inside a Teflon bag using a hydraulic press. Rock chips were rinsed several times with deionized water during ultrasonication. The cleaned material was powdered in an agate shatterbox. In some cases, I removed material from the crushed chips containing significant detrital component (e.g., lenses of siliciclastic sediments) using a binocular microscope.

Sample powders were weighed in 5 mL Teflon beakers and dissolved using 2 mL of concentrated trace metal grade $HNO_3$ with 2 mL of concentrated HF. After evaporation on a hot plate at 50°C, complete dissolution and Fe oxidation were achieved by a second evaporation step using 4 mL of *aqua regia*. The dry residue was then dissolved in 4 mL of 6N HCl and 1 drop of $H_2O_2$ by heating at 40°C in a closed vessel. Organic carbon was not attacked by this procedure and was always present in trace amounts. Carbonates were dissolved in pre-cleaned 14 mL polypropylene test tubes in 5% sub-boiling triple-distilled $HNO_3$.

Analyses of REEs + Y and Ba were performed on a ThermoElectron Inc. Element2 inductively coupled plasma–mass spectrometer (ICP–MS) at the Woods Hole Oceanographic Institution (WHOI) and on a ThermoElectron Inc. XSeriesII ICP–MS at Laurentian University. At WHOI, solutions were injected into the plasma using a Cetac Aridus® desolvating nebulizer to reduce isobaric interferences (e.g., $^{135}Ba^{16}O^+$ on $^{151}Eu^+$). Formation of Ba and REE oxides was monitored throughout the analytical session by periodic aspiration of Ba and Ce spikes. Ba–oxide formation was significantly less than 1% of the total Ba in solution. Any isobaric interference of $BaO^+$ on $Eu^+$ would have decreased the measured $^{151}Eu/^{153}Eu$ ratio below that naturally occurring (~0.89). In almost all samples no bias was observed, and no correction for BaO interference was required.

REE–oxide formation was typically less than ~ 4 % of total REE concentration. Samples were spiked with 5 ppb of internal In standard to correct for fluctuations of the plasma during the analytical session. Unknown sample concentrations were calibrated against matrix–matched, multi–REE standards prepared with Specpure plasma solution standards. Background intensities were measured periodically by aspirating 5% $HNO_3$ blanks. Accuracy of our analyses is conservatively estimated to be ±10%, and rare earth element ratios are estimated to be accurate within ±5%, based on multiple analyses of randomly selected samples across multiple analytical sessions. Analytical precision and the accuracy of our measurements of REE abundances and ratios were also checked by multiple analyses of the geostandards IF-G and BHVO-1 (Table 2). Reproducibility at WHOI was better than 5% for all REEs + Y.

I analyzed trace element concentrations at Laurentian University using a method modified from Eggins et al. (1997), which employs internal standards ($^{6}$Li, In, Re, Bi, and $^{235}$U) and external drift correction. The instrument was tuned to 1.5% $CeO^+/Ce^+$, and all isobaric interferences were corrected using oxide formation rates determined for pure elemental solution measured immediately after sample analysis. With this method, REE in basaltic rock standards such as BHVO-1 and -2 can be reproduced to better than 1% rsd using a quartz spray chamber (see (Kamber, 2009), for more information). Carbonates normally have low trace element concentrations, and precision for carbonate samples was consequently only better than 2% for all REEs + Y.

Major elements in the Fe formation samples (Fe, Al, Ca, and Mg) were determined using the medium-resolution mode of the *Element II* at WHOI with a quartz spray chamber. Similarly to the REE procedure, In was used as an internal standard, and the data were calibrated by standardization to the geostandard BHVO-1. Analytical precision and accuracy of element abundances were checked by multiple analyses of the geostandards IF-G and BHVO-2; reproducibility was better than 5%. Selected samples representative of the various matrices were sent to Activation Laboratories Ltd. (Ancaster, Ontario) for additional geochemical analysis. Major and trace elements were analyzed at Activation Laboratories by ICP-AES and ICP-MS, respectively, after lithium metaborate/tetraborate fusion. Major element compositions and REE anomalies determined by both techniques are reproducible within 5%.

## Results

### *Rare Earth Elements in Fe formations*

I observe several temporal trends in REE patterns normalized to shale composites (Post-Archean Australian Shale - PAAS), hereafter referred to as $REE_{(SN)}$ (Fig. 1.1). First, none of the samples of Fe formation contain statistically significant negative $Ce_{(SN)}$ anomalies. True negative $Ce_{(SN)}$ anomalies, as defined in Figure 1.2, have Ce/Ce* ($Ce_{(SN)}/(0.5Pr_{(SN)} + 0.5La_{(SN)})$) and Pr/Pr* ($Pr_{(SN)}/(0.5Ce_{(SN)} + 0.5Nd_{(SN)})$) values less than and greater than unity, respectively. This approach, described by Bau and Dulski (1996), discriminates between positive La and true negative $Ce_{(SN)}$ anomalies. Positive $Ce_{(SN)}$ anomalies are not present in our samples older than ca. 1.9 Ga (Fig. 1.2).

Second, late Paleoproterozoic Fe formations display a much wider range of light-to-heavy REE ratios compared to the older Fe formations. Light-to-heavy REE ratios are calculated as the $Pr_{(SN)}/Yb_{(SN)}$ ratio (Fig. 1.1C). Early Paleoproterozoic and Archean Fe formations are characterized by light REE depletion, while the late Paleoproterozoic examples show a wide range of light-to-heavy REE ratios that are well above and below the ratio of the shale composite (Fig. 1.1C). Fe formations with a significant siliciclastic contribution are characterized by shale-like, flat REE patterns.

Thirdly, there are significant differences in the shale-normalized behavior of Y in late Paleoproterozoic Fe formations compared to those of early Paleoproterozoic and Archean age. The Archean and early Paleoproterozoic examples have positive $Y_{(SN)}$ anomalies (Fig. 1.1D). The average Y/Ho ratio for Archean and early Paleoproterozoic Fe formations in our sample set is 39, which is markedly higher than the shale composite ratio of ~27. In contrast, late Paleoproterozoic Fe formations have a wide range of Y/Ho ratios, both above and below the shale composite value, with an average Y/Ho ratio for our sample set of 32. Ferruginous shales—that is, samples with more than 5% $Al_2O_3$—are characterized by Y/Ho ratios that are similar to that of the shale composite.

Finally, nearly all of the analyzed Fe formations contain significant positive shale-normalized Eu anomalies. Eu anomalies are calculated as $Eu_{(SN)}/(0.66Sm_{(SN)} + 0.33Tb_{(SN)})$ because seawater can have a slight positive Gd anomaly. $Eu_{(SN)}$ anomalies range from

1.01 to 4.29 and have an average of 2.1 for Archean and late Paleoproterozoic Fe formations. The late Paleoproterozoic examples contain lower $Eu_{(SN)}$ anomalies, ranging from 1.15 to 2.46 with an average of 1.5.

### *Rare Earth Elements in Mosher carbonates*

Carbonates sampled from the Steep Rock Group have REE+Y concentrations that vary from 0.01 to 6.26 ppm. These REE concentrations are similar to those reported for other non-skeletal carbonates with only low concentrations of the elements associated with clastic sediment, such as Ga and Zr. Concentrations of Zr in the Mosher carbonates vary from 0.02 to 0.27 ppm, which is much less than the shale composite values of ~200 ppm. The Mosher carbonates have shale-normalized REE patterns similar to those of the Archean and early Paleoproterozoic Fe formations (Fig. 1.3). Specifically, the patterns lack significant negative $Ce_{(SN)}$ anomalies (Fig. 1.4), are light $REE_{(SN)}$-depleted, have Y/Ho ratios higher than shale composites, and exhibit positive $Eu_{(SN)}$ anomalies. On a Ce and Pr anomaly scatter diagram (Fig. 1.4), the Steep Rock carbonates plot in the same field as Archean Fe formations and ca. 2.5 Ga Campbellrand carbonates. It is interesting to compare the Mosher and Campbellrand carbonates since they both were deposited in shallow-water environments and stratigraphically underlie Fe formations. Their $Ce_{(SN)}$ and $Pr_{(SN)}$ anomalies are distinct from those observed in modern (e.g., KAMBER and WEBB, 2000) and early Phanerozoic (e.g., NOTHDURFT et al., 2004) non-skeletal and microbial carbonates (Fig. 1.4). The Steep Rock $Eu_{(SN)}$ anomalies ($Eu_{(SN)}/(0.66Sm_{(SN)} + 0.33Tb_{(SN)})$) range from 2.75 to 3.86, which is, on average, higher than the values seen in the analyzed Archean Fe formations or in the Campbellrand carbonates.

There are similar correlations (Fig. 1.5) between REE characteristics in the Mosher carbonates and those in the Campbellrand carbonates (Kamber and Webb, 2001), likely linked with water column REE fractionations. Similar to the Campbellrand carbonates, within the Mosher carbonates there is a correlation between $Ce_{(SN)}$ and $Y_{(SN)}$ anomalies and between both $Ce_{(SN)}$ and $Y_{(SN)}$ anomalies and the degree of light REE depletion (Fig. 1.5). Variation in the $Ce_{(SN)}$ anomaly of the Mosher carbonates reflects La-enrichment rather than non-conservative Ce behavior, given the limited range of the $Pr_{(SN)}$ anomalies (Fig. 1.4; cf. (Kamber and Webb, 2001)). There is not a strong correlation between the $Eu_{(SN)}$ anomalies and either Y/Ho or $Pr_{(SN)}/Yb_{(SN)}$ ratios either the Campbellrand or Steep Rock carbonates (Fig. 1.5D).

## Discussion

### *REE signatures of redox-stratified basins and their preservation in marine Fe-oxide deposits and carbonates*

REE behavior in modern redox-stratified basins is well known. The capture and preservation of aqueous REE patterns in marine chemical precipitates provides a window into ancient ocean chemistry and redox state. In general, oxygenated modern marine settings display a strong negative $Ce_{(SN)}$ anomaly when normalized to shale composites, while suboxic and anoxic waters lack significant negative $Ce_{(SN)}$ anomalies (Byrne and Sholkovitz, 1996; German and Elderfield, 1990). Essentially following German and

Elderfield (1990), I consider waters suboxic if they contain low levels of dissolved oxygen (0.05-5 μmol $O_2$) and no dissolved sulfide. Oxidation of Ce(III) greatly reduces Ce solubility, resulting in preferential removal onto Mn–Fe oxyhydroxides, organic matter, and clay particles (Byrne and Sholkovitz, 1996). In contrast, suboxic and anoxic waters lack significant negative $Ce_{(SN)}$ anomalies due to reductive dissolution of settling Mn-Fe-rich particles (Byrne and Sholkovitz, 1996; German et al., 1991). Similarly, light REE depletion develops in oxygenated water bodies due to preferential removal of light versus heavy REEs onto Mn–Fe oxyhydroxides and other reactive surfaces due to differential REE particle reactivity, which is linked with REE carbonate complexation. The ratio of light to heavy REEs increases markedly across redox boundaries due to reductive dissolution of Mn-Fe oxyhydroxides (Byrne and Sholkovitz, 1996; German et al., 1991) see also Fig. 1.6A). In many redox-stratified basins the $Ce_{(SN)}$ anomaly and the light to heavy REE ratio return to near-shale composite values across the Mn and Fe redox boundaries. In some basins, however, positive $Ce_{(SN)}$ anomalies and light REE enrichment develop in anoxic and suboxic waters due to reductive dissolution (Bau et al., 1997b; De Carlo and Green, 2002; Debaar et al., 1988; Schijf et al., 1995). Redox-induced change in REE patterns in some modern redox-stratified basins can be linked directly to Mn cycling in the suboxic zone (De Carlo and Green, 2002; German et al., 1991).

Yttrium displays the inverse behavior of light REEs and Ce in redox-stratified basins. It is less particle-reactive than its geochemical analogue Ho, resulting in Y/Ho ratios in marine environments that are higher than shale composites (Bau et al., 1997b; Nozaki et al., 1997). Since the difference in Y and Ho particle reactivity is well expressed in metal oxides, there is a decrease in dissolved seawater Y/Ho ratios in suboxic and anoxic waters driven by an increase in Ho relative to Y as Mn-Fe-rich particles dissolve (Bau et al., 1997b).

Marine sediments rich in authigenic Fe and non-skeletal carbonates have been shown to provide a qualitative record of seawater REE and Y patterns (e.g., Bau and Dulski, 1996). Fe oxides at close to neutral pH record Ce anomalies and REE patterns of the water column from which they precipitated qualitatively, in contrast to Mn oxides that scavenge Ce and heavy REE preferentially (De Carlo et al., 1998; BAU, 1999; Ohta and Kawabe, 2001). For instance, particles from Mn-poor hydrothermal plumes essentially record a seawater REE pattern (e.g., (Sherrel et al., 1999). There is preferential Ho relative to Y sorption onto Fe oxides at circum-neutral pH (Bau, 1999), but particles from modern Mn-poor hydrothermal plumes nevertheless record near-seawater Y/Ho ratios that are notably higher than ratios of shale composites (Edmonds and German, 2004).

The primary, near-seawater REE patterns in carbonate precipitates and Fe oxide-rich sediments are unlikely to change significantly during typical burial diagenesis and metamorphism. REEs in siliceous, Fe oxide-rich sediments and non-skeletal carbonates appear to be rock buffered under the low water-rock ratios typical of most early to late stage diagenetic and metamorphic conditions (Klein and Beukes, 1989). REE sorption to Fe oxides and dissolved speciation are strongly influenced by aquatic carbonate chemistry (e.g. Moller and Bau, 1993; Quinn et al., 2006). However, the marine carbonic acid system is likely to have been constant enough through Earth's history (e.g. Holland, 1984) that this characteristic does not undermine the paleoproxy potential of REE. One significant caveat is that carbonate and siliceous Fe oxide-rich sediments can be useful as a paleoceanographic proxy only if their siliciclastic contents are very low (Kamber and Webb, 2001; Nothdurft et al., 2004). Thus, Fe oxides and non-skeletal carbonates essentially record the REE patterns of the waters from which they precipitated. These patters are likely to be retained as the sediments become rock and experience low grade metamorphism (Bau, 1999; Bau and Dulski, 1996; Slack et al., 2007).

### *Rare Earth Element patterns in Fe formations as tracers of ancient ocean redox*

The observed temporal trends in REE patterns in Fe formations likely reflect the long-term evolution of marine redox structure. The absence of any deviations from trivalent Ce behavior in Archean and early Paleoproterozoic Fe formations in our dataset suggests that the basins in which Fe formations were deposited were reducing with respect to Ce. Cerium has a redox potential close to Mn, indicating that the water column remained reducing with respect to Mn prior to the rise in atmospheric oxygen at ca. 2.4 Ga (Bekker et al., 2004). In contrast, ca. 1.9 Ga Fe formations deposited after the rise of atmospheric oxygen commonly show positive Ce anomalies. The positive Ce anomalies indicate an oxidative Ce cycle in combination with a shuttle of Mn oxyhydroxide particles across a redoxcline. Dissolution of these metal oxyhydroxides would have increased the seawater dissolved Ce content. As seen in some modern basins (Bau et al., 1997b; De Carlo and

Green, 2002; Debaar et al., 1988)this dissolution would at times have led to the formation of positive dissolved Ce anomalies in deeper, anoxic-suboxic waters. Positive Ce anomalies would be transferred to the sedimentary record when Fe oxyhydroxide precipitation occurred in these suboxic or anoxic waters. Positive Ce anomalies in samples of ca. 1.9 Ga Mn-poor Fe formation likely indicate a dissolved positive Ce anomaly, given that experimental work suggests (in contrast to Mn oxides) that minimal or no preferential Ce scavenging onto Fe oxyhydroxides occurs in the pH range relevant to marine conditions (Bau, 1999; Koeppenkastrop and Decarlo, 1992)

I propose that the observed temporal trend in trivalent REE+Y patterns also reflects evolution of marine redox structure. Light REE depletion and high Y/Ho ratios in Archean and early Paleoproterozoic Fe formations are at odds with the assumption that Fe oxide precipitation occurred in the transition zone between oxic and anoxic waters. Under such transitional conditions, as described above for modern redox-stratified basins, significant variability is expected in light-to-heavy REE and Y/Ho ratios, with variability induced by oxidative scavenging and reductive dissolution. By analogy to these modern settings, I would also expect nearly flat aqueous REE patterns and low Y/Ho ratios in the water column near the Mn redoxcline (Fig. 1.6). These patterns should be recorded in Fe oxide-rich sediments if the ferrous Fe oxidation and ferric Fe particle formation (the precursor particles of to Fe formations) occurred in low oxygen conditions. I see evidence for this oxide shuttle in late Paleoproterozoic Fe formations, which have significant ranges in both Y/Ho and light-to-heavy REE (Pr/Yb$_{(SN)}$) ratios (both below and above the shale composite values). I interpret this range of light-to-heavy REE and Y/Ho ratios in late Paleoproterozoic Fe formations as a proxy for deposition in water masses with varying contributions of REE +Y from precipitation and dissolution of Mn-Fe-oxyhydroxides. This interpretation implies deposition of late Paleoproterozoic Fe formations under varying redox conditions in basins with a strong redoxcline separating the oxic upper portion of the water column from the suboxic to anoxic deeper portion (Planavsky et al., 2009). In contrast, strong light REE depletion and Y enrichments in almost all Archean Fe formations suggest the absence of an oxide shuttle across a Mn redoxcline.

The wide range of Y/Ho and $Pr/Yb_{(SN)}$ ratios in late Paleoproterozoic Fe formations is unlikely to be related to basin isolation or varying degrees of detrital contribution. In the Biwabik Fe Formation of the ca. 1.9 Ga Lake Superior region (Table 1), there is no systematic stratigraphic trend in either $Pr/Yb_{(SN)}$ or Y/Ho ratios within the LWD-99-2 drill core (Fig. 1.7), which penetrates the entire formation. Gradual basin isolation, potentially related to large-scale tectonic processes is, therefore, an unlikely cause for the observed range in the $Pr/Yb_{(SN)}$ and Y/Ho ratios. There is no covariation between $Pr/Yb_{(SN)}$ and Y/Ho ratios and the level of siliciclastic contribution (e.g., $Al_2O_3$; Fig. 1.8) in any of the examined Fe formations. Lack of significant covariation between light-to-heavy REE and Y/Ho ratios and proxies for detrital mineral contribution precludes the possibility that siliciclastic input was the predominant control over the trivalent REE+Y patterns. Similarly, there is no covariation in cross plots of Mn concentration and REE anomalies.

### *Rare Earth Element Patterns in Archean carbonates as tracers of ocean redox*

The REE+Y patterns of the Archean Mosher and Campbellrand carbonates provide additional support for widespread reducing conditions during Fe formation deposition prior to the rise of atmospheric oxygen. The lack of any significant deviation from trivalent Ce behavior in these units (Fig. 1.4) indicates that Ce(III) oxidation was not prevalent during the Archean Eon even on shallow-water carbonate platforms. Given that Ce oxidation is kinetically inhibited, and as such is typically microbially mediated (MOFFETT, 1994), this conclusion does not necessarily demand that the shallow ocean was completely devoid of $O_2$. However, the lack of Ce anomalies suggests that free $O_2$ was not consistently present even at low ($< 5\ \mu$M) levels, conservatively assuming that Ce and Mn oxidation require similar levels of free $O_2$ (for a case study on Mn oxidation kinetics see (Kamber and Webb, 2001)).

The Mosher carbonates analyzed for REE+Y composition span a significant depth gradient. For instance, I have analyzed deeper-water fenestrate microbialites and shallow-water bioherms surrounded by grainstones (Appendix Table 3). Lack of true negative Ce anomalies is, therefore, not an artifact of local Ce maxima in surface waters (*cf.* MOFFETT, 1994). Additionally, covariation among $Pr/Yb_{(SN)}$ and Y/Ho ratios and $La_{(SN)}$ anomalies in both the Steep Rock and Campbellrand carbonates suggests aquatic REE processing, likely along a water-column depth gradient (*cf.* (Kamber and Webb, 2001)). Since Ce appears to be released preferentially during early diagenesis under reducing conditions (Byrne and Sholkovitz, 1996; Haley et al., 2004), lack of true negative $Ce_{(SN)}$ anomalies in Late Archean carbonates is unlikely to be linked to early diagenetic alteration.

Presence of strong positive $Eu_{(SN)}$ anomalies in both the Steep Rock and Campbellrand carbonates is also consistent with widespread reducing conditions. Eu enrichment in chemical sedimentary rocks precipitated from seawater indicates a strong influence of high-temperature reducing hydrothermal fluids on the dissolved REE load of seawater (Derry and Jacobsen, 1988, 1990; Klinkhammer et al., 1983). Presence of a hydrothermal REE signature reveals information about the redox state of the deep ocean. Under oxic conditions, hydrothermal plumes act as a sink for seawater REEs due to their co-precipitation with Fe oxides (Kamber and Webb, 2001). Under anoxic conditions, hydrothermal systems are a REE source to the ocean.

Sedimentary features and trace element composition of Earth's earliest carbonates are also consistent with generally reducing Archean and early Paleoproterozoic shallow seawater. A predominance of *in situ* carbonate production is thought to reflect high levels of carbonate supersaturation and significant concentrations of aqueous Mn and Fe (SUMNER and GROTZINGER, 2004). Fe and, to a lesser extent, Mn are strong inhibitors of calcite and aragonite nucleation. Nucleation inhibition due to presence of high dissolved

Fe concentrations thus provides a simple explanation for enigmatic carbonate precipitates, such as the giant aragonite fans and thick herringbone calcite beds that are common on the Steep Rock and Campbellrand carbonate platforms (Kusky and Hudleston, 1999; Sumner, 1997; Sumner and Grotzinger, 2004). Consistent with this model, well-preserved Archean limestones have Fe and Mn concentrations significantly higher than those of Proterozoic and Phanerozoic carbonates (Veizer et al., 1989). These enrichments are thought to reflect high aqueous concentrations of these metals (Sumner and Grotzinger, 2004; Veizer et al., 1989), implying reducing conditions on shallow Archean carbonate platforms.

### *Comparison with previous REE studies of Fe formations*

REE studies of Fe formations have a long history (Alexander et al., 2008; Bau and Dulski, 1996; Bau and Moller, 1993; Derry and Jacobsen, 1990; Frei et al., 2008; Freyer, 1976; Kato et al., 2006; Klein and Beukes, 1989), which invites a comparison between previous results and those obtained in this study. While many studies of the trace element composition of Fe formations have yielded REE+Y patterns generally consistent with the temporal trends elucidated in this study (Alexander et al., 2008; Bau and Dulski, 1996; Bau et al., 1997a; Bau and Moller, 1993; Frei et al., 2008; Freyer, 1976; Prakash and Devapriyan, 1996), many others have suggested that there is a deviation from trivalent Ce behavior in Archean and early Paleoproterozoic seawater (e.g. (Kato et al., 2002; Kato et al., 1996; Kato et al., 1998; Kato et al., 2006; Khan and Naqvi, 1996; Klein and Beukes, 1989; Ohmoto et al., 2006; Spier et al., 2007). This assertion stands in contrast to the conclusions of this study (Fig. 1.2). Although the significance of each reported case of negative or positive Ce anomalies in Archean rocks needs to be discussed individually, it is important to note some of the potential reasons underlying the disparity between this and previous studies of REE in Fe formations.

Many previous REE studies may be compromised by inaccurate and incomplete measurements (Bau and Dulski, 1996). For example, many of the REE studies that infer an oxidative Ce cycle were performed using instrumental neutron activation analysis (e.g., (Klein and Beukes, 1989) rather than with more accurate and precise inductively coupled plasma mass spectrometry. Isotope dilution studies could not measure monoisotopic Pr (the neighboring element of Ce in the REE series), making it impossible to quantify Ce anomalies meaningfully. Because La displays non-conservative behavior in marine systems, the true Ce anomaly must thus be calculated using Nd and Pr (see (Bau and Dulski, 1996), for discussion). ICP-MS datasets can also be affected by analytical issues. One potentially problematic issue arises when Ce, the most abundant REE in calibration standards, is analyzed in an analogue detector mode, while the REE-poor BIFs and carbonates are analyzed in a pulse count mode.

Differences in sampling strategy can also account for disparities in perceived Ce behavior. For example, some of the Ce anomalies in Archean Fe formations were observed in microdrilled samples (e.g., (Ohmoto et al., 2006). Our analyses, in contrast, were performed on bulk samples. Interestingly, most of the previously observed negative

Ce anomalies were documented in solitary samples, and none of these studies showed consistent Ce anomalies in stratigraphic context in a suite of representative samples. Therefore, at least some of these negative Ce anomalies likely reflect metamorphic or more recent weathering-related redistribution of REEs between metamorphic minerals and compositionally different layers or between soil horizon and bedrock. Analyzing bulk samples discriminates against these finer patterns. Although a microsampling strategy may capture interesting primary redox dynamics, this approach is more susceptible to record the effects of post-depositional redistribution. Bulk sampling should instead reveal the overall ambient primary conditions independent of local repartitioning.

Our observation of high Y/Ho ratios and light REE depletion in Archean Fe formations is generally consistent with previous work, but there are exceptions. For example, flat or light REE enriched (shale normalized) REE patterns are common in some Archean Fe formations (e.g., KATO et al., 2006). These patterns could be linked with an oxide shuttling processes as outlined above for late Paleoproterozoic Fe formations, but they could also reflect a strong hydrothermal influence, high detrital contribution, or later-stage alteration. Interestingly, similar to our findings, Frei et al. (2008), in an extensive study of Fe formations from the Black Hills area of the central United States, found that low Y/Ho ratios were much more common in Fe formations deposited after 2.4 Ga.

### *Implications of Rare Earth Element patterns for the origin of Fe formations*

Our REE study provides evidence for redox evolution in the Archean to late Paleoproterozoic ocean, which has mechanistic implications for the production of Fe formation. Late Paleoproterozoic examples display a clear REE signature of ocean redox stratification and Fe formation deposition under varying redox conditions. Thus, the late Paleoproterozoic Fe formations appear to have formed through a combination of abiotic Fe oxidation at a redox interface and Fe oxidation under suboxic or anoxic conditions, which was likely microbially mediated. Archean and early Paleoproterozoic Fe formations, in contrast, do not show REE patterns indicative of deposition from a water column with a Fe-Mn redoxcline. Archean and early Paleoproterozoic carbonate successions deposited under conditions shallower than those of the basinal metalliferous sediments also contain REE patterns indicative of persistently reducing conditions. Thus, the late Paleoproterozoic and older Fe formations hold signatures of differing ocean redox structure, which suggests different modes of formation. Given the lack of evidence for either a Mn oxide shuttle or marked redox stratification as well as the apparently low oxidizing potential of shallow-water environments in Archean and early Paleoproterozoic oceans, classical models for Fe formation genesis that assumed oxidation at or above a well-established redoxcline should be reevaluated. Constraints on ocean redox structure provided by this study, coupled with evidence for an initial Fe oxyhydroxide phase in the majority of Fe formations (Ahn and Buseck, 1990; Beukes and Gutzmer, 2008; Kaufman et al., 1990; Klein, 2005; Pecoits et al., 2009), suggest that anoxic Fe oxidation was a common process in the Archean and early Paleoproterozoic before the rise of atmospheric oxygen.

Abiotic anoxic ferrous Fe oxidation mechanisms do not currently appear to have important in Fe formation genesis in the Archean and early Paleoproterozoic. UV-driven photochemical Fe oxidation in anoxic oceans would be consistent with our geochemical results. UV photolysis, however, has not been demonstrated to be efficient in complex seawater solutions (Konhauser et al., 2007). Under otherwise anoxic conditions, hydrothermal hypersaline brines may develop oxidizing and alkaline conditions along with metal enrichments due to phase separation (into vapor and brine) and the strong affinity of transition metals for chloro-complexes. It is possible that Fe oxyhydroxides could form in these brines (Foustoukos and Bekker, 2008). However, this process cannot explain Superior-type Fe formations deposited on stable continental shelves not in the immediate proximity of submarine volcanic activity. Further, currently there is no empirical evidence that this process can occur.

In this light, the rain of ferric oxides that drove Fe formation accumulation in the Archean and early Paleoproterozoic is most likely linked with metabolic microbial Fe oxidation. Our study does not offer insights into the relative importance of photoferrotrophy, microaerophilic Fe oxidation, and nitrate-dependant Fe oxidation. The relative importance of these pathways of metabolic Fe oxidation likely varied widely among different basins and under different oceanographic conditions, but nitrate was likely insignificant in the Archean and early Paleoproterozoic anoxic oceans before the rise of atmospheric oxygen. Considering these redox constraints over metabolic pathways, photoferrotrophy (and possibly microaerophilic Fe oxidation) is the most viable biological pathway for Fe oxidation in the early Earth's anoxic oceans.

There is also a strong theoretical basis for suggesting that metabolic Fe oxidation could drive Fe formation deposition. Konhauser et al. (Konhauser et al., 2002) demonstrated that even modest populations of photosynthetic Fe oxidizers could account for deposition of Fe formations, despite their inferred rapid rates of accumulation (Barley et al., 1997). Recent modeling indicates that metabolic Fe oxidation can result in near quantitative drawdown of upwelling ferrous Fe under a wide range of ocean mixing and circulation rates (Kappler et al., 2005). Even under the present oxygenated surface conditions, photoferrotrophy is an important means of Fe oxidation in Lake Matano, a ferruginous modern redox-stratified lake in Indonesia that appears to be a good analog for the Archean ocean (CroI et al., 2008). Our study provides empirical support for Fe formation deposition by metabolic Fe oxidation in the Archean and early Paleoproterozoic, which complements the growing mass of geobiological and microbiological evidence for the importance of this process.

Evidence for extensive metabolic Fe oxidation implies that the Fe distribution in the Archean and early Paleoproterozoic oceans could have been controlled by microbial Fe utilization rather than by the redox potential of shallow environments. Additionally, Fe oxidizing microbial ecosystems would have used upwelling dissolved phosphorous and ammonium as well as dissolved Fe. This relationship could have forced oligotrophic conditions in many shallow environments (depending on the balance of Fe and nutrient availability), limiting the levels of oxygenic photosynthesis and allowing for persistence of reducing conditions in shallow environments. Indeed, photoferrotrophs in modern Lake Matano force oligotrophic conditions in surface waters (CroI et al., 2008) due to microbial nutrient consumption and adsorption of dissolved phosphorous onto microbial Fe oxyhydroxides, providing a modern example of the effects of metabolic microbial Fe oxidation on ecosystem stratification and redox structure. This positive feedback favoring anoxic conditions in shallow-water environments would likely be lessened during periods of low hydrothermal Fe flux.

## Conclusions

I have analyzed the REE+Y compositions of bulk samples from 18 separate Fe formations and provide a reevaluation of Fe formation trace element compositions. There are several temporal trends in our Fe formation dataset that appear to reflect the evolution of the ocean redox structure. None of the analyzed Archean and Paleoproterozoic Fe formations contains statistically significant negative shale-normalized Ce anomalies. Positive Ce anomalies are not present in our dataset until ca. 1.9 Ga. Lower Y/Ho and higher light-to-heavy REE ratios compared to those of shale composites also first appear in ca. 1.9 Ga BIFs.

The lack of significant ocean redox stratification prior to the rise of atmospheric oxygen at ca. 2.3 Ga is the most parsimonious explanation of these trends. In a stratified ocean, metal and Ce oxides from oxic waters will be transported and redissolved below the redoxcline. Mn and Ce oxide dissolution in an anoxic water column would lower the Y/Ho ratio, raise the light-to-heavy REE ratio, and increase the concentration of Ce relative to neighboring REEs. Fe oxides precipitated near the chemocline will capture these seawater REE patterns, and their settling will lead to deposition of Mn-poor Fe formations. These Fe formations will record evidence of an active oxidative Mn cycle. Evidence for this oxide shuttling appears to be absent until sometime after the early Paleoproterozoic. I also present REE data from a shallow-water Archean carbonate platform. Carbonates from this environment similarly lack Ce anomalies, providing additional evidence for the absence of a Mn redoxcline in Archean and early Paleoproterozoic oceans. However, our results do not imply a total absence of oxygen in the Earth's early oceans; transient or very low levels of free oxygen in the surface ocean are consistent with our model.

REE evidence provided in this study for evolution of Precambrain ocean redox structure also has implications for our understanding of the origin of Fe formations. Late Paleoproterozoic Fe formations display a clear REE signature indicative of basin- and potentially even ocean-scale redox stratification and deposition of Fe formation under varying redox conditions. Therefore, the late Paleoproterozoic (ca. 1.9 Ga) Fe formations appear to have formed through a combination of metabolic microbial Fe oxidation in suboxic and anoxic conditions and non-biological oxidation of Fe at a redox interface. In contrast, the lack of evidence for marked redox stratification and an oxide shuttle, along with the low oxidizing potential of shallow-water environments in Archean and early

Paleoproterozoic ocean, questions the plausibility of classical models for BIF deposition, which invoke non-biological Fe oxidation at the redoxcline by free oxygen (*cf*. Cloud, 1973). In most cases Archean Fe formations do record a flux of ferric oxyhydroxides to the sediments, which suggests that anoxic Fe oxidation was likely a common process in Archean and early Paleoproterozoic oceans. Given the uncertainty about the importance of Fe oxidation by UV photochemistry or other anoxic Fe oxidation mechanisms in the ancient ocean (Konhauser et al., 2007), our study provides empirical evidence for metabolic Fe oxidation driving Fe formation deposition. Growing evidence for metabolic Fe oxidation in Archean and early Paleoproterozoic oceans implies that the distribution of Fe in the early ocean could have been controlled by microbial Fe utilization rather than by the oxidative potential of shallow-water environments. Episodic Fe delivery to the oceans during peaks in submarine volcanic activity could, therefore, have had dramatic impacts on ocean productivity and ecosystem structure—given that anoxygenic photosynthetic Fe oxidizers were likely important components of the early Earth's biosphere.

## References

Ahn, J.H., Buseck, P.R., 1990. Hematite nanospheres of possible colloidal origin from a Precambrian banded iron formation. Nature 250, 111-113.

Alexander, B.W., Bau, M., Andersson, P., Dulski, P., 2008. Continentally-derived solutes in shallow Archean seawater: Rare earth element and Nd isotope evidence in iron formation from the 2.9 Ga Pongola Supergroup, South Africa. Geochimica et Cosmochimica Acta 72, 378-394.

Anbar, A.D., Holland, H.D., 1992. The Photochemistry of Manganese and the Origin of Banded Iron Formations. Geochimica et Cosmochimica Acta 56, 2595-2603.

Barley, M.E., Pickard, A.L., Sylvester, P.J., 1997. Emplacement of a large igneous province as a possible cause of banded iron formation 2.45 billion years ago. Nature 385, 55-58.

Bau, M., 1999. Scavenging of dissolved yttrium and rare earths by precipitating iron oxyhydroxide: Experimental evidence for Ce oxidation, Y-Ho fractionation, and lanthanide tetrad effect. Geochimica et Cosmochimica Acta 63, 67-77.

Bau, M., Dulski, P., 1996. Distribution of yttrium and rare-earth elements in the Penge and Kuruman Iron-Formations, Transvaal Supergroup, South Africa. Precambrian Reasearch 79, 37-55.

Bau, M., Hohndorf, A., Dulski, P., Beukes, N.J., 1997a. Sources of rare-earth elements and iron in paleoproterozoic iron-formations from the Transvaal Supergroup, South Africa: Evidence from neodymium isotopes. Journal of Geology 105, 121-129.

Bau, M., Moller, P., 1993. Rare-Earth Element Systematics of the Chemically Precipitated Component in Early Precambrian Iron Formations and the Evolution of the Terrestrial Atmosphere-Hydrosphere-Lithosphere System. Geochimica et Cosmochimica Acta 57, 2239-2249.

Bau, M., Moller, P., Dulski, P., 1997b. Yttrium and lanthanides in eastern Mediterranean seawater and their fractionation during redox-cycling. Marine Chemistry 56, 123-131.

Bekker, A., Holland, H.D., Wang, P.L., Rumble, D., Stein, H.J., Hannah, J.L., Coetzee, L.L., Beukes, N.J., 2004. Dating the rise of atmospheric oxygen. Nature 427, 117-120.

Beukes, N.J., Gutzmer, J., 2008. Origin and Paleoenvironmental Significance of Major Iron Formations at the Archean-Paleoproterozoic Boundary Society of Economic Geologists Reviews 15, 5-47.

Braterman, P.S., Cairnssmith, A.G., Sloper, R.W., 1983. Photooxidation of Hydrated Fe-2+ - Significance for Banded Iron Formations. Nature 303, 163-164.
Byrne, R., Sholkovitz, E., 1996. Marine chemistry and geochemistry of the lanthanides, in: Gschneider Jr., K.A., Eyring, L. (Eds.), Handbook on the Physics and Chemistry of the Rare Earths. Elsevier, Amsterdam, pp. 497–593.
Canfield, D.E., Teske, A., 1996. Late Proterozoic rise in atmospheric oxygen concentration inferred from phylogenetic and sulphur-isotope studies. Nature 382, 127-132.

Cloud, P., 1973. Paleoecological Significance of Banded Iron-Formation. Economic Geology 68, 1135-1143.

Cloud, P.E., 1965. Significance of Gunflint ( Precambrian ) Microflora - Photosynthetic Oxygen May Have Had Important Local Effects before Becoming a Major Atmospheric Gas. Science 148, 27-35.

Crowe, S.A., Jones, C., Katsev, S., Magen, C., O'Neill, A.H., Sturm, A., Canfield, D.E., Haffner, G.D., Mucci, A., Sundby, B., Fowle, D.A., 2008. Photoferrotrophs thrive in an Archean Ocean analogue. Proceedings of the National Academy of Sciences 105, 15938-15943.

De Carlo, E.H., Green, W.J., 2002. Rare earth elements in the water column of Lake Vanda, McMurdo Dry Valleys, Antarctica. Geochimica et Cosmochimica Acta 66, 1323-1333.

Debaar, H.J.W., German, C.R., Elderfield, H., Vangaans, P., 1988. Rare-Earth Element Distributions in Anoxic Waters of the Cariaco Trench. Geochimica et Cosmochimica Acta 52, 1203-1219.

Derry, L.A., Jacobsen, S.B., 1988. The Nd and Sr Isotopic Evolution of Proterozoic Seawater. Geophysical Research Letters 15, 397-400.

Derry, L.A., Jacobsen, S.B., 1990. The Chemical Evolution of Precambrian Seawater - Evidence from REEs in Banded Iron Formations. Geochimica et Cosmochimica Acta 54, 2965-2977.

Edmonds, H.N., German, C.R., 2004. Particle geochemistry in the Rainbow hydrothermal plume, Mid-Atlantic Ridge Geochimica et Cosmochimica Acta 68, 759-772.

Edwards, K.J., Rogers, D.R., Wirsen, C.O., McCollom, T.M., 2003. Isolation and characterization of novel psychrophilic, neutrophilic, Fe-oxidizing, chemolithoautotrophic alpha- and, gamma-Proteobacteria from the deep sea. Applied and Environmental Microbiology 69, 2906-2913.

Foustoukos, D.I., Bekker, A., 2008. Hydrothermal Fe(II) oxidation during phase separation: Relevance to the origin of Algoma-type BIFs. Geochimica et Cosmochimica Acta 72, A280.

Fralick, P., Hollings, P., King, P., 2008. Stratigraphy, geochemistry, and depositional environments of Mesoarchean sedimentary units in western Superior Province: Implications for generation of early crust Geological Society of America Special Papers 440, 77-96.

Frei, R., Dahl, P.S., Duke, E.F., Frei, K.M., Hansen, T.R., Frandsson, M.M., Jensen, L.A., 2008. Trace element and isotopic characterization of Neoarchean and Paleoproterozoic iron formations in the Black Hills (South Dakota, USA): Assessment of chemical change during 2.9-1.9 Ga deposition bracketing the 2.4-2.2 Ga first rise of atmospheric oxygen. Precambrian Research 162, 441-474.

Freyer, B.J., 1976. Rare earth evidence in iron-formations for changing Precambrian oxidation states. Geochimica et Cosmochimica Acta 41, 361- 367.

Garrels, R.M., Perry, E.A.J., 1974. Cycling of carbon, sulfur, and oxygen through geologic time, in: Goldberg, E.A. (Ed.), The Sea. Wiley, New York, pp. 303-336.
German, C.R., Elderfield, H., 1990. Application of the Ce-anomaly as a paleoredox indicator: The ground rules. Paleoceanography 5, 823-833.

German, C.R., Holliday, B.P., Elderfield, H., 1991. Redox cycling of rare earth elements in the suboxic zone of the Black Sea. Geochimica et Cosmochimica Acta 55, 3553-3558.
Habicht, K.S., Gade, M., Thamdrup, B., Berg, P., Canfield, D.E., 2002. Calibration of sulfate levels in the Archean Ocean. Science 298, 2372-2374.

Haley, B.A., Klinkhammer, G.P., McManus, J., 2004. Rare earth elements in pore waters of marine sediments. Geochimica et Cosmochimica Acta 68, 1265-1279.

Harder, E.C., 1919. Iron-depositing bacteria and their geological relations. USGS, p. 89.
Holland, H.D., 1973. Oceans - Possible Source of Iron in Iron-Formations. Economic Geology 68, 1169-1172.

Holland, H.D., 1984. The Chemical Evolution of the Atmosphere and Oceans Princeton University Press, Princeton, NJ.

Holland, H.D., 2005. 100th anniversary special paper: Sedimentary mineral deposits and the evolution of earth's near-surface environments. Economic Geology 100, 1489-1509.
Isley, A.E., Abbott, D.H., 1999. Plume-related mafic volcanism and the deposition of banded iron formation. Journal of Geophysical Research-Solid Earth 104, 15461-15477.

Johnson, C.M., Beard, B.L., Klein, C., Beukes, N.J., Roden, E.E., 2008. Iron isotopes constrain biologic and abiologic processes in banded iron formation genesis. Geochimica et Cosmochimica Acta 72, 151-169.

Johnson, C.M., Beard, B.L., Roden, E.E., Newman, D.K., Nealson, K.H., 2004. Isotopic constraints on biogeochemical cycling of Fe. Geochemistry of Non-Traditional Stable Isotopes 55, 359-408.
Kamber, B.S., 2009. Geochemical fingerprinting: 40 years of analytical development and real world applications Applied Geochemistry 24, 1074-1068.

Kamber, B.S., Webb, G.E., 2001. The geochemistry of late Archaean microbial carbonate: Implications for ocean chemistry and continental erosion history. Geochimica et Cosmochimica Acta 65, 2509-2525.

Kappler, A., Pasquero, C., Konhauser, K.O., Newman, D.K., 2005. Deposition of banded iron formations by anoxygenic phototrophic Fe(II)-oxidizing bacteria. Geology 33, 865-868.

Kato, Y., Kano, T., Kunugiza, K., 2002. Negative Ce anomaly in the Indian banded iron formations: Evidence for the emergence of oxygenated deep-sea at 2.9 similar to 2.7 Ga. Resource Geology 52, 101-110.

Kato, Y., Kawakami, T., Kano, T., Kunugiza, K., Swamy, N.S., 1996. Rare-earth element geochemistry of banded iron formations and associated amphibolite from the Sargur belts, south India. Journal of Southeast Asian Earth Sciences 14, 161-164.

Kato, Y., Ohta, I., Tsunematsu, T., Watanabe, Y., Isozaki, Y., Maruyama, S., Imai, N., 1998. Rare earth element variations in mid-Archean banded iron formations: Implications for the chemistry of ocean and continent and plate tectonics. Geochimica et Cosmochimica Acta 62, 3475-3497.

Kato, Y., Yamaguchi, K.E., Ohmoto, H., 2006. Chemical and biological evolution of early Earth: Constraints from banded iron-formations, in: Ohmoto, S.K.H. (Ed.), Rare earth elements in Precambrian banded iron formations: Secular changes of Ce and Eu anomalies and evolution of atmospheric oxygen Geological Society of America, Denver, pp. 269-289.

Kaufman, A.J., Hayes, J.M., Klein, C., 1990. Primary and Diagenetic Controls of Isotopic Compositions of Iron-Formation Carbonates. Geochimica et Cosmochimica Acta 54, 3461-3473.

Khan, R.M.K., Naqvi, S.M., 1996. Geology, geochemistry and genesis of BIF of Kushtagi schist belt, Archaean Dharwar Craton, India. Mineralium Deposita 31, 123-133.

Klein, C., 2005. Some Precambrian banded iron-formations (BIFs) from around the world: Their age, geologic setting, mineralogy, metamorphism, geochemistry, and origin. American Mineralogist 90, 1473-1499.

Klein, C., Beukes, N.J., 1989. Geochemistry and Sedimentology of a Facies Transition from Limestone to Iron-Formation Deposition in the Early Proterozoic Transvaal Supergroup, South-Africa. Economic Geology 84, 1733-1774.

Klinkhammer, G., Elderfield, H., Hudson, A., 1983. Rare-Earth Elements in Seawater near Hydrothermal Vents. Nature 305, 185-188.
Koeppenkastrop, D., Decarlo, E.H., 1992. Sorption of Rare-Earth Elements from Seawater onto Synthetic Mineral Particles - an Experimental Approach. Chemical Geology 95, 251-263.

Konhauser, K.O., Amskold, L., Lalonde, S.V., Posth, N.R., Kappler, A., Anbar, A., 2007. Decoupling photochemical Fe(II) oxidation from shallow-water BIF deposition. Earth and Planetary Science Letters 258, 87-100.

Konhauser, K.O., Hamade, T., Raiswell, R., Morris, R.C., Ferris, F.G., Southam, G., Canfield, D.E., 2002. Could bacteria have formed the Precambrian banded iron formations? Geology 30, 1079-1082.

Kump, L.R., Seyfried, W.E., 2005. Hydrothermal Fe fluxes during the Precambrian: Effect of low oceanic sulfate concentrations and low hydrostatic pressure on the composition of black smokers. Earth and Planetary Science Letters 235, 654-662.

Kusky, T.P., Hudleston, P.J., 1999. Growth and demise of an Archean carbonate platform, Steep Rock Lake, Ontario, Canada. Canadian Journal of Earth Sciences 36, 565-584.

Moller, P., Bau, M., 1993. Rare-Earth Patterns with Positive Cerium Anomaly in Alkaline Waters from Lake Van, Turkey. Earth and Planetary Science Letters 117, 671-676.

Nothdurft, L.D., Webb, G.E., Kamber, B.S., 2004. Rare earth element geochemistry of Late Devonian reefal carbonates, canning basin, Western Australia: Confirmation of a seawater REE proxy in ancient limestones. Geochimica et Cosmochimica Acta 68, 263-283.

Nozaki, Y., Zhang, J., Amakawa, H., 1997. The fractionation between Y and Ho in the marine environment. Earth and Planetary Science Letters 148, 329-340.

Ohmoto, H., Watanabe, Y., Kumazawa, K., 2004. Evidence from massive siderite beds for a CO2-rich atmosphere before, 1.8 billion years ago. Nature 429, 395-399.

Ohmoto, H., Watanabe, Y., Yamaguchi, K.E., Naraoka, H., Kakegawa, T., Haruna, M., Hayashi, K., Kato, Y., 2006. Chemical and biological evolution of early Earth: Constraints from banded iron-formations, in: Ohmoto, S.K.H. (Ed.), Evolution of the Atmosphere, Hydrosphere, and Biosphere on Early Earth: Constraints from Ore Deposits. Geological Society of America, Denver, pp. 291-331.

Pecoits, E., Gingras, M.K., Barley, M.E., Kappler, A., Posth, N.R., Konhauser, K.O., 2009. Petrography and geochemistry of the Dales Gorge banded iron formation: Paragenetic sequence, source and implications for palaeo-ocean chemistry Precambrian Reasearch 172, 163-187.

Planavsky, N., Rouxel, O., Bekker, A., Shapiro, R., Fralick, P., Knudsen, A., 2009. Iron-oxidizing microbial ecosystems thrived in late Paleoproterozoic redox-stratified oceans. Earth and Planetary Science Letters 286, 230-242.

Poulton, S.W., Fralick, P.W., Canfield, D.E., 2004. The transition to a sulphidic ocean similar to 1.84 billion years ago. Nature 431, 173-177.

Prakash, H.S.M., Devapriyan, G.V., 1996. REE enrichment in the oxide facies BIF of Chitradurga schist belt, Karnataka (vol 46, pg 202, 1995). Journal of the Geological Society of India 47, 265-265.

Quinn, K.A., Byrne, R.H., Schijf, J., 2006. Sorption of yttrium and rare earth elements by amorphous ferric hydroxide: Influence of solution complexation with carbonate. Geochimica et Cosmochimica Acta 70, 4151-4165.

Schijf, J., de Baar, H.J.W., Millero, F.J., 1995. Vertical distributions and speciation of dissolved rare earth elements in the anoxic brines of Bannock Basin, eastern Mediterranean. Geochimica et Cosmochimica Acta 57, 1419-1432.

Sherrel, R.M., Field, M.P., Ravizza, G., 1999. Uptake and fractionation of rare earth elements on hydrothermal plume particles at 9°45' N, East Pacific Rise. Geochimica et Cosmochimica Acta 63 1709 –1722.

Slack, J.F., Grenne, T., Bekker, A., Rouxel, O.J., Lindberg, P.A., 2007. Suboxic deep seawater in the late Paleoproterozoic: Evidence from hematitic chert and iron formation related to seafloor-hydrothermal sulfide deposits, central Arizona, USA. Earth and Planetary Science Letters 255, 243-256.

Spier, C.A., de Oliveira, S.M.B., Sial, A.N., Rios, F.J., 2007. Geochemistry and genesis of the banded iron formations of the Caue Formation, Quadrilatero Ferrifero, Minas Gerais, Brazil. Precambrian Research 152, 170-206.

Sumner, D.Y., 1997. Carbonate precipitation and oxygen stratification in late Archean seawater as deduced from facies and stratigraphy of the Gamohaan and Frisco formations, Transvaal Supergroup, South Africa. American Journal of Science 297, 455-487.

Sumner, D.Y., Grotzinger, J.P., 2004. Implications for Neoarchaean ocean chemistry from primary carbonate mineralogy of the Campbellrand-Malmani Platform, South Africa. Sedimentology 51, 1273-1299.

Veizer, J., Hoefs, J., Lowe, D.R., Thurston, P.C., 1989. Geochemistry of Precambrian Carbonates II: Archean Greenstone Belts and Archean Sea-Water. Geochimica et Cosmochimica Acta 53, 859-871.

Walker, J.C.G., 1984. Suboxic Diagenesis in Banded Iron Formations. Nature 309, 340-342.

Webb, G.E., Kamber, B.S., 2000. Rare earth elements in Holocene reefal microbialites: A new shallow seawater proxy. Geochimica et Cosmochimica Acta 64, 1557-1565.
Widdel, F., Schnell, S., Heising, S., Ehrenreich, A., Assmus, B., Schink, B., 1993. Ferrous Iron Oxidation by Anoxygenic Phototrophic Bacteria. Nature 362, 834-836.

## Figures and Figure Legends

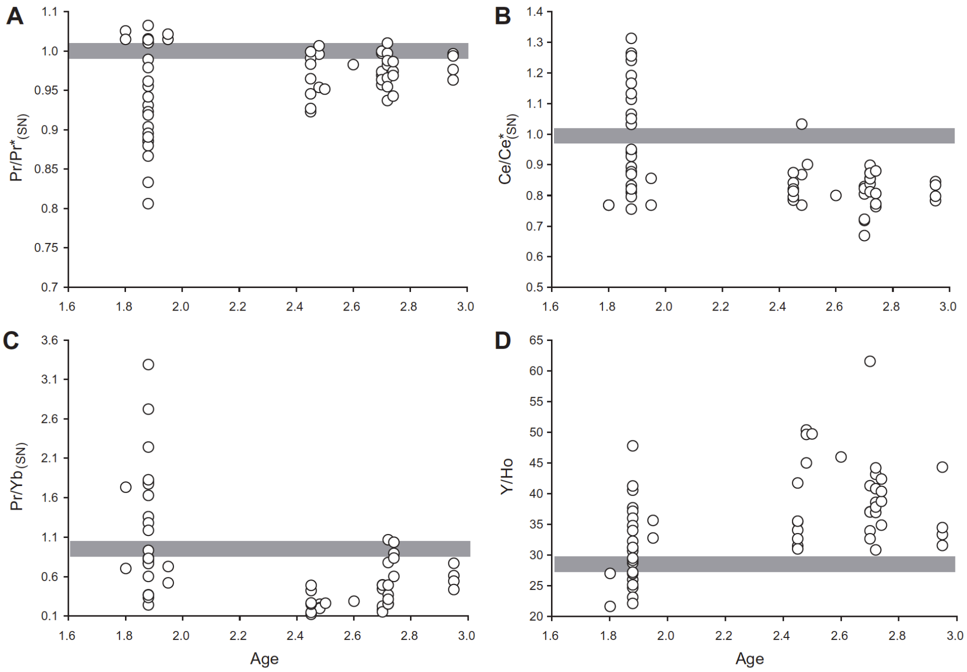

Figure 1.1. Temporal trends in REE+Y characteristics of Fe formations. A.) Pr anomalies ($Pr_{SN}/(0.5(Ce_{SN} + Nd_{SN})$). B.) Ce anomalies ($Ce_{SN}/(0.5(Pr_{SN} + La_{SN})$). C.) Light to heavy REE ratios ($Pr/Yb_{SN}$). D.) Y/Ho ratios. Black bar indicates PAAS shale composite values. Positive $Ce_{SN}$ anomalies are not present in Archean Fe formations but are common in late Paleoproterozoic Fe formations. Archean Fe formations are characterized by higher Y/Ho ratios than that of shale composite and lower light to heavy REE ratios than that of shale composite, while late Paleoproterozoic Fe formation have a large range of Y/Ho and light to heavy REE ratios. The observed temporal trend in REE+Y characteristics is best explained by the absence of a Fe-Mn redoxcline in the Archean oceans prior to the rise of atmospheric oxygen.

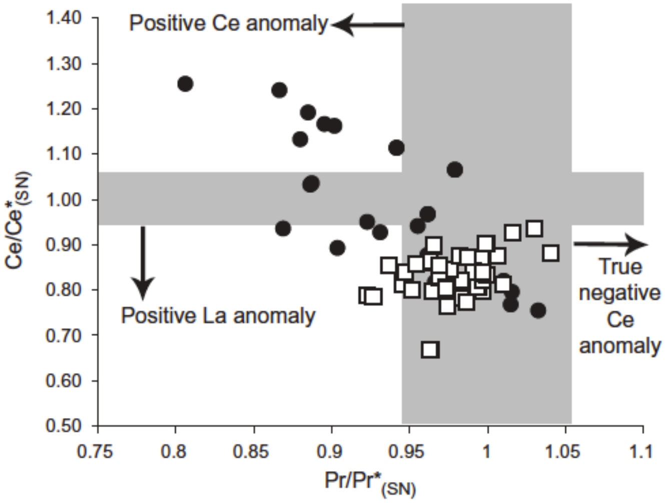

Figure 1.2. Plot of $Ce_{SN}$ and $Pr_{SN}$ anomalies for late Paleoproterozoic (●) and Archean and early Paleoproterozoic (□) Fe formations. Positive Ce anomalies are only present in late Paleoproterozoic Fe formations whereas all analyzed Fe formations do not display true negative Ce anomalies. True negative Ce anomalies are defined by $Ce/Ce*_{SN}$ ($Ce_{SN}/(0.5(Pr_{SN} + La_{SN})$) and $Pr/Pr*_{SN}$ ($Pr_{SN}/(0.5Ce_{SN} + 0.5Nd_{SN})$) values above and below the unity, respectively. The approach first described by Bau et al. (1996) discriminates between positive La and true negative Ce anomalies.

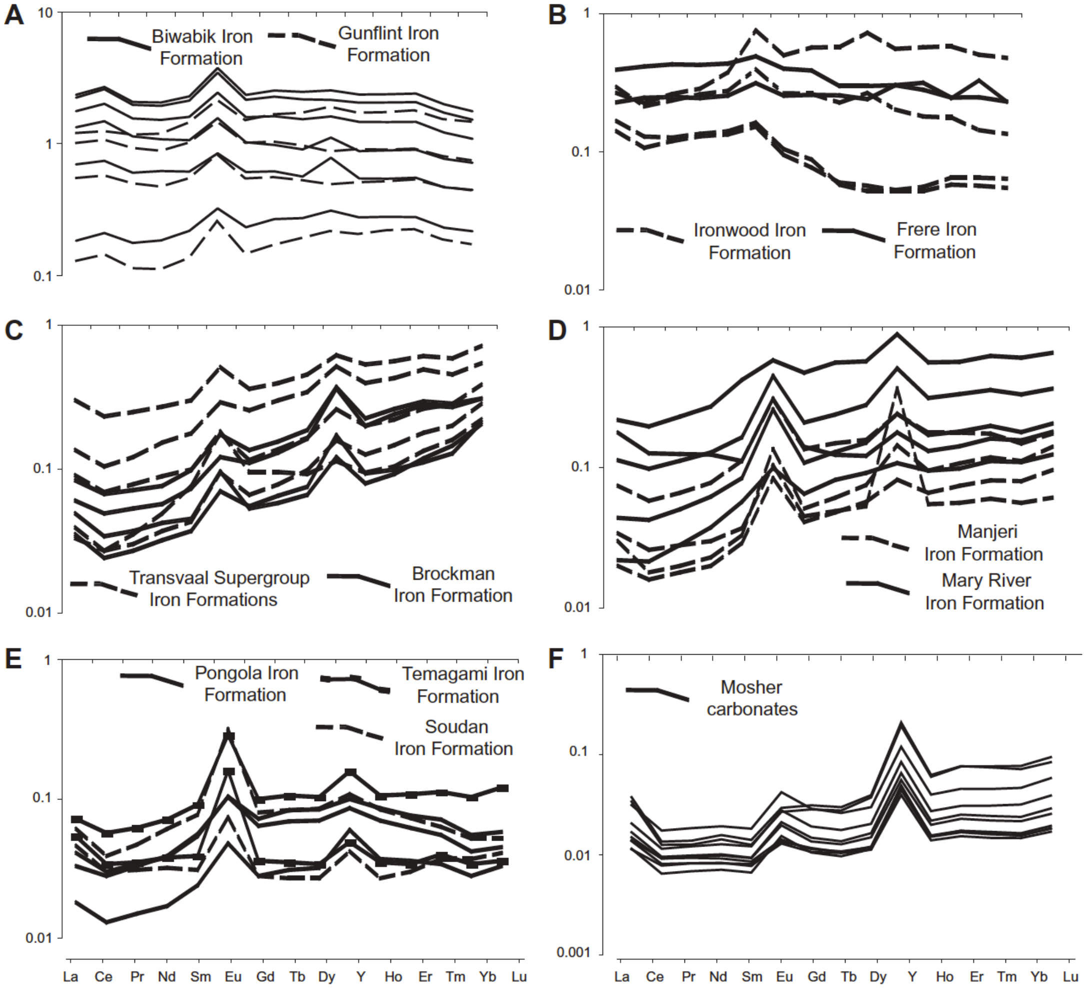

Figure 1.3. Shale-normalized (PAAS) REE patterns for representative samples of late Paleoproterozoic (A, B), early Paleoproterozoic (C), and Archean (D, E) Fe formations and carbonates from the Steep Rock Group (F).

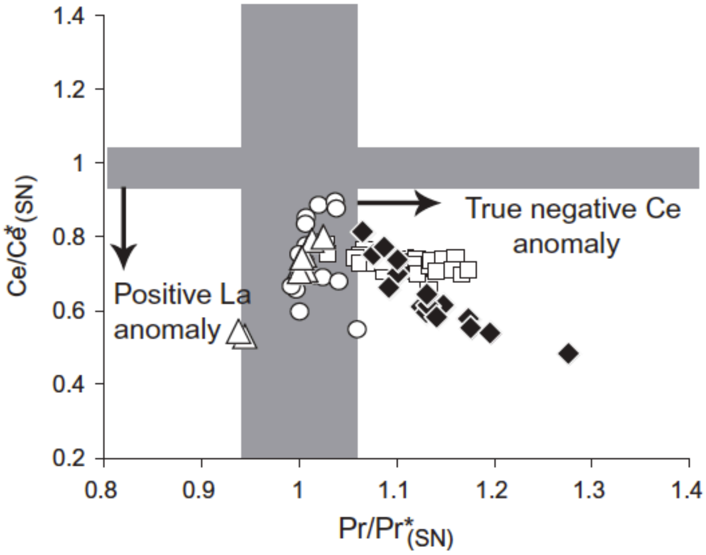

Figure 1.4. Plot of $Ce_{SN}$ and $Pr_{SN}$ anomalies in microbialite-containing carbonates of the ca. 2.8 Ga Steep Rock Group (△) and ca. 2.52 Ga Campbellrand Subgroup (Kamber and Webb, 2001; ○). Carbonates of the Devonian Canning Basin (Northdurft et al., 2004; ◆) and Holocene Herron Island (Webb and Kamber, 2000; □) are also shown for comparison. The Archean carbonates lack true negative Ce anomalies in contrast to Devonian and Holocene carbonates. The Steep Rock and Campbellrand carbonates suggest that the shallow-water high-productivity Archean carbonate platforms had a low oxidizing potential.

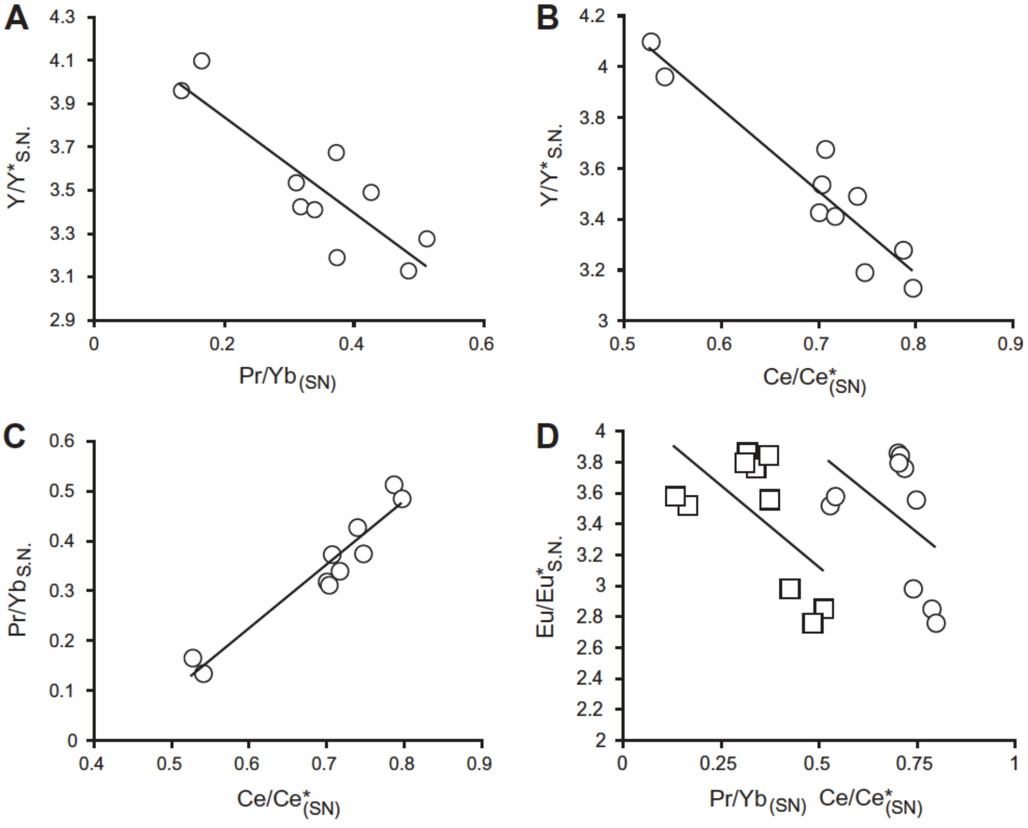

Figure 1.5. Cross-plots of REE+Y characteristics of the Mosher carbonates from the Steep Rock Group. A.) Y anomalies ($Y_{SN}$/($Er_{SN}$ + $Ho_{SN}$) versus the light to heavy REE ratios ($Pr_{SN}$/$Yb_{SN}$). B.) Y anomalies versus Ce anomalies ($Ce_{SN}$/(0.5($Pr_{SN}$ + $La_{SN}$). C.) Light to heavy REE ratios ($Pr_{SN}$/$Yb_{SN}$) versus Ce anomalies. Co-variation between Y anomalies, Ce anomalies, and light to heavy REE ratios is consistent with oceanographic REE+Y processing. The Ce anomalies likely reflect non-conservative La behavior given the lack of significant Pr anomalies. The lack of significant Ce anomalies despite evidence for oceanographic REE+Y processing indicates that the water column on the shallow-water, high-productivity Steep Rock carbonate platform was reducing with respect to Ce and Mn. D.) Eu anomalies ($Eu_{SN}$/(0.66*$Sm_{SN}$ + 0.33*$Tb_{SN}$) versus Ce anomalies (○) and light to heavy REE ratios ($Pr_{SN}$/$Yb_{SN}$) (□). Weak negative correlation between Eu anomalies and apparent Ce anomalies, reflecting La anomalies, and Eu anomalies and light to heavy REE ratios suggests mixing between deep hydrothermally-dominated seawater and shallow-waters affected by REE scavenging on particles and organic matter.

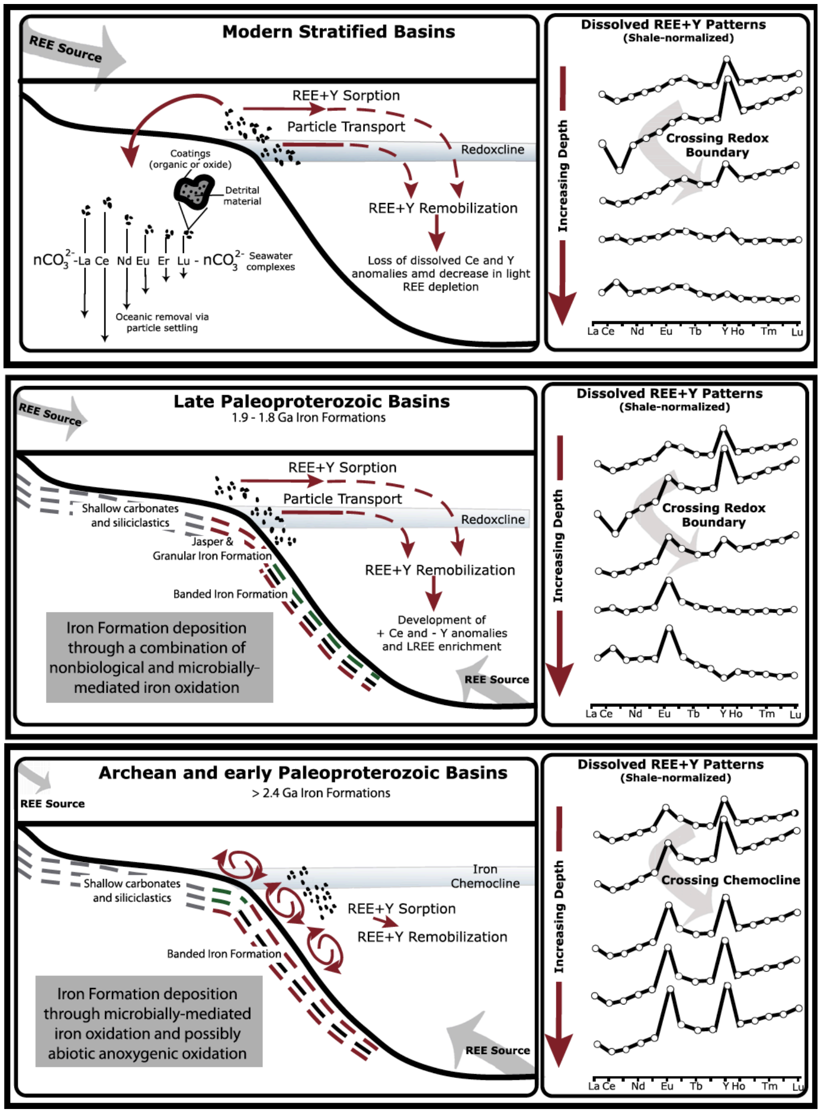

Figure 1.6. Model for the evolution of ocean redox structure based on new REE analyses of 18 Fe formations with ages ranging from ca. 3.0 Ga to 1.88 Ga. Fe formations can serve as a qualitative proxy for seawater REE pattern and, therefore, offer insight into the evolution of marine redox conditions. Similarly to modern redox-stratified basins (A), the REE+Y pattern of late Paleoproterozoic Fe formations (B) records evidence for a shuttle of metal and Ce oxides from oxic shallow seawater across the redoxcline. Oxide, mainly Mn-oxide, dissolution in anoxic water column lowers the Y/Ho ratios, raises the light to heavy REE ratios, and increases the Ce concentration relative to neighboring REE (La and Pr). In contrast, Archean Fe formations do not display REE+Y pattern indicative of an oxide shuttle (C), which implies a lack of significant Mn cycling across redoxcline prior to the rise of atmospheric oxygen in the early Paleoproterozoic. The model for REE particle sorption shown in part A is redrafted from Sholkovitz and others (1994).

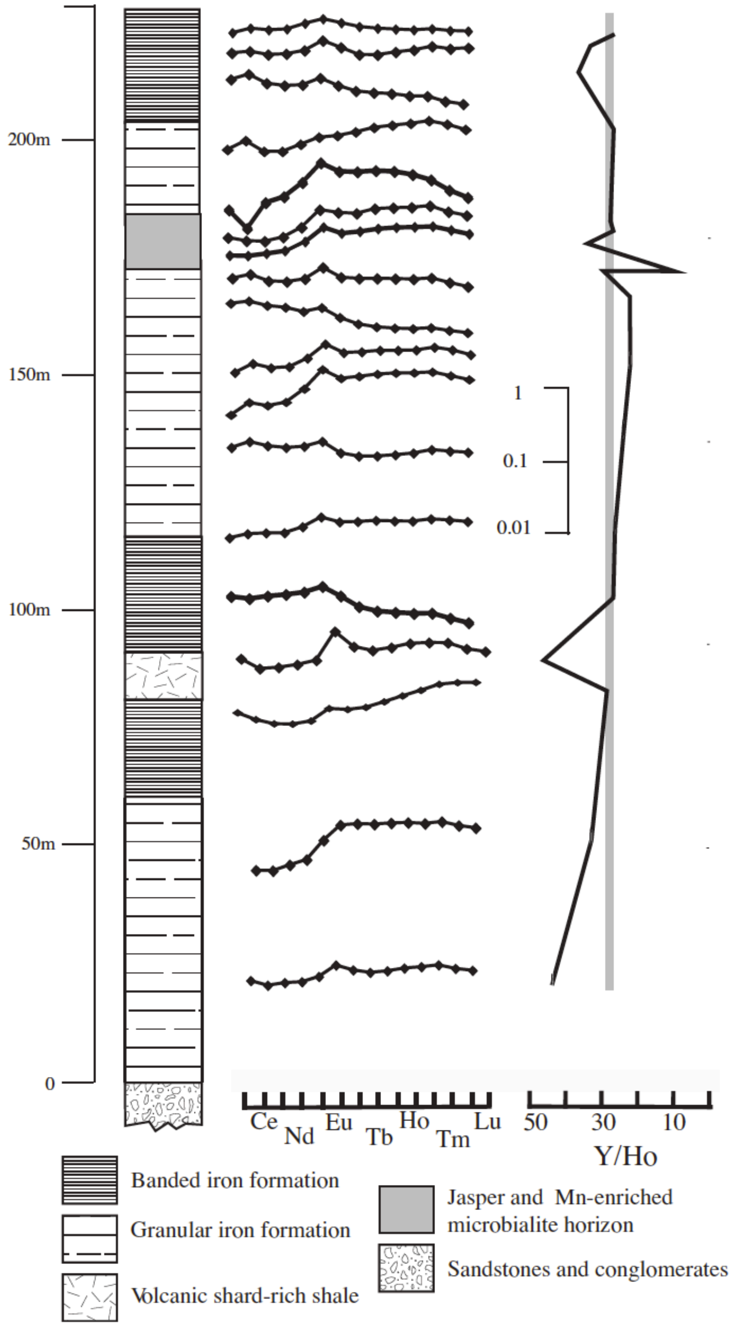

Figure 1.7. REE+Y patterns for samples from the LWD-99-2 drill core through the Biwabik Fe Formation. Note large variations in the light/heavy REE and Y/Ho ratios without any systematic stratigraphic trend. Vertical dark-grey bar represents shale composite Y/Ho ratio of ~27. Horizontal grey bar represent the REE+Y pattern for the average shale normalized to PAAS.

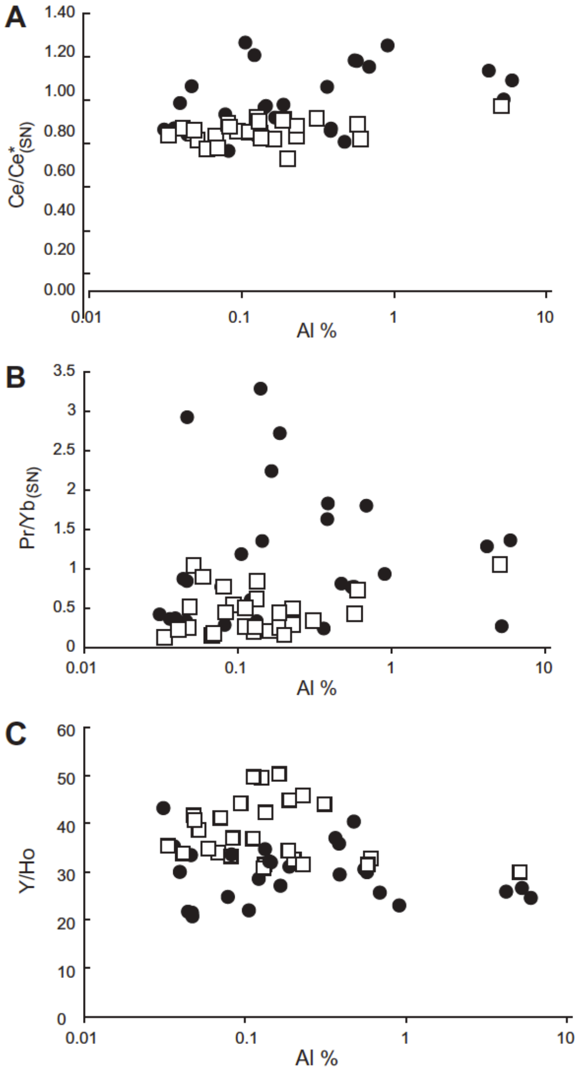

Figure 1.8. Cross-plots of REE+Y characteristics and Al (weight %) for Archean and Paleoproterozoic Fe formations. A.) Ce anomalies ($Ce_{SN}/(0.5(Pr_{SN} + La_{SN})$ versus Al (weight %). B.) Light to heavy REE ratios ($Pr/Yb_{SN}$) versus Al (weight %). C.) Y/Ho ratios versus Al (weight %).Variability in the REE+Y characteristics does not correspond with degrees of detrital sediment contribution.

## Appendix 1: Descriptions of sampled formations

### 1.88 Ga Vulcan, Negaunee, Ironwood, Gunflint, and Biwabik iron formations, Animikie Basin, USA and Canada and ca. 2.0 Ga Glen Township Formation, MN, USA

The Paleoproterozoic Animikie Basin is located in the Lake Superior region of Canada and the USA and contains several geographically separate but nearly coeval thick, iron formation-bearing sedimentary successions (Ojakangas et al., 2001). The basin extends northeastward from the Mesabi Range in north-central Minnesota (containing the Biwabik Iron Formation) to the Gunflint Range in Ontario (containing the Gunflint Iron Formation). The Gogebic, Marquette, and Menominee ranges in north-central Wisconsin and the Upper Peninsula of Michigan lie along the eastern extension of the basin and contain the Ironwood, Negaunee, and Vulcan iron formations. The ca. 2.0 Ga Glen Township Formation is located along the western margin of the basin but represents a period of iron formation deposition preceding the Biwabik and Gunflint iron formations. The tectonic model for the Animikie Basin has been debated for many years. The basin has been interpreted as a foreland basin that formed in response to crustal loading during the Penokean orogeny. More recently, however, an analysis based on syntectonic intrusions and sedimentology has revitalized the notion that the iron formations formed in extensional basins north of the subduction zone during the earliest stages in the Penokean orogeny (Fralick et al., 2002; Schulz and Cannon, 2007). The Gunflint Iron Formation contains the shallowest facies in the basin and is dominated by granular iron formation. All of the iron formations, however, also contain deeper-water, finely-laminated units. There are large massive sulfide deposits within the Animikie Basin but the iron formations are not directly related to them and are distal to volcanic activity, although interlayered iron formations with mafic and felsic volcanic rocks and volcaniclastic layers were documented (Fralick et al., 2002; Schneider et al., 2002). The Animikie Basin iron formations contain a wide range of lithologies, but samples included in this study are Fe carbonate- or Fe oxide-dominated. The age of Animikie Basin sedimentary units is well-constrained by several U-Pb ages on individual zircons (Fralick et al., 2002; Schneider et al., 2002).

### *ca. 1.8 Ga Frere Iron Formation, Western Australia*

The Frere Iron Formation is exposed both along the southern and northern margins of the Earaheedy Basin in Western Australia and is folded into a broad east-trending, south-verging asymmetric synclinal structure, with a steep to overturned northern limb. The Frere Iron Formation was deposited in a foreland basin during a transpressional stage in the Earaheedy Basin (Krapez and Martin, 1999). The Frere Iron Formation contains both granular and well-laminated lithologies, but samples included in this compilation are from laminated facies. On the southern margin, the Frere Formation is unmetamorphosed, undeformed or only mildly deformed, forming layers that are shallow-dipping to the north. The total thickness of the formation is estimated to be about 600 m. Age constraints for the Frere Iron Formation come from detrital zircon and late-stage mineralization ages bracketing the age of the formation (Pirajno et al., 2004).

### *2.45 Ga Brockman Iron Formation, Dales Gorge Member, Australia*

The Brockman Iron Formation is a part of the Hamersley Supergroup located in the northwestern part of Australia (Cheney, 1996). The precursor sediments to BIF are interpreted to have been hydrothermal muds that were deposited on the flanks of submarine volcanoes and resedimented by density currents (Krapez et al., 2003). The age of the Brockman iron formation is well constrained by U-Pb ages of zircons from ash beds within the iron formation (Pickard, 2002).

### *ca. 2.48 Ga Kuruman Iron Formation, South Africa*

The Kuruman Iron Formation in South Africa was deposited on the Kaapvaal craton in the Griqualand West basin (Beukes and Gutzmer, 2008). In the supplementary information table the iron formation samples are referred to as the Kuruman Iron Formation samples and they are from the Koegas, Westerberg, and Kuruman areas. Age constraints for the Kuruman Iron Formation come from U-Pb ages of zircons from tuffaceous sediments (Pickard, 2003).

### *ca. 2.5 Ga Benchmark Iron Formation, USA*

The Benchmark Iron Formation is preserved in the Nemo area of the Black Hills uplift which is the easternmost Laramide exposure of the Archean Wyoming Province in the central United States (Bekker and Eriksson, 2003). The age constraints for the unit are based on U-Pb zircon geochronology of the Blue Draw Metagabbro (Bekker and Eriksson, 2003; McCombs et al., 2004) that intrudes the early Paleoproterozoic rift sequence including the oxide-facies Benchmark Iron Formation (Bekker and Eriksson, 2003). The REE systematics of the Benchmark Iron Formation was discussed in Frei and others (Frei et al., 2008).

### *ca. 2.6 Ga Bjornevanns Iron Formation, Norway*

The Bjornevanns Iron Formation is a part of the Fisketind Formation of the upper part of the Bjørnevann Group near Kirkenes in northern Norway and associated with amphibolites, locally containing pillow structures, hornblende gneisses, and subordinate quartz-biotite gneisses (Siedlecka et al., 1985). The iron formation is interpreted as a volcanic-exhalative deposit. The Bjørnevatn deposit sampled for our study represents the largest accumulation of BIF ores of this unit. The BIF ores consist of alternating magnetite- and quartz-dominated bands, 2-10 mm thick. Additional minerals in the ore include hornblende, grünerite, epidote, biotite, and hematite together with traces of pyrite and chalcopyrite that are mainly confined to the magnetite bands (Siedlecka et al., 1985). In some areas the BIF contain nearly monomineralic silicate facies bands of hornblende and grünerite. The ores were affected by three phases of isoclinal to tight folding and are crosscut by late orogenic granitic dykes and Mesoproterozoic dolerite dykes. The age is poorly constrained and based on U-Pb ages of a late orogenic granitic dyke cutting the Bjørnevann Group and a deformed pegmatite intruding the correlative Garsjø Complex. REE analysis of this iron formation was earlier reported by Derry and Jacobsen (Derry and Jacobsen, 1990).

### *ca. 2.7 Ga Manjeri Iron Formation, Zimbabwe*

The Manjeri Formation is part of the volcano-sedimentary succession of the Belingwe Greenstone Belt and overlies older Neoarchean greenstone assemblage and basement gneisses. The Manjeri Formation is up to 250 m thick and contains conglomerates, shallow-water sandstones and stromatolitic limestones grading stratigraphically upwards into shale, graywacke, and iron formation. The iron formation does not appear to be directly linked to volcanic activity associated with the overlying komatiite-basalt sequence, although it is difficult to establish due to unresolved structural complexities. The age of the Manjeri Formation is poorly constrained and may be diachronous along strike. It is younger than an underlying 2831 ± 6 Ma greenstone succession, but older than or in part contemporaneous with a structurally overlying, ca. 2.7 Ga ultramafic to mafic subaqueous lava plain sequence (Hunter et al., 1998; Prendergast, 2004) HOFMANN and KUSKY, 2004). The Manjeri Formations has been correlated with similar successions in other greenstone belts of Zimbabwe (PRENDERGAST, 2004). One of our samples (Z04-12) is derived from such unit from the Cactus Mine area of the Midlands greenstone belt.

### *ca. 2.72 Ga Mary River Iron Formation, Canada*

Supracrustal rocks of the Mary River Group are located on northern Baffin Island, Canada. The samples are from the Mary River area. The iron formation is associated with mafic and ultramafic volcanics. Age constraints for the iron formation come from U–Pb zircon ages on associated felsic volcanics (Bethune and Scammell, 2003).

### *ca. 2.72 Ga Soudan Iron Formation, USA*

The Soudan Iron Formation belongs to the Soudan Iron Formation Member of the Ely Greenstone in the Soudan Belt of the Vermillion District located in the northeastern part of Minnesota, United States. The iron formations are found in a volcanic-dominated sequence and their epiclastic equivalents. The iron formation is thought to be directly associated with seamount-type volcanic activity (Bayley and James, 1973). It is an oxide-facies cherty iron formation with hematite layers. The age of the Soudan iron formation is

2722 ± 0.9 Ma based on a U-Pb single zircon age of rhyolite from the Ely Greenstone (Peterson et al., 2001).

### *ca. 2.74 Ga Temagami Iron Formation, Canada*

The Temagami Iron Formation is located in the Temagami Greenstone Belt in northern Ontario, Canada. The iron formation occurs at or near the stratigraphic top of a metavolcanic sequence that is overlain by turbiditic metasedimentary rocks. Age constraints come from U-Pb zircon ages on a rhyolite flow underlying the iron formation and a rhyolite porphyry dike cutting andesitic flows above the iron formation (Bowins and Heaman, 1991).

### *ca. 2.9 Ga Steep Rock carbonate platform, ON, Canada*

The Steep Rock Group of northwestern Ontario is situated in the Wabigoon Subprovince of the Superior Province. The 500 meter thick Mosher carbonate was deposited in a diverse range of environments ranging from sabkha to subtidal as indicated by small domal stromatolites and microbial laminites grading upsection into large elongated stromatolite mounds potentially indicating upward-deepening (Fralick et al., 2008; Kusky and Hudleston, 1999). The age of this carbonate succession is poorly constrained between 3.0 and 2.7 Ga based on U-Pb dating in the Steep Rock Greenstone Belt (Tomlinson et al., 2003) but inferred to be close to 2.9 Ga based on regional correlations (Fralick et al., 2008).

### *ca. 2.95 Ga Pongola Supergroup Iron Formation, South Africa*

The Pongola Supergroup is located in eastern South Africa and southwestern Swaziland. The iron formation sampled for this study belongs to the Sinqeni Formation of the

Mozaan Group (Beukes and Cairncross, 1991). The Mozaan Group sediments are thought to have been deposited on a broad marine shelf during thermal subsidence of the Pongola Basin. The Sinqeni Formation consists of quartz arenite, shale, and minor conglomerate and iron formation (Beukes and Cairncross, 1991). The 3 to 5 meter thick iron formation occurs within shales of the Ijzermijn Member and was deposited on a shallow starved outer continental shelf during a time of maximum transgression (Beukes and Cairncross, 1991). The age for the Mozaan Group is based on U–Pb zircon dates for rhyolites within the Nsuze Group, which underlies the Mozaan Group (Hegner et al., 1984) and a pre-folding quartz porphyry sill that intruded the Mozaan Group (Gutzmer et al., 1999). REE systematics of the Sinqeni Iron Formation was recently studied in detail by Alexander and others (Alexander et al., 2008).

### *ca. 2.95 Ga Witwatersrand Supergroup Iron Formation, South Africa*

Iron formation of the Witwatersrand Supergroup sampled for this study belongs to the Contorted Bed of the Parktown Formation, West Rand Group. The iron formation has a sharp basal contact and a gradational upper contact and is up to 13 m thick. It sits within a shale and shale-siltstone succession and represents the condensed section at the base of an upward-coarsening cycle (Frimmel, 1996). The iron formation is composed of a magnetite-rich lower part with hematite and jasper at the very base and a siderite-rich upper part. The iron formation was likely deposited on a passive continental margin (Catuneanu, 2001). The age of the Witwatersrand Supergroup is reasonably well constrained by U-Pb ages of overlying and underlying units, detrital zircons, and detrital and authigenic xenotimes (Armstrong et al., 1991; Kositcin and Krapez, 2004).

## References

Alexander, B.W., Bau, M., Andersson, P., Dulski, P., 2008. Continentally-derived solutes in shallow Archean seawater: Rare earth element and Nd isotope evidence in iron formation from the 2.9 Ga Pongola Supergroup, South Africa. Geochimica et Cosmochimica Acta 72, 378-394.

Armstrong, R.A., Compston, W., Retief, E.A., William, L.S., Welke, H.J., 1991. Zircon ion microprobe studies bearing on the age and evolution of the Witwatersrand triad. Precambrian Research 53, 243–266.

Bayley, R.W., James, H.L., 1973. Precambrian Iron-Formations of United-States. Economic Geology 68, 934-959.

Bekker, A., Eriksson, K.A., 2003. A Paleoproterozoic drowned carbonate platform on the southeastern margin of the Wyoming Craton: a record of the Kenorland breakup. Precambrian Research 120, 327-364.

Bethune, K.M., Scammell, R.J., 2003. Geology, geochronology, and geochemistry of Archean rocks in the Eqe Bay area, north-central Baffin Island, Canada: constraints on the depositional and tectonic history of the Mary River Group of northeastern Rae Province. Canadian Journal of Earth Sciences 40, 1137-1167.

Beukes, N.J., Cairncross, B., 1991. A lithostratigraphic-sedimentological reference profile for the Late Archean Mozaan Group, Pongola Sequence: application to sequence stratigraphy and correlation with the Witwatersrand Supergroup. South African Journal of Geology 94, 44-49.

Beukes, N.J., Gutzmer, J., 2008. Origin and Paleoenvironmental Significance of Major Iron Formations at the Archean-Paleoproterozoic Boundary Society of Economic Geologists Reviews 15, 5-47.

Bowins, R.J., Heaman, L.M., 1991. Age and timing of igneous activity in the Temagami greenstone belt, Ontario: A preliminary report. Canadian Journal of Earth Sciences 28, 1873-1876.

Catuneanu, O., 2001. Flexural partitioning of the Late Archaean Witwatersrand foreland system, South Africa. Sedimentary Geology 141, 95-112.

Cheney, E.S., 1996. Sequence stratigraphy and plate tectonic significance of the Transvaal succession of southern Africa and its equivalent in Western Australia. Precambrian Research 79, 3-24.

Derry, L.A., Jacobsen, S.B., 1990. The Chemical Evolution of Precambrian Seawater - Evidence from REEs in Banded Iron Formations. Geochimica et Cosmochimica Acta 54, 2965-2977.
Fralick, P., Davis, D.W., Kissin, S.A., 2002. The age of the Gunflint Formation, Ontario, Canada: single zircon U-Pb age determinations from reworked volcanic ash. Canadian Journal of Earth Sciences 39, 1085-1091.

Fralick, P., Hollings, P., King, P., 2008. Stratigraphy, geochemistry, and depositional environments of Mesoarchean sedimentary units in western Superior Province: Implications for generation of early crust Geological Society of America Special Papers 440, 77-96.

Frei, R., Dahl, P.S., Duke, E.F., Frei, K.M., Hansen, T.R., Frandsson, M.M., Jensen, L.A., 2008. Trace element and isotopic characterization of Neoarchean and Paleoproterozoic iron formations in the Black Hills (South Dakota, USA): Assessment of chemical change during 2.9-1.9 Ga deposition bracketing the 2.4-2.2 Ga first rise of atmospheric oxygen. Precambrian Research 162, 441-474.

Frimmel, H.E., 1996. Witwatersrand iron-formations and their significance for gold genesis and the composition limits of orthoamphibole. Mineralogy and Petrology 56, 273-295.

Gutzmer, J., Nhleko, N., Beukes, N.J., Pickard, A., Barley, M.E., 1999. Geochemistry and ion microprobe (SHRIMP) age of a quartz porphyry sill in the Mozaan Group of the Pongola Supergroup; implications for the Pongola and Witwatersrand supergroups South African Journal of Geology 102, 139-146.

Hegner, E., Kröner, A., Hofmann, A.W., 1984. Age and isotope geochemistry of the Archaean Pongola and Usushwana suites in Swaziland, southern Africa: a case for crustal contamination of mantle-derived magma. Earth and Planetary Science Letters 70 267-279.

Hunter, M.A., Bickle, M.J., Nisbet, E.G., Martin, A., Chapman, H.J., 1998. Continental extensional setting for the Archean Belingwe Greenstone Belt, Zimbabwe. Geology 26, 883-886.

Kositcin, N., Krapez, B., 2004. SHRIMP U–Pb detrital zircon geochronology of the Late Archaean Witwatersrand Basin of South Africa: relation between zircon provenance age spectra and basin evolution. Precambrian Research 129, 141–168.

Krapez, B., Barley, M.E., Pickard, A.L., 2003. Hydrothermal and resedimented origins of the precursor sediments to banded iron formation: sedimentological evidence from the Early Palaeoproterozoic Brockman Supersequence of Western Australia. Sedimentology 50, 979-1011.

Krapez, B., Martin, D., 1999. Sequence stratigraphy of the Palaeoproterozoic Nabberu Province of Western Australia. Australian Journal of Earth Sciences 46, 89-103.
Kusky, T.P., Hudleston, P.J., 1999. Growth and demise of an Archean carbonate platform, Steep Rock Lake, Ontario, Canada. Canadian Journal of Earth Sciences 36, 565-584.

McCombs, J.A., Dahl, P.S., Hamilton, M.A., 2004. U–Pb ages of Neoarchean granitoids from the Black Hills, South Dakota, USA: implications for crustal evolution in the Archean Wyoming province Precambrian Research 130, 161-184.

Ojakangas, R.W., Morey, G.B., Southwick, D.L., 2001. Paleoproterozoic basin development and sedimentation in the Lake Superior region, North America. Sedimentary Geology 141, 319-341.

Peterson, D.M., Gallup, C., Jirsa, M.A., Davis, D.W., 2001. Correlation of Archean assemblages across the U.S.-Canadian border: Phase I geochronology. Proceedings of the Institute on Lake Superior Geology 47, 77–78.

Pickard, A.L., 2002. SHRIMP U-Pb zircon ages of tuffaceous mudrocks in the Brockman Iron Formation of the Hamersley Range, Western Australia. Australian Journal of Earth Sciences 49, 491-507.

Pickard, A.L., 2003. SHRIMP U-Pb zircon ages for the Palaeoproterozoic Kuruman Iron Formation, Northern Cape Province, South Africa: evidence for simultaneous BIF deposition on Kaapvaal and Pilbara Cratons. Precambrian Research 125, 275-315.

Pirajno, F., Jones, J.A., Hocking, R.M., Halilovic, J., 2004. Geology and tectonic evolution of Palaeoproterozoic basins of the eastern Capricorn Orogen, Western Australia. Precambrian Research 128, 315-342.

Prendergast, M.D., 2004. The Bulawayan Supergroup: a late Archaean passive margin-related large igneous province in the Zimbabwe craton. Journal of the Geological Society 161, 431-445.

Schneider, D.A., Bickford, M.E., Cannon, W.F., Schulz, K.J., Hamilton, M.A., 2002. Age of volcanic rocks and syndepositional iron formations, Marquette Range Supergroup: implications for the tectonic setting of Paleoproterozoic, iron formations of the Lake Superior region. Canadian Journal of Earth Sciences 39, 999-1012.

Schulz, K.J., Cannon, W.F., 2007. The penokean orogeny in the lake superior region. Precambrian Research 157, 4-25.

Siedlecka, A., Iversen, E., A.G., K., Lieungh, B., Often, M., Sandstad, J.S., Solli, A., 1985. Lithostratigraphy and correlation of the Archean and Early Proterozic rocks of Finnmarksvidda and Sorvaranger district. Norges Geologiske Undersokelse 403, 7-36.

Tomlinson, K., Davis, D., Stone, D., Hart, T., 2003. U-Pb age and Nd isotopic evidence for Archean terrane development and crustal recycling in the south-central Wabigoon subprovince, Canada. Contributions to Mineralogy and Petrology 144, 684-702.

Table 1.1A: Major element and REE concentrations and REE anomalies

| Sample Name | Facies Type | Al2O3 (wt%) | Fe2O3 (T) (wt%) | MnO (wt%) | MgO (wt%) | CaO (wt%) | Ba (ppm) | Y (ppm) | La (ppm) | Ce (ppm) | Pr (ppm) | Nd (ppm) | Sm (ppm) | Eu (ppm) | Tb (ppm) | Dy (ppm) | Ho (ppm) | Er (ppm) | Tm (ppm) | Yb (ppm) | Lu (ppm) | Ce* | Pr* | Y/Ho S.N. | Pr/Yb S.N. | Eu* |
|---|---|---|---|---|---|---|---|---|---|---|---|---|---|---|---|---|---|---|---|---|---|---|---|---|---|---|
| ***Frere Iron Formation, ca. 1.8 Ga, Western Australia*** | | | | | | | | | | | | | | | | | | | | | | | | | | |
| EAR-160.2 | GIF | 2.0 | 30.0 | | 3.0 | 1.5 | 7.0 | 8.10 | 15.00 | 33.00 | 3.80 | 14.40 | 2.40 | 0.53 | 0.30 | 1.40 | 0.30 | 0.80 | 0.10 | 0.70 | 0.10 | 0.77 | 1.03 | 27.00 | 1.73 | 1.18 |
| EAR-162.6 | MIF | 3.9 | 37.5 | | 2.6 | 2.9 | 58.0 | 6.5 | 8.7 | 19.6 | 2.2 | 8.3 | 1.40 | 0.34 | 0.20 | 1.20 | 0.30 | 0.90 | 0.10 | 1.00 | 0.10 | 0.77 | 1.01 | 21.67 | 0.70 | 1.24 |
| ***Cliffs Eire Mine, 1.88 Ga, Biwabik Iron Formation, USA*** | | | | | | | | | | | | | | | | | | | | | | | | | | |
| AB5 | SIF | 0.1 | 10.6 | 0.0 | 0.0 | 0.1 | 9.9 | 4.29 | 2.93 | 4.76 | 0.51 | 2.26 | 0.46 | 0.12 | 0.09 | 0.55 | 0.11 | 0.30 | 0.04 | 0.21 | 0.03 | 0.89 | 0.90 | 37.71 | 0.77 | 1.22 |
| AB-9 | BIF | 0.9 | 35.6 | 0.0 | 2.7 | 4.3 | 64.7 | 38.56 | 21.08 | 31.42 | 4.36 | 19.03 | 3.65 | 0.90 | 0.68 | 4.31 | 0.95 | 2.60 | 0.34 | 1.72 | 0.24 | 0.76 | 1.03 | 40.56 | 0.81 | 1.15 |
| AB-9* | BIF | 0.9 | 30.1 | 0.0 | 2.4 | 4.4 | 65.0 | 32.60 | 19.80 | 32.50 | 4.09 | 17.20 | 3.35 | 0.90 | 0.64 | 3.77 | 0.79 | 2.30 | 0.30 | 1.56 | 0.20 | 0.83 | 1.01 | 41.27 | 0.84 | 1.24 |
| LA-LS-1 | BIF | 0.7 | 35.1 | 1.1 | 4.0 | 0.5 | 16.9 | 7.51 | 2.48 | 5.01 | 0.50 | 2.23 | 0.50 | 0.18 | 0.11 | 0.81 | 0.20 | 0.66 | 0.11 | 0.67 | 0.11 | 1.03 | 0.89 | 37.15 | 0.24 | 1.57 |
| ***Devils Icebox Mine, 1.88 Ga, Ironwood Iron Formation, USA*** | | | | | | | | | | | | | | | | | | | | | | | | | | |
| DI3 | BIF | 0.4 | 37.0 | 0.1 | 0.1 | 0.0 | 3.6 | 1.19 | 4.78 | 8.54 | 0.91 | 3.66 | 0.51 | 0.13 | 0.05 | 0.20 | 0.04 | 0.11 | 0.02 | 0.11 | 0.02 | 0.94 | 0.96 | 31.22 | 2.72 | 1.43 |
| AB11 | BIF | 0.3 | 39.1 | 0.1 | 0.1 | 0.1 | 5.5 | 3.97 | 11.91 | 21.71 | 2.44 | 10.87 | 1.80 | 0.45 | 0.18 | 0.73 | 0.12 | 0.31 | 0.04 | 0.24 | 0.04 | 0.93 | 0.93 | 32.26 | 3.29 | 1.42 |
| ***Empire Mine, 1.88 Ga, Negaunee Iron Formation, USA*** | | | | | | | | | | | | | | | | | | | | | | | | | | |
| AB4 | BIF | 0.7 | 49.4 | 0.3 | 0.6 | 0.5 | 7.8 | 7.22 | 11.21 | 17.05 | 2.08 | 8.85 | 1.52 | 0.43 | 0.20 | 1.06 | 0.20 | 0.51 | 0.07 | 0.41 | 0.06 | 0.81 | 0.99 | 35.99 | 1.63 | 1.46 |
| ***GF-3 Drill Core, 1.88 Ga, Gunflint Iron Formation, Canada*** | | | | | | | | | | | | | | | | | | | | | | | | | | |
| DH3-27 | GIF | 0.2 | 29.3 | 0.4 | 0.4 | 16.0 | 29.1 | 5.84 | 4.90 | 11.42 | 0.99 | 3.76 | 0.74 | 0.28 | 0.13 | 0.90 | 0.20 | 0.63 | 0.09 | 0.53 | 0.07 | 1.19 | 0.88 | 28.70 | 0.60 | 1.78 |
| DH3-42 | BIF | 11.2 | 25.9 | 0.0 | 2.9 | 0.2 | 268.1 | 7.45 | 16.09 | 34.30 | 3.43 | 12.26 | 2.27 | 0.62 | 0.30 | 1.58 | 0.30 | 0.85 | 0.13 | 0.80 | 0.12 | 1.07 | 0.98 | 24.72 | 1.36 | 1.43 |
| DH3-43 | BIF | 7.9 | 31.1 | 0.0 | 2.7 | 0.7 | 218.8 | 10.40 | 17.87 | 39.84 | 3.80 | 14.05 | 2.63 | 0.70 | 0.37 | 2.09 | 0.40 | 1.10 | 0.16 | 0.95 | 0.13 | 1.11 | 0.94 | 25.99 | 1.28 | 1.36 |
| ***Kakabeka Falls, 1.88 Ga, Gunflint Iron Formation, Canada*** | | | | | | | | | | | | | | | | | | | | | | | | | | |
| AB-KF-1 | BIF | 0.3 | 36.5 | 2.0 | 4.0 | 10.4 | 9.5 | 28.18 | 7.45 | 14.01 | 2.18 | 10.54 | 2.40 | 0.74 | 0.50 | 3.52 | 0.81 | 2.41 | 0.36 | 2.09 | 0.32 | 0.80 | 1.02 | 34.78 | 0.33 | 1.38 |
| ***LWD-99-2 Drill Core, 1.88 Ga, Biwabik Iron Formation, USA*** | | | | | | | | | | | | | | | | | | | | | | | | | | |
| 317-8 | GIF | 1.0 | 40.7 | 2.5 | 4.5 | 8.1 | 24.4 | 8.38 | 7.00 | 16.69 | 1.56 | 6.25 | 1.20 | 0.35 | 0.21 | 1.27 | 0.27 | 0.79 | 0.11 | 0.65 | 0.09 | 1.17 | 0.90 | 30.68 | 0.77 | 1.39 |
| 317-10 | GIF | 1.3 | 66.5 | 1.1 | 2.0 | 0.9 | 78.0 | 12.74 | 19.59 | 42.28 | 3.76 | 14.77 | 2.18 | 0.56 | 0.27 | 1.36 | 0.27 | 0.75 | 0.11 | 0.67 | 0.10 | 1.13 | 0.88 | 47.80 | 1.80 | 1.39 |
| 317-10* | GIF | 1.2 | 61.7 | 1.0 | 1.6 | 0.8 | 102.0 | 8.90 | 24.30 | 58.90 | 4.72 | 15.60 | 2.47 | 0.78 | 0.28 | 1.60 | 0.33 | 0.99 | 0.14 | 0.85 | 0.12 | 1.26 | 0.89 | 26.97 | 1.77 | 1.73 |
| 317-12 | GIF | 1.7 | 59.9 | 1.1 | 2.5 | 1.6 | 81.0 | 13.44 | 16.55 | 42.01 | 3.68 | 14.76 | 2.95 | 0.95 | 0.49 | 2.94 | 0.58 | 1.62 | 0.23 | 1.26 | 0.16 | 1.24 | 0.87 | 23.16 | 0.93 | 1.56 |
| 317-12* | GIF | 1.7 | 57.5 | 1.1 | 2.4 | 1.7 | 94.0 | 14.60 | 18.00 | 46.50 | 3.70 | 14.30 | 2.89 | 1.10 | 0.51 | 2.99 | 0.58 | 1.70 | 0.24 | 1.42 | 0.19 | 1.31 | 0.83 | 25.17 | 0.83 | 1.81 |
| 317-13 | SIF | 0.1 | 22.1 | 9.3 | 0.2 | 3.3 | 15.7 | 10.51 | 4.38 | 8.16 | 0.89 | 3.95 | 0.89 | 0.32 | 0.20 | 1.41 | 0.31 | 0.90 | 0.14 | 0.77 | 0.10 | 0.95 | 0.92 | 34.00 | 0.37 | 1.55 |
| 317-13* | SIF | 0.1 | 20.2 | 10.1 | 0.2 | 3.5 | 17.0 | 7.00 | 3.68 | 7.58 | 0.75 | 3.04 | 0.70 | 0.30 | 0.17 | 1.16 | 0.24 | 0.71 | 0.11 | 0.65 | 0.09 | 1.05 | 0.92 | 29.17 | 0.37 | 1.88 |
| 317-22 | GIF | 0.1 | 27.5 | 1.7 | 3.2 | 2.7 | 1.3 | 1.63 | 0.92 | 1.34 | 0.15 | 0.59 | 0.12 | 0.07 | 0.03 | 0.19 | 0.05 | 0.15 | 0.02 | 0.13 | 0.02 | 0.82 | 0.98 | 35.42 | 0.36 | 2.46 |
| 317-26 | GIF | 1.1 | 39.4 | 2.2 | 4.1 | 7.0 | 21.1 | 8.09 | 7.57 | 17.88 | 1.66 | 6.56 | 1.21 | 0.34 | 0.20 | 1.25 | 0.27 | 0.81 | 0.12 | 0.69 | 0.10 | 1.16 | 0.90 | 30.01 | 0.77 | 1.35 |
| ***Mink Mountain, 1.88 Ga, Gunflint Iron Formation, Canada*** | | | | | | | | | | | | | | | | | | | | | | | | | | |
| MM2(A) | GIF | 0.2 | 11.4 | 0.1 | 0.2 | 0.1 | 50.3 | 1.54 | 4.55 | 10.14 | 0.74 | 2.73 | 0.42 | 0.12 | 0.06 | 0.35 | 0.07 | 0.20 | 0.03 | 0.20 | 0.03 | 1.26 | 0.81 | 22.14 | 1.19 | 1.40 |

| | | | | | | | | | | | | | | | | | | | | | | | | | | |
|---|---|---|---|---|---|---|---|---|---|---|---|---|---|---|---|---|---|---|---|---|---|---|---|---|---|---|
| ***Norway Mining District, 1.88 Ga, Vulcan Iron Formation, USA*** | | | | | | | | | | | | | | | | | | | | | | | | | | |
| Curry1 | GIF | 0.3 | 29.2 | 0.0 | 0.3 | 0.0 | 6.4 | 1.40 | 6.38 | 10.26 | 1.12 | 4.56 | 0.78 | 0.18 | 0.07 | 0.27 | 0.05 | 0.15 | 0.02 | 0.16 | 0.02 | 0.88 | 0.96 | 27.22 | 2.24 | 1.34 |
| Curry2 | MIF | 0.7 | 44.5 | 0.0 | 0.5 | 0.1 | 8.3 | 1.54 | 5.39 | 8.52 | 1.06 | 4.40 | 0.74 | 0.16 | 0.06 | 0.28 | 0.05 | 0.16 | 0.03 | 0.18 | 0.03 | 0.82 | 1.01 | 29.53 | 1.83 | 1.34 |
| Curry2* | MIF | 0.7 | 46.3 | 0.0 | 0.5 | 0.0 | 8.0 | 5.00 | 5.98 | 9.96 | 1.16 | 4.54 | 0.79 | 0.21 | 0.12 | 0.72 | 0.16 | 0.47 | 0.07 | 0.38 | 0.05 | 0.87 | 1.01 | 31.25 | | 1.33 |
| ***A6 Drill Core, ca. 2.0 Ga, Glen Township Formation, USA*** | | | | | | | | | | | | | | | | | | | | | | | | | | |
| A6-1344 | BIF | 1.1 | 37.7 | 3.7 | 3.0 | 2.3 | 76.3 | 13.74 | 10.59 | 16.60 | 2.34 | 10.67 | 2.24 | 0.75 | 0.36 | 2.16 | 0.42 | 1.11 | 0.16 | 1.03 | 0.16 | 0.77 | 1.01 | 32.80 | 0.73 | 1.64 |
| A6-1344* | BIF | 1.1 | 38.7 | 4.1 | 3.0 | 2.5 | 76.0 | 19.60 | 10.20 | 18.00 | 2.31 | 9.70 | 2.07 | 0.82 | 0.44 | 2.68 | 0.55 | 1.63 | 0.23 | 1.42 | 0.21 | 0.86 | 1.02 | 35.64 | 0.52 | 1.73 |
| ***Dales Gorge Member, ca. 2.45 Ga, Brockman Iron Formation, Western Australia*** | | | | | | | | | | | | | | | | | | | | | | | | | | |
| RM-4 | MIF | 0.1 | 17.8 | 0.0 | 1.6 | 0.6 | 22.1 | 7.03 | 1.27 | 2.13 | 0.31 | 1.64 | 0.42 | 0.19 | 0.11 | 0.77 | 0.20 | 0.63 | 0.11 | 0.80 | 0.17 | 0.87 | 0.92 | 35.46 | 0.12 | 1.86 |
| RM-5 | MIF | 0.1 | 35.2 | 0.0 | 3.5 | 0.9 | 12.8 | 4.26 | 1.49 | 2.14 | 0.26 | 1.25 | 0.24 | 0.10 | 0.06 | 0.46 | 0.12 | 0.42 | 0.07 | 0.56 | 0.12 | 0.79 | 0.93 | 34.09 | 0.15 | 1.74 |
| RM-8 | BIF | 1.1 | 60.0 | 0.4 | 2.0 | 2.5 | 101.8 | 16.60 | 11.47 | 18.35 | 2.19 | 9.16 | 1.65 | 0.55 | 0.31 | 2.12 | 0.53 | 1.60 | 0.25 | 1.65 | 0.31 | 0.78 | 0.99 | 31.51 | 0.42 | 1.55 |
| RM9 | BIF | | 40.1 | | | | 96.8 | 3.05 | 3.45 | 5.49 | 0.69 | 3.03 | 0.54 | 0.20 | 0.07 | 0.43 | 0.09 | 0.30 | 0.05 | 0.45 | 0.10 | 0.84 | 0.98 | 32.66 | 0.49 | 1.89 |
| RM-7 (DD475/1) | BIF | 0.1 | 30.1 | 0.0 | 2.9 | 1.8 | 21.9 | 3.27 | 1.88 | 2.72 | 0.32 | 1.41 | 0.25 | 0.10 | 0.05 | 0.31 | 0.08 | 0.26 | 0.05 | 0.41 | 0.09 | 0.82 | 0.96 | 41.75 | 0.25 | 1.96 |
| DDH75/1 | BIF | | 49.5 | | | | 18.7 | 13.91 | 5.14 | 8.28 | 1.07 | 5.16 | 0.97 | 0.31 | 0.23 | 1.60 | 0.39 | 1.22 | 0.20 | 1.28 | 0.23 | 0.80 | 0.95 | 35.51 | 0.27 | 1.35 |
| DDH75/1-466 | MIF | | 19.5 | | | | 2.4 | 2.00 | 0.38 | 0.72 | 0.09 | 0.38 | 0.10 | 0.03 | 0.03 | 0.25 | 0.06 | 0.24 | 0.05 | 0.38 | 0.07 | 0.81 | 1.00 | 31.02 | 0.08 | 1.01 |
| ***Koegas area, ca. 2.48 Ga, Kuruman Iron Formation, South Africa*** | | | | | | | | | | | | | | | | | | | | | | | | | | |
| KOEN-2 | BIF | 0.4 | 37.5 | 0.7 | 3.1 | 1.5 | 41.2 | 9.99 | 3.16 | 5.31 | 0.63 | 2.57 | 0.54 | 0.19 | 0.12 | 0.87 | 0.22 | 0.74 | 0.12 | 0.80 | 0.13 | 0.77 | 1.00 | 45.01 | 0.25 | 1.49 |
| ***Kuruman area, ca. 2.48 Ga, Kuruman Iron Formation, South Africa*** | | | | | | | | | | | | | | | | | | | | | | | | | | |
| KU-9-537 | MIF | 0.3 | 75.4 | 0.0 | 3.2 | 0.9 | 8.1 | 4.64 | 1.34 | 1.89 | 0.23 | 1.09 | 0.20 | 0.08 | 0.05 | 0.35 | 0.09 | 0.28 | 0.04 | 0.36 | 0.09 | 1.03 | 0.95 | 50.35 | 0.21 | 1.53 |
| ***Westerberg area , 2.48 Ga, Kuruman Iron Formation, South Africa*** | | | | | | | | | | | | | | | | | | | | | | | | | | |
| W-18-740A | BIF | 0.2 | 59.9 | 1.4 | 3.2 | 1.8 | 66.2 | 9.75 | 2.27 | 3.93 | 0.47 | 1.92 | 0.40 | 0.13 | 0.10 | 0.76 | 0.20 | 0.68 | 0.11 | 0.76 | 0.13 | 0.87 | 1.01 | 49.63 | 0.20 | 1.33 |
| ***Black Hills area, ca. 2.5 Ga, Benchmark Iron Formation, USA*** | | | | | | | | | | | | | | | | | | | | | | | | | | |
| BIF-1 | BIF | 0.2 | 53.8 | 0.0 | 0.5 | 2.6 | 29.1 | 4.35 | 1.11 | 1.66 | 0.20 | 0.92 | 0.21 | 0.09 | 0.05 | 0.36 | 0.09 | 0.27 | 0.04 | 0.25 | 0.04 | 0.90 | 0.95 | 49.74 | 0.26 | 1.86 |
| ***Kirkenes area, ca. 2.6 Ga, Bjornevanns Iron Formation, Norway*** | | | | | | | | | | | | | | | | | | | | | | | | | | |
| IF-5 | BIF | 0.4 | 50.8 | 0.1 | 2.6 | 0.9 | 0.6 | 5.59 | 1.73 | 2.46 | 0.30 | 1.28 | 0.27 | 0.13 | 0.07 | 0.48 | 0.12 | 0.38 | 0.06 | 0.33 | 0.05 | 0.80 | 0.98 | 45.97 | 0.29 | 1.96 |
| ***Manjeri Iron Formation, ca. 2.7 Ga, Zimbabwe*** | | | | | | | | | | | | | | | | | | | | | | | | | | |
| Z04-12 | BIF | 0.1 | 22.2 | 0.0 | 0.0 | 0.2 | 5.5 | 3.89 | 1.16 | 1.44 | 0.17 | 0.78 | 0.18 | 0.15 | 0.05 | 0.35 | 0.09 | 0.30 | 0.05 | 0.31 | 0.06 | 0.72 | 0.96 | 41.31 | 0.18 | 3.23 |
| Z04-26 | BIF | 0.2 | 18.3 | 0.0 | 0.0 | 0.1 | 4.6 | 6.49 | 2.82 | 4.59 | 0.58 | 2.63 | 0.61 | 0.33 | 0.12 | 0.74 | 0.18 | 0.50 | 0.07 | 0.42 | 0.08 | 0.72 | 0.97 | 37.06 | 0.44 | 2.47 |
| Z04-31 | BIF | 0.2 | 30.8 | 0.2 | 0.1 | 0.4 | 113.0 | 4.13 | 3.34 | 4.74 | 0.53 | 2.20 | 0.41 | 0.20 | 0.07 | 0.45 | 0.11 | 0.35 | 0.05 | 0.34 | 0.06 | 0.83 | 0.97 | 37.02 | 0.50 | 2.41 |
| Z04-32 | BIF | 0.1 | 12.8 | 0.1 | 0.4 | 0.4 | 4.3 | 2.22 | 0.78 | 1.26 | 0.16 | 0.69 | 0.16 | 0.09 | 0.04 | 0.26 | 0.07 | 0.21 | 0.03 | 0.23 | 0.04 | 0.80 | 1.00 | 33.95 | 0.22 | 2.40 |
| BMA-1 | BIF | 0.4 | 20.1 | 0.0 | 0.0 | 0.2 | 0.9 | 4.35 | 1.63 | 1.77 | 0.21 | 0.92 | 0.23 | 0.08 | 0.07 | 0.57 | 0.13 | 0.42 | 0.07 | 0.44 | 0.07 | 0.82 | 0.96 | 32.65 | 0.15 | 1.26 |
| BMA-2 | BIF | 0.4 | 17.5 | 0.2 | 3.2 | 2.0 | 1.3 | 9.84 | 1.29 | 2.03 | 0.24 | 1.00 | 0.20 | 0.11 | 0.04 | 0.25 | 0.05 | 0.16 | 0.02 | 0.16 | 0.03 | 0.67 | 1.00 | 61.55 | 0.49 | 2.55 |
| ***Mary River Iron Formation, ca. 2.72 Ga, Canada*** | | | | | | | | | | | | | | | | | | | | | | | | | | |
| JD-65-114C11 | BIF | 0.2 | 30.0 | 0.0 | 1.6 | 1.0 | 3.4 | 23.9 | 8.33 | 15.57 | 2.0 | 9.2 | 2.31 | 0.62 | 0.4 | 2.7 | 0.55 | 1.60 | 0.3 | 1.7 | 0.28 | 0.87 | 0.98 | 43.13 | 0.37 | 1.26 |

| | | | | | | | | | | | | | | | | | | | | | | | | | | |
|---|---|---|---|---|---|---|---|---|---|---|---|---|---|---|---|---|---|---|---|---|---|---|---|---|---|---|
| JD-65-207/2 | BIF | | | | | | 1.8 | 6.5 | 1.68 | 3.37 | 0.4 | 2.1 | 0.46 | 0.28 | 0.1 | 0.7 | 0.17 | 0.51 | 0.1 | 0.5 | 0.09 | 0.90 | 0.97 | 38.57 | 0.26 | 2.53 |
| JD-65-260-1 | BIF | | | | | | 3.5 | 4.8 | 6.75 | 10.05 | 1.1 | 4.2 | 0.61 | 0.33 | 0.1 | 0.6 | 0.13 | 0.40 | 0.1 | 0.4 | 0.08 | 0.84 | 1.00 | 36.94 | 0.78 | 2.30 |
| JD-65-285-C11 | BIF | | | | | | 0.4 | 2.9 | 0.84 | 1.71 | 0.2 | 1.3 | 0.31 | 0.11 | 0.1 | 0.4 | 0.09 | 0.28 | 0.0 | 0.3 | 0.05 | 0.86 | 0.95 | 30.86 | 0.25 | 1.53 |
| JD-65-296-1 | BIF | | | | | | 1.7 | 1.8 | 2.84 | 4.34 | 0.5 | 2.0 | 0.35 | 0.17 | 0.0 | 0.2 | 0.05 | 0.14 | 0.0 | 0.1 | 0.02 | 0.85 | 0.94 | 37.81 | 1.07 | 2.17 |
| JD-65-C-199-3 | BIF | 0.6 | 38.7 | 0.0 | 3.1 | 2.2 | 32.6 | 13.7 | 4.30 | 7.78 | 1.0 | 4.3 | 0.90 | 0.48 | 0.2 | 1.3 | 0.31 | 0.94 | 0.1 | 0.9 | 0.16 | 0.87 | 0.99 | 44.20 | 0.31 | 2.25 |
| JD-C165A | BIF | 0.1 | 50.8 | 0.0 | 2.2 | 0.4 | 1.3 | 3.9 | 2.36 | 3.90 | 0.5 | 2.3 | 0.39 | 0.21 | 0.1 | 0.4 | 0.09 | 0.31 | 0.0 | 0.3 | 0.06 | 0.81 | 1.01 | 40.79 | 0.49 | 2.26 |
| *Soudan Iron Formation, ca. 2.72 Ga, USA* | | | | | | | | | | | | | | | | | | | | | | | | | | |
| IF-17 | BIF | 0.1 | 30.6 | 0.0 | 0.0 | 0.0 | 7.2 | 1.34 | 2.05 | 2.70 | 0.31 | 1.29 | 0.21 | 0.17 | 0.03 | 0.16 | 0.03 | 0.10 | 0.02 | 0.10 | 0.02 | 0.81 | 0.97 | 38.74 | 1.03 | 4.29 |
| IF-18 | BIF | 0.1 | 44.8 | 0.0 | 0.0 | 0.1 | 24.7 | 2.92 | 2.33 | 3.08 | 0.41 | 2.06 | 0.42 | 0.34 | 0.06 | 0.40 | 0.08 | 0.21 | 0.03 | 0.15 | 0.02 | 0.76 | 0.94 | 34.87 | 0.89 | 4.04 |
| *Temagami Iron Formation, ca. 2.74 Ga, Canada* | | | | | | | | | | | | | | | | | | | | | | | | | | |
| IF-6 | BIF | 0.3 | 42.4 | 0.0 | 0.2 | 0.1 | 7.4 | 1.14 | 1.78 | 2.37 | 0.27 | 1.10 | 0.17 | 0.08 | 0.02 | 0.12 | 0.03 | 0.09 | 0.01 | 0.10 | 0.02 | 0.88 | 0.99 | 42.36 | 0.84 | 2.50 |
| IF-7 | BIF | | 47.3 | | | | 18.9 | 4.25 | 2.75 | 4.57 | 0.55 | 2.41 | 0.50 | 0.31 | 0.08 | 0.48 | 0.11 | 0.31 | 0.05 | 0.29 | 0.05 | 0.77 | 0.97 | 40.38 | 0.60 | 3.01 |
| *Iron Formation in the Pongola Supergroup, ca. 2.95 Ga, South Africa* | | | | | | | | | | | | | | | | | | | | | | | | | | |
| P05-1 | BIF | 0.2 | 26.8 | 3.1 | 0.0 | 0.2 | 94.7 | 2.31 | 1.28 | 2.22 | 0.29 | 1.32 | 0.31 | 0.11 | 0.05 | 0.33 | 0.07 | 0.18 | 0.02 | 0.12 | 0.02 | 0.78 | 0.98 | 33.33 | 0.77 | 1.71 |
| P05-6 | BIF | 0.3 | 35.7 | 3.0 | 0.1 | 0.2 | 17.6 | 2.69 | 1.56 | 2.36 | 0.30 | 1.28 | 0.30 | 0.11 | 0.06 | 0.39 | 0.09 | 0.22 | 0.03 | 0.15 | 0.02 | 0.85 | 1.00 | 31.56 | 0.61 | 1.66 |
| P05-7 | BIF | 0.2 | 16.0 | 1.4 | 0.1 | 0.2 | 4.8 | 1.63 | 0.67 | 1.05 | 0.13 | 0.59 | 0.13 | 0.05 | 0.02 | 0.15 | 0.04 | 0.10 | 0.01 | 0.08 | 0.01 | 0.80 | 0.99 | 44.33 | 0.54 | 1.82 |
| *Iron Formation in the Witwatersrand Supergroup, ca. 2.95 Ga, South Africa* | | | | | | | | | | | | | | | | | | | | | | | | | | |
| IF-9 | BIF | 0.4 | 37.0 | 0.1 | 0.0 | 0.0 | 2.7 | 6.41 | 2.67 | 4.79 | 0.62 | 2.87 | 0.64 | 0.25 | 0.13 | 0.88 | 0.19 | 0.52 | 0.07 | 0.45 | 0.07 | 0.83 | 0.96 | 34.47 | 0.43 | 1.74 |

*Samples analyzed at Woods Hole Oceanographic Institute*
** Samples duplicated at Activation Laboratories*
*BIF, banded iron formation; MIF massive iron formation; GIF, granular iron formation; SIF, stromatolitic iron formation*

## Table 1.1B: Trace element and REE concentrations and REE anomalies

| Sample Name / Core depth in m | Facies Type | Ti (ppm) | Ga (ppm) | Zr (ppm) | Ba (ppm) | Y (ppm) | La (ppm) | Ce (ppm) | Pr (ppm) | Nd (ppm) | Sm (ppm) | Eu (ppm) | Gd (ppm) | Tb (ppm) | Dy (ppm) | Ho (pm) | Er (ppm) | Tm (ppm) | Yb (ppm) | Lu (ppm) | Ce* | Pr* | Pr/Yb S.N. | Y/Ho S.N. | Eu* |
|---|---|---|---|---|---|---|---|---|---|---|---|---|---|---|---|---|---|---|---|---|---|---|---|---|---|
| ***LWD-99-2 Drill Core, 1.88 Ga, Biwabik Iron Formation, USA*** | | | | | | | | | | | | | | | | | | | | | | | | | |
| LWD-193 | BIF | 0.0 | 4.57 | 20.28 | 27.80 | 4.70 | 5.69 | 14.56 | 1.50 | 6.01 | 1.25 | 0.30 | 1.08 | 0.15 | 0.86 | 0.17 | 0.48 | 0.07 | 0.46 | 0.07 | 0.88 | 1.01 | 1.04 | 26.97 | 1.49 |
| LWD-195 | BIF | 0.0 | 6.96 | 31.02 | 4.00 | 2.76 | 3.12 | 6.83 | 0.69 | 2.69 | 0.49 | 0.13 | 0.45 | 0.06 | 0.36 | 0.08 | 0.26 | 0.04 | 0.26 | 0.04 | 1.08 | 0.94 | 0.84 | 33.17 | 1.42 |
| LSD-202 | GIF | 0.00 | 3.20 | 13.42 | 17.28 | 5.04 | 8.40 | 20.64 | 1.71 | 6.14 | 1.02 | 0.25 | 0.85 | 0.12 | 0.67 | 0.14 | 0.37 | 0.05 | 0.31 | 0.04 | 1.25 | 0.88 | 1.77 | 36.50 | 1.33 |
| LWD-216 | GIF | 0.01 | 0.17 | 0.92 | 1.41 | 0.32 | 0.20 | 0.57 | 0.04 | 0.17 | 0.03 | 0.01 | 0.04 | 0.01 | 0.05 | 0.01 | 0.04 | 0.01 | 0.04 | 0.00 | 1.41 | 0.81 | 0.38 | 26.62 | 1.10 |
| LWD-238 | GIF | 0.1 | 13.12 | 54.35 | 26.49 | 22.17 | 31.74 | 77.75 | 6.57 | 24.37 | 4.45 | 1.41 | 4.04 | 0.64 | 3.85 | 0.81 | 2.27 | 0.34 | 1.96 | 0.25 | 1.24 | 0.88 | 1.07 | 27.48 | 1.62 |
| LWD-241 | GIF | 0.1 | 6.32 | 25.31 | 113.4 | 8.46 | 46.18 | 107.56 | 9.44 | 32.87 | 4.25 | 1.03 | 2.63 | 0.31 | 1.60 | 0.32 | 0.88 | 0.13 | 0.79 | 0.11 | 1.19 | 0.92 | 3.80 | 26.65 | 1.49 |
| LWD-244 | GIF | 0.00 | 0.20 | 1.23 | 17.15 | 2.10 | 0.36 | 1.31 | 0.13 | 0.57 | 0.17 | 0.08 | 0.23 | 0.04 | 0.28 | 0.06 | 0.18 | 0.03 | 0.16 | 0.02 | 1.39 | 0.87 | 0.26 | 33.85 | 1.92 |
| LWD-251 | SIF | 0.00 | 0.40 | 1.11 | 8.99 | 2.21 | 2.09 | 2.18 | 0.63 | 3.04 | 0.84 | 0.34 | 1.07 | 0.18 | 1.11 | 0.23 | 0.58 | 0.07 | 0.32 | 0.04 | 0.43 | 1.23 | 0.63 | 9.68 | 1.80 |
| LWD-252 | SIF | 0.00 | 0.30 | 1.64 | 5.51 | 6.54 | 2.07 | 4.25 | 0.53 | 2.32 | 0.59 | 0.25 | 0.78 | 0.14 | 0.98 | 0.22 | 0.65 | 0.10 | 0.55 | 0.07 | 0.93 | 0.99 | 0.31 | 29.37 | 1.72 |
| LWD-257 | BIF | 0.00 | 0.10 | 2.70 | 10.38 | 0.39 | 0.29 | 0.85 | 0.08 | 0.32 | 0.07 | 0.02 | 0.08 | 0.01 | 0.08 | 0.02 | 0.05 | 0.01 | 0.05 | 0.01 | 1.30 | 0.89 | 0.49 | 22.02 | 1.62 |
| LWD-274 | BIF | 0.2 | 5.52 | 36.39 | 83.50 | 2.50 | 5.82 | 15.21 | 1.43 | 5.17 | 0.87 | 0.21 | 0.58 | 0.08 | 0.52 | 0.11 | 0.35 | 0.06 | 0.37 | 0.05 | 1.21 | 0.94 | 1.23 | 21.85 | 1.37 |
| LWD-291 | BIF | 0.01 | 0.65 | 2.73 | 0.46 | 0.96 | 0.80 | 1.98 | 0.23 | 0.87 | 0.18 | 0.05 | 0.18 | 0.03 | 0.19 | 0.04 | 0.12 | 0.02 | 0.12 | 0.02 | 1.07 | 1.01 | 0.60 | 23.66 | 1.38 |
| LWD-314 | GIF | 0.01 | 0.22 | 2.71 | 0.85 | 0.72 | 1.93 | 3.71 | 0.45 | 1.85 | 0.33 | 0.08 | 0.24 | 0.03 | 0.14 | 0.03 | 0.08 | 0.01 | 0.06 | 0.01 | 0.92 | 1.01 | 2.30 | 25.98 | 1.46 |
| LWD-331 | BIF | 0.04 | 1.21 | 6.74 | 2.21 | 1.95 | 0.77 | 1.78 | 0.25 | 1.07 | 0.29 | 0.09 | 0.35 | 0.06 | 0.36 | 0.07 | 0.21 | 0.03 | 0.20 | 0.03 | 0.92 | 1.05 | 0.39 | 26.40 | 1.39 |
| LWD-347 | BIF | 0.00 | 0.33 | 1.33 | 4.49 | 7.82 | 3.89 | 5.77 | 0.67 | 2.82 | 0.53 | 0.28 | 0.72 | 0.10 | 0.70 | 0.17 | 0.51 | 0.07 | 0.41 | 0.06 | 0.81 | 0.98 | 0.53 | 45.79 | 2.41 |
| LWD-354 | GIF | 0.00 | 0.08 | 0.58 | 5.00 | 0.16 | 0.08 | 0.10 | 0.01 | 0.03 | 0.01 | 0.00 | 0.01 | 0.00 | 0.02 | 0.01 | 0.02 | 0.00 | 0.04 | 0.01 | 0.87 | 0.88 | 0.08 | 28.13 | 1.52 |
| LWD-391 | GIF | 0.02 | 0.71 | 0.41 | 0.65 | 1.41 | 0.37 | 0.75 | 0.10 | 0.46 | 0.14 | 0.04 | 0.20 | 0.03 | 0.20 | 0.04 | 0.12 | 0.02 | 0.11 | 0.02 | 0.90 | 0.99 | 0.28 | 32.34 | 1.34 |
| LWD-426 | BIF | 0.01 | 3.42 | 11.67 | 12.54 | 5.44 | 2.98 | 5.16 | 0.64 | 2.52 | 0.51 | 0.15 | 0.55 | 0.08 | 0.54 | 0.13 | 0.38 | 0.06 | 0.36 | 0.05 | 0.86 | 1.04 | 0.57 | 43.10 | 1.49 |
| ***Mosher carbonates, ca. 2.9 Ga, Steep Rock Group, Canada*** | | | | | | | | | | | | | | | | | | | | | | | | | |
| SR 5-2 | SC | | | 0.07 | 2.24 | 3.87 | 1.15 | 1.39 | 0.17 | 0.69 | 0.13 | 0.07 | 0.03 | 0.19 | 0.18 | 0.05 | 0.16 | 0.02 | 0.15 | 0.03 | 0.70 | 1.01 | 0.32 | 78.98 | 3.86 |
| SR 7-1-4 | SC | | | 0.02 | 1.55 | 2.12 | 0.62 | 0.76 | 0.09 | 0.36 | 0.07 | 0.03 | 0.01 | 0.10 | 0.10 | 0.03 | 0.09 | 0.01 | 0.08 | 0.01 | 0.72 | 1.00 | 0.34 | 78.57 | 3.76 |
| SR 7-1-3 | SC | | | 0.04 | 3.56 | 1.81 | 0.55 | 0.73 | 0.09 | 0.35 | 0.07 | 0.03 | 0.01 | 0.09 | 0.09 | 0.02 | 0.08 | 0.01 | 0.07 | 0.01 | 0.75 | 1.01 | 0.37 | 73.55 | 3.56 |
| SR 4-2-2 | SC | | | 0.05 | 3.24 | 1.44 | 0.51 | 0.73 | 0.09 | 0.33 | 0.06 | 0.02 | 0.01 | 0.07 | 0.07 | 0.02 | 0.06 | 0.01 | 0.05 | 0.01 | 0.79 | 1.01 | 0.51 | 77.00 | 2.85 |

| | | | | | | | | | | | | | | | | | | | | | | | |
|---|---|---|---|---|---|---|---|---|---|---|---|---|---|---|---|---|---|---|---|---|---|---|---|
| SR 4-1-2 | SC | 0.11 | 4.20 | 1.60 | 0.42 | 0.52 | 0.06 | 0.25 | 0.05 | 0.02 | 0.01 | 0.07 | 0.07 | 0.02 | 0.06 | 0.01 | 0.05 | 0.01 | 0.71 | 1.01 | 0.37 | 84.45 | 3.84 |
| SRS-1 | SC | 0.07 | 1.55 | 2.73 | 0.76 | 0.92 | 0.11 | 0.46 | 0.09 | 0.04 | 0.02 | 0.13 | 0.12 | 0.03 | 0.11 | 0.02 | 0.10 | 0.02 | 0.70 | 1.00 | 0.31 | 81.36 | 3.80 |
| SRC-1 | CP | 0.04 | 2.00 | 6.78 | 1.38 | 1.08 | 0.13 | 0.56 | 0.10 | 0.05 | 0.03 | 0.21 | 0.24 | 0.08 | 0.26 | 0.04 | 0.24 | 0.04 | 0.53 | 0.95 | 0.17 | 87.95 | 3.52 |
| SR 7-1 | SC | 0.27 | 1.76 | 1.57 | 0.50 | 0.65 | 0.08 | 0.30 | 0.06 | 0.02 | 0.01 | 0.08 | 0.07 | 0.02 | 0.06 | 0.01 | 0.05 | 0.01 | 0.74 | 1.00 | 0.43 | 81.45 | 2.98 |
| SRC-2 | CP | 0.04 | 2.31 | 1.28 | 0.42 | 0.62 | 0.08 | 0.29 | 0.06 | 0.02 | 0.01 | 0.07 | 0.07 | 0.02 | 0.05 | 0.01 | 0.05 | 0.01 | 0.80 | 1.03 | 0.48 | 74.40 | 2.76 |
| SRC-3 | CP | 0.13 | 3.30 | 6.26 | 1.25 | 1.00 | 0.12 | 0.51 | 0.09 | 0.04 | 0.03 | 0.19 | 0.23 | 0.07 | 0.26 | 0.04 | 0.25 | 0.05 | 0.54 | 0.94 | 0.13 | 84.71 | 3.58 |

***Samples analyzed at Laurentian University***

***BIF, Banded Iron Formation; GIF, Granular Iron Formation; SIF, Stromatolitic Iron Formation; SC, stromatolitic carbonate; CP, carbonate precipitate***

Table 1.2: Sample mineralogy

| Sample Name | Facies Type | Mineral 1 | Mineral 2 | Mineral 3 | Mineral 4 | Mineral 5 | Mineral 6 |
|---|---|---|---|---|---|---|---|
| ***Frere Iron Formation, ca. 1.8 Ga, Western Australia*** | | | | | | | |
| EAR-160.2 | GIF | | | | | | |
| EAR-162.6 | BIF | | | | | | |
| ***Cliffs Eire Mine, 1.88 Ga, Biwabik Iron Formation, USA*** | | | | | | | |
| AB5 | SIF | Quartz | Hematite | | | | |
| AB-9 | BIF | Quartz | Hematite | Siderite | Ankerite | | |
| AB-9* | BIF | Quartz | Hematite | Siderite | Ankerite | | |
| LA-LS-1 | BIF | Quartz | Ankerite | Siderite | Hematite | Magnetite | Stilpnomelane |
| ***Devils Icebox Mine, 1.88 Ga, Ironwood Iron Formation, USA*** | | | | | | | |
| DI3 | BIF | Quartz | Hematite | Magnetite | | | |
| AB11 | BIF | Quartz | Hematite | Magnetite | | | |
| ***Empire Mine, 1.88 Ga, Negaunee Iron Formation, USA*** | | | | | | | |
| AB4 | BIF | Magentite | Hematite | Quartz | | | |
| ***GF-3 Drill Core, 1.88 Ga, Gunflint Iron Formation, Canada*** | | | | | | | |
| DH3-27 | GIF | Magnetite | Hematite | Dolomite | Siderite | Ankerite | Quartz |
| DH3-42 | BIF | Hematite | Magnetite | Quartz | | | |
| DH3-43 | BIF | Hematite | Quartz | | | | |
| ***Kakabeka Falls, 1.88 Ga, Gunflint Iron Formation, Canada*** | | | | | | | |
| AB-KF-1 | BIF | Quartz | Siderite | Ankerite | Magnetite | Greenalite | |
| ***LWD-99-2 Drill Core, 1.88 Ga, Biwabik Iron Formation, USA*** | | | | | | | |
| 317-8 | GIF | Quartz | Siderite | Ankerite | | | |
| 317-10 | BIF | Magentite | Hematite | Quartz | | | |
| 317-10* | BIF | Magentite | Hematite | Quartz | | | |
| 317-12 | BIF | Siderite | Ankerite | Quartz | | | |
| 317-12* | BIF | Siderite | Ankerite | Quartz | | | |
| 317-13 | SIF | Quartz | Hematite | Pyrolusite | Ankerite | | |
| 317-13* | SIF | Quartz | Hematite | Pyrolusite | Ankerite | | |
| 317-22 | GIF | Quartz | Siderite | Ankerite | Hematite | | |
| 317-26 | GIF | Quartz | Hematite | Greenalite | Pyrite | | |
| ***Mink Mountain, 1.88 Ga, Gunflint Iron Formation, Canada*** | | | | | | | |
| MM2(A) | GIF | Quartz | Hematite | | | | |
| ***Norway Mining District, 1.88 Ga, Vulcan Iron Formation, USA*** | | | | | | | |
| Curry1 | MIF | Quartz | Magnetite | | | | |
| Curry2 | MIF | Magentite | Quartz | | | | |
| Curry2* | MIF | Magentite | Quartz | | | | |
| ***A6 Drill Core, ca. 2.0 Ga, Glen Township Formation, USA*** | | | | | | | |
| A6-1344 | BIF | Magentite | Ankerite | Siderite | Quartz | | |
| A6-1344* | BIF | Magentite | Ankerite | Siderite | Quartz | | |

| | | | | | | |
|---|---|---|---|---|---|---|
| ***Frere Iron Formation, ca. 1.8 Ga, Western Australia*** | | | | | | |
| EAR-160.2 | GIF | | | | | |
| EAR-162.6 | MIF | | | | | |
| ***Koegas area, ca. 2.48 Ga, Kuruman Iron Formation, South Africa*** | | | | | | |
| KOEN-2 | BIF | Quartz | Siderite | Clays | Hematite | |
| ***Kuruman area, ca. 2.48 Ga, Kuruman Iron Formation, South Africa*** | | | | | | |
| KU-9-537 | BIF | Quartz | Magnetite | Hematite | | |
| ***Westerberg area , 2.48 Ga, Kuruman Iron Formation, South Africa*** | | | | | | |
| W-18-740A | BIF | | | | | |
| ***Dales Gorge Member, ca. 2.45 Ga, Brockman Iron Formation, Western Australia*** | | | | | | |
| RM-4 | MIF | Quartz | Magnetite | Siderite | Hematite | |
| RM-5 | BIF | Quartz | Magnetite | Siderite | Hematite | |
| RM-8 | BIF | Quartz | Magnetite | Hematite | Ankerite | Siderite |
| RM9 | BIF | | | | | |
| RM-7 (DD475/1 | BIF | Quartz | Magnetite | Siderite | | |
| DDH75/1 | BIF | Quartz | Magnetite | Hematite | Siderite | |
| DDH75/1-466 | MIF | Quartz | Magnetite | Siderite | | |
| ***Black Hills area, ca. 2.5 Ga, Benchmark Iron Formation, USA*** | | | | | | |
| BIF-1 | BIF | Magentite | Quartz | | | |
| ***Kirkenes area, ca. 2.6 Ga, Bjornevanns Iron Formation, Norway*** | | | | | | |
| IF-5 | BIF | Quartz | Magnetite | Hematite | | |
| ***Manjeri Iron Formation, ca. 2.7 Ga, Zimbabwe*** | | | | | | |
| Z04-12 | BIF | Quartz | Hematite | Siderite | | |
| Z04-26 | BIF | Quartz | Hematite | Magnetite | | |
| Z04-31 | BIF | Quartz | Hematite | Magnetite | | |
| Z04-32 | BIF | Quartz | Hematite | Siderite | | |
| BMA-1 | BIF | Quartz | Hematite | Magnetite | | |
| BMA-2 | BIF | Quartz | Siderite | Magnetite | Hematite | |
| ***Mary River Iron Formation, ca. 2.72 Ga, Canada*** | | | | | | |
| JD-65-114C11 | BIF | Magentite | Quartz | Hematite | | |
| JD-65-207/2 | BIF | Quartz | Magnetite | Hematite | | |
| JD-65-260-1 | BIF | Quartz | Magnetite | Hematite | | |
| JD-65-285-C11 | BIF | Quartz | Magnetite | Hematite | | |
| JD-65-296-1 | BIF | Quartz | Magnetite | Hematite | | |
| JD-65-C-199-3 | BIF | Quartz | Magnetite | Hematite | | |
| JD-C165A | BIF | Quartz | Magnetite | Hematite | | |
| ***Soudan Iron Formation, ca. 2.72 Ga, USA*** | | | | | | |
| IF-17 | BIF | Quartz | Hematite | Magnetite | | |
| IF-18 | BIF | Quartz | Hematite | Magnetite | | |
| ***Temagami Iron Formation, ca. 2.74 Ga, Canada*** | | | | | | |
| IF-6 | BIF | Quartz | Magnetite | Hematite | | |
| IF-7 | BIF | Quartz | Magnetite | Hematite | | |

|  |  |  |  |  |  |  |
|---|---|---|---|---|---|---|
| ***Iron Formation of the Pongola Supergroup, ca. 2.95 Ga, South Africa*** |  |  |  |  |  |  |
| P05-1 | BIF | Quartz | Hematite | Magnetite |  |  |
| P05-6 | BIF | Quartz | Hematite | Magnetite |  |  |
| P05-7 | BIF | Quartz | Hematite | Magnetite |  |  |
| ***Iron Formation of the Witwatersrand basin, ca. 2.95 Ga, South Africa*** |  |  |  |  |  |  |
| IF-9 | BIF | Quartz | Hematite | Magnetite |  |  |
| ***LWD-99-2 Drill Core, 1.88 Ga Biwabik Iron Formation, USA*** |  |  |  |  |  |  |
| LWD-193 | BIF | Quartz |  |  |  |  |
| LWD-195 | BIF | Quartz | Siderite |  |  |  |
| LSD-202 | GIF | Quartz | Siderite |  |  |  |
| LWD-216 | GIF | Quartz | Siderite | Magnetite |  |  |
| LWD-238 | GIF | Quartz | Hematite | Magnetite |  |  |
| LWD-241 | GIF | Quartz | Hematite | Magnetite |  |  |
| LWD-244 | GIF | Quartz | Hematite | Magnetite |  |  |
| LWD-251 | SIF | Quartz | Hematite | Magnetite |  |  |
| LWD-252 | SIF | Quartz | Hematite | Magnetite | Pyrolusite | Siderite |
| LWD-257 | BIF | Quartz | Hematite | Magnetite |  |  |
| LWD-274 | BIF | Quartz | Magnetite |  |  |  |
| LWD-291 | BIF | Quartz | Magnetite | Hematite |  |  |
| LWD-314 | GIF | Quartz | Magnetite |  |  |  |
| LWD-331 | BIF | Quartz | Magnetite | Siderite | Pyrite |  |
| LWD-347 | BIF | Quartz | Magnetite | Siderite | Ankerite |  |
| LWD-354 | GIF | Quartz | Magnetite | Hematite |  |  |
| LWD-391 | GIF | Quartz | Siderite |  |  |  |
| LWD-426 | BIF | Quartz | Hematite |  |  |  |
| ***Mosher carbonates, ca. 2.9 Ga, Steep Rock Group, Canada*** |  |  |  |  |  |  |
| SR 4-2-2 | SC | Calcite | Dolomite |  |  |  |
| SRC-2 | CP | Calcite |  |  |  |  |
| SR 7-1 | SC | Calcite |  |  |  |  |
| SR 7-1-3 | SC | Calcite | Dolomite |  |  |  |
| SR 4-1-2 | SC | Calcite | Dolomite |  |  |  |
| SR 7-1-4 | SC | Calcite |  |  |  |  |
| SR 5-2 | SC | Calcite | Dolomite |  |  |  |
| SRS-1 | SC | Calcite | Dolomite |  |  |  |
| SRC-1 | CP | Calcite | Dolomite |  |  |  |
| SRC-3 | CP | Calcite | Dolomite |  |  |  |

BIF, banded iron formation; MIF massive iron formation; GIF, granular iron formation; SIF, stromatolitic iron formation SC, stromatolitic carbonates; CP, carbonate precipitates

**Table 1.3: Details of Mosher carbonate samples**

| Sample Name | Mineralogy | Sample description | Inferred paleodepth within Mosher carbonate succession |
|---|---|---|---|
| SR 4-2-2 | Calcite, Dolomite | Portion of a low-relief hemispheroidal stromatolite. The stromatolite was surrounded by carbonate grainstone with stromatolite rip-up clasts | shallow |
| SRC-2 | Calcite | Radiating crystal fans forming low-relief domes. Overlying sedimentary layers contain carbonate grains | shallow |
| SR 7-1 | Calcite | Portion of a columnar stromatolite that developed from a low-relief elongated stromatolite | intermediate |
| SR 7-1-3 | Calcite, Dolomite | Portion of a small (less than half a meter in largest dimension) elongated stromatolite | intermediate |
| SR 4-1-2 | Calcite, Dolomite | Portion of an small (less than half a meter in largest dimension) hemispheroidal stromatolite | shallow to intermediate |
| SR 7-1-4 | Calcite | Portion of an small (less than half a meter in largest dimension) elongated stromatolite | intermediate |
| SR 5-2 | Calcite, Dolomite | Portion of a large (approximately one meter in largest dimension) elongated stromatolite that contains fenestrate fabrics and radiating crystal fans | deep |
| SRS-1 | Calcite, Dolomite | Portion of a large (approximately one meter in largest diameter) elongated stromatolite that contains fenestrate fabrics and radiating crystal fans | deep |
| SRC-1 | Calcite, Dolomite | Sedimentary layers of carbonate precipitates without obvious crystal fan structures | deep (?) |
| SRC-3 | Calcite, Dolomite | Sedimentary layers of carbonate precipitates without obvious crystal fan structures | deep (?) |

## Chapter 2: Iron isotope composition of some Archean and Proterozoic iron formations

### Abstract

Fe isotopes can provide new insight into redox-dependent biogeochemical processes. Precambrian iron formations (IF) are deserving targets for Fe isotope studies because they are composed predominantly of authigenic Fe phases and record a period of unprecedented iron deposition in Earth’s history. I present Fe isotope data for bulk samples from 24 Archean and Proterozoic IF and eight Phanerozoic Fe oxide-rich deposits. These data reveal that many Archean and early Paleoproterozoic iron formations were a sink for isotopically heavy Fe, in contrast to later Proterozoic and Phanerozoic Fe oxide-rich rocks. The positive $\delta^{56}$Fe values in IF are best explained by delivery of particulate ferric oxides formed in the water column to the sediment-water interface. Because IF are a net sink for isotopically heavy Fe, there must be a corresponding pool of isotopically light Fe in the sedimentary record. Earlier work suggested that Archean pyritic black shales were an important part of this light sink before 2.35 billion years ago (Ga). It is therefore likely that the persistently and anomalously low $\delta^{56}$Fe values in shales are linked with the deposition of isotopically heavy Fe in IF of the deeper parts of basins. IF deposition produced a residual isotopically light dissolved Fe pool that was captured by pyritic Fe in shales. Local dissimilatory Fe reduction in porewater and associated diagenetic reactions resulting in pyrite and carbonate precipitation may have further enhanced Fe isotope heterogeneity in

marine sediments, and an ‘iron shuttle’ may have transported isotopically light Fe from shelf sediments to the basin. Nevertheless, water-column processing of hydrothermally delivered Fe likely had the strongest influence on the bulk iron isotope composition of Archean and Paleoproterozoic iron formations and other marine sediments.

## Introduction

The ocean-atmosphere system was largely anoxic in the early Precambrian, which led to a Fe cycle much different than today’s (Canfield, 2005; Holland, 2005; Rouxel et al., 2005). Iron would have been highly soluble in the anoxic and sulfate-poor early ocean, resulting in a period of intense Fe cycling before the rise of atmospheric oxygen and ocean oxygenation (Bekker et al., 2010; Holland, 2005). Microbial Fe oxidizers and reducers likely fueled a significant portion of this cycle; these metabolisms were probably important components of Earth’s early biosphere (Crowe, 2008; Hartman, 1984; Johnson et al., 2008b; Kappler et al., 2005; Konhauser et al., 2002; Walker, 1984; Widdel et al., 1993). Laterally extensive, highly Fe-rich sedimentary deposits—iron formations (IF)—are the most conspicuous evidence for substantial Fe redox cycling in the early oceans (Holland, 2005). Despite extensive research on IF, mechanisms for IF deposition and their role in the early Fe cycle remain debated (Bekker et al., 2010; Beukes and Gutzmer, 2008; Klein, 2005).

Iron isotopes allow us to trace Fe cycling and thus can improve our understanding of the mechanisms of IF deposition (Anbar and Rouxel, 2007; Dauphas and Rouxel, 2006; Johnson and Beard, 2006; Johnson et al., 2003; Johnson et al., 2008b). Much of the utility of Fe isotopes lies with their ability to fingerprint redox processes because the largest isotope fractionations are associated with redox transformations. For example, partial microbial and abiotic ferrous oxidation produces ferric oxides enriched in heavy Fe isotopes. Isotopic fractionations induced by oxidation in closed systems and in systems where Fe removal dominates over Fe supply are well-described by a Rayleigh fractionation model (Balci et al., 2006; Bullen et al., 2001; Johnson et al., 2008b; Welch et al., 2003). The exact mechanisms of fractionation during ferrous Fe oxidation and ferric oxide precipitation remain debated (Anbar et al., 2005; Bullen et al., 2001; Croal et al., 2004; Welch et al., 2003; Beard et al., 2010), but there appears to be a maximum fractionation [$Fe(III)_{solid}$ - $Fe(II)_{aq}$] of around 1 to 3‰ at 25°C. Experimental work suggests two-step fractionation during ferric oxide formation: an equilibrium isotope exchange between $Fe(III)_{aq}$ and $Fe(II)_{aq}$ is responsible for a 3.0‰ effect, and kinetic isotope fractionation upon precipitation of $Fe(OH)_3$ results in ~1‰ fractionation in the opposite direction (Welch et al., 2003). Recently, Beard and others (Beard et al., 2010) experimentally determined Fe isotope fractionation between aqueous ferrous iron and goethite and found an equilibrium isotope fractionation of 1.05±0.08‰ at 22°C. These experiments indicate that the interaction of $Fe(II)_{aq}$ and goethite results in near-complete

Fe isotope exchange over 30 days, involving at least four components: Fe(II)aq, goethite, adsorbed Fe(II), and Fe(III)$_{surface}$.

Dissimilatory microbial Fe reduction (DIR) can produce large Fe isotope fractionations between Fe(III)$_{solid}$ and Fe(II)$_{aq}$ with variably depleted $\delta^{56}$Fe values in the generated dissolved Fe (Beard et al., 1999; Crosby et al., 2007; Icopini et al., 2004). The extent of fractionation during DIR varies with the proportions of aqueous Fe(II), adsorbed Fe(II) and reactive Fe(III) on particle surfaces (Crosby et al., 2005; Crosby et al., 2007). There are typically smaller fractionations associated with non redox-dependent processes. Siderite formation, for example, has an equilibrium fractionation factor of ~ –0.5‰ with aqueous Fe(II) (Wiesli et al., 2004). There are several recent detailed reviews covering the magnitude and mechanisms of Fe isotope fractionations (Anbar and Rouxel, 2007; Dauphas and Rouxel, 2006; Johnson et al., 2008b).

The $\delta^{56}$Fe values of modern marine Fe sources are relatively well known. Igneous rocks have near-zero $\delta^{56}$Fe values that cluster at 0.09‰ relative to the IRMM-14 standard (Anbar and Rouxel, 2007; Dauphas and Rouxel, 2006; Johnson et al., 2008b). Deep-sea hydrothermal vents (Bennett et al., 2009; Rouxel et al., 2008a; Severmann et al., 2004) and shelf sediment porewaters (Homoky et al., 2009; Severmann et al., 2006; Staubwasser et al., 2006) generally have dissolved ferrous Fe with negative $\delta^{56}$Fe values, ranging from +0.1 to –0.9 and from +0.4 to <–3, respectively. With some rare exceptions

(Bergquist and Boyle, 2006; Escoube et al., 2009), fluvial systems also typically carry isotopically light dissolved Fe. Likewise, the Fe isotope composition of dissolved Fe in open and coastal seawater has been shown to range between slightly positive (+0.7‰) to negative (–1.8‰) values (John and Adkins, 2010; Lacan et al., 2008; Rouxel and Auro, 2010). Hydrothermal systems are generally considered to be the primary source of Fe to the early Precambrian ocean (Bau et al., 1997; Isley, 1995; Krapež et al., 2003), indacting there was a strong flux of dissolved Fe to bottom waters with an average $\delta^{56}$Fe value somewhere between 0 and –0.5‰.

Since we have now a basic understanding of Fe isotope fractionation factors and the $\delta^{56}$Fe values of different iron species entering the oceans, Fe isotope composition of marine sediments can offer insight into processes of Fe deposition, the $\delta^{56}$Fe values of dissolved Fe in ancient oceans, and specific mechanisms of Fe cycling. Here, I present new Fe isotope data for bulk samples from 24 Archean and Proterozoic IF and eight Phanerozoic distal hydrothermal deposits for comparison.

An estimate of the average $\delta^{56}$Fe value of IF is essential to constructing an iron isotope mass balance for the early ocean (Dauphas and Rouxel, 2006). There is typically little (< 1‰) isotopic variation in Phanerozoic marine siliciclastic deposits (Beard et al., 2003; Rouxel et al., 2003) and chemically (i.e., hydrogeneous) precipitated sediments (Levasseur et al., 2004; Rouxel et al., 2003). In contrast, Archean sediments show much larger Fe isotope variations; the observed 4.5‰ range includes both positive and negative values relative to average continental crust (e.g., Rouxel et al., 2005; Johnson et al., 2008b).

A secular $\delta^{56}$Fe trend, foremost from the sedimentary black shale record, is now widely recognized. However, the mechanisms behind this trend are still debated (Rouxel et al., 2005; Yamaguchi et al., 2005). The unmatched variability seen in Archean and early Paleoproterozoic sedimentary rocks has been linked to deposition of isotopically heavy IF, reflecting high delivery of hydrothermal Fe to a sulfur-poor anoxic deep ocean (Rouxel et al., 2005). Alternatively, this peak in Fe isotope variability may reflect a period of enhanced microbial Fe reduction when microbial sulfate reduction was limited due to the low levels of seawater sulfate and abundant Fe oxides (Johnson et al., 2008b). Additionally, Severmann and others (2008) argued that an enhanced flux of isotopically light Fe transported from shallow-marine settings to the deep ocean might explain the observed Precambrian pattern. Shallow-to-deep Fe shuttling is suggested in redox-stratified marine basins, such as the modern Black Sea (reviewed in Lyons and Severmann, 2006) and could have relevance to the deep past. Our new iron isotope data, when viewed in light of available facies models for IF, can help to refine our understanding of various Fe sources and sinks in Precambrian oceans.

## Analytical Methods

Ten to over a hundred grams of cleaned drill-core or fresh outcrop material were crushed between two plexiglass discs inside a polypropylene bag using a hydraulic press. The resulting rock chips were further cleaned using several rinses with deionized water and ultrasonification. The cleaned material was homogenized and powdered in an agate shatter-box. About 100 mg of powder were then dissolved in an ultra-pure $HNO_3$-HCl-HF acid mixture. Iron was purified on Bio-Rad AG1X8 anion resin, and Fe isotope ratios were determined with a Thermo-Electron *Neptune* multicollector inductively coupled plasma mass-spectrometer (MC-ICP-MS) following previously published methods (Rouxel et al., 2008a; Rouxel et al., 2008b; Rouxel et al., 2005). I operated the MC-ICP-MS in either medium or high-resolution mode, and I used Ni as an internal standard for mass bias correction. Fe isotope values are reported relative to the standard IRMM-14 using the conventional delta notations (Table 1). I measured several georeference materials, including one IF (IF-G) and one Hawaiian Basalt (BHVO-1). I obtained a $\delta^{56}$Fe value of 0.67‰ for the IF-G standard, which is similar to previously reported values (Dauphas and Rouxel, 2006). Based on duplicate chemical purifications and isotope analyses, the long-term external reproducibility is 0.08‰ for $\delta^{56}$Fe and 0.11‰ for $\delta^{57}$Fe (2 standard deviations). Mineralogy was determined through a combination of standard petrographic techniques and X-Ray diffraction (XRD).

## Sample details

I present Fe isotope data from Si- and Fe-dominated sedimentary rocks with low levels of detrital siliciclastic and volcaniclastic material. Most of the samples in this study are Al-poor (< 1 weight % $Al_2O_3$) and Fe-rich (>10 weight % $Fe_2O_3$). The Fe is present predominantly in a carbonate, silicate or oxide phases. Our sample set is composed largely of granular and banded IF, as well as ferruginous cherts that have limited spatial distribution (e.g., hydrothermal jaspers). However, I also present results for some ferruginous shales associated with IF and some cherts that contain less than 10% $Fe_2O_3$, since their elevated Fe/Al ratios (>5 compared to ~0.5 for average continental crust) indicate that Fe in these rocks is also predominantly of an authigenic origin.

Following Beukes and Gutzmer (2008) and Gross (1980) I group IFs into two broadly defined types: Superior-type and Algoma-type IF. Superior-type IF typically reflect deposition in close association with shelf sediments such as carbonates and shales (Beukes and Gutzmer, 2008). Even IF deposited in shelf settings, however, appear to be linked to strong hydrothermal Fe supply, albeit from distal sources (Bekker et al., 2010). Algoma-type IF, in contrast, occur in close spatial association with bimodal (mafic and felsic) volcanic rocks, basinal shales, and hydrothermal deposits. Superior-type IF commonly extend over hundreds of square kilometers; Algoma-type iron formations are typically more restricted in their aerial extent.

I have avoided samples from sequences that have experienced obvious secondary ore-forming processes (e.g., supergene Fe-enrichment). Samples with visible sign of fluid flow (extensive veining, disruption of sedimentary features, and mineral phases cross-cutting sedimentary layers) were also avoided. Given that mineral assemblages in even the best-preserved samples of Archean and early Paleoproterozoic IF have been strongly influenced by post-depositional alteration (e.g., Bekker et al., 2010), I focused on bulk (hand sample-sized) analyses rather than analysis of individual mineral separates. For instance, magnetite is a ubiquitous component of IF and, in most cases, is thought to be a late-stage diagenetic or metamorphic mineral, even in well-preserved IF like those in the Hamersley province (e.g., Krapež et al., 2003; Tompkins and Cowan, 2001). I also chose to use a bulk sample approach because one of the central goals of this work was to provide an estimate of the average Fe isotope composition of IF, rather than distinct mineral phases. Sample details and relevant references with locality information are listed in Appendix Tables 1 and 2.

## Results

I found a wide range of $\delta^{56}$Fe values for bulk samples of IF (Fig. 2.1). Archean to early Paleoproterozoic IF (ca. 3.0 to 2.45 Ga) have values ranging from –1.53‰ to 1.61‰ (Fig. 2.2) with a mean of 0.4‰ (n=43). These formations were deposited before the rise of atmospheric oxygen at ca. 2.4 Ga (Bekker et al., 2004) and are from both Algoma-type and Superior-type IF (Table 1). There is no statistically significant difference in the data for Superior-type and Algoma-type IF (see Table 1). However, the mean for Algoma-type IF ($\delta^{56}$Fe = 0.55‰) is slightly higher than that for Superior-type IF ($\delta^{56}$Fe = 0.29‰). Furthermore, the Superior-type IF contain the most negative $\delta^{56}$Fe values (e.g., for the ca. 2.95 Ga Pongola IF). Our sample set is composed predominately of oxide-facies IF.

In apparent contrast to the Archean record, IF deposited in the middle to late Paleoproterozoic (ca. 2.3 Ga to 1.85 Ga) yielded $\delta^{56}$Fe values ranging from –0.66‰ to 1.1‰, with an average $\delta^{56}$Fe value of 0.03‰ (n=19). These samples are from cratonic settings and deep-water hydrothermal jaspers. The ca. 1.88 Ga IF have on average slightly more positive $\delta^{56}$Fe values (e.g., Planavsky et al., 2009). IF and jaspers deposited in the Mesoproterozoic, Neoproterozoic, and Phanerozoic show $\delta^{56}$Fe values ranging from –0.87‰ to 1.66‰, with an average $\delta^{56}$Fe value of 0.1‰ (n= 28). This group of iron-rich units consists largely of distal hydrothermal deposits but also includes IF associated with the 'Snowball Earth' glacial events (Table 1).

## Discussion

### Iron-formation depositional processes

Iron isotopes provide evidence that Fe enrichment in IF is predominantly caused by a deposition of Fe-oxides and Fe-oxyhydroxides. There is positive Fe isotope fractionation during microbial and abiotic Fe oxidation with a maximum fractionation of ~2-3‰ (Balci et al., 2006; Bullen et al., 2001; Croal et al., 2004; Welch et al., 2003). This enrichment in heavy Fe isotopes contrasts with the isotope fractionations associated with siderite, ankerite, and green rust deposition, which are depleted in the heavy isotope relative to the ambient $Fe(II)_{aq}$ pool (Wiesli et al., 2004). Our bulk Fe isotope data are likely to reflect marine sedimentary and diagenetic processes, as I avoided samples that have been strongly influenced by ore-forming processes. Furthermore, late-stage, post-depositional (metamorphic) mineral transformations in IF determine Fe isotope composition of secondary minerals but not the whole rock (e.g., Frost et al., 2007). Fe repartitioning among minerals occurs in a closed system at our scale of observation. Therefore, predominantly positive $\delta^{56}$Fe values in IF can be a signal of ferrous iron oxidation in the marine water column (Dauphas et al., 2004). This model builds on strong evidence that Fe in IF was derived from a seawater-dissolved pool, which was initially supplied from a hydrothermal source (Bau et al., 1997; Beukes and Gutzmer, 2008; Isley, 1995; Krapež et al., 2003) and therefore had near crustal or negative $\delta^{56}$Fe value (Dauphas and Rouxel, 2006; Johnson et al., 2008a; Severmann et al., 2004). This framework implies that the preserved mineral assemblage did not precipitate in isotopic equilibrium with the ancient oceans in cases where IF are dominated by reduced or mixed valence Fe mineral phases but positive bulk $\delta^{56}$Fe values (see Johnson et al., 2008b). The reduced and mixed valence IF minerals (e.g., magnetite, siderite, and greenalite) therefore must have formed largely during early to late diagenesis or metamorphism, likely by nearly quantitative reduction of Fe oxides with positive $\delta^{56}$Fe values (Craddock and Dauphas, 2011; Johnson et al., 2008a; Steinhoefel et al., 2009). This interpretation for the origin of siderite and magnetite in IF is fully consistent with previous detailed petrographic and carbon isotope data (e.g., Ahn and Buseck, 1990; Kaufman et al., 1990; Pecoits et al., 2009) and is also consistent with some interpretations of the fine-scale Fe isotope variations in IF (e.g., Craddock and Dauphas, 2011; Johnson et al., 2008a; Johnson et al., 2008b).

The presence of positive $\delta^{56}$Fe values in bulk IF likely points to low oxidizing potential in basins where the IF were deposited. Rather than showing positive Fe isotope values, bulk rock Fe-oxides should record the $\delta^{56}$Fe value of initial dissolved iron when there is near-quantitative oxidation. For example, plume fallout deposits near the Rainbow hydrothermal vent along the Mid-Atlantic Ridge are generally similar in their $\delta^{56}$Fe values to vent fluids due to quantitative Fe oxidation in oxic seawater (Severmann et al., 2004). Since IF are also chemically precipitated sediments with the Fe derived from hydrothermal fluids, modern submarine hydrothermal plume deposits provide useful analogs, as they also lack sulfide minerals and appreciable organic C enrichment. In contrast to what I observe, the variably negative $\delta^{56}$Fe values in Late Cenozoic hydrogeneous crusts, although not fully understood, likely reflect quantitative precipitation of oceanic Fe derived from diverse sources, such as atmospheric input, shelf-derived Fe, and hydrothermal sources (Anbar and Rouxel, 2007; Rouxel et al., 2008b; Severmann et al., 2006; Severmann et al., 2008; Staubwasser et al., 2006). Complex interactions with organic ligands in the water column may also contribute to the $\delta^{56}$Fe variations. As previously discussed in Rouxel et al. (2003), both positive and negative $\delta^{56}$Fe values in Phanerozoic Fe-rich hydrothermal cherts are likely the result of partial oxidation near or below the seafloor during the circulation of low-temperature hydrothermal fluids through volcanics on the ocean floor. In all cases, incomplete oxidation is required for the expression of the Fe-oxide Fe isotope fractionation and requires low oxygen or anoxic conditions. It follows that the $\delta^{56}$Fe values of bulk samples of IF are likely to be strongly influenced by the extent of oxidation (Dauphas and Rouxel, 2006; Planavsky et al., 2009; Steinhoefel et al., 2009).

The REE compositions of the same IF samples examined in this study for their Fe properties provide strong support for the partial oxidation model (cf. Planavsky et al., 2010). IF deposited before ca. 2.4 Ga show no deviation from trivalent Ce behavior, suggesting that the water column from which ferric oxides and oxyhydroxides precipitated was reducing with respect to manganese (cf. Bau and Dulski, 1996). There is also a shift in the variation in trivalent REE behavior in IF deposited before and after the rise of atmospheric oxygen. Archean and early Paleoproterozoic IF are characterized by consistent depletion in light REE and high Y/Ho ratios. These features contrast markedly with late Paleoproterozoic IF, which show significant ranges in light-to-heavy REE (Pr/Yb$_{(SN)}$) and Y/Ho ratios both below and above the reference value of the shale composite. The range of light-to-heavy REE and Y/Ho ratios in late Paleoproterozoic IF likely reflects varying impacts from Mn- and Fe-oxyhydroxide precipitation/dissolution. This interpretation implies deposition of late Paleoproterozoic (ca. 1.88 Ga) IF in basins with widely varying redox conditions. A dynamic redoxcline must have separated the oxic upper part of the water column from the suboxic to anoxic deeper parts in the late Paleoproterozoic, but this redox stratification was rare or absent in Archean basins (Planavsky et al., 2010).

Alternatively, positive $\delta^{56}$Fe values in IF may reflect extensive re-reduction and release of isotopically light Fe following near-quantitative rather than partial Fe oxidation (Johnson et al., 2008a). Since DIR has been proposed to preferentially release light Fe isotopes to solution (e.g., Beard et al., 1999), partial reduction within the sediments of ferric oxides that rained down through the water column would leave residual oxides with positive $\delta^{56}$Fe values. However, it is unlikely that DIR would have had a major influence on the Fe isotope composition of bulk sediments in extremely organic matter-poor, oxide-dominated IF, since the flux of reactive iron oxides was much greater than the input of organic matter. Additionally, even though DIR can be highly efficient, it is likely that only a small portion of Fe(II) would be lost back to the water column, with a larger fraction being absorbed onto Fe(III) oxyhydroxides or precipitated as Fe carbonates or Fe silicates. Importantly, diagenetic precipitation of mixed valence Fe oxides should not significantly alter the whole-rock Fe isotope composition of IF.

The negative whole-rock $\delta^{56}$Fe values in our Archean and Paleoproterozoic IF samples, although relatively rare (<20% of the dataset), likely provide additional insight into the early Fe cycle. Early diagenetic Fe cycling in low sulfate environments creates two Fe reservoirs: one mobile and isotopically light and the other immobile and isotopically heavy. As discussed above, unless there is a net loss into the overlying water column of isotopically light Fe by diffusion through the sediment, bulk sediment values should not be affected by microbial reduction of the Fe(III) load . Accordingly, negative values of the bulk samples of IF indicate a particulate flux of isotopically light Fe to the sediments.

There are two commonly proposed models for fluxes of isotopically negative Fe to sediments from the overlying water column, and both could have contributed to the origin of IF with negative whole-rock $\delta^{56}$Fe values. The flux of light Fe could be the result of near-quantitative oxidation in the water column of DIR products (e.g., Severmann et al., 2008). Second, Rayleigh-type fractionation during partial Fe(II) oxidation could create an isotopically light reservoir of residual dissolve Fe that is transferred to the sediment pile with later oxidation (e.g., Rouxel et al., 2005; Steinhoefel et al., 2009; Tsikos et al., 2010). Importantly, in both models, negative whole-rock $\delta^{56}$Fe signatures likely reflect temporal or spatial variation in seawater $\delta^{56}$Fe values.

In the Rayleigh fractionation model, the isotopically light Fe would be sourced from hydrothermal systems, with the dissolved Fe experiencing partial oxidation during transport from hydrothermal centers to shallower depositional settings (cf., von

Blanckenburg et al., 2008). Partial oxidation could also occur in a hydrothermal plume with little vertical movement. Oxidation would result in a greater enrichment in the lighter Fe isotopes in the remaining dissolved Fe pool. A possibility is that anoxygenic phototropic oxidation could establish significant water column Fe concentration gradients—and therefore Fe isotope gradients—through ferric Fe removal during upwelling. This model is consistent with the generally accepted genetic models for Archean and Paleoproterozoic IF—specifically, a hydrothermal Fe supply in combination with a water column Fe concentration gradient (Bau and Dulski, 1996; Sumner, 1997; Sumner and Grotzinger, 2004). The lack of evidence for a discrete (sharp) redoxcline based on the REE composition of the Archean shallow-water carbonates (Planavsky et al., 2010) is also consistent with this model. Accordingly, the Fe isotope composition throughout the water column in the Archean oceans likely mimicked the isotope behavior of nutrient-type elements that show variations with depth in the modern ocean, such as Si (e.g., Reynolds et al., 2006),

Alternatively, the isotopically light Fe could have been supplied by a "benthic Fe shuttle" (Severmann et al., 2008). In this model DIR creates an isotopically light Fe pool in porewaters, which diffuses from the sediments and is transported to and eventually precipitated in the deeper portion of the basin. In modern redox-stratified basins (e.g., Black Sea), there is a flux of Fe from sediments on the oxic shelf into the deep, euxinic portion of the basin (e.g., Lyons and Severmann, 2006). Similar processes may have operated in Archean basins (Raiswell, 2006; Severmann et al., 2008). However, it is likely that in shallow stretches of the Archean oceans the relatively small flux Fe oxides was rapidly and quantitatively reduced in the upper part of the sediment pile. This would have limited isotopic expression of microbial Fe reduction and thus of the modern "benthic Fe shuttle". In the Archean, the shallow oceans, in contrast to the Fe oxide-rich deep oceans, were extremely oxidant limited—a redox structure coined the upside-down biosphere (Walker, 1984). Partial Fe reduction was more common in the deep oceans than on the continental shelves in the Archean (Walker, 1984).

## Comparison with previous Fe isotope studies of IF

Our Fe isotope results for a broad survey of IF are consistent with several studies of Eoarchean (ca. 3.8 Ga) and Neoarchean (ca. 2.7 Ga) deposits (Dauphas et al., 2004; Rouxel et al., 2005; Steinhoefel et al., 2009), which also revealed predominantly positive iron isotope values. Johnson et al. (2008) concluded that IF in the Transvaal basin and Hamersley province (Beukes and Gutzmer, 2008) have an average bulk $\delta^{56}$Fe value around 0‰, which they interpreted to represent the average composition of late Neoarchean and early Paleoproterozic IF. This 0‰ average value is significant because it is just slightly above the average Fe isotope value of hydrothermally derived Fe (Rouxel et al., 2003; Severmann et al., 2004), implying near-quantitative oxidation of dissolved iron in seawater. However, since the study by Johnson et al. (2008) was based on samples from mineralogically pure siderite and magnetite microlaminae, the data should be viewed with some caution. Specifically, this sampling strategy has a potential to skew the data toward negative values (relative to the bulk samples), since these microlaminae might be linked to Fe derived from microbial Fe reduction (Johnson et al., 2008a). A subsequent study found that the Brockman Iron Formation in the Hamersley province has slightly positive average $\delta^{56}$Fe values (Craddock and Dauphas, 2011).

Further work is needed to explore whether there was a temporal change in the Fe isotope composition of IF prior to the rise of atmospheric oxygen. Although an extensive dataset is already available for Late Archean and early Paleoproterozoic IF (e.g., Heimann et al., 2010; Johnson et al., 2008a), additional data including whole-rock analyses would test the idea that Late Archean IFs have a near-crustal iron isotope composition. Further, although our study is a step forward in establishing the whole-rock Fe isotope composition of diverse Archean IF, it should be regarded as preliminary given the number and diversity of Archean IF.

Tsikos and others (2010) recently interpreted markedly negative Fe isotope values in the Fe- and Mn-rich Hotazel Formation in South Africa to be the result of Rayleigh distillation and deposition of isotopically heavy Fe oxide-rich rocks. This is consistent with our interpretation that the negative values in bulk samples of IF likely reflect dissolved marine Fe isotope compositions.

## Iron isotope mass balance in the Earth's early oceans

Since our study suggests that IF older than ca. 2.4 Ga are a sink for isotopically heavy Fe, there must be a corresponding contemporaneous sink of isotopically light Fe in the sedimentary record. Pyritic black shale and, to a lesser extent, carbonates appear to be at least part of this sink (Fig. 2.3). Bulk samples of Archean black shales and sedimentary pyrites are characterized by persistently and anomalously low $\delta^{56}$Fe values (Rouxel et al., 2005, 2006; Yamaguchi et al., 2005). Carbonates of this age also have highly negative $\delta^{56}$Fe values (Czaja et al., 2010; von Blanckenburg et al., 2008). As discussed above, bulk IF can also be sinks of isotopically light Fe. The origin of these highly negative $\delta^{56}$Fe values in sedimentary pyrite and carbonates has been heavily debated. For example, they have been linked to a period of extensive DIR in a low sulfate ocean at the end of the Archean (e.g., Heimann et al., 2010; Johnson et al., 2008a). However, large Fe isotope fractionations have not been observed during DIR in modern sulfate-poor aquatic systems (e.g., Tangalos et al., 2010; Teutsch et al., 2009)—in conflict with this model. Guilbaud and others (2011) suggested that the light Fe isotope values in Archean sedimentary rocks were linked to fractionation during pyrite formation. Instead, Rouxel et al. (2005) attributed these values to deposition of isotopically heavy, Fe oxide-rich IF in the deep-water portions of basins, which left the residual dissolved pool light. Our results provide additional support for this model. Specifically, I confirm that many IFs have positive average $\delta^{56}$Fe values.

In most reconstructions of Archean basins, black shales are inferred to have formed landward with respect to the deeper-water IF (Bekker et al., 2009; Beukes and Gutzmer, 2008; Reinhard et al., 2009). The black shales, which contain the lowest $\delta^{56}$Fe values, often display evidence for formation in euxinic settings or near the interface between shallow euxinic and deeper ferruginous conditions (Bekker et al., 2009; Reinhard et al., 2009; Scott et al., 2008). By analogy with modern marine euxinic settings (e.g., Lyons, 1997) and modern ferruginous lakes (e.g., Bura-Naki et al., 2009), a large portion of the sulfides found in black shales likely formed in the water column. Thus, partial Fe oxidation that drove IF deposition would have left a pool of isotopically light dissolved iron that was transferred to the sedimentary record as pyrite. In this scenario, the negative Fe isotope values in Archean black shales are linked predominantly to ocean-scale removal of heavy Fe via Fe oxide phases.

An assumption in the above outlined model is that there is limited Fe isotope fractionation during pyrite formation, so that the observed negative $\delta^{56}$Fe values for pyrite are an archive of an ocean pool of light dissolved Fe (Rouxel et al., 2005). This assumption is valid if the sulfides formed in sulfide-rich/Fe-limiting euxinic conditions, where there will be nearly quantitative Fe removal. The exact fractionation factor during pyrite formation in Fe-unlimited conditions is unclear. Based on theoretical calculation, it is likely that the equilibrium fractionation factor during pyrite formation is around -1‰ ($Fe[II]_{aq}$- mineral) (Polyakov et al., 2007). In contrast, there is evidence from experiments and observations in natural systems for significant positive ($Fe[II]_{aq}$- mineral) kinetic—and possibly equilibrium—isotope fractionation during precipitation of 'FeS', a pyrite precursor (Butler et al., 2005), and pyrite (Guilbaud et al., 2011). The fractionation during FeS formation can be up to 0.9‰ in both hydrothermal and sedimentary settings and probably depends on the rate of FeS formation. There can also be a several per mil negative kinetic isotope fractionation during pyrite formation (Guilbaud et al., 2011). However, there is Fe isotope exchange and a progressive change towards isotopically heavy FeS on a relatively short (hourly) time scale—pushing the particulate sulfides heavy (Butler et al., 2005). Since large portion of the sulfide in modern Fe-rich aquatic systems is present as nanometer-scale aggregates (nanoparticles) of metal sulfide molecular clusters (Luther and Rickard, 2005), isotopic exchange is expected to be rapid while settling times to be very slow, which argues against a positive fractionation ($Fe[II]_{aq}$- mineral) during pyrite formation in anoxic aquatic systems. However, further Fe isotope work in modern Fe-rich aquatic systems is needed to better understand Fe isotope fractionation during sulfide formation.

Despite uncertainties about Fe isotope fractionation during pyrite formation in ferruginous conditions, available evidence points towards redox evolution as the origin for markedly light iron isotope values in the Archean. I propose that the markedly negative $\delta^{56}$Fe values (down to -3.5‰) present in the Archean sedimentary pyrites, which are unknown in the Phanerozoic black shale geological record (Rouxel et al., 2005), reflect a time period when reducing marine conditions prevailed and yet significant iron oxidation occurred in the water column. This combination would have allowed for separation and burial of isotopically distinct pools of Fe as facilitated by partial Fe oxidation even when the size of the marine dissolved iron reservoir was diminished. Precipitation of around half of an initial hydrothermal Fe pool as isotopically heavy Fe oxides is needed for formation of sulfides with $\delta^{56}$Fe values of –1.5 to –2.0‰ that are typical of Late Archean sulfides. The partial oxidation model requires that more than 90% of Fe is removed by precipitation of Fe oxides to explain the most negative iron isotope values as low as -3.5‰ (Rouxel et al., 2005). This level of iron drawdown is consistent with geologic and petrographic evidence for a large water column Fe concentration gradient and $\mu$M levels of iron even in the mixed layer of the Archean ocean (Sumner, 1997). Further, given Fe oxidation rates typical of modern anoxygenic photosynthesizers, a simple box model suggests variable extents of Fe oxidation during upwelling using the observed range of upwelling rates in the modern ocean. There is even the potential for quantitative oxidation despite high initial dissolved Fe concentrations (Kappler et al., 2005). Therefore, there are likely have been water column Fe isotope gradients in the Archean ocean.

In a reducing ocean, Fe emanating from hydrothermal centers could undergo partial oxidation in the upper water column by anoxic oxidation (e.g., anoxygenic photosynthetic Fe oxidation) or microaerophilic oxidation during plume transport. Partial oxidation would produce Fe-rich sediments with positive $\delta^{56}$Fe values—as I observe in our bulk samples. If the matured plume/water parcel entered the sulfidic zone in shallower waters (likely on continental shelves), sulfides with negative $\delta^{56}$Fe values would have precipitated (e.g., Bekker et al., 2009). This model is consistent with the presence of markedly negative Fe isotope values in shales independently determined to be deposited under euxinic (Fe limited) conditions (Rouxel et al., 2005; Reinhard et al., 2009; Scott et al., 2008, 2011). In contrast, with a high surface-water oxidizing potential, the zone of partial Fe oxidation would condense, resulting in limited expression of Rayleigh isotope fractionation due to quantitative oxidation (Fig. 2.4).

Oxidative removal of dissolved Fe could have facilitated the formation of sulfidic water masses; removal of Fe oxides would increase the $SO_4^{2-}/Fe^{2+}$ ratio in the water column, favoring euxinia. Oxide burial would dominate over pyrite burial if there was a limited sulfate supply or when there was a limited organic matter flux to fuel sulfate reduction. Since organic productivity varies greatly within oceans, the redox chemistry of a water mass would likely change along a circulation path. This model provides a simple explanation for why organic matter-rich shales deposited under euxinic conditions, a sedimentary rock type relatively common throughout the Earth's history, would have unusually negative Fe isotope values prior to the Great Oxidation Event (Fig. 2.3, 2.4).

## Conclusions

New whole-rock Fe isotope data for IF and other iron-rich sedimentary rocks indicate that Archean and early Paleoproterozoic IF were a sink for isotopically heavy Fe, in contrast to the later Proterozoic and Phanerozoic iron oxide-rich rocks. The positive $\delta^{56}$Fe values indicate that IF deposition in the Archean was linked with a rain of ferric oxides and oxyhydroxides to the sediment-water interface. Positive Fe isotope values are likely linked to Fe isotope fractionation associated with partial ferrous Fe oxidation under Fe-replete conditions. These fractionations, in contrast, are muted by near-complete oxidation in younger deposits. The prevalence of partial oxidation is consistent with other evidence for a diffuse rather than sharp redoxcline and generally reducing conditions in the Archean oceans (Alexander et al., 2008; Bau and Dulski, 1996; Planavsky et al., 2010; Sumner, 1997).

Since our study suggests that IF are a sink for isotopically heavy Fe, there must be a corresponding reservoir of isotopically light Fe in the sedimentary record. Pyrite in black shales appear to be part of this sink. The persistently and anomalously low $\delta^{56}$Fe values seen in these rocks (Rouxel et al., 2005; Yamaguchi et al., 2005) can be linked with deposition of isotopically heavy Fe in the deeper parts of basins and the transport of Fe with negative $\delta^{56}$Fe values to shallower, more shoreward settings where shale deposition and abundant pyrite formation occurred.

Archean black shales with notably low and variable Fe isotope values are typically inferred to have formed landward of the deeper-water IF, and often in a sulfidic zone (Bekker et al., 2009; Reinhard et al., 2009, Scott et al., 2011). The markedly negative $\delta^{56}$Fe values of the Archean sedimentary pyrite could reflect a time when reducing marine conditions prevailed. This redox state would have allowed for separation and burial of isotopically distinct pools of Fe as well as for partial oxidation even as the size of dissolved Fe pool decreased by ferric oxide and oxyhydroxide deposition. At times with higher surface-water oxidation potential, the zone of partial iron oxidation would have shrunk, resulting in limited expression of the fractionation associated with Fe oxidation since Fe removal under these conditions would be quantitative. Thus, the Fe isotope records of marine shales and IF, when viewed together, capture the redox evolution of the oceans and suggest that the Archean and early Paleoproterozoic oceans before the rise of atmospheric oxygen typically lacked a sharp, persistent, and pervasive redoxcline, consistent with independent arguments based on REE systematics (e.g., Planavsky et al., 2010).

## References

Ahn, J.H., Buseck, P.R., 1990. Hematite nanospheres of possible colloidal origin from a Precambrian banded iron formation. Nature 250, 111-113.

Alexander, B.W., Bau, M., Andersson, P., Dulski, P., 2008. Continentally-derived solutes in shallow Archean seawater: Rare earth element and Nd isotope evidence in iron formation from the 2.9 Ga Pongola Supergroup, South Africa. Geochimica et Cosmochimica Acta 72, 378-394.

Anbar, A.D., Jarzecki, A.A., Spiro, T.G., 2005. Theoretical investigation of iron isotope fractionation between Fe(H2O)(3+)(6) and Fe(H2O)(2+)(6) : Implications for iron stable isotope geochemistry. Geochimica et Cosmochimica Acta 69, 825-837.

Anbar, A.D., Rouxel, O., 2007. Metal stable isotopes in paleoceanography. Annual Review of Earth and Planetary Sciences 35, 717-746.

Balci, N., Bullen, T.D., Witte-Lien, K., Shanks, W.C., Motelica, M., Mandernack, K.W., 2006. Iron isotope fractionation during microbially stimulated Fe(II) oxidation and Fe(III) precipitation. Geochimica et Cosmochimica Acta 70, 622-639.

Bau, M., Dulski, P., 1996. Distribution of yttrium and rare-earth elements in the Penge and Kuruman Iron-Formations, Transvaal Supergroup, South Africa. Precambrian Reasearch 79, 37-55.

Bau, M., Hohndorf, A., Dulski, P., Beukes, N.J., 1997. Sources of rare-earth elements and iron in paleoproterozoic iron-formations from the Transvaal Supergroup, South Africa: Evidence from neodymium isotopes. Journal of Geology 105, 121-129.

Beard, B., Handler, R., Scherer, M., Wu, L., Czaja, A., Heimann, A., Johnson, C., 2010. Iron isotope fractionation between aqueous ferrous iron and goethite. Earth and Planetary Science Letters 295, 241-250.

Beard, B.L., Johnson, C.M., Cox, L., Sun, H., Nealson, K.H., Aguilar, C., 1999. Iron isotope biosignatures. Science 285, 1889-1892.

Bekker, A., Holland, H. D., Wang, P.-L., Rumble III, D., Stein, H. J., Hannah, J. L., Coetzee, L. L., and Beukes, N. J., 2004. Dating the rise of atmospheric oxygen. Nature 427, 117-120.

Bekker, A., Barley, M.E., Fiorentini, M.L., Rouxel, O.J., Rumble, D., Beresford, S.W., 2009. Atmospheric Sulfur in Archean Komatiite-Hosted Nickel Deposits. Science 326, 1086-1089.

Bekker, A., Slack, J., Planavsky, N., Krapež, B., Hofmann, A., Konhauser, K.O., Rouxel, O.J., 2010. Iron Formation: The Sedimentary Product of a Complex Interplay Among Mantle, Tectonic, Oceanic, and Biospheric Processes. Economic Geology 105, 467-508.

Bennett, S.A., Rouxel, O., Schmidt, K., Garbe-Schonberg, D., Statham, P.J., German, C.R., 2009. Iron isotope fractionation in a buoyant hydrothermal plume, 5 degrees S Mid-Atlantic Ridge. Geochimica et Cosmochimica Acta 73, 5619-5634.

Bergquist, B.A., Boyle, E.A., 2006. Iron isotopes in the Amazon River system: Weathering and transport signatures. Earth and Planetary Science Letters 248, 54-68.

Beukes, N.J., Gutzmer, J., 2008. Origin and Paleoenvironmental Significance of Major Iron Formations at the Archean-Paleoproterozoic Boundary Society of Economic Geologists Reviews 15, 5-47.

Bullen, T.D., White, A.F., Childs, C.W., Vivit, D.V., Schulz, M.S., 2001. Demonstration of significant abiotic iron isotope fractionation in nature. Geology 29, 699-702.

Bura-Naki, E., Viollier, E., Jezequel, D., Thiam, A., Ciglenecki, I., 2009. Reduced sulfur and iron species in anoxic water column of meromictic crater Lake Pavin (Massif Central, France) Chemical Geology 266, 311-317.

Butler, I.B., Archer, C., Vance, D., Oldroyd, A., Rickard, D., 2005. Fe isotope fractionation on FeS formation in ambient aqueous solution. Earth and Planetary Science Letters 236, 430-442.

Canfield, D.E., 2005. The early history of atmospheric oxygen: Homage to Robert A. Garrels. Annual Review of Earth and Planetary Sciences 33, 1-36.

Clayton, R.E., Nederbragt, A.J., Malinovsky, D., Andersson, P., Thurow, J., 2007. Iron isotope geochemistry of mid-Cretaceous organic-rich sediments at Demerara Rise (ODP Leg 207). Proceedings of the Ocean Drilling Program, Scientific Results 207, 1–14.

Craddock, P.R., Dauphas, N., 2011. Iron and carbon isotope evidence for microbial iron respiration throughout the Archean. Earth and Planetary Science Letters 303, 121–132.

Croal, L.R., Johnson, C.M., Beard, B.L., Newman, D.K., 2004. Iron isotope fractionation by Fe(II)-oxidizing photoautotrophic bacteria. Geochimica et Cosmochimica Acta 68, 1227-1242.

Crosby, H.A., Johnson, C.M., Roden, E.E., Beard, B.L., 2005. Coupled Fe(II)-Fe(III) electron and atom exchange as a mechanism for Fe isotope fractionation during dissimilatory iron oxide reduction. Environmental Science & Technology 39, 6698-6704.

Crosby, H.A., Roden, E.E., Johnson, C.M., Beard, B.L., 2007. The mechanisms of iron isotope fractionation produced during dissimilatory Fe(III) reduction by Shewanella putrefaciens and Geobacter sulfurreducens. Geobiology 5, 169-189.

Crowe, S.A.J., C. Katsev, S. Magen, C.  O'Neill, A.H. Sturm, A.  Canfield, D.E. Haffner, G.D. Mucci, A. Sundby, B. Fowle, D.A., 2008. Photoferrotrophs thrive in an Archean Ocean analogue. Proceedings of the National Academy of Sciences 105, 15938-15943.

Czaja, A., Johnson, C., Beard, B., Eigenbrode, J., Freeman, K., Yamaguchi, K., 2010. Iron and carbon isotope evidence for ecosystem and environmental diversity in the ~2.7 to 2.5 Ga Hamersley Province, Western Australia. Earth and Planetary Science Letters 292, 170-180.

Dauphas, N., Rouxel, O., 2006. Mass spectrometry and natural variations of iron isotopes. Mass Spectrometry Reviews 25, 515-550.

Dauphas, N., van Zuilen, M., Wadhwa, M., Davis, A.M., Marty, B., Janney, P.E., 2004. Clues from iron isotope variations on the origin of early Archaean banded iron formations from Greenland. Science 306, 2077-2080.

Escoube, R., Rouxel, O.J., Sholkovitz, E., Donard, O.F.X., 2009. Iron isotope systematics in estuaries: The case of North River, Massachusetts (USA). Geochimica Et Cosmochimica Acta 73, 4045-4059.

Fehr, M.A., Andersson, P.S., Hålenius, U., Gustafsson, O., Morth, C.-M., 2010. Iron enrichments and Fe isotopic compositions of surface sediments from the Gotland Deep, Baltic Sea  Chemical Geology  277, 310-322.

Fehr, M.A., Andersson, P.S., Hålenius, U., Morth, C.-M., 2008. Iron isotope variations in Holocene sediments of the Gotland Deep, Baltic Sea Geochimica et Cosmochimica Acta 72, 807-826.

Gross, G., 1980. A classification of iron-formation based on depositional environments. Canadian Mineralogist 18, 223-229.

Guilbaud, R., Butler, I.B., Ellam, R.M., 2011. Abiotic Pyrite Formation Produces a Large Fe Isotope Fractionation. Science 332, 1548-1551.

Hartman, H., 1984. The Evolution of photosynthesis and microbial mats: A speculation on the banded iron formations, in: Cohen, Y., Castenholz, R.W., Halvorson, H.O. (Eds.), Microbial mats: Stromatolites. Alan R. Liss, New York, pp. 449-453.

Heimann, A., Johnson, C., Beard, B., Valley, J., Roden, E., Spicuzza, M., Beukes, N., 2010. Fe, C, and O isotope compositions of banded iron formation carbonates demonstrate a major role for dissimilatory iron reduction in ~ 2.5 Ga marine environments. Earth and Planetary Science Letters 294, 8-18.

Holland, H.D., 2005. Sedimentary mineral deposits and the evolution of earth's near-surface environments. Economic Geology 100, 1489-1509.

Homoky, W.B., Severmann, S., Mills, R.A., Statham, P.J., Fones, G.R., 2009. Pore-fluid Fe isotopes reflect the extent of benthic Fe redox recycling: Evidence from continental shelf and deep-sea sediments. Geology 37, 751-754.

Icopini, G.A., Anbar, A.D., Ruebush, S.R., Tien, M., and Brantley, S.L., 2004. Iron isotope fractionation during microbial reduction of iron. Geology 32, 205-208.

Isley, A.E., 1995. Hydrothermal Plumes and the Delivery of Iron to Banded Iron-Formation. Journal of Geology 103, 169-185.

Jenkyns, H.C., Matthews, A., Tsikos, H., Erel, Y., 2007. Nitrate reduction, sulfate reduction, and sedimentary iron isotope evolution during the Cenomanian-Turonian oceanic anoxic event Paleooceanography 22, doi:10.1029/2006PA001355.

John, S.G., Adkins, J.F., 2010. Analysis of dissolved iron isotopes in seawater. Marine Chemistry 119, 65-76.

Johnson, C., Beard, B., 2006. Fe isotopes: an emerging technique in understanding modern and ancient biogeochemical cycles. GSA Today 16, 4-10.

Johnson, C.M., Beard, B.L., Beukes, N.J., Klein, C., O'Leary, J.M., 2003. Ancient geochemical cycling in the Earth as inferred from Fe isotope studies of banded iron formations from the Transvaal Craton. Contributions to Mineralogy and Petrology 144, 523-547.

Johnson, C.M., Beard, B.L., Klein, C., Beukes, N.J., Roden, E.E., 2008a. Iron isotopes constrain biologic and abiologic processes in banded iron formation genesis. Geochimica et Cosmochimica Acta 72, 151-169.

Johnson, C.M., Beard, B.L., Roden, E.E., 2008b. The iron isotope fingerprints of redox and biogeochemical cycling in the modern and ancient Earth. Annual Review of Earth and Planetary Sciences 36, 457-493.

Kappler, A., Pasquero, C., Konhauser, K.O., Newman, D.K., 2005. Deposition of banded iron formations by anoxygenic phototrophic Fe(II)-oxidizing bacteria. Geology 33, 865-868.

Kaufman, A.J., Hayes, J.M., Klein, C., 1990. Primary and Diagenetic Controls of Isotopic Compositions of Iron-Formation Carbonates. Geochimica et Cosmochimica Acta 54, 3461-3473.

Klein, C., 2005. Some Precambrian banded iron-formations (BIFs) from around the world: Their age, geologic setting, mineralogy, metamorphism, geochemistry, and origin. American Mineralogist 90, 1473-1499.

Konhauser, K.O., Hamade, T., Raiswell, R., Morris, R.C., Ferris, F.G., Southam, G., Canfield, D.E., 2002. Could bacteria have formed the Precambrian banded iron formations? Geology 30, 1079-1082.

Krapež, B., Barley, M.E., Pickard, A.L., 2003. Hydrothermal and resedimented origins of the precursor sediments to banded iron formation: sedimentological evidence from the Early Palaeoproterozoic Brockman Supersequence of Western Australia. Sedimentology 50, 979-1011.

Lacan, F., Radic, A., Jeandel, C., Poitrasson, F., Sarthou, G., Pradoux, C., Freydier, R., 2008. Measurement of the isotopic composition of dissolved iron in the open ocean. Geophysical Research Letters 35, DOI: 10.1029/2008GL035841.

Levasseur, S., Frank, M.,, Hein, J.R., Halliday  A.N., 2004. The global variation in the iron isotope composition of marine hydrogenetic ferromanganese deposits: implications for seawater chemistry? Earth and Planetary Science Letters 224, 91-105.

Luther, G.W., Rickard, D.T., 2005. Metal sulfide cluster complexes and their biogeochemical importance in the environment. Journal of Nanoparticle Research 7, 389-407.

Lyons, T.W., 1997. Sulfur isotopic trends and pathways of iron sulfide formation in upper Holocene sediments of the anoxic Black Sea Geochimica et Cosmochimica Acta 61, 3367-3382.

Lyons, T.W., Severmann, S., 2006. A critical look at iron paleoredox proxies: New insights from modern euxinic marine basins. Geochimica et Cosmochimica Acta 70, 5698-5722.

Pecoits, E., Gingras, M.K., Barley, M.E., Kappler, A., Posth, N.R., Konhauser, K.O., 2009. Petrography and geochemistry of the Dales Gorge banded iron formation: Paragenetic sequence, source and implications for palaeo-ocean chemistry Precambrian Research 172, 163–187.

Planavsky, N., Bekker, A., Rouxel, O., Knudsen, A., Lyons, T.W., 2010. Rare earth element and yttrium compositions of Archean and Paleoproterozoic iron formations revisited: New perspectives on the significance and mechanisms of deposition. Geochimica et Cosmochimica Acta 74, 6387-6405.

Planavsky, N., Rouxel, O., Bekker, A., Shapiro, R., Fralick, P., Knudsen, A., 2009. Iron-oxidizing microbial ecosystems thrived in late Paleoproterozoic redox-stratified oceans. Earth and Planetary Science Letters 286, 230-242.

Polyakov, V.B., Clayton, R.N., Horita, J., Mineev, S.D., 2007. Equilibrium iron isotope fractionation factors of minerals: Reevaluation from the data of nuclear inelastic resonant X-ray scattering and Mössbauer spectroscopy. Geochimica et Cosmochimica Acta 71, 3833-3846.

Raiswell, R., 2006. An evaluation of diagenetic recycling as a source of iron for banded iron formations, in: Kesler, S.E., Ohmoto, H. (Eds.), Evolution of early Earth’s atmosphere, hydrosphere and biosphere—Constraints from ore deposits. Geological Society of America, Boulder, pp. 228–238.

Reinhard, C.T., Raiswell, R., Scott, C., Anbar, A.D., Lyons, T.W., 2009. A Late Archean Sulfidic Sea Stimulated by Early Oxidative Weathering of the Continents. Science 326, 713-716.

Reynolds, B.C., Frank, M., Halliday, A.N., 2006. Silicon isotope fractionation during nutrient utilization in the North Pacific. Earth and Planetary Science Letters 244, 431-443.

Rouxel, O., Dobbek, N., Ludden, J., Fouquet, Y., 2003. Iron isotope fractionation during oceanic crust alteration. Chemical Geology 202, 155-182.

Rouxel, O.J., Bekker, A., Edwards, K.J., 2005. Iron isotope constraints on the Archean and Paleoproterozoic ocean redox state. Science 307, 1088-1091.

Rouxel O., Bekker A. and Edwards K. 2006. Response to Comment on "Iron isotope constraints on the Archean and Paleo-Proterozoic Ocean Redox State" by Yamaguchi K. and Ohmoto H. *Science,* 311, 177b.

Rouxel, O., Shanks, W.C., Bach, W., Edwards, K.J., 2008a. Integrated Fe- and S-isotope study of seafloor hydrothermal vents at East Pacific rise 9-10 degrees N. Chemical Geology 252, 214-227.

Rouxel, O., Sholkovitz, E., Charette, M., Edwards, K.J., 2008b. Iron isotope fractionation in subterranean estuaries. Geochimica et Cosmochimica Acta 72, 3413-3430.

Rouxel, O.J., Auro, M., 2010. Iron isotope variations in coastal seawater determined by Multicollector ICP-MS4. Geostandards and Geoanalytical Research DOI: 10.1111/j.1751-908X.2010.00063.x.

Scott, C., Lyons, T.W., A., B., Shen, Y., Poulton, S.W., Chu, X., Anbar, A.D., 2008. Tracing the stepwise oxygenation of the Proterozoic ocean Nature 452, 457-460.

Scott, C., Bekker, A., Reinhard, C.R., Schnetger, B., Krapež, B., Rumble, D., Lyons, T.W., 2011. Late Archean euxinic conditions before the rise of atmospheric Geology 39, 119-122.

Severmann, S., Johnson, C.M., Beard, B.L., German, C.R., Edmonds, H.N., Chiba, H., Green, D.R.H., 2004. The effect of plume processes on the Fe isotope composition of hydrothermally derived Fe in the deep ocean as inferred from the Rainbow vent site, Mid-Atlantic Ridge, 36 degrees 14' N. Earth and Planetary Science Letters 225, 63-76.

Severmann, S., Johnson, C.M., Beard, B.L., McManus, J., 2006. The effect of early diagenesis on the Fe isotope compositions of porewaters and authigenic minerals in continental margin sediments. Geochimica et Cosmochimica Acta 70, 2006-2022.

Severmann, S., Lyons, T.W., Anbar, A., McManus, J., Gordon, G., 2008. Modern iron isotope perspective on the benthic iron shuttle and the redox evolution of ancient oceans. Geology 36, 487-490.

Staubwasser, M., von Blanckenburg, F., Schoenberg, R., 2006. Iron isotopes in the early marine diagenetic iron cycle. Geology 34, 629-632.

Steinhoefel, G., Horn, I., von Blanckenburg, F., 2009. Micro-scale tracing of Fe and Si isotope signatures in banded iron formation using femtosecond laser ablation Geochimica et Cosmochimica Acta 73, 5343-5360.

Sumner, D.Y., 1997. Carbonate precipitation and oxygen stratification in late Archean seawater as deduced from facies and stratigraphy of the Gamohaan and Frisco formations, Transvaal Supergroup, South Africa. American Journal of Science 297, 455-487.

Sumner, D.Y., Grotzinger, J.P., 2004. Implications for Neoarchaean ocean chemistry from primary carbonate mineralogy of the Campbellrand-Malmani Platform, South Africa. Sedimentology 51, 1273-1299.

Tangalos, G.E., Beard, B.L., Johnson, C.M., Alpers, C.N., Shelobolina, E.S., Xu, H., Konishi, H., and Roden, E.E. 2010. Microbial production of isotopically light iron(II) in a modern chemically-precipitated sediment and implications for isotopic variations in ancient rocks. Geobiology 8:197-208

Tompkins, L.A., Cowan, D.R., 2001. Opaque mineralogy and magnetic properties of selected banded iron-formations, Hamersley Basin, Western Australia. Australian Journal of Earth Sciences 48, 427-437.

Tsikos, H., Matthews, A., Erel, Y., Moore, J.M., 2010. Iron isotopes constrain biogeochemical redox cycling of iron and manganese in a Palaeoproterozoic stratified basin. Earth and Planetary Science Letters 298, 125-134.

von Blanckenburg, F., Marnberti, M., Schoenberg, R., Kamber, B.S., Webb, G.E., 2008. The iron isotope composition of microbial carbonate. Chemical Geology 249, 113-128.
Walker, J.C.G., 1984. Suboxic Diagenesis in Banded Iron Formations. Nature 309, 340-342.

Walker, J.C.G., 1984. Suboxic diagenesis in banded iron formations. Nature 309, 340-342.

Welch, S.A., Beard, B.L., Johnson, C.M., Braterman, P.S., 2003. Equilibrium Fe isotope fractionation between ferrous and ferric iron. Geochimica et Cosmochimica Acta 67, A529-A529.

Widdel, F., Schnell, S., Heising, S., Ehrenreich, A., Assmus, B., Schink, B., 1993. Ferrous Iron Oxidation by Anoxygenic Phototrophic Bacteria. Nature 362, 834-836.

Wiesli, R.A., Beard, B.L., Johnson, C.M., 2004. Experimental determination of Fe isotope fractionation between aqueous Fe(II), siderite and "green rust" in abiotic systems. Chemical Geology 211, 343-362.

Yamaguchi, K.E., Johnson, C.M., Beard, B.L., Ohmoto, H., 2005. Biogeochemical cycling of iron in the Archean-Paleoproterozoic Earth: Constraints from iron isotope variations in sedimentary rocks from the Kaapvaal and Pilbara Cratons. Chemical Geology 218, 135–169.

**Figures and Figure Legends**

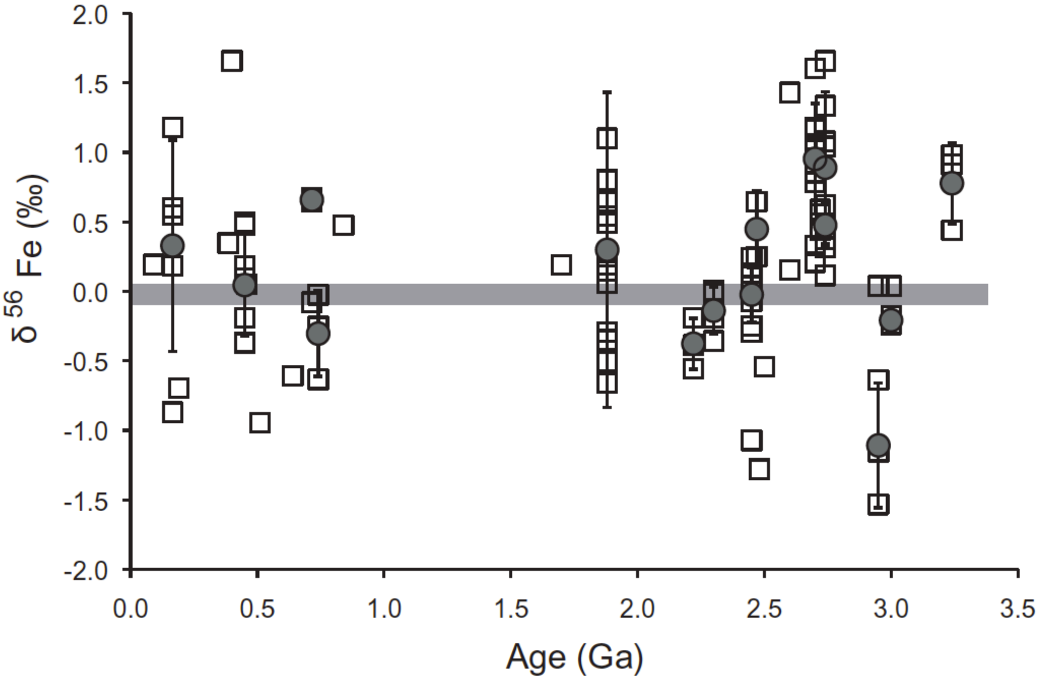

Figure 2.1. Secular trend of whole-rock $\delta^{56}$Fe values for iron formations. The open squares represent individual data points. The gray circles represent averages for formations for which several samples were analyzed and the black lines extending from the grey circles mark two standard deviations. The data for the ca. 1.88 Ga Animikie IF are a combination of new results and data from Planavsky et al. (2009).

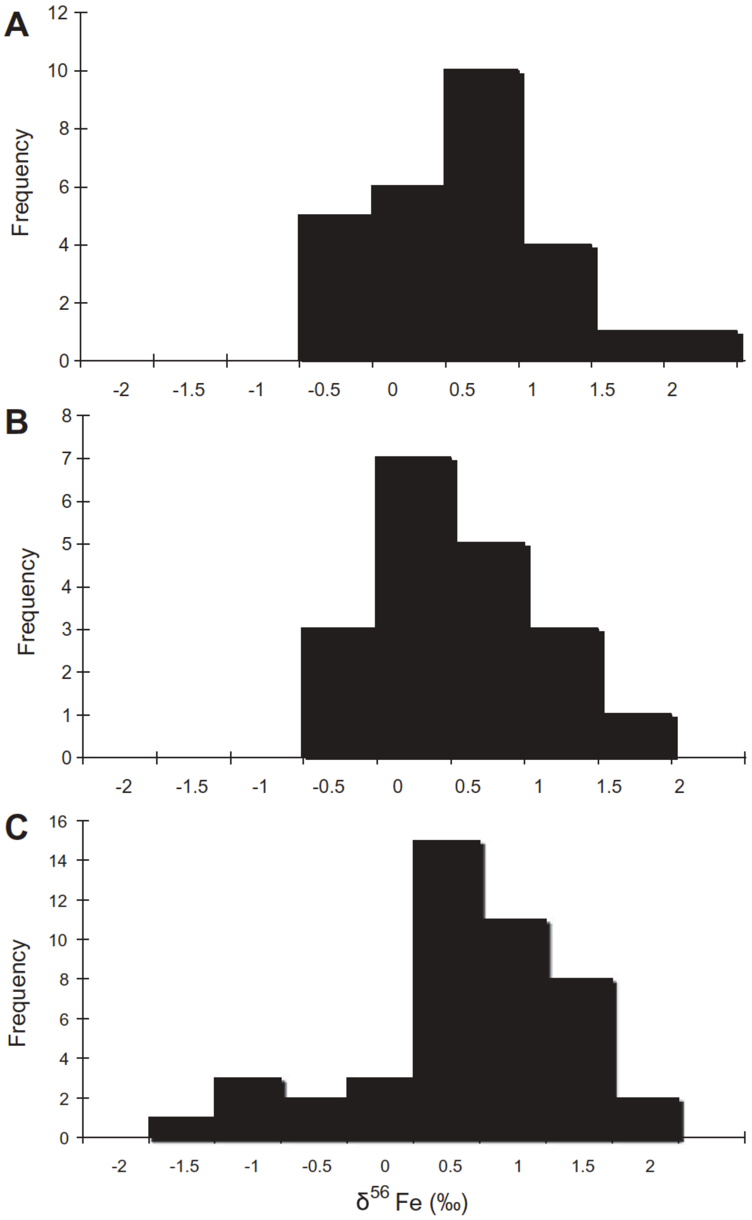

Figure 2.2. Histograms of whole-rock $\delta^{56}$Fe values for iron formations A). Mesoproterozoic, Neoproterozoic, and Phanerozoic iron formations (0.1‰ average). B.) IF ranging in age from ca. 2.32 to ca. 1.88 Ga (0.0‰ average). C.) Samples with ages ranging from ca. 3.0 to ca. 2.4 Ga. The IF deposited before the rise of atmospheric oxygen at ca. 2.4 Ga (Bekker et al., 2004) have predominantly positive iron isotope values (0.4‰ average). The data for the ca. 1.88 Ga IF are a combination of new results and data from Planavsky et al. (2009).

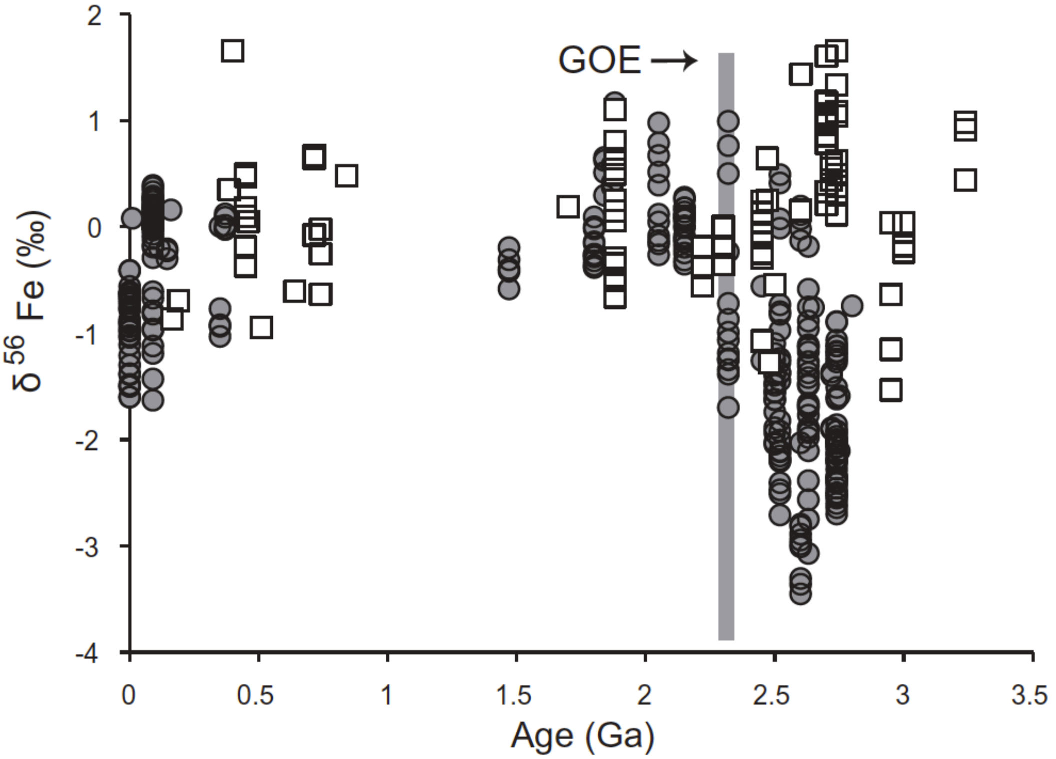

Figure 2.3. Secular trend of whole-rock $\delta^{56}$Fe values for iron formations from this study (empty squares) and $\delta^{56}$Fe values for sedimentary pyrites (grey circles) from literature (Bekker et al., 2010; Clayton et al., 2007; Fehr et al., 2010; Fehr et al., 2008; Jenkyns et al., 2007; Rouxel et al., 2005; Severmann et al., 2006; Yamaguchi et al., 2005). Grey vertical bar delineates the Great Oxidation Event (GOE).

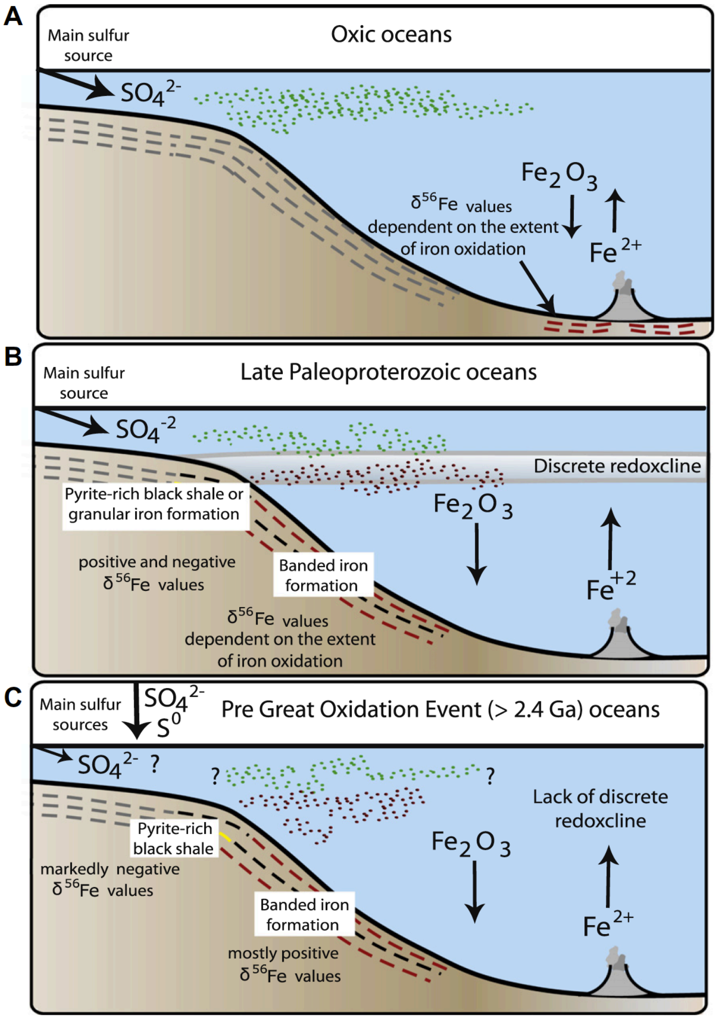

Figure 2.4. A). Iron has a short residence time in the modern oxidized open ocean; a redoxcline is lacking. B). In the late Paleoproterozoic (ca. 1.88 Ga) ocean, Fe had a longer residence time and was deposited forming Fe formations at a discrete redoxcline separating anoxic to suboxic deep-waters and oxic shallow-waters. Above and at the redoxcline, Fe was deposited with granular iron formations and pyrite-rich black shales. C). Model explaining the presence of markedly negative $\delta^{56}$Fe values in pre-GOE black shales and sedimentary pyrites. Partial ferrous Fe oxidation led to deposition of iron formations and other iron-rich sediments with positive $\delta^{56}$Fe values in the deeper water part of the ocean. This gave rise to an isotopically light pool of iron, which precipitated as Fe sulfides or Fe carbonates on the shelf and upper slope. A diffuse rather than a sharp redoxcline was present in the oceans at that time.

# Appendix

Table 2.1. Fe isotope and major element composition of examined iron formations and hydrothermal sediments

| | | | | | | | | | |
|---|---|---|---|---|---|---|---|---|---|
| WIT-18-740A | **-1.28** | 0.08 | **-1.82** | 0.11 | 41.93 | 1.11 | 0.13 | 1.25 | 1.93 |
| **ca. 2.5 Ga Nemo Iron Formation** | | | | | | | | | |
| BIF-1 | **-0.54** | 0.08 | **-0.83** | 0.11 | 37.65 | 0.03 | 0.11 | 1.88 | 0.28 |
| **ca. 2.6 Ga Bjornevanns Iron Formation** | | | | | | | | | |
| IF-5 | **0.15** | 0.08 | **0.28** | 0.11 | 35.52 | 0.07 | 0.23 | 0.61 | 1.58 |
| **ca. 2.6 Ga Cheshire Iron Formation** | | | | | | | | | |
| B/B4 | **1.43** | 0.08 | **2.07** | 0.11 | 5.18 | 0.04 | 0.07 | 0.13 | 0.48 |
| **ca. 2.7 Ga Manjeri Iron Formation** | | | | | | | | | |
| Z04-12 | **0.86** | 0.08 | **1.33** | 0.11 | 15.53 | <0.01 | 0.07 | 0.18 | 0.01 |
| Z04-26 | **0.96** | 0.08 | **1.42** | 0.11 | 12.78 | 0.01 | 0.08 | 0.07 | 0.01 |
| Z04-31 | **0.79** | 0.08 | **1.19** | 0.11 | 21.52 | 0.15 | 0.11 | 0.25 | 0.09 |
| Z04-32 | **0.85** | 0.08 | **1.26** | 0.11 | 8.94 | 0.10 | 0.04 | 0.26 | 0.26 |
| BMA-1 | **0.33** | 0.08 | **0.51** | 0.11 | 14.03 | 0.02 | 0.20 | 0.12 | 0.02 |
| BMA-2 | **0.21** | 0.08 | **0.32** | 0.11 | 12.22 | 0.17 | 0.23 | 1.43 | 1.93 |
| MHZ 7b | **1.02** | 0.08 | **1.48** | 0.11 | | | | | |
| MHZ 7e | **1.06** | 0.08 | **1.52** | 0.11 | | | | | |
| TR 40 | **1.18** | 0.08 | **1.68** | 0.11 | | | | | |
| TR 42 | **1.16** | 0.08 | **1.70** | 0.11 | | | | | |
| TR 43 | **1.61** | 0.08 | **2.47** | 0.11 | | | | | |
| **2.72 Ga Soudan Iron Formation** | | | | | | | | | |
| IF-17-1 | **0.55** | 0.08 | **0.90** | 0.11 | 19.21 | | | | |
| IF-17-2 | **0.59** | 0.08 | **0.87** | 0.11 | 21.44 | <0.01 | 0.05 | 0.03 | <0.01 |
| IF-18 | **0.44** | 0.08 | **0.67** | 0.11 | 31.36 | <0.01 | 0.06 | 0.04 | <0.01 |
| **2.74 Ga Temagami Iron Formation** | | | | | | | | | |
| IF-6 | **0.32** | 0.08 | **0.45** | 0.11 | 29.65 | <0.01 | 0.13 | 0.11 | 0.10 |
| IF-7 | **0.49** | 0.08 | **0.71** | 0.11 | 33.10 | | | | |
| IF-8 | **0.62** | 0.08 | **0.93** | 0.11 | 34.84 | 0.18 | 0.21 | 0.90 | 0.25 |
| **2.74 Ga Mary River Iron Formation** | | | | | | | | | |

| | | | | | | | | | |
|---|---|---|---|---|---|---|---|---|---|
| JD-65-114C11 | **0.62** | 0.08 | **0.98** | 0.11 | 19.22 | | | | |
| JD-65-207/2 | **0.38** | 0.08 | **0.57** | 0.11 | 39.24 | 0.04 | 0.05 | 0.29 | 0.13 |
| JD-65-260-1 | **1.04** | 0.08 | **1.53** | 0.11 | 39.93 | 0.01 | 0.04 | <0.01 | 0.01 |
| JD-65-285-C11 | **1.34** | 0.08 | **1.97** | 0.11 | 20.98 | 0.03 | 0.13 | 0.71 | 0.99 |
| JD-65-296-1 | **1.08** | 0.08 | **1.53** | 0.11 | 26.41 | | | | |
| JD-65-C-199-3 | **0.11** | 0.08 | **0.18** | 0.11 | 27.05 | 0.03 | 0.31 | 1.58 | 1.88 |
| JD-C165A | **1.66** | 0.08 | **2.51** | 0.11 | 35.55 | 0.02 | 0.05 | 0.29 | 1.32 |
| **ca. 2.95 Ga West Rand Group, Witwatersrand Supergroup Iron Formation** | | | | | | | | | |
| IF-9 | **0.04** | 0.08 | **0.08** | 0.11 | 25.86 | 0.07 | 0.19 | 0.03 | 0.03 |
| **ca. 2.95 Ga Mozaan Group, Pongola Supergroup Iron Formation** | | | | | | | | | |
| P05-1 | **-1.53** | 0.08 | **-2.34** | 0.11 | 18.77 | 2.40 | 0.08 | 0.14 | <0.01 |
| P05-6 | **-0.64** | 0.08 | **-0.90** | 0.11 | 24.95 | 2.30 | 0.13 | 0.11 | 0.05 |
| P05-7 | **-1.15** | 0.08 | **-1.75** | 0.11 | 11.22 | 1.06 | 0.09 | 0.18 | 0.04 |
| **3.24 Ga Fig Tree Group, Manzimnyama Iron Formation** | | | | | | | | | |
| FS5 | **0.91** | 0.08 | **1.35** | 0.11 | 7.43 | 0.02 | 0.06 | 0.03 | 0.08 |
| FS8 | **0.98** | 0.08 | **1.40** | 0.11 | 6.36 | | | | |
| IF-5(2) | **0.44** | 0.08 | **0.66** | 0.11 | 4.88 | | | | |

Table 2.2. Location, depositional setting, mineralogy and age of the examined units

| | | | | | |
|---|---|---|---|---|---|
| Wittenoon Gorge area Iron Formation | Australia | S-IF | Magnetite, Hematite | 2.47 | SI-Table 2 ref. 16 |
| Westerberg area Iron Formation | South Africa | S-IF | Hematite, Magnetite | 2.48 | SI-Table 2 ref. 17 |
| Nemo Iron Formation | USA | A-IF | Hematite, Magnetite | ca. 2.5 | SI-Table 2 ref. 18 |
| Bjornevanns Iron Formation | Norway | A-IF | Hematite, Magnetite | ca. 2.6 | SI-Table 2 ref. 19 |
| Manjeri Iron Formation | Zimbabwe | S-IF | Magnetite, Hematite | ca. 2.6 | SI-Table 2 ref. 20 |
| Manjeri Iron Formation | Zimbabwe | S-IF | Magnetite, Hematite | ca. 2.7 | SI-Table 2 ref. 20 |
| Temagami Iron Formation | Canada | A-IF | Magnetite, Hematite | ca. 2.7 | SI-Table 2 ref. 21 |
| Soudan Iron Formation | USA | A-IF | Hematite, Magnetite | 2.72 | SI-Table 2 ref. 22 |
| Mary River Iron Formation | Canada | A-IF | Magnetite, Hematite | 2.74 | SI-Table 2 ref. 23 |
| Pongola Supergroup iron formation | South Africa | S-IF | Hematite, Magnetite | ca. 2.95 | SI-Table 2 ref. 24 |
| Witwatersrand Supergroup iron formation | South Africa | S-IF | Hematite, Magnetite | ca. 2.95 | SI-Table 2 ref. 24 |
| Fig Tree Group iron formation | South Africa | A-IF | Hematite, Magnetite | 3.24 | SI-Table 2 ref. 25 |

HS, distal hydrothermal sediments; S-IF, Superior-type iron formation; R-IF; Rapitan-type iron formation; A-IF, Algoma-type iron formation

**Table 2.2 References**

1. Elderfield, H., Gass, I. G., Hammond, A., and Bear, L. M., 1972. The Origin of Ferromanganese Sediments Associated with the Troodos Massif of Cyprus. Sedimentology, 19, 1-19.

2. Knüttel, S., 1986. Calcareous Nannofossil Biostratigraphy of the Central East Pacific Rise, Deep Sea Drilling Project Leg 92: Evidence for downslope transport of sediments*, DSDP* Proceedings, 92, 255-290.

3. Little, C., Danelian, T., Herrington, R. & R., H. Early Jurassic hydrothermal vent community from the Franciscan Complex, California., 2004. Journal of Paleontology 78, 542-559.

4. Zonenshain, L.P., Kuzmin, M.I. & Natapov, L.M., 1990. *Geology of USSR: A plate tectonic synthesis*, (American Geophysical Union, Washington DC).

5. Grenne, T. and Slack, J. F., 2003. Bedded jaspers of the Ordovician Lokken ophiolite, Norway: seafloor deposition and diagenetic maturation of hydrothermal plume-derived silica-iron gels. Mineralium Deposita 38, 625-639.

6. Lentz, D.R., van Staal, C.R., 2004. Predeformational origin of massive sulfide mineralization and associated footwall alteration at the Brunswick No. 12, Pb– Zn–Cu deposit, Bathurst, New Brunswick: evidence from the porphyry dike. Economic Geology. 90, 453-463.

7. Gross, G.A., 1967. Geology of Iron Deposits in Canada, Vol. II, Iron Deposits in the Appalachian and Grenville Regions of Canada; *Geological Survey of Canada,* Economic Geology Reports, 22, 111 pp.

8. Maslov, A.V., 2000. Some Specific Features of Early Vendian Sedimentation in the Southern and Middle Urals. Lithology and Mineral Resources, 35, 556-570.

9. Macdonald, F.A. et al., 2010. Calibrating the Cryogenian. Science 327, 1241 - 1243 (2010).

10. Hoffman, P.F., Hawkins, D.P., Isachsen, C.E., Bowring, S.A., 1996. Precise U–Pb zircon ages for early Damaran magmatism in the Summas Mountains and Welwitschia Inlier, northern Damara belt, Namibia. Communications of the Geological Survey of Namibia 11, 47–52.

11. Rainbird, R.H., Jefferson, C.W., Hilderbrand, R.S., and Worth, J.K. 1994. The Shaler Supergroup and revision of the Neoproterozoic stratigraphy in the Amundsen basin, Northwest Territories: Geological Survey of Canada Paper 94, 61–70.

12. Miller, A.R., Cumming, G.L., Krstic, D., 1989. U–Pb, Pb–Pb and K–Ar isotope study of the uraniferous phosphate-bearing rocks in the Thelon Formation, Dubawnt Group, Northwest Territories, Canada. Canadian Journal of Earth Sciences 26, 867–880.

13. Schneider, D.A., Bickford, M.E., Cannon, W.F., Schulz, K.J., Hamilton, M.A., 2002. Age of volcanic rocks and syndepositional iron formations, Marquette Range Supergroup: implications for the tectonic setting of Paleoproterozoic, iron formations of the Lake Superior region. Canadian Journal of Earth Sciences 39, 999-1012.

14. Cornell, D. H., Schutte, S. S., and Eglington, B. L., 1996. Ongeluk basaltic andesite formation in Griqualand West, South Africa: submarine alteration in a 2222 Ma Proterozoic sea. Precambrian Research 79, 101-123.

15. Hannah, J.L., Bekker, A., Stein, H.J., Markey, R.J., and Holland, H.D., 2004. Primitive Os and 2316 Ma age for marine shale: implications for Paleoproterozoic glacial events and the rise of atmospheric oxygen: Earth and Planetary Science Letters, 225, 43-52.

16. Pickard, A.L., 2002. SHRIMP U-Pb zircon ages of tuffaceous mudrocks in the Brockman Iron Formation of the Hamersley Range, Western Australia. Australian Journal of Earth Sciences 49, 491-507.

17. Pickard, A.L., 2003. SHRIMP U-Pb zircon ages for the Palaeoproterozoic Kuruman Iron Formation, Northern Cape Province, South Africa: evidence for simultaneous BIF deposition on Kaapvaal and Pilbara Cratons. Precambrian Research 125, 275-315.

18. McCombs, J.A., Dahl, P.S., Hamilton, M.A., 2004. U-Pb ages of Neoarchean granitoids from the Black Hills, South Dakota, USA: implications for crustal evolution in the Archean Wyoming province. Precambrian Research 130, 161- 184.

19. Siedlecka, A. et al., 1985. Lithostratigraphy and correlation of the Archean and Early Proterozic rocks of Finnmarksvidda and Sorvaranger district. Norges Geologiske Undersokelse 403, 7-36.

20. Bolhar, R., Hofmann, A., Woodhead, J.M., Hergt, J.M., Dirks, P.H.G.M., 2002. Pb- and Nd-isotope systematics of stromatolitic limestones from the 2.7 Ga Ngezi Group

of the Belingwe Greenstone Belt: constraints on provenance, deposition and deformation. Precambrian Research, 114, 277-294.

21. Bowins, R.J., Heaman, L.M., 1991. Age and timing of igneous activity in the Temagami greenstone belt, Ontario: A preliminary report. Canadian Journal of Earth Sciences 28, 1873-1876.

22. Peterson, D.M., Gallup, C., Jirsa, M.A., Davis, D.W., 2001. Correlation of Archean assemblages across the U.S.-Canadian border: Phase I geochronology. Proceedings of the Institute on Lake Superior Geology 47, 77–78.

23. Bethune, K.M. & Scammell, R.J., 2003. Geology, geochronology, and geochemistry of Archean rocks in the Eqe Bay area, north-central Baffin Island, Canada: constraints on the depositional and tectonic history of the Mary River Group of northeastern Rae Province. Canadian Journal of Earth Sciences 40, 1137-1167.

24. Gutzmer, J., Nhleko, N., Beukes, N.J., Pickard, A. ]Barley, M.E., 1999. Geochemistry and ion microprobe (SHRIMP) age of a quartz porphyry sill in the Mozaan Group of the Pongola Supergroup; implications for the Pongola and Witwatersrand supergroups. South African Journal of Geology 102, 139-146.

25. Byerly, G.R., Kröner, A., Lowe, D.R., Todt, W., Walsh, M.M., 1996. Prolonged magmatism and time constraints for sediment deposition in the early Archean Barberton greenstone belt: evidence from the Upper Onverwacht and Fig Tree groups. Precambrian Research, 78, 125-138.

## Chapter 3: Widespread Iron-rich Conditions in Mid-Proterozoic Oceans

### Abstract, Introduction, Results, Discussion, and Conclusions

The chemical composition of the ocean changed dramatically with the oxidation of the Earth surface (Holland, 2005), and this process has profoundly influenced the evolutionary and ecological history of life (Canfield, 2005; Lyons et al., 2009b). The early Earth was characterized by a reducing ocean-atmosphere system, while the Phanerozoic Eon (<542 million years ago) is known for a stable and oxygenated biosphere conducive to the radiation of animals. The redox characteristics of surface environments during the Earth's middle age (1.8 to 1 billion years ago) are less well known, but it is generally assumed that the mid-Proterozoic was home to a globally sulphidic (euxinic) deep ocean (Canfield, 2005; Lyons et al., 2009a; Lyons et al., 2009b). Here, I present iron data from a suite of mid-Proterozoic marine mudstones. Contrary to the popular model, our results indicate that ferruginous (anoxic and $Fe^{2+}$-rich) conditions were both spatially and temporally extensive across diverse paleogeographic settings in the mid-Proterozoic ocean, inviting new models for the temporal distribution of iron formations and the availability of bioessential trace elements during a critical window for eukaryotic evolution.

It is well established that Earth evolved from having an early anoxic ocean devoid of eukaryotes to one fully oxygenated teeming with complex life. However, the timing and mechanisms of Earth's redox evolution are still debated. Foremost, marine redox conditions and atmospheric oxygen levels remain poorly constrained during the period between the Earth's oxygen-deficient early history (> ~2.4 billion years ago [Ga]) and the dominantly oxygenated realm of the Phanerozoic (the last ~0.542 billion years). Traditional arguments held that ocean oxygenation was responsible for the disappearance of large iron formations (IFs) at 1.8 Ga (Holland, 2005). More recently, the majority opinion amongst Precambrian workers has favoured instead a deep mid-Proterozoic ocean with a vast or perhaps even global reservoir of hydrogen sulphide (Canfield, 1998; Lyons et al., 2009b; Poulton et al., 2004), and $H_2S$, much like oxygen, would have titrated the dissolved Fe needed for the deposition of IFs. It is further proposed that these euxinic (anoxic and sulphidic) conditions would have hindered the expansion and diversification of eukaryotes due to the insolubility of bioessential trace elements, such as molybdenum , in sulphidic waters (Anbar and Knoll, 2002). Consistent with a shift to euxinia, well-preserved sedimentary rocks from the Animikie basin on the Superior craton were suggested to capture the transition to a global sulphidic ocean (Poulton et al., 2004) at ~ 1.8 Ga. It is now apparent, however, that large IFs were deposited tens of millions of years after the deposition of this sedimentary succession (Bekker et al., 2010; Pirajno et al., 2009; Wilson et al., 2010) and that iron-rich conditions persisted in deep waters in the Animikie basin even after the deposition of the largest Animikie IFs (Bekker et al., 2010; Poulton et al., 2010), demanding that we rethink the spatiotemporal details of Proterozoic ocean redox and specifically the character of the mid-Proterozoic ocean.

In contrast to end-member euxinic or oxic Proterozoic deep-ocean models, a third possibility has recently emerged suggesting that anoxic and Fe-rich deepwater conditions may have been common throughout the Precambrian, including the mid-Proterozoic (1.8-1.0 Ga) (Bekker et al., 2010; Lyons et al., 2009a; Poulton et al., 2010). This surprising view of ocean evolution finds its origins in part with recent evidence that the ocean was ferruginous in the terminal Proterozoic (Canfield et al., 2008; Johnston et al., 2010; Li et al., 2010), suggesting continuity with the IF-favoring conditions present before 1.8 Ga. Alternatively, researchers have also asserted that the Neoproterozoic was instead a special case—marked by a return to the Fe-rich state of the early Precambrian as a consequence of supercontinent breakup (Johnston et al., 2010), extensive glaciations(Swanson-Hysell et al., 2010), and drawdown of marine sulphate caused by a billion years of deepwater euxinia and pyrite burial (Canfield et al., 2008). Although tantalizing, the ferruginous mid-Proterozoic model[11] is currently hindered by a billion year gap in direct evidence from the geological record for this marine redox state. Our study fills that data gap with results from four diverse mid-Proterozoic depositional settings that all point to Fe-rich marine waters. Included are samples from the McArthur basin in north-central Australia—the only basin to date that has yielded direct evidence for mid-Proterozoic euxinia (Brocks et al., 2005; Johnston et al., 2008).

To evaluate ancient redox chemistry, I have applied a well-established sequential Fe extraction scheme to fine-grained sedimentary rocks (Poulton and Canfield, 2005). The accumulation of biogeochemically reactive Fe, termed ‘highly reactive Fe’, is linked to the redox conditions in the water column overlying the site of sedimentary deposition. In modern oxic marine sediments, highly reactive Fe ($Fe_{HR}$) comprises less than 38% of the total sedimentary Fe pool (i.e., $Fe_{HR}/Fe_T < 0.38$), reflecting the detrital sediment flux in the absence of dissolved Fe in the $O_2$-containing water column. Enrichments beyond this limit ($Fe_{HR}/Fe_T > 0.38$) are a clear signature of transport, scavenging, and deposition of additional Fe from an anoxic water column (Canfield et al., 2008; Lyons et al., 2009a). Because mineralogical changes associated with even moderate burial alteration (such as Fe uptake into secondary silicate minerals) can reduce the pool of $Fe_{HR}$, the upper limit is possibly much lower than 0.38 in older rocks (Raiswell, 2008), suggesting that essentially all of our samples could have formed under anoxic conditions (Fig. 3.1). Where anoxia is indicated, we can further distinguish between ferruginous ($Fe^{2+} > H_2S$) and euxinic ($H_2S > Fe^{2+}$) environments by measuring the extent to which $Fe_{HR}$ has reacted with $H_2S$ to form pyrite ($Fe_{PY}/Fe_{HR}$). Accordingly, anoxic shales with $Fe_{PY}/Fe_{HR} > 0.8$ are considered to have been deposited under euxinic conditions (Canfield et al., 2008).

Because the McArthur basin has played a defining role in past arguments for mid-Proterozoic euxinia (Brocks et al., 2005; Johnston et al., 2008; Kendall et al., 2009; Shen et al., 2003), I began my search for ferruginous conditions with additional analysis of fresh drill cores of shale from deep-water settings in this region. I specifically investigated the iron chemistry of the ~1.64 Ga Barney Creek and Lady Loretta formations in the McArthur and Mount Isa basins, respectively. Our samples are from geographically widespread marine sequences that extend over more than 2000 kilometers across northern Australia, including locations from paleogeographic positions closer to the open ocean than have previously been investigated from this region. Additionally, I targeted the deepest-water facies as delineated in previous detailed basin analysis (e.g., Ref. McGoldrick et al., 2010).

$Fe_{HR}/Fe_T$ values in both the Barney Creek and Lady Loretta formations are generally above 0.38, conservatively indicating deposition under anoxic conditions (Fig. 3.1A). The vast majority of these samples have $Fe_{PY}/Fe_{HR}$ ratios well below 0.8, consistent with a persistently sulphide-free water column. Together, these ratios point to widespread ferruginous conditions over thick (hundreds of meters) stratigraphic intervals, indicating prolonged periods of persistently ferruginous deep waters, with the likelihood of laterally contemporaneous occurrences of euxina (Brocks et al., 2005; Johnston et al., 2008) in certain small or isolated sub-basins and/or on the shallower margins. Previous regional studies argue for a relatively strong marine connection during deposition at our specific sample locations (See SI), suggesting that deep ocean waters enriched in dissolved $Fe^{2+}$ may have exchanged with the McArthur and Mt Isa basins.

Given these exciting results, I was obliged to look beyond this region for records of mid-Proterozoic ferruginous waters. With this goal, I analyzed additional suites of carbonaceous shales from other, widely distributed mid-Proterozoic basins, emphasizing well-preserved (sub-greenschist) shales from diverse paleogeographic settings spanning the mid-Proterozoic. Each of these additional units yielded abundant samples with $Fe_{HR}/Fe_T > 0.38$ and $Fe_{Py}/Fe_{HR} < 0.8$ (Fig. 3.1A), signifying widespread ferruginous depositional conditions. Our data include samples from the 1.7 Ga Chuanlinggou Formation in northern China, the 1.45 Ga Belt Supergroup in the north-central USA, and the 1.2 Ga Borden basin in Arctic Canada. The Chuanlinggou Formation is interpreted to be a passive-margin sequence, suggesting a strong connection to the open ocean, and the Borden basin is a passive margin that evolved into a foredeep setting. In contrast, the Belt basin likely represents an extensional marine setting with transiently more restricted depositional conditions (See SI).

A small subset of samples from the Mt. Isa superbasin, the Belt Supergroup, and the Borden basin have significant iron enrichments and $Fe_{Py}/Fe_{HR}$ near 0.8 (Fig. 3.1A), suggesting that sulphidic conditions may have developed episodically. The lack of persistently euxinic conditions in the Belt Supergroup is surprising. As a semi-isolated, likely marginal marine system with evidence for high rates of primary productivity (Lyons et al., 2000), the Belt basin would seem ideally suited to developing euxinia—as we see in the modern, restricted Black Sea. Clear fingerprints of ferruginous conditions in the Chuanlinggou Formation are also revealing: as a passive-margin sequence lacking indications of appreciable basin restriction, this setting provides one of our best windows to conditions in the open Proterozoic ocean.

Our finding of Fe-rich conditions in several mid-Proterozoic marine settings contrasts with the widely accepted view of globally persistent and pervasive deep euxinia. However, this discovery is entirely consistent with an emerging view of Precambrian ocean chemistry brought to light by the most recent trace metal and Fe speciation studies from younger and older portions of the Precambrian ocean. Specifically, there is evidence for co-existing Fe- and $H_2S$-rich conditions in several Neoarchaean (Kendall et al., 2010; Reinhard et al., 2009; Scott et al., in press; Scott et al., 2008), early and middle Paleoproterozoic (Bekker et al., 2008; Poulton et al., 2010), and early and late Neoproterozoic settings (Johnston et al., 2010; Li et al., 2010) (Fig. 3.2). Ferruginous conditions were apparently widespread in the deeper portions of the ocean, while sulphide was likely limited to highly productive regions along the continental margins (Johnston et al., 2010; Poulton et al., 2010; Reinhard et al., 2009; Scott et al., in press), which is analogous to the more reducing conditions in modern oxygen minimum zones. Importantly, our data fill a billion-year gap in the evidence for this marine redox state, pointing provocatively to a heretofore undocumented continuity of Fe-rich conditions throughout the Precambrian.

Our finding of extensive ferruginous conditions is also consistent with a recent study of marine molybdenum inventories[27], which argued that the extent of euxinic depositional environments during the mid-Proterozoic could have been several times that of the modern ocean (<< 1%) but nothing like whole ocean euxinia. Similarly, mid-Proterozoic Mo isotope data are easily explained through greatly expanded (relative to today) but still largely local euxinia, with deep waters that were dominantly ferruginous and thus inefficient at fractionating Mo isotopes (e.g., Ref. Kendall et al., 2009).

I argue that the flux of organic matter was likely the predominant control underlying the redox landscape of the mid-Proterozoic ocean, as suggested for older and younger euxinia (Johnston et al., 2010; Poulton et al., 2010; Reinhard et al., 2009). Estimates for dissolved sulphate levels in the mid-Proterozoic ocean range from 500 to 3000 $\mu$M (See SI). Even the lower estimate for sulphate is well above the upper limit for dissolved Fe, which is fixed at roughly 100 $\mu$M by the solubilities of Fe carbonates and silicates (Canfield, 2005). As such, ferruginous marine conditions must instead mirror limited sulphide production[13]. Sulphide is produced anaerobically by bacteria at the expense of organic matter. It follows that spatial gradients in the organic flux and, ultimately, organic productivity may have limited the extent of euxinia.

Consistent with an organic matter delivery control on the distribution of sulphidic marine conditions, the analyzed samples contain substantially less organic carbon than do typical euxinic Precambrian and Phanerozoic shales. Samples in our study contain on average <1% organic carbon, which is several times lower than concentrations common in euxinic shales (e.g. Ref. 27). Low levels of organic matter in ferruginous shales suggest relatively low productivity in the overlying water column. Additionally, there is a sulphur isotope signal for bacterial sulphate reduction (BSR) occurring predominately in the porewaters. Pyrite in our samples have $\delta^{34}$S values that are slighter lower or equivalent to coeval sulphate (Fig. 3.1B). A simple explanation for these results is that BSR is occurring largely in sediments where potentially high isotopic fractionations are muted by limited sulphate availability. Sulphate supplies in the sediments would be controlled by rates of diffusional replenishment, and associated deficiencies would be exacerbated by the comparatively low amount of sulphate in mid-Proterozoic seawater. In other words, limited availability of organic matter likely restricted the onset of appreciable BSR to the sediments.

In order for ferruginous conditions to have been extensive in the mid-Proterozoic ocean, dissolved oxygen acquired in surface waters through photosynthesis and gas exchange with the overlying atmosphere must have been consumed as deep water masses aged. Oxygen will be consumed through degradation of sinking organic matter and, if oxygen remains available, by hydrothermally sourced reductants (e.g., Ref. Slack et al., 2007). Our results indicate that the flux of $Fe^{2+}$ into deep waters typically exceeded rates of sulphide generation in all but nearshore or restricted regions with relatively high rates of primary productivity that fueled localized sulphate reduction in the water column.

Importantly, our results also call for a reconsideration of the factors controlling the temporal distribution of large iron formations. In contrast to the canonical view wherein IFs disappeared as the deep ocean evolved from iron to oxygen or sulphide domination (Canfield, 1998; Holland, 2005), the long persistence of ferruginous conditions in our model argues that IFs are anomalous sedimentary deposits linked in most cases to an enhanced Fe supply via strong hydrothermal inputs (Bekker et al., 2010; Isley and Abbott, 1999). Importantly, and consistent with our ocean model, the amount of hydrothermal iron released to the oceans has varied greatly with marine sulphate concentrations (Kump and Seyfried, 2005) and mantle plume activity as reflected by dyke swarms and large igneous provinces (Bekker et al., 2010; Isley and Abbott, 1999).

Our findings cast a new perspective on mid-Proterozoic environmental conditions, ecology, and evolution. For example, evidence for extensive ferruginous conditions throughout the Proterozoic ocean provides a simple answer to the apparent conundrum of increasing enzymatic utilization of Fe, Mo, and Co during the mid-Proterozoic as inferred by a recent study of the evolution of almost 4000 gene families (Lawrence and Alm, 2010). It is possible for these bioessential metals to have been readily available in an ocean with pervasively ferruginous deep waters, in contrast to the likelihood of biolimitation if deep waters were globally sulphidic (Anbar and Knoll, 2002), given that free sulphide in the water column greatly decreases the solubility of these elements. It remains to be tested, however, whether broad, but far from global, extents of euxinia were still able to pull down trace metal inventories at least locally to biologically critical levels, as suggested in previous work (Scott et al., 2008). More generally, our data now provide the foundation for a unified model for the chemical evolution of the Precambrian ocean consistent with diverse redox tracers and bridging past work bracketing the mid-Proterozoic. Recognizing the spatial and temporal heterogeneity expected in a dynamic early ocean, I propose virtually continuous coexistence of sulphide- and iron-rich conditions for billions of years beneath oxic surface waters as the backdrop for Precambrian biological evolution and specifically the protracted radiation of eukaryotes and the ultimate rise of animals.

## Methods

The extraction method used in this study to speciate between the reactive iron pools in fine-grained siliciclastic rocks and sediments has been described in detail elsewhere, and I therefore provide only an overview here. In short, our iron speciations were performed at UCR, using a well-calibrated sequential extraction protocol designed to quantify the different pools of $Fe_{HR}$ Poulton and Canfield, 2005) $Fe_{HR}$ is subdivided into three subpools, each with the potential to react with hydrogen sulphide on diagenetic timescales: carbonate-associated iron extracted with a sodium acetate solution ($Fe_{Carb}$), ferric oxides extracted with a dithionite solution ($Fe_{Ox}$), and mixed-valence iron oxides, principally magnetite, extracted with ammonium oxalate ($Fe_{Mag}$). I used, 100mg of sample powder, and the sequential extracts were analysed with an Agilent 7500ce ICP-MS. Pyrite ($Fe_{Py}$) is also included in the $Fe_{HR}$ pool. $Fe_{Py}$ was calculated (assuming a stoichiometry of $FeS_2$) on the basis of the weight percentage of sulphur extracted during a 2-h hot chromous chloride distillation followed by iodometric titration. The assumption of a FeS2 stoichiometry in the sulphide pool was tested through extensive extrac- tions for acid-volatile sulphide with hot $SnCl_2$-HCl (15% $SnCl_2$, 6 M HCl) for 1 hour. The samples included here all contain less than 0.1% sulphur extractable by HCl. Total iron concentrations where determined by one of two methods: X-ray fluor- escence at the CODES Research Centre at the University of Tasmania, or a three- acid digestion followed by ICP-MS analysis at UCR. On the basis of duplicate analyses and Geostandard monitoring, reproducibility of iron measurements was better than 5%.

However, samples with less than 0.1% iron were found to be reproducible to two decimal places, but the error can exceed 5%. At such low levels of iron, these errors have no impact on our conclusions.

I determined concentrations of total organic carbon by taking the difference between carbonate carbon liberated by 4 M HCl and total carbon released by combustion at 1,450 uC, both of which were measured with an ELTRA C/S deter- minator at UCR. Last, also at UCR, pyrite-S was extracted for isotope measure- ments by using the same chromous chloride distillation but, in this case, reprecipitating the pyrite-S as Ag2S. Suphur isotope measurements were made with a ThermoFinnigan Delta V continuous-flow stable-isotope-ratio mass spectrometer. Reproducibility was better than 0.2% on the basis of single-run and long-term standard monitoring.

## References

Anbar, A.D., Knoll, A.H., 2002. Proterozoic ocean chemistry and evolution: a bioinorganic bridge. Science 297, 1137-1142.

Bekker, A., Holmden, C., Beukes, N.J., Kenig, F., Eglinton, B., Patterson, W.P., 2008. Fractionation between inorganic and organic carbon during the Lomagundi (2.22–2.1 Ga) carbon isotope excursion Earth and Planetary Science Letters 271, 278-291.

Bekker, A., Slack, J., Planavsky, N., Krapež, B., Hofmann, A., Konhauser, K.O., Rouxel, O.J., 2010. Iron Formation: The Sedimentary Product of a Complex Interplay Among Mantle, Tectonic, Oceanic, and Biospheric Processes. Economic Geology 105, 467-508.

Brocks, J.J., Love, G.D., Summons, R.E., Knoll, A.H., Logan, G.A., Bowden, S.A., 2005. Biomarker evidence for green and purple sulphur bacteria in a stratified Palaeoproterozoic sea. Nature 437, 866-870.

Canfield, D.E., 1998. A new model for Proterozoic ocean chemistry. Nature 396, 450-453.

Canfield, D.E., 2005. The early history of atmospheric oxygen: Homage to Robert A. Garrels. Annual Review of Earth and Planetary Sciences 33, 1-36.

Canfield, D.E., Poulton, S.W., Knoll, A.H., Narbonne, G.M., Ross, G., Goldberg, T., Strauss, H., 2008. Ferruginous conditions dominated later neoproterozoic deep-water chemistry. Science 321, 949-952.

Chu, X., Zhang, T., Zhang, Q., Lyons, T.W., 2007. Sulfur and carbon isotope records from 1700 to 800 Ma carbonates of the Jixian section, northern China: Implications for secular isotope variations in Proterozoic seawater and relationships to global supercontinental events. Geochimica et Cosmochimica Acta 71, 4668–4692.

Gellatly, A.M.  Lyons, T.W., 2005. Trace sulfate in mid-Proterozoic carbonates and the sulfur isotope record of biospheric evolution Geochimica et Cosmochimica Acta 69, 3813–3829.

Holland, H.D., 2005. Sedimentary mineral deposits and the evolution of earth's near-surface environments. Economic Geology 100, 1489-1509.

Isley, A.E., Abbott, D.H., 1999. Plume-related mafic volcanism and the deposition of banded iron formation. Journal of Geophysical Research-Solid Earth 104, 15461-15477.

Johnston, D.T., Farquhar, J., Summons, R.E., Shen, Y., Kaufman, A.J., Masterson, A.L., Canfield, D.E., 2008. Sulfur isotope biogeochemistry of the Proterozoic McArthur Basin. Geochimica et Cosmochimica Acta 72, 4278-4290.

Johnston, D.T., Poulton, S.W., Dehler, C., Porter, S., Husson, J., Canfield, D.E., Knoll, A.H., 2010. An emerging picture of Neoproterozoic ocean chemistry: Insights from the Chuar Group, Grand Canyon, USA. Earth and Planetary Science Letters 290, 64-73.

Kendall, B., Creaser, R.A., Gordon, G.W., Anbar, A.D., 2009. Re-Os and Mo isotope systematics of black shales from the Middle Proterozoic Velkerri and Wollogorang Formations, McArthur Basin, northern Australia. Geochimica et Cosmochimica Acta 73, 2534-2558.

Kendall, B., Reinhard, C.T., Lyons, T., Kaufman, A.J., Poulton, S.W., Anbar, A.D., 2010. Pervasive oxygenation along late Archaean ocean margins. Nature Geoscience 3, 647-652.

Kump, L.R., Seyfried, W.E., 2005. Hydrothermal Fe fluxes during the Precambrian: Effect of low oceanic sulfate concentrations and low hydrostatic pressure on the composition of black smokers. Earth and Planetary Science Letters 235, 654-662.

Lawrence, A.D., Alm, E.J., 2010. Rapid evolutionary innovation during an Archaean genetic expansion. Nature.

Li, C., Love, G.D., Lyons, T.W., Fike, D.A., Sessions, A.L., Chu, X.L., 2010. A Stratified Redox Model for the Ediacaran Ocean. Science 328, 80-83.

Lyons, T.W., Anbar, A., Severmann, S., Scott, C., Gill, B., 2009a. Tracking Euxinia in the Ancient Ocean: A Multiproxy Perspective and Proterozoic Case Study. Annual Review of Earth and Planetary Sciences 37, 507-534.

Lyons, T.W., Luepke, J.J., Schreiber, M.E., Zieg, G.A., 2000. Sulfur geochemical constraints on Mesoproterozoic restricted marine deposition: lower Belt Supergroup, northwestern United States. Geochimica et Cosmochimica Acta 64, 427-437.

Lyons, T.W., Reinhard, C.T., Scott, C., 2009b. Redox Redux. Geobiology 7, 489-494.

McGoldrick, P., Winefield P., Bull, S., Selley, D., Scott, R., 2010. Sequences, Synsedimentary Structures, and Sub-Basins: the Where and When of SEDEX Zinc Systems in the Southern McArthur Basin, Australia. Society of Economic Geologists, Special Publications 15, 1-23.

Pirajno, F., Hocking, R.M., Reddy, S.M., Jones, A.J., 2009. A review of the geology and geodynamic evolution of the Palaeoproterozoic Earaheedy Basin, Western Australia. Earth-Science Reviews 94, 39-77.

Poulton, S.W., Canfield, D.E., 2005. Development of a sequential extraction procedure for iron: implications for iron partitioning in continentally derived particulates. Chemical Geology 214, 209-221.

Poulton, S.W., Fralick, P.W., Canfield, D.E., 2004. The transition to a sulphidic ocean similar to 1.84 billion years ago. Nature 431, 173-177.

Poulton, S.W., Fralick, P.W., Canfield, D.E., 2010. Spatial variability in oceanic redox structure 1.8 billion years ago Nature Geoscience 3, 486 - 490.

Raiswell, R., 2008. Turbidite depositional influences on the diagenesis of Beecher's Trilobite Bed and the Hunsrück Slate; sites of soft tissue pyritization. American Journal of Science 305, 105-129.

Reinhard, C.T., Raiswell, R., Scott, C., Anbar, A.D., Lyons, T.W., 2009. A Late Archean Sulfidic Sea Stimulated by Early Oxidative Weathering of the Continents. Science 326, 713-716.

Scott, C., Bekker, A., Reinhard, C.R., Schnetger, B., Krapež, B., Rumble, D., Lyons, T.W., in press. Late Archean euxinic conditions before the rise of atmospheric Geology.
Scott, C., Lyons, T.W., A., B., Shen, Y., Poulton, S.W., Chu, X., Anbar, A.D., 2008. Tracing the stepwise oxygenation of the Proterozoic ocean Nature 452, 457-460.

Shen, Y., Knoll, A.H., Walter, M.R., 2003. Evidence for low sulphate and anoxia in a mid-Proterozoic marine basin. Nature 423, 632-635.

Slack, J.F., Grenne, T., Bekker, A., Rouxel, O.J., Lindberg, P.A., 2007. Suboxic deep seawater in the late Paleoproterozoic: Evidence from hematitic chert and iron formation related to seafloor-hydrothermal sulfide deposits, central Arizona, USA. Earth and Planetary Science Letters 255, 243-256.

Swanson-Hysell, N.L., Rose, C.V., Calmet, C.C., Halverson, G.P., Hurtgen, M.T., Maloof, A.C., 2010. Cryogenian glaciation and the onset of carbon-isotope decoupling. Science 328 608-611.

Wilson, J.P., Fischer, W.W., Johnston, D.T., Knoll, A.H., Grotzinger, J.P., Walter, M.R., McNaughton, N.J., Simon, M., Abelson, J., Schrag, D.P., Summons, R., Allwood, A., Andres, M., Gammon, C., Garvin, J., Rashby, S., Schweizer, M., Watters, W.A., 2010. Geobiology of the late Paleoproterozoic Duck Creek Formation, Western Australia. Precambrian Research 179, 135-149.

## Figures and Figure Legends

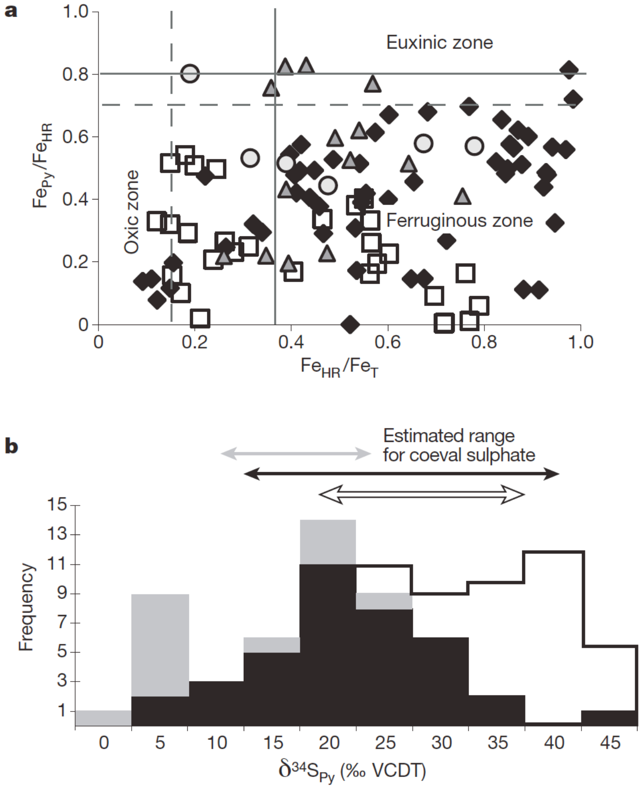

Figure 3.1. Iron speciation data for shales from the 1.64 Ga Mt. Isa Superbasin (black diamonds), the 1.7 Ga Chuanlinggou Formation (white squares), the 1.45 Ga Newland Formation (dark grey triangles), and 1.2 Ga Borden Basin (grey circles). These mid-Proterozoic sedimentary units are characterized by high ratios of highly reactive to total iron ($Fe_{HR}/Fe_T$) and low ratios of pyrite to highly reactive iron ($Fe_{Py}/Fe_{HR}$). Importantly, our samples have experienced only low degrees of burial alteration. Nevertheless, the effect of burial alteration, if any, would be to shift $Fe_{HR}$ into the unreactive pool. Burial effects lower the $Fe_{HR}/Fe_T$ boundary for anoxia (dashed grey line denotes the average for oxic Phanerozoic shales)(Raiswell et al., 2008). Despite potential alteration effects, however, the vast majority of our samples have $Fe_{HR}/Fe_T$ and $Fe_{Py}/Fe_{HR}$ ratios falling above the conservative 0.38 threshold and below 0.8, respectively—values diagnostic of sediment accumulation beneath an anoxic and Fe-rich (non-sulphidic) water column. B. Pyrite $\delta^{34}S$ isotope values. Pyrite $\delta^{34}S$ values are slightly depleted relative to or roughly equivalent to coeval sulphate, suggesting sulphate reduction occurring largely in porewaters, where restricted-system behavior prevents significant isotope fractionation during BSR. Estimates for sulphate $\delta^{34}S$ values from Refs. Chu et al., 2007, Gellatly and Lyons, 2005.

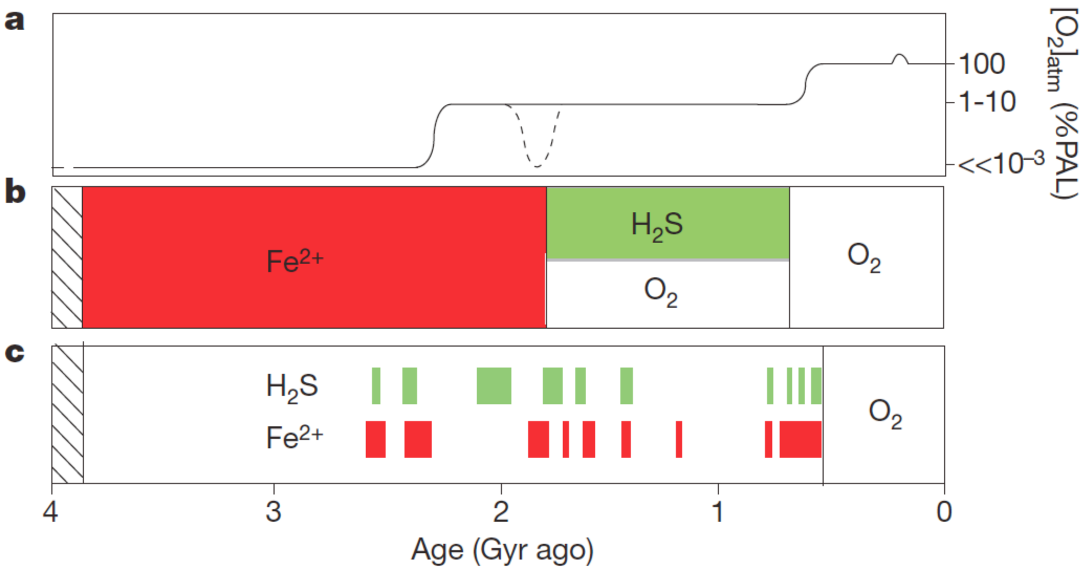

Figure 3.2. Summary of marine chemical conditions in the Precambrian. Our study provides evidence for extensively developed ferruginous conditions in the deep ocean during the mid-Proterozoic, which was thought previously to have been characterized by either oxygenated or sulphide-rich conditions. The emerging view based on redox studies of marine shales is that under the relatively low levels of atmospheric oxygen throughout the mid-Proterozoic, both euxinic and ferruginous waters were common below the surface mixing zone (see text for details).

# Appendix: Widespread Iron-rich Conditions in Mid-Proterozoic Oceans

## Formation Descriptions

### *Chuanlinggou Formation, Lower Changcheng Group, Jixian Region, North China*

The Chuanlinggou Formation, part of the Changcheng Group in North China, was deposited approximately 1700 million years before present (Ma). The maximum age is constrained by several whole-rock and illite Pb-Pb ages at around 1750 Ma (Kusky and Li, 2003; Li et al., 1984), and the minimum age is known from a U–Pb age of 1683 ± 67 Ma obtained from synsedimentary zircons in the immediately overlying Tuanshanzi Formation (Lu et al., 2002). Fresh outcrop samples come from recent excavation sites in the Jixian region. These samples lie stratigraphically near (within 200 meters) the contact with the Tuanshanzi Formation. There is significant amount Na-acetate extractable iron (carbonate-bound iron) in our fresh outcrop samples, but low amount of iron oxides, confirming that our samples were not significantly affected by surface oxidation and that dissolved iron was high at the time of deposition (e.g. Canfield et al., 2008). Deposition of the Changcheng Group started in a series of extensional basins and sub-basins. By the time of Chuanlinggou deposition, rifting had progressed to the point of a major continental passive margin along the southwest edge of the North China craton, where marine sedimentation continued until ~1.5 Ga (Kusky and Li, 2003). There is a tidal signature in the Changzhougou Formation, which conformably underlies the Chuanlinggou Formation (e.g. Lamb et al., 2009), consistent with open-marine deposition. Our samples from the ClG-1, CLG-4 and CLG-5 localities are part of the finely laminated shale sequences that lack any obvious shallow water sedimentary features, suggesting deposition below the storm wave base. These localities contain some highly carbonate-rich, possibly concretionary beds. We avoided these beds since they are unlikely to be simply representative of primary depositional conditions. The CLG-2 locality contained some massive, possibly reworked, shale beds and scouring features suggesting a shallower, possibly storm influenced depositional environment.

### *Northern Australia: Barney Creek, Mount Les Siltstone and Lady Loretta Formations*

Well-preserved late Paleoproterozoic to early Mesoproterozoic sedimentary sequences are found in several marine basins developed across north Queensland, the Northern Territory, and northeast Western Australia. Earlier models for basin development in the late Paleoproterozoic in northern Australia invoked small-scale mantle convection beneath thick continental crust resulting in a series of successive ‘rift-sag’ basins (Blake, 1987; Etheridge et al., 1987). More recently, it has been recognized that major tectonothermal events in the basins coincide with tectonic evolution along the southern margin of the proto-Australian continent, and the basins are now thought to have formed in a far-field continental back-arc setting (Giles et al., 2002).

The ~1670 to 1570 Ma McArthur basin in the Northern Territory and Mount Isa basin in Queensland comprise the Isa superbasin (Southgate et al., 2000). The superbasin extends over 1200 km from south of Mount Isa, Queensland, to Arnhem Land in the Northern Territory. The McArthur basin is essentially unmetamorphosed (Jackson et al., 1987; Page et al., 2000), and the effects of post-depositional alteration are limited. Weathering effects are not a factor because of our use of recently collected drill core material. There is a general southward and eastward increase in metamorphic grade and deformation effects in the Mount Isa basin, with sedimentary sequences reaching greenschist facies around Mount Isa (Blake, 1987).

Sedimentary environments in the Isa Superbasin ranged from terrestrial to shallow (evaporitic) and tidally influenced to deep water (sub-storm wave base) (Jackson et al., 1987; Lindsay, 2001). The presence of tidal facies suggests an open connection to the ocean[15]. Facies distribution was controlled by a combination of tectonically generated accommodation space and sea-level change (McGoldrick et al., 2010; Southgate et al., 2000) and is also consistent with a marine setting.  Evaporitic facies contain evidence for typical marine evaporite minerals (halite casts and pseudomorphs after gypsum and anhydrite) (Jackson et al., 1987). The depositional succession of evaporite minerals is not well resolved, but gypsum pseudomorphs are far more common than halite casts, suggesting it precipitated first in the evaporation sequence. During tectonically more active periods in basin development, such as during deposition of the 'River Supersequence', a mosaic of different sedimentary environments probably co-existed in small, fault-bounded sub-basins (McGoldrick et al., 2010).  Importantly, the recognition that sequences within sub-basins can be correlated regionally (Southgate et al., 2000) indicates connectivity among the sub-basins and with the open ocean.

The chronology of the sedimentary units in the Isa superbasin are well constrained by zircon U-Pb ages for tuffaceous interbeds in these sequences (Page et al., 2000), and for our study we targeted 1640 - 1650 Ma mudstones from three geographically separate locations. Our samples consisted of powdered 10 to 25 cm lengths of half or quarter drill core from intervals dominated by laminated shale with rare silt interbeds. Our McArthur basin samples derive from two drill cores through the Barney Creek Formation (Myrtle prospect drill holes MY3 and MY4), which has three dated tuffs 1638±7, 1639±3, and 1640±3 Ma (Page et al., 2000)—and two drill cores (WFDD84 and A83-4) through the Mount Les Siltstone (1640±7 Ma) (Page et al., 2000) near the Walford Creek prospect 250 km to the south. The Barney Creek Formation and the Mount Les Siltstone are coeval units assigned to the River Supersquence (Southgate et al., 2000). Our samples from the Mt. Isa basin are from the LA64 drill core, which contains the Lady Loretta Formation. The Lady Loretta Formation yields zircons that are slightly older (1647±4 Ma) (Page et al., 2000) than those from the Barney Creek Formation and Mount Les Silstone and is part of the Loretta supersequence (Southgate et al., 2000).

The drill cores we sampled are from the deepest water sections of the McArthur and Mt. Isa basins. Relative water depths within the Isa superbasin were inferred based on basin geometry, but sedimentological features (the presence of finely laminated beds) are consistent with these interpretations (Southgate et al., 2000). In some areas, the deep-water sections of the Mt. Isa superbasin host significant stratiform Zn mineralization. However, our geochemical signal for iron-rich deep water is not linked to the Zn mineralization. The McArthur and Mt. Isa basins contain ‘sedex’ deposits that are thought to have formed in brine pools located at, or close to, relatively low-temperature hydrothermal vents. Base metal sulphides appear to have precipitated from both a locally euxinic water column(Ireland et al., 2004; Large and McGoldrick, 1998) and within the upper few centimeters of unconsolidated sediment (Ireland et al., 2004; Large and McGoldrick, 1998). Hydrothermal, metal-transporting fluids were derived from shallow-water, oxidized, sulphate-enriched saline brines convectively circulating within deeper parts of the basins and driven tectonically to the seafloor along regional-scale faults (Garven et al., 2001; Yang et al., 2006). The deposits have large primary dispersion metal halos (marked by heavy oxygen isotope signature in carbonates) (Large et al., 2000; Large and McGoldrick, 1998), which are likely linked to precipitation of hydrothermally and seawater-derived metals in the brine pool (Cooke et al., 2000). Our samples were collected distal to these mineralization zones. Further, sulphide textures point to euxinic conditions in the local brine pools, which should have effectively sequestered any Fe carried by the base-metal mineralizing fluids and inhibited release to the ambient water column of the ocean/basin. Lastly, and perhaps most importantly, our samples typically contain very low (near crustal levels) zinc concentrations (SI Table 1). Very low zinc concentrations also indicate that our samples have not been influenced by mineralizing fluids; the inferred metal-rich fluids and the mineral deposits in the Mt. Isa Superbasin are famously zinc-rich (Ireland et al., 2004).

### *Newland Formation, the lower Belt Supergroup, Montana, USA*

The minimum age of the Newland Formation in the lower part of the Belt Supergroup is constrained by 1469 ± 2.5 Ma and 1457 ± 2 Ma zircon ages from younger mafic sills(Sears, 1998). The formation—consisting of intraclast conglomerates; silty black shales with nodular, laminated, and finely-disseminated pyrites; and calcareous gray shale beds—was deposited in a deep-water environment likely well below wave base. The lower Belt Supergroup was deposited during the rifting stage of the Belt basin; the Belt basin is believed to be an extensional feature with a tectonically active western side (Ross and Villeneuve, 2003; Sears, 1998). To avoid the affects of surface oxidation, samples were collected from the fresh drill cores SC-93 and M16, which, in contrast to the large areas of the Belt basin, particularly to the west, are at relatively low metamorphic grade. As for our Australian materials, the Belt samples used in the present study were stratigraphically and spatially removed from local ore mineralization, as constrained by petrographic observations and trace element data. The samples we analyzed were selected because previous reflected light microscopy found that the pyrite was present as fabrics strongly suggestive of early, low-temperature formation. Sulphides are present mainly as abundant finely disseminated pyrite and framboidal pyrites, suggesting that the sulphide pool formed through typical marine processes. Further, the samples typically contain low zinc concentrations (SI Table 1), which, given that Belt mineralization is zinc-rich, also provides strong support that mineralizing fluids have not significantly influenced our samples.

### *Bylot Supergroup formations, Borden basin, northern Baffin and Bylot Islands, Canada*

The Bylot Supergroup was deposited between ca. 1270 and 1000 Ma (Knight and Jackson, 1994) in the fault-bounded Borden basin. Sediments experienced sub-greenschist facies metamorphism. The Borden basin is interpreted as a failed rift arm with a connection to the Poseidon Ocean. The basin, however, progressed through phases of tectonic (extensional) and thermal subsidence and inversion. Shale samples were analyzed from three stratigraphic levels: the base (Arctic Bay Formation), middle (Victor Bay Formation), and at the top (Athole Point Formation) of the supergroup. The Arctic Bay Formation was deposited during the transgressive stage in a shallow-marine shelf to subtibal basinal setting and includes beds of black to dark-grey, locally pyritiferous shale (Kah, 2001). The lower part of the Victor Bay Formation includes beds of dark-grey, thinly bedded shale, which were deposited under subtidal conditions, but the formation also has several shallow intervals (Hofmann and Jackson, 1994). The uppermost targeted unit, the Athole Point Formation, contains dark-grey to black stromatolitic bioherms and turbiditic calcareous siliciclastic beds believed to be deposited in a semi-restricted basin (Kah, 2001).

## Marine sulphate concentrations and sulphur isotope systematics

Pyrite $\delta^{34}S$ values in examined drill cores and outcrop samples range from -2.4 to +42‰ (relative to the Vienna-Cañon Diablo Troilite, V-CDT), with an average of +16‰ (SI

Table 1). This average is close to the isotopic composition of coeval sulphate (Chu et al., 2007; Gellatly and Lyons, 2005; Kah et al., 2004), suggesting that essentially quantitative sulphate reduction was relatively common. However, the presence of some sedimentary pyrite in our samples with lighter $\delta^{34}S$ values than coeval sulphate can be interpreted as evidence for open system sulphate reduction. The dominantly$^{34}$S-enriched sulphur isotope ratios are most easily explained by having a large portion of sulphate reduction occurring in the sediments under locally restricted pore water conditions. Therefore, sulphur isotopes suggest that mid-Proterozoic ferruginous marine conditions are not linked to water column dissolved Fe levels in excess of total dissolved S (sulphate and sulphide) (see SI Ref. (Johnston et al., 2010) for discussion). Fe-rich deep-water marine conditions are more likely linked to limited water column sulphide production relative to the source Fe(II) flux (e.g. upwelling dissolved Fe).

Estimates of marine sulphate levels in the mid-Proterozoic (1.8 to 1 Ga) oceans range from 0.5 M to 4.5 mM. Although these levels are much lower than those in the modern ocean (28 mM), they are significantly higher than marine sulphate levels in the Archean (<200 $\mu$M) (Habicht et al., 2002). Several methods have been used to estimate marine sulphate levels. Briefly, the current estimates come from maximum isotope fractionation between coeval sulphide and marine sulphate, from the extent of sulphur isotope variability in marine sulphate, and from the sequence of mineral precipitates during evaporation of seawater. Recently, seawater sulphate has been estimated to be <1 mM, based on the small observed sulphate-sulphide isotope fractionation in numerous

Proterozoic sedimentary successions (Canfield et al., 2010). Rapid shifts in marine sulphate-S isotopes in several marine sedimentary sequences suggest that sulphate levels rose from 0.5 mM to 4.5 mM from ca. 1.7 to 1.2 Ga (Kah et al., 2004). However, abundant sulphate evaporites (for example at ca. 1.65 Ga, 1.3 Ga, and 1.2 Ga) suggest marine sulphate levels above ~2.5 mM (Jackson et al., 1987; Kah, 2001; Schröder et al., 2008). Importantly, all these estimates of marine sulphate levels are higher than expected dissolved marine Fe concentrations and therefore place critical constraints on our model for ferruginous domination—tied most parsimoniously to the distribution of organic matter.

Previous evidence for euxinia within the McArthur basin concurrent with our evidence for ferruginous conditions allows us to explore the influence of the water-column organic matter flux on the marine redox landscape in the mid-Proterozoic ocean. Sulphidic conditions are well recorded in the Barney Creek Formation in the Glyde River subbasin of the McArthur basin. These shales contain average TOC values of 2.5% and peak TOC concentrations of over 5%. In marked contrast, our McArthur Basin samples that contain evidence for deposition under ferruginous conditions have an average TOC concentration of 0.8%. This fundamental difference in TOC concentration supports the claim that extent of sulphide production (tied to organic availability) rather than sulphate limitation dictated the distribution of euxinia in the McArthur Basin and more broadly in the mid-Proterozoic ocean.

## Appendix References

Blake, D.H., 1987. Geology of the Mount Isa Inlier and environs, Queensland and the Northern Territory. B.M.R. Australia Bulletin 225, 83pp.

Canfield, D.E., Farquhar, J., Zerkle, A.L., 2010. High isotope fractionations during sulfate reduction in a low-sulfate euxinic ocean analog. Geology 38, 415-418.

Canfield, D.E., Poulton, S.W., Knoll, A.H., Narbonne, G.M., Ross, G., Goldberg, T., Strauss, H., 2008. Ferruginous conditions dominated later neoproterozoic deep-water chemistry. Science 321, 949-952.

Chu, X., Zhang, T., Zhang, Q., Lyons, T.W., 2007. Sulfur and carbon isotope records from 1700 to 800 Ma carbonates of the Jixian section, northern China: Implications for secular isotope variations in Proterozoic seawater and relationships to global supercontinental events. Geochimica et Cosmochimica Acta 71, 4668–4692.

Cooke, D.R., Bull, S.W., Large, R.R., McGoldrick, P.J., 2000. The importance of oxidised brines for the formation of Australian Proterozoic stratiform sediment-hosted Pb-Zn (Sedex) deposits. Economic Geology 95, 1-17.

Etheridge, M.A., Rutland, R.W.R., Wyborn, L.A.I., 1987. Orogenesis and tectonic process in the Early to Middle Proterozoic of northern Australia, in: Kröner, A. (Ed.), Precambrian Lithospheric Evolution. American Geophysical Union Geodynamic Series, pp. 131-147.

Garven, G., Bull, S.W., Large, R.R., 2001. Hydrothermal fluid flow models of stratiform ore genesis in the McArthur Basin, Northern Territory, Australia. Geofluids 1, 289-311.

Gellatly, A.M., Lyons, T.W., 2005. Trace sulfate in mid-Proterozoic carbonates and the sulfur isotope record of biospheric evolution Geochimica et Cosmochimica Acta 69, 3813–3829.

Giles, D., Betts, P., Lister, G., 2002. Far-field continental backarc setting for the 1.80-1.67 Ga basins of northeastern Australia. Geology [Geology] 30, 823-826.

Habicht, K.S., Gade, M., Thamdrup, B., Berg, P., Canfield, D.E., 2002. Calibration of sulfate levels in the Archean Ocean. Science 298, 2372-2374.

Hofmann, H.J., Jackson, G.D., 1994. Shelf-facies microfossils from the Proterozoic Bylot Supergroup, Baffin Island, Canada. . Journal of Paleontology 68, 361-382.

Ireland, T., Large, R.R., McGoldrick, P., Blake, M., 2004. Spatial distribution patterns of sulfur Isotopes, nodular carbonate and ore textures in the McArthur River (HYC) Zn-Pb-Ag deposit, Northern Territory, Australia. Economic Geology 99, 1687-1709.

Jackson, M.J., Muir, M.D., Plumb, K.A., 1987. Geology of the southern McArthur Basin. B. M. R. Bulletin 220, 173 pp.

Johnston, D.T., Poulton, S.W., Dehler, C., Porter, S., Husson, J., Canfield, D.E., Knoll, A.H., 2010. An emerging picture of Neoproterozoic ocean chemistry: Insights from the Chuar Group, Grand Canyon, USA. Earth and Planetary Science Letters 290, 64-73.

Kah, L.C., Lyons, T.W., Frank, T., 2004. Low marine sulphate and protracted oxygenation of the Proterozoic biosphere. Nature 431, 834-837.

Kah, L.C., Lyons, T.W. & Chesley, J.T. , 2001. Geochemistry of a 1.2 Ga carbonate-evaporite succession, northern Baffin and Bylot Islands: implications for Mesoproterozoic marine evolution. Precambrian Research 111, 203-234.

Knight, R.D., Jackson, G.D., 1994. Sedimentology and stratigraphy of the Mesoproterozoic Elwin Subgroup (Aqigilik and Sinasiuvik Formations), Uppermost Bylot Supergroup, Borden Rift Basin, Northern Baffin Island. Geological Survey of Canada Bulletin 455, 1-43.

Kusky, T.M., Li, J., 2003. Paleoproterozoic tectonic evolution of the North China Craton. Journal of Asian Earth Sciences 22, 383–397.

Lamb, D.M., Awramik, S.M., Chapman, D.J., Zhu, S., 2009. Evidence for eukaryotic diversification in the 1800 million-year-old Changzhougou Formation, North China. Precambian Reasearch 173, 93-104.

Large, R.R., Bull, S.W., McGoldrick, P.J., 2000. Lithogeochemical halos and geochemical vectors to stratiform sediment hosted Zn-Pb-Ag deposits Part 2. HYC deposit, McArthur River, Northern Territory. Journal of Geochemical Exploration 68, 105-126.

Large, R.R., McGoldrick, P.J., 1998. Lithogeochemical halos and geochemical vectors to stratiform sediment-hosted Zn-Pb-Ag deposits. Part 1: Lady Loretta deposit, Queensland. Journal of Geochemical Exploration 63, 37-56.

Li, S., Lin, Y., Zhang, X., 1984. A report on the age of the Changzhougou and Chuanlinggou Formations of the Changcheng System in the Yanshan Range. Precambrian Geology 2, 129–134.

Lindsay, J.F., 2001. Basin dynamics and mineralisation, McArthur Basin, northern Australia. Australian Journal of Earth Sciences 48, 703-720.

Lu, S., Yang, C., Li, H., Li, H., 2002. A group of rifting events in the terminal Paleoproterozoic in the North China Craton. Gondwana Research 5, 123–131.

McGoldrick, P., Winefield P., Bull, S., Selley, D., Scott, R., 2010. Sequences, Synsedimentary Structures, and Sub-Basins: the Where and When of SEDEX Zinc Systems in the Southern McArthur Basin, Australia. Society of Economic Geologists, Special Publications 15, 1-23.

Page, R.W., Jackson, M.J., Krassay, A.A., 2000. Constraining sequence stratigraphy in north Australian basins: SHRIMP U–Pb zircon geochronology between Mt Isa and McArthur River Australian Journal of Earth Sciences 47, 431 – 459.

Ross, G.R., Villeneuve, M., 2003. Provenance of the Mesoproterozoic (1.45 Ga) Belt basin (western North America): Another piece in the pre-Rodiniapaleogeographic puzzle. Geological Society of America Bulletin 115, , 1191-1217.

Schröder, S., Bekker, A., Beukes, N.J., Strauss, H., van Niekerk, H.S., 2008. Rise in seawater sulphate concentration associated with the Paleoproterozoic positive carbon isotope excursion: evidence from sulphate evaporites in the ~2.2–2.1 Gyr shallow-marine Lucknow Formation, South Africa. Terra Nova 20, 108-117.

Sears, J.W., Chamberlain, K.R., and Buckley, S.N., 1998. Structural and U-Pb geochronological evidence for 1.47 Ga rifting in the Belt basin, western Montana. Canadian Journal of Earth Sciences 35, 467–475.

Southgate, P.N., Bradshaw, B.E., Domagala, J., Jackson, M.J., Idnurm, M., Krassay, A.A., Page, R.W., Sami, T.T., Scott, D.L., Lindsay, J.F., McConachie, B.A., Tarlowski, C., 2000. Chronostratigraphic basin framework for Palaeoproterozoic rocks (1730–1575 Ma) in northern Australia and implications for base-metal mineralisation Australian Journal of Earth Sciences 47, 461 – 483.

Yang, C., Large, R.R., Bull, S., Scott, D.L., 2006. Basin-Scale Numerical Modeling to Test the Role of Buoyancy-Driven Fluid Flow and Heat Transfer in the Formation of Stratiform Zn-Pb-Ag Deposits in the Northern Mount Isa Basin. Economic Geology 101, 1275-1292.

# Appendix Figures and Figure Legends

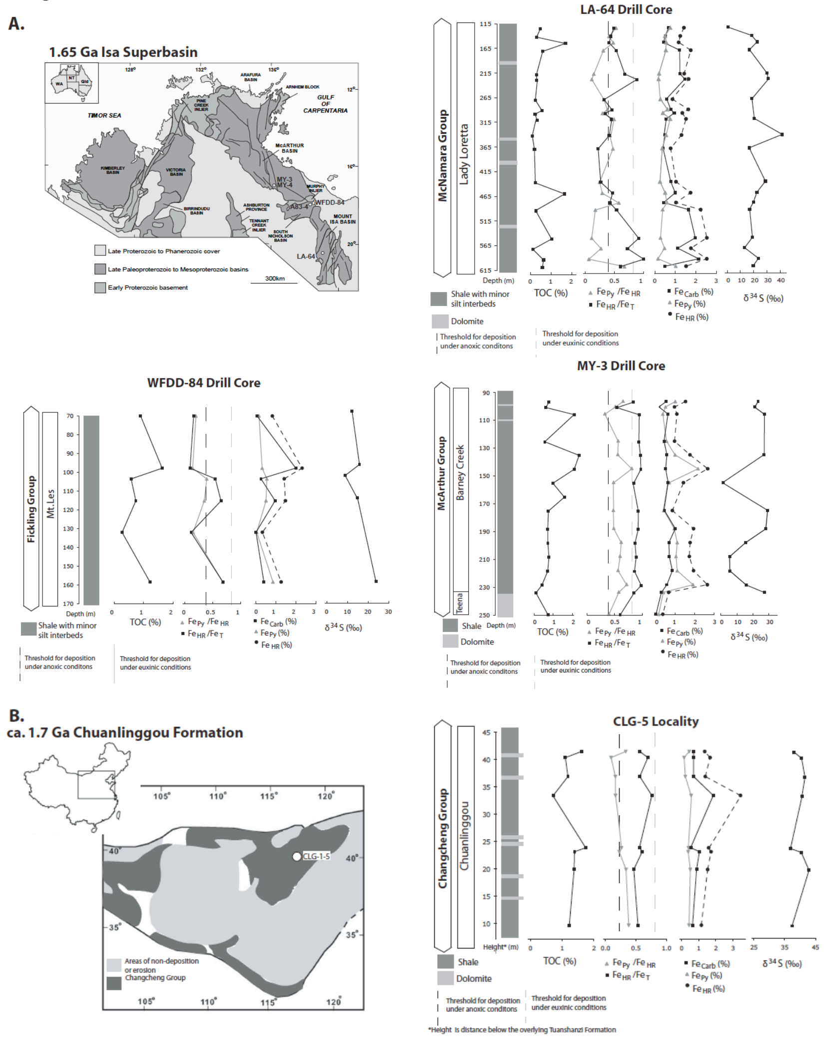

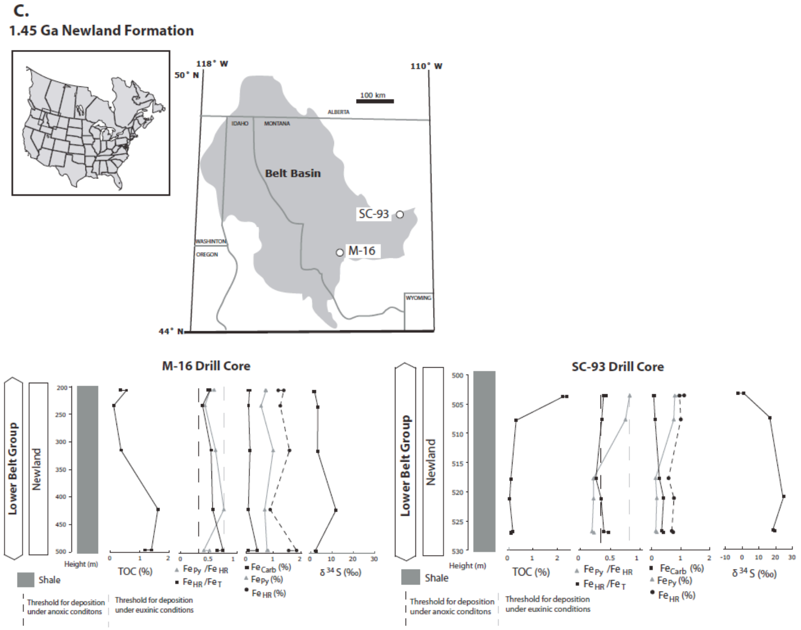

Appendix Figure 3.3. Sample locations and stratigraphic presentation of data. A. Location of and data from the 1.65 Ga Mt. Isa Superbasin. Samples come from the McArthur and Mt. Isa basins, which are located in the eastern half of the Mt. Isa Superbasin. Data are from five drill cores, three of which (LA-64, WFDD-84, and MY-3) cover thick (>100 m) stratigraphic intervals. Although there is some variability in the geochemical results, the majority of the samples have high (>0.38) highly reactive to total iron (FeHR/FeT) and low (<0.8) pyrite to highly reactive iron (FePy/FeHR) ratios, which is a signal for deposition under a ferruginous water column. Total organic carbon (TOC) is typically less than 1%, suggesting a relatively low flux of organic matter to the sediment water interface. There is a fairly large (>25‰) range of sulphur isotope values. B. Location of and data from the 1.7 Ga Chuanlinggou Formation. Samples come from five outcrop localities in northern China. The CLG-5 locality contains consistent reactive iron enrichments and low sulphide concentrations. TOC is between 1-2% and sulphur isotope values are consistently greater than 35‰. C. Location of and data from the 1.45 Ga Newland Formation. Samples come from two drill cores from the southeastern section of the Belt Basin. Both drill cores have consistent reactive iron enrichments, but interestingly have variable FePy/FeHR ratios that track TOC contents. Specifically, samples with higher TOC contents have higher FePy/FeHR ratios. There is a fairly large (>25‰) range of sulphur isotope values.

Appendix Table 3.1. Fe speciation and pyrite sulfur isotope data

| Drill Hole-Sample Name | Depth | $Fe_{Ox}$ (%) | $Fe_{Mag}$ (%) | $Fe_{Carb}$ (%) | $Fe_{Py}$ (%) | $Fe_{HR}$ (%) | $Fe_{Total}$ (%) | $Fe_{HR}$/ $Fe_{Total}$ | $Fe_{Py}$/ $Fe_{HR}$ | TIC (%) | TOC (%) | $\delta^{34}S$ ‰ (VCDT) | Zn (ppm) |
|---|---|---|---|---|---|---|---|---|---|---|---|---|---|
| **1.64 Ga Mt. Isa Superbasin** | | | | | | | | | | | | | |
| LA64 | 116.8 | 0.00 | 0.00 | 0.67 | 0.75 | 1.42 | 2.92 | 0.5 | 0.5 | 2.0 | 0.5 | 0.7 | 33 |
| LA64 | 133.6 | 0.13 | 0.10 | 0.51 | 0.51 | 1.24 | 2.84 | 0.4 | 0.4 | 1.9 | 0.3 | 18.5 | 33 |
| LA64 | 146.5 | 0.11 | 0.07 | 0.42 | 0.56 | 1.17 | 2.87 | 0.4 | 0.5 | 1.9 | 1.7 | 22.6 | 42 |
| LA64 | 162.5 | 0.00 | 0.00 | 1.22 | 0.54 | 1.76 | 3.30 | 0.5 | 0.3 | 3.2 | 0.6 | 16.9 | 42 |
| LA64 | 210 | 0.00 | 0.00 | 1.22 | 0.21 | 1.44 | 2.13 | 0.7 | 0.1 | 6.6 | 0.3 | 30.1 | 13 |
| LA64 | 221 | 0.00 | 0.00 | 1.47 | 0.19 | 1.65 | 1.87 | 0.9 | 0.1 | 7.8 | 0.3 | 31.0 | 14 |
| LA64 | 261.8 | 0.00 | 0.00 | 0.59 | 0.28 | 0.87 | 2.70 | 0.3 | 0.3 | 2.9 | 0.2 | 18.6 | 34 |
| LA64 | 282.5 | 0.13 | 0.11 | 0.78 | 0.62 | 1.64 | 3.57 | 0.5 | 0.4 | 2.9 | 0.6 | | 46 |
| LA64 | 289.8 | 0.00 | 0.00 | 0.95 | 0.40 | 1.35 | 3.97 | 0.3 | 0.3 | 3.1 | 0.2 | | 41 |
| LA64 | 301.8 | 0.12 | 0.09 | 0.56 | 0.75 | 1.53 | 3.41 | 0.4 | 0.5 | 3.4 | 0.3 | 20.5 | 67 |
| LA64 | 334.5 | 0.14 | 0.13 | 0.49 | 0.55 | 1.31 | 3.18 | 0.4 | 0.4 | 1.7 | 0.1 | 41.5 | 37 |
| LA64 | 361.5 | 0.00 | 0.00 | 0.41 | 0.37 | 0.78 | 3.50 | 0.2 | 0.5 | 1.4 | 0.2 | 16.6 | 46 |
| LA64 | 429.2 | 0.00 | 0.00 | 0.78 | 0.26 | 1.04 | 3.92 | 0.3 | 0.2 | 1.7 | 0.2 | 28.9 | 55 |
| LA64 | 451.5 | 0.13 | 0.11 | 1.00 | 0.51 | 1.75 | 3.75 | 0.5 | 0.3 | 2.8 | 1.6 | 22.4 | 39 |
| LA64 | 471.4 | 0.00 | 0.00 | 0.44 | 0.59 | 1.03 | 2.46 | 0.4 | 0.6 | 1.4 | | 19.9 | 32 |
| LA64 | 485.8 | 0.01 | 0.19 | 1.65 | 0.39 | 2.24 | 4.18 | 0.5 | 0.2 | 4.3 | 0.2 | 17.0 | 30 |
| LA64 | 543 | 0.13 | 0.15 | 1.98 | 0.28 | 2.54 | 2.78 | 0.9 | 0.1 | 6.3 | 1.0 | 19.1 | 41 |
| LA64 | 564 | 0.00 | 0.17 | 1.12 | 0.48 | 1.77 | 2.45 | 0.7 | 0.3 | 4.5 | 0.1 | 13.1 | 24 |
| LA64 | 585.5 | 0.18 | 0.06 | 2.14 | 0.16 | 2.54 | 2.54 | 1.0 | 0.1 | 5.4 | 0.6 | 23.7 | 28 |
| LA64 | 600.5 | 0.00 | 0.00 | 0.50 | 1.03 | 1.53 | 2.54 | 0.6 | 0.7 | 2.2 | 0.6 | 19.7 | 20 |
| WFDD84 | 70 | 0.21 | 0.38 | 0.07 | 0.16 | 0.83 | 5.34 | 0.2 | 0.2 | 0.1 | 0.9 | 12.2 | 29 |
| WFDD84 | 97.8 | 0.00 | 0.00 | 1.99 | 0.32 | 2.31 | 25.21 | 0.1 | 0.1 | 5.2 | 1.6 | 15.8 | 64 |
| WFDD84 | 103.5 | 0.49 | 0.12 | 0.26 | 0.55 | 1.42 | 2.60 | 0.5 | 0.4 | 3.2 | 0.6 | 8.8 | 31 |
| WFDD84 | 115.2 | 0.00 | 0.00 | 0.97 | 0.51 | 1.48 | 2.29 | 0.6 | 0.3 | 4.8 | 0.7 | 14.7 | 82 |
| WFDD84 | 132 | 0.15 | 0.12 | 0.02 | 0.05 | 0.33 | 3.01 | 0.1 | 0.1 | 2.7 | 0.3 | | 43 |
| WFDD84 | 158.5 | 0.00 | 0.00 | 0.41 | 0.86 | 1.26 | 1.85 | 0.7 | 0.7 | 3.1 | 1.2 | 23.9 | 46 |
| A83-4 | 223.9 | 0.10 | 0.09 | 1.07 | 0.21 | 1.47 | 2.27 | 0.6 | 0.1 | 2.6 | 2.2 | | 21 |
| A83-4 | 236 | 0.00 | 0.00 | 0.62 | 0.60 | 1.22 | 2.92 | 0.4 | 0.5 | 5.3 | 0.2 | | 10 |
| A83-4 | 247.3 | 0.16 | 0.16 | 0.02 | 0.05 | 0.39 | 2.62 | 0.1 | 0.1 | 2.2 | | | 14 |
| A83-4 | 271.1 | 0.15 | 0.17 | 0.00 | 0.03 | 0.35 | 2.85 | 0.1 | 0.1 | 1.1 | 0.2 | | 20 |
| A83-4 | 289.95 | 0.00 | 0.00 | 0.48 | 1.11 | 1.59 | 2.07 | 0.8 | 0.7 | 3.0 | 1.5 | | 27 |
| MY3 | 96.7 | 0.00 | 0.00 | 0.53 | 1.00 | 1.53 | 1.83 | 0.8 | 0.7 | 2.1 | | 23.1 | 7 |
| MY3 | 100.6 | 0.31 | 0.00 | 0.15 | 0.49 | 0.96 | 1.77 | 0.5 | 0.5 | 0.5 | 0.6 | 21.0 | 60 |
| MY3 | 105.7 | 0.00 | 0.11 | 0.62 | 0.35 | 1.08 | 1.14 | 0.9 | 0.3 | 7.9 | 2.1 | 27.2 | 3 |
| MY3 | 125.2 | 0.00 | 0.00 | 0.42 | 0.55 | 0.96 | 1.02 | 0.9 | 0.6 | 6.2 | 0.6 | | 3 |
| MY3 | 135.0 | 0.12 | 0.09 | 0.57 | 0.99 | 1.76 | 1.82 | 1.0 | 0.6 | 4.7 | 2.3 | 26.8 | 11 |
| MY3 | 145.0 | 0.00 | 0.00 | 0.50 | 2.18 | 2.68 | 2.75 | 1.0 | 0.8 | 3.1 | 2.1 | | 13 |
| MY3 | 155.0 | 0.00 | 0.11 | 0.63 | 0.69 | 1.42 | 1.69 | 0.8 | 0.5 | 5.2 | 1.0 | 1.1 | 9 |
| MY3 | 175.0 | 0.00 | 0.00 | 0.44 | 0.40 | 0.85 | 0.91 | 0.9 | 0.5 | 2.1 | 0.7 | 29.1 | 52 |
| MY3 | 188.0 | 0.00 | 0.00 | 1.00 | 0.95 | 1.95 | 2.10 | 0.9 | 0.5 | 4.2 | 0.7 | 28.0 | 36 |
| MY3 | 198.0 | 0.00 | 0.00 | 0.67 | 1.10 | 1.77 | 2.03 | 0.9 | 0.6 | 3.2 | 0.7 | 15.2 | 12 |
| MY3 | 208.0 | 0.00 | 0.00 | 0.69 | 1.04 | 1.73 | 1.94 | 0.9 | 0.6 | 3.6 | 0.8 | 5.4 | 42 |
| MY3 | 218.2 | 0.00 | 0.00 | 0.85 | 1.10 | 1.95 | 2.26 | 0.9 | 0.6 | 4.3 | 0.7 | 5.5 | 19 |
| MY3 | 228.3 | 0.10 | 0.08 | 0.57 | 1.92 | 2.66 | 2.71 | 1.0 | 0.7 | 4.8 | 0.4 | 15.7 | 22 |
| MY3 | 233.8 | 0.00 | 0.00 | 0.28 | 0.38 | 0.66 | 0.77 | 0.9 | 0.6 | 10.2 | 0.1 | 27.2 | 32 |
| MY3 | 249.5 | 0.12 | 0.09 | 0.00 | 0.14 | 0.35 | 0.59 | 0.6 | 0.4 | 11.1 | 0.7 | | 3 |
| MY4 | 37.0 | 0.21 | 0.10 | 0.34 | 0.50 | 1.14 | 1.24 | 0.9 | 0.4 | 0.3 | | 14.7 | 57 |
| MY4 | 51.0 | 0.00 | 0.00 | 1.20 | b.d. | 1.20 | 2.30 | 0.5 | | 3.6 | 2.7 | | 32 |
| MY4 | 61.5 | 0.00 | 0.00 | 0.55 | 0.88 | 1.43 | 2.50 | 0.6 | 0.6 | 6.5 | 1.8 | 10.3 | 41 |
| MY4 | 88.5 | 0.16 | 0.13 | 0.00 | 0.25 | 0.54 | 0.83 | 0.7 | 0.5 | 2.7 | 1.2 | 22.3 | 25 |

**ca. 1.7 Ga Chuanlinggou Formation**

| | | | | | | | | | | | | |
|---|---|---|---|---|---|---|---|---|---|---|---|---|
| CLG1-02 | 1.4 | 0.74 | 0.80 | 0.18 | 1.17 | 2.90 | 5.26 | 0.6 | 0.4 | 0.2 | 4.3 | 36.1 |
| CLG1-03 | 3.2 | 0.03 | 0.85 | 0.26 | 0.34 | 1.48 | 5.27 | 0.3 | 0.2 | 0.5 | 3.2 | 32.9 |
| CLG1-07 | 5.8 | 0.10 | 0.32 | 3.68 | 0.26 | 4.36 | 5.52 | 0.8 | 0.1 | 8.3 | 0.8 | 30.5 |
| CLG1-10 | 8.9 | 0.13 | 0.25 | 2.36 | 0.02 | 2.75 | 3.84 | 0.7 | 0.01 | 6.5 | 0.4 | 29.1 |
| CLG1-11 | 10.2 | 0.12 | 0.18 | 3.01 | 0.04 | 3.35 | 4.35 | 0.8 | 0.01 | 7.3 | 0.5 | 22.5 |
| CLG1-13 | 12.5 | 0.19 | 0.05 | 2.46 | b.d. | 2.72 | 3.80 | 0.7 | | 6.4 | 0.4 | 31.2 |
| CLG2-01 | 0.0 | 0.06 | 0.07 | 0.21 | 0.35 | 0.69 | 3.45 | 0.2 | 0.5 | 0.2 | 0.6 | 34.9 |
| CLG2-02 | 0.7 | 0.07 | 0.20 | 0.96 | 0.41 | 1.63 | 5.25 | 0.3 | 0.2 | 1.5 | 1.0 | 32.2 |
| CLG2-03 | 1.3 | 0.02 | 0.16 | 0.12 | 0.35 | 0.65 | 3.63 | 0.2 | 0.5 | 0.1 | 0.5 | 34.7 |
| CLG2-04A | 1.8 | 0.05 | 0.30 | 0.66 | 0.37 | 1.38 | 5.26 | 0.3 | 0.3 | 0.8 | 0.9 | 33.0 |
| CLG2-04B | 1.6 | 0.09 | 0.15 | 0.11 | 0.17 | 0.51 | 4.24 | 0.1 | 0.3 | 0.02 | 0.4 | 36.6 |
| CLG2-05 | 2.7 | 0.02 | 0.19 | 0.35 | 0.23 | 0.78 | 4.23 | 0.2 | 0.3 | 0.3 | 0.4 | 35.1 |
| CLG2-06 | 3.2 | 0.03 | 0.19 | 0.21 | 0.20 | 0.63 | 4.25 | 0.1 | 0.3 | 0.1 | 0.4 | 36.7 |
| CLG2-08 | 3.8 | 0.05 | 0.22 | 0.64 | 0.24 | 1.15 | 4.81 | 0.2 | 0.2 | 0.8 | 0.4 | 35.9 |
| CLG2-09 | 40.5 | 0.03 | 0.12 | 0.10 | 0.26 | 0.51 | 3.45 | 0.1 | 0.5 | 0.1 | 0.2 | 37.5 |
| CLG2-10 | 41.1 | 0.01 | 0.11 | 0.35 | 0.09 | 0.55 | 3.61 | 0.2 | 0.2 | 0.6 | 0.5 | 39.8 |
| CLG2-12 | 42.4 | 0.13 | 0.05 | 0.19 | 0.36 | 0.73 | 2.99 | 0.2 | 0.5 | 0.2 | 0.7 | 36.1 |
| CLG4-03 | | 0.25 | 0.30 | 0.17 | 0.08 | 0.79 | 4.66 | 0.2 | 0.1 | 0.02 | 0.3 | 28.2 |
| CLG4-05 | | 0.18 | 1.52 | 1.31 | 0.06 | 3.08 | 14.61 | 0.2 | 0.02 | 1.0 | 0.8 | 26.2 |
| CLG5-31 | 41.2 | 0.16 | 0.04 | 0.70 | 0.45 | 1.35 | 2.40 | 0.6 | 0.3 | 5.4 | 1.6 | 38.1 |
| CLG5-32 | 40.1 | 0.73 | 0.08 | 0.70 | 0.15 | 1.67 | 2.39 | 0.7 | 0.1 | 6.1 | 1.1 | 40.5 |
| CLG5-35 | 36.7 | 0.40 | 0.06 | 0.71 | 0.23 | 1.39 | 2.46 | 0.6 | 0.2 | 5.1 | 1.2 | 41.6 |
| CLG5-37 | 33.3 | 0.66 | 0.36 | 1.85 | 0.56 | 3.44 | 4.52 | 0.8 | 0.2 | 5.9 | 0.7 | 40.6 |
| CLG5-43 | 23.9 | 0.56 | 0.06 | 0.56 | 0.41 | 1.58 | 2.79 | 0.6 | 0.3 | 4.3 | 1.7 | 36.9 |
| CLG5-44 | 23.2 | 0.24 | 0.05 | 1.05 | 0.39 | 1.73 | 2.86 | 0.6 | 0.2 | 4.7 | 1.4 | 40.4 |
| CLG5-45 | 20 | 0.08 | 0.05 | 0.88 | 0.51 | 1.53 | 3.28 | 0.5 | 0.3 | 4.0 | 1.4 | 42.9 |
| CLG5-53 | 10 | 0.02 | 0.06 | 0.64 | 0.44 | 1.16 | 2.17 | 0.5 | 0.4 | 4.9 | 1.2 | 37.4 |
| CLG7-01 | | 0.02 | 1.17 | 0.20 | 0.49 | 1.89 | 5.09 | 0.4 | 0.3 | 0.2 | 2.0 | 35.4 |
| CLG7-02 | | 0.03 | 1.62 | 0.40 | 0.13 | 2.18 | 6.75 | 0.3 | 0.1 | 0.5 | 1.7 | 31.8 |
| CLG7-03 | | 0.01 | 1.08 | 0.14 | 0.36 | 1.58 | 4.75 | 0.3 | 0.2 | 0.1 | 1.6 | 35.5 |
| CLG7-04 | | 0.02 | 1.01 | 0.13 | 0.27 | 1.42 | 4.57 | 0.3 | 0.2 | 0.1 | 1.5 | 24.6 |

**1.45 Ga Newland Formation***

| | | | | | | | | | | | | | |
|---|---|---|---|---|---|---|---|---|---|---|---|---|---|
| M16 | 204.8 | 0.13 | 0.28 | 0.06 | 0.70 | 1.17 | 2.39 | 0.5 | 0.6 | 0.1 | 0.4 | 1.4 | 72 |
| M16 | 204.85 | 0.22 | 0.32 | 0.11 | 0.72 | 1.38 | 2.64 | 0.5 | 0.5 | 0.1 | 0.6 | 1.8 | 51 |
| M16 | 232.8 | 0.20 | 0.43 | 0.08 | 0.54 | 1.25 | 3.21 | 0.4 | 0.4 | 0.0 | 0.1 | 3.3 | 56 |
| M16 | 313.6 | 0.15 | 0.32 | 0.13 | 0.99 | 1.59 | 2.94 | 0.5 | 0.6 | 1.1 | 0.4 | 3.2 | 64 |
| M16 | 420.9 | 0.03 | 0.10 | 0.07 | 0.67 | 0.88 | 1.54 | 0.6 | 0.8 | 1.4 | 1.6 | 11.8 | 91 |
| M16 | 495 | 0.18 | 0.51 | 0.40 | 0.76 | 1.85 | 2.45 | 0.8 | 0.4 | 0.3 | 1.4 | 2.1 | 93 |
| M16 | 495.05 | 0.20 | 0.49 | 0.06 | 0.80 | 1.56 | 2.42 | 0.6 | 0.5 | 0.3 | 1.2 | 2.5 | 99 |
| SC93 | 503.7 | 0.04 | 0.06 | 0.09 | 0.93 | 1.12 | 2.60 | 0.4 | 0.8 | 0.3 | 2.4 | -2.4 | 286 |
| SC93 | 503.75 | 0.05 | 0.06 | 0.06 | 0.79 | 0.96 | 2.48 | 0.4 | 0.8 | 0.9 | 2.2 | 1 | 262 |
| SC93 | 507.8 | 0.06 | 0.08 | 0.11 | 0.76 | 1.00 | 2.80 | 0.4 | 0.8 | 1.0 | 0.3 | 16.5 | 78 |
| SC93 | 517.8 | 0.06 | 0.13 | 0.26 | 0.13 | 0.58 | 2.22 | 0.3 | 0.2 | 3.2 | 0.1 | | 43 |
| SC93 | 521.2 | 0.06 | 0.13 | 0.41 | 0.17 | 0.76 | 2.20 | 0.3 | 0.2 | 3.7 | 0.1 | 24.8 | 56 |
| SC93 | 526.8 | 0.05 | 0.17 | 0.34 | 0.13 | 0.69 | 1.75 | 0.4 | 0.2 | 6.6 | 0.2 | 18.3 | 22 |
| SC93 | 527 | 0.05 | 0.13 | 0.39 | 0.17 | 0.74 | 1.56 | 0.5 | 0.2 | 6.0 | 0.1 | 19.4 | 25 |

| | | | | | | | | | | |
|---|---|---|---|---|---|---|---|---|---|---|
| **1.2 Ga Borden Basin** | | | | | | | | | | |
| JD-79-138D | 0.02 | 0.02 | 0.07 | 0.42 | 0.53 | 2.77 | 0.2 | 0.8 | 3.76 | 3.1 |
| JD-79-113-B | 0.00 | 0.15 | 0.22 | 0.51 | 0.87 | 1.30 | 0.7 | 0.6 | 5.88 | 1.0 |
| JD-77-70 E | 0.05 | 0.18 | 0.24 | 0.51 | 0.98 | 2.52 | 0.4 | 0.5 | 8.97 | 2.3 |
| JD-79-I 112 C-2 | 0.05 | 0.31 | 0.60 | 1.26 | 2.22 | 2.84 | 0.8 | 0.6 | 2.91 | 3.8 |
| JD-79-186K | 0.17 | 0.14 | 0.07 | 0.42 | 0.79 | 2.52 | 0.3 | 0.5 | 8.95 | 1.0 |
| JD-79 112-C1 | 0.27 | 0.10 | 0.35 | 0.59 | 1.31 | 2.45 | 0.5 | 0.5 | 5.88 | 2.2 |

## Chapter 4: The Evolution of the Marine Phosphate Reservoir

### Abstract, Introduction, Results, Discussion, and Conclusions

Phosphorus is a biolimiting nutrient that plays an important role in regulating organic matter burial and the redox state of the ocean-atmosphere system (Holland, 1984). The ratio of phosphorus to iron in iron oxide-rich sedimentary rocks can be used to track dissolved phosphate concentrations if the dissolved silica concentration of seawater is estimated (Bjerrum and Canfield, 2002; Edmonds and German, 2004; Feely et al., 1998; Poulton and Canfield, 2006). Here we present iron and phosphorus concentration ratios from distal hydrothermal sediments and iron formations through time in order to evaluate the evolution of the marine phosphate reservoir. The data suggest that phosphate concentrations have been relatively constant over the Phanerozoic, the past 542 million years of Earth's history. In contrast, phosphate concentrations appear to have been elevated in Precambrian oceans. Specifically, there is a peak in phosphorus to iron ratios in Neoproterozoic iron formations dating from ~760 to ~635 million years ago (Ma), indicating unusually high dissolved phosphate concentrations in the aftermath of widespread, low latitude 'Snowball Earth' glaciations. An enhanced postglacial phosphate flux would have caused high rates of primary productivity and organic carbon burial and a transition to more oxidizing conditions in the ocean and atmosphere. The 'Snowball Earth' glaciations and Neoproterozoic oxidation are both suggested as triggers for the evolution and radiation of metazoans (Hoffman and Schrag, 2002; Knoll and Carroll, 1999). We propose that these two factors are intimately linked; a glacially induced nutrient surplus could have led to an increase in atmospheric oxygen, paving the way for the rise of metazoan life.

In almost all modern aquatic systems, primary production of organic matter is typically thought to be limited by either phosphorus or bioavailable nitrogen (Howarth, 1988). Temporally extended deficiencies in fixed nitrogen availability are buffered by biological fixation of a virtually limitless supply of atmospheric $N_2$. By contrast, phosphorus is sourced primarily by weathering of continental materials; accordingly, it is generally thought that phosphorus ultimately limits net primary productivity on geological timescales (Howarth, 1988; Tyrrell, 1999). An estimate of marine phosphate reservoir size through time is therefore essential to unravel basic aspects of biological and geochemical evolution (Holland, 2006).

Ratios of phosphorous to iron in ferric oxides scale with ambient concentrations of dissolved phosphate, as predicted by distribution coefficient ($K_D$) relationships: $[P_D] = (1/K_D)*(P_{ads}/Fe)$(Feely et al., 1998). P/Fe ratios in ferric oxyhydroxides within hydrothermal plumes emanating from mid-ocean ridges remain constant during transport[3]. Similarly, P/Fe ratios in modern iron oxide-rich sediments appear to remain essentially constant or show only slight decreases during burial, despite mineralogical transformations (Edmonds and German, 2004; Poulton and Canfield, 2006). Consequently, P/Fe ratios in ferruginous sediments can be used to track dissolved phosphate concentrations in ancient seawater (Bjerrum and Canfield, 2002). Because the

$K_D$ value for phosphate-iron oxyhydroxide sorption varies inversely with dissolved Si concentrations due to competitive adsorption of aqueous silica species (Konhauser et al., 2007), it is also important to consider the evolution of the silica cycle when using P/Fe ratios as a paleoproxy. Marine silica concentrations have varied dramatically through Earth's history, significantly influencing phosphate sorption by Fe oxyhydroxides.

The data for this study (~700 individual samples of Fe oxide-rich rocks) include new results and those obtained from a comprehensive literature survey. Consistent with previous studies in which iron formations have been used to decipher ancient seawater chemistry (Bjerrum and Canfield, 2002; Konhauser et al., 2009), our samples were passed through a series of strict filters to select for authigenic Fe-rich rocks that most likely retain bulk seawater signatures. All samples have a negligible detrital component and contain only minor amounts of pyrite, siderite, and Mn phases (see supplementary information).

We identify four well-defined stages in P/Fe ratios in Fe oxide-rich rocks through time (Fig. 4.1). These stages reflect both shifts in the size of the marine phosphate reservoir and the evolution of the global silica cycle. Stages 1 and 2, defined by distal hydrothermal sediments from fourteen different localities of Phanerozoic age (< 542 Ma), span the Quaternary through the Cretaceous and the Jurassic through the Cambrian, respectively. The molar P/Fe ratios (multiplied by one hundred, $P/Fe_{(100)}$) in Stage 1 yield an average of 2.55 with a range of <1 to 8.6 and a standard deviation of 1.2. In Stage 2 there is an average P/$Fe_{(100}$ ratio of 0.38 with a range from <1 to 1.8 and a standard deviation of 0.26 (Fig. 4.1).

The marked change in P/Fe ratios between stages 1 and 2 is coincident with the initial radiation of diatoms, when marine silica concentrations are thought to have decreased substantially (Racki and Cordey, 2000; Siever, 1992). Dissolved silica concentrations are assumed to have been <0.1 mM in the modern through Cretaceous ocean and, taking a conservative estimate, ~0.67 mM in the Cambrian through mid-Jurassic ocean, which is near cristobalite saturation (see supplementary information for a discussion of constraints on dissolved Si concentrations). Recent experimental results indicate that an approximately seven-fold increase in dissolved silica from modern levels (i.e., from <0.1 mM to 0.67 mM) would cause an 84.5% decrease in the amount of phosphate sorbed to ferric oxides. This decrease is virtually identical to the magnitude of the observed increase in P/Fe ratios occurring subsequent to the expansion of siliceous phytoplankton (85%), when dissolved silica concentrations would have decreased. Thus, when viewed in light of varying silica content, marine phosphate concentrations seem to have been roughly constant though the Phanerozoic, in accordance with independent estimates for marine phosphate concentrations (Arvidson et al., 2006).

Stage 3 occurred during the Cryogenian (~750-620 Ma). Samples for this time interval are from seven iron formations (IF) associated with the low-latitude, 'Snowball Earth' glaciations (Hoffman and Schrag, 2002) and contain average P/$Fe_{(100)}$ of 1.96 with a range from <1 to 6.8 and a standard deviation of 1.2. This average is markedly higher than those seen during the early and middle Phanerozoic. Dissolved marine silica concentrations in the Neoproterozoic were likely high relative to the Phanerozoic; the radiation of radiolarians and siliceous sponges in the earliest Phanerozoic resulted in a shift to a biologically controlled silica cycle and likely caused a decrease in marine silica concentrations (Racki and Cordey, 2000). Therefore, Cryogenian IF point to very high marine phosphate concentrations. Using even the most conservative estimates for dissolved silica concentrations, and assuming that concentrations were similar to those in the early Phanerozoic (~0.67 mM), P/Fe ratios in Cryogenian IF suggest marine dissolved phosphate concentrations that were over five times greater than Phanerozoic levels. Neoproterozoic IF were deposited in shelf or slope setting under shallower conditions than the majority of deepwater (sub-storm wave base to abyssal depths) deposits in our compilation. Because of the non-conservative, nutrient-type behavior of dissolved phosphorous in the ocean, shallow waters would be expected to show signs of phosphate depletion, making the anomalous enrichments we see in the shallow Cryogenian IF samples even more remarkable. The occurrence of high P/Fe ratios in seven separate, geographically widespread successions (see supplementary information for formation details) supports our assertion that the observed high P/Fe ratios reflect global conditions during glacial periods in the Cryogenian rather than conditions unique to isolated basins.

Stage 4 spans the Paleoproterozoic through the Archean (1.7-3.0 Ga) and is represented by IF and distal hydrothermal sediments from 24 localities. The $P/Fe_{(100)}$ ratio in Stage 4 is

0.37 with a range from <1 to 2.9 and standard deviation of 0.42. This average P/$\mathrm{Fe}_{(100)}$ ratio is approximately equal to that found in early and middle Phanerozoic-aged rocks but significantly below ratios found in IF deposited during the 'Snowball Earth' glacial period. Dissolved silica levels in the Archean and Paleoproterozoic oceans may have been as low as cristobalite saturation (~0.67 mM) but were more likely near amorphous silica saturation (~2.2 mM) (Maliva et al., 2005; Siever, 1992). Correspondingly, phosphate concentrations in the Earth's early oceans are estimated to have been, at minimum, equivalent to Phanerozoic levels but were more likely several times higher (~4 times assuming 2.2 mM Si). However, since most of the Archean and early Proterozoic samples in our compilation contain mixed valence Fe oxides, some caution should be exercised when making comparisons to exclusively ferric iron-dominated rocks (see supplementary information).

Changes in the global biogeochemical cycle of Phosphorous can be related to the evolution of Earth's surface conditions. It is likely that the major removal fluxes for phosphate from modern oceans were attenuated during the Precambrian. Ferric oxyhydroxides represent a substantial sink in modern oceans (Wheat et al., 1996), but the importance of this sink would have been lower in the Precambrian because of less phosphate sorption onto ferric oxides at high dissolved silica concentrations. In addition, substantial portions of the deep ocean were likely anoxic prior to and even during the Neoproterozoic (Canfield et al., 2008), which would have removed the large phosphate sink associated with ferric oxyhydroxide formation during off-axis hydrothermal alteration of basalts (Wheat et al., 1996). Perhaps more importantly, the formation of carbonate fluorapatite (CFA) during early diagenesis, the largest marine phosphate sink today (Ruttenberg and Berner, 1993), was likely much less effective during the early Precambrian. CFA solubility scales with carbonate alkalinity (Jahnke, 1984), which was almost certainly high prior to the onset of enzymatic carbonate formation in the late Neoproterozoic (Ridgwell and Zeebe, 2005). Lastly, high marine phosphate concentrations during the extensive Cryogenian glaciations are expected, given that weathering rates in modern glaciated settings are higher than those in comparable unglaciated catchments (Föllmi et al., 2009). Enhanced post and syn-glacial phosphorous delivery to marine systems results in part from an elevated detrital flux to and high dissolution rates within proglacial environments (Föllmi et al., 2009). Importantly, in the Neoproterozoic, prior to soil stabilization by vascular plants, the temporal extent of enhanced phosphorous delivery from glaciated catchments was likely much greater than in the Pleistocene.

Since phosphorous is believed to be the ultimate nutrient controlling marine primary productivity on geological timescales (Tyrrell, 1999), elevated marine phosphate concentrations should lead to higher levels of organic matter production and increased carbon burial. However, because of high biological metal demands, especially in diazotrophic ($N_2$-fixing) organisms, trace elements may also limit primary productivity. Non-ferrous trace-element stress is likely to have been severe in Earth’s early oceans. Under an essentially anoxic atmosphere during the Archean there would have been limited continental weathering and delivery of dissolved redox-sensitive metals to the oceans (Scott et al., 2008) (e.g., Co, Cd, Cu, Mo, and V, which are common cofactors and play a crucial role in many major metabolic processes, including nitrogen assimilation and fixation). Our study points to high phosphate concentrations in the Archean and Paleoproterozoic oceans, thereby strengthening earlier arguments asserting that non-ferrous trace metals, rather than phosphorus, were the most important factors limiting carbon fixation in the Earth's early biosphere. Under a later oxidizing atmosphere and widespread euxinic (anoxic and sulfidic) or oxic conditions in the ocean, trace element stress is also possible[24]. For instance, trace metals (Fe) appear to be limiting nitrogen fixation in regions of the modern ocean (Martin, 1990; Wu et al., 2000).

We suggest that a combination of upwelling Fe-rich waters (Canfield et al., 2008) and significantly elevated marine P concentrations following the "Snowball Earth" glaciations would have caused a nutrient surplus—stimulating high rates of primary productivity and increased organic carbon burial. Unprecedented continental phosphorous fluxes would be expected following these glaciations (during post-glacial and interglacial time periods), given the extraordinary extent and duration of Cryogenian ice cover and the high levels of phosphorus delivery expected from glaciated catchments. Persistently high carbonate-carbon isotope values for significant time periods of the Cryogenian (Halverson et al., 2005) confirm this increase in organic carbon burial. Additionally, perturbations to the carbon cycle connected to the "Snowball Earth" events, for instance extensive methane calthrate release, may have muted the carbonate-carbon isotope signature for high post-glacial organic carbon burial (Hoffman and Schrag, 2002; Jiang et al., 2003). A long-lived, glacially induced nutrient surplus and a corresponding organic carbon burial event would have resulted in a shift to more oxidizing ocean-atmosphere conditions in the late Neoproterozoic, since net burial of organic carbon results in a corresponding rise in atmospheric $O_2$ (Holland, 2006). The evolution and ecological expansion of metazoans is largely dependent on the oxidation state of marine systems (Knoll and Carroll, 1999). Therefore, this redox shift could have paved the way for the rise of metazoans — providing a mechanistic explanation for the intimate link (Cohen et al., 2009; Hoffman and Schrag, 2002; Love et al., 2008) between the 'Snowball Earth' events and early animal evolution.

### Methods

Data in the compilation reflect our analytical efforts and a literature survey and include distal hydrothermal sediments and samples from iron formations (See SI, Table 1). The criteria used to filter the data are outlined in the supplementary information. The new trace and major element concentrations were determined using a ThermoFinnigan *Element II* ICP-MS operated at Woods Hole Oceanographic Institution following a three-acid digest. Analytical precision and accuracy for our measurements were checked by multiple analyses of the geostandards IF-G and BHVO-1, and reproducibility was better than 5%. Reproducibility of literature data is estimated to be better than 10%. See SI for additional method details.

## References

Arvidson, R.S., Mackenzie, F.T., Guidry, M.W., 2006. MAGic: A Phanerozoic Model for the Geochemical Cycling of Major Rock-Forming Components. American Journal of Science 306, 135–190.

Bjerrum, C.J., Canfield, D.E., 2002. Ocean productivity before about 1.9 Gyr ago limited by phosphorus adsorption onto iron oxides. Nature 417, 159-162.

Canfield, D.E., Poulton, S.W., Knoll, A.H., Narbonne, G.M., Ross, G., Goldberg, T., Strauss, H., 2008. Ferruginous conditions dominated later neoproterozoic deep-water chemistry. Science 321, 949-952.

Cohen, P.A., Knoll, A.H., Kodner, R.B., 2009. Large spinose microfossils in Ediacaran rocks as resting stages of early animals. Proceedings of the National Academy of Sciences 106 6519-6524.

Edmonds, H.N., German, C.R., 2004. Particle geochemistry in the Rainbow hydrothermal plume, Mid-Atlantic Ridge. Geochimica et Cosmochimica Acta 68, 759-772.

Feely, R.A., Trefry, J.H., Lebon, G.T., German, C.R., 1998. The relationship between P/Fe and V/Fe ratios in hydrothermal precipitates and dissolved phosphate in seawater. Geophysical Research Letters 25, 2253-2256.

Föllmi, K.B., Hosein, R., Arn, K., Steinmann, P., 2009. Weathering and the mobility of phosphorus in the catchments and forefields of the Rhône and Oberaar glaciers, central Switzerland: Implications for the global phosphorus cycle on glacial–interglacial timescales. Geochimica et Cosmochimica Acta 73, 2252-2282.

Halverson, G.P., Hoffman, P.F., Schrag, D.P., A.C., M., H.N., R., 2005. Toward a Neoproterozoic composite carbon-isotope record Geological Society of America Bulletin 117, 1181-1207.

Hoffman, P.F., Schrag, D.P., 2002. The Snowball Earth hypothesis: Testing the limits of global change. Terra Nova 14, 129-155.

Holland, H.D., 1984. The Chemical Evolution of the Atmosphere and Oceans Princeton University Press, Princeton, NJ.

Holland, H.D., 2006. The oxygenation of the atmosphere and oceans. Philosophical Transactions of the Royal Society B-Biological Sciences 361, 903-915.

Howarth, R.W., 1988. Nutrient Limitation of Net Primary Production in Marine Ecosystems. Annual Review of Ecology and Systematics 19, 89-110.

Jahnke, R.A., 1984. The synthesis and solubility of carbonate fluorapatite. American Journal of Science 284, 58-78.

Jiang, G., Kennedy, M.J., Christie-Blick, N., 2003. Stable isotope evidence for methane seeps in Neoproterozoic postglacial cap carbonates. Nature 426, 822-826.

Knoll, A.H., Carroll, S.B., 1999. Early animal evolution: Emerging views from comparative biology and geology. Science 284, 2129 - 2137.

Konhauser, K.O., Lalonde, S.V., Amskold, L., Holland, H.D., 2007. Was there really an Archean phosphate crisis? Science 315, 1234-1234.

Konhauser, K.O., Pecoits, E., Lalonde, S.V., Papineau, D., Nisbet, E.G., Barley, M.A., Arndt, N.T., Zahnle, K., Kamber, B.S., 2009. Oceanic nickel depletion and a methanogen famine before the Great Oxidation Event. Nature 458, 750-753.

Love, G.D., Grosjean, E., Stalvies, C., Fike, D.A., Grotzinger, J.P., A.S., B., Kelly, A.E., Bhatia, M., W., M., Snape, C.E., Bowring, S.A., D.J., C., R.E., S., 2008. Fossil steroids record the appearance of Demospongiae during the Cryogenian period. Nature 457, 718-721.

Maliva, R.G., Knoll, A.H., Simonson, B.M., 2005. Secular change in the Precambrian silica cycle: Insights from chert petrology. Geological Society of America Bulletin 117, 835-845.

Martin, J., 1990. Glacial-interglacial CO2 change: The iron hypothesis. Paleoceanography 5, 1-13.

Poulton, S.W., Canfield, D.E., 2006. Co-diagenesis of iron and phosphorus in hydrothermal sediments from the southern East Pacific Rise: Implications for the evaluation of paleoseawater phosphate concentrations. Geochimica et Cosmochimica Acta 70, 5883-5898.

Racki, G., Cordey, F., 2000. Radiolarian palaeoecology and radiolarites: is the present the key to the past? Earth-Science Reviews 52, 83-120.

Ridgwell, A., Zeebe, R.E., 2005. The role of the global carbonate cycle in the regulation and evolution of the Earth system. Earth and Planetary Science Letters 234, 299-315.

Ruttenberg, K.C., Berner, R.A., 1993. Authigenic apatite formation and burial in sediments from non-upwelling, continental-margin environments. Geochimica et Cosmochimica Acta 57, 991-1007.

Scott, C., Lyons, T.W., A., B., Shen, Y., Poulton, S.W., Chu, X., Anbar, A.D., 2008. Tracing the stepwise oxygenation of the Proterozoic ocean Nature 452, 457-460.
Siever, R., 1992. The Silica Cycle in the Precambrian. Geochimica et Cosmochimica Acta 56, 3265-3272.

Tyrrell, T., 1999. The relative influences of nitrogen and phosphorus on oceanic primary production. Nature 400, 525-531.

Wheat, C.G., Feely, R.A., Mottl, M.J., 1996. Phosphate removal by oceanic hydrothermal processes: An update of the phosphorus budget in the oceans. Geochimica et Cosmochimica Acta 60, 3593-3608.

Wu, J.F., Sunda, W., Boyle, E.A., Karl, D.M., 2000. Phosphate depletion in the western North Atlantic Ocean. Science 289, 759-762.

## Figures and Figure Legends

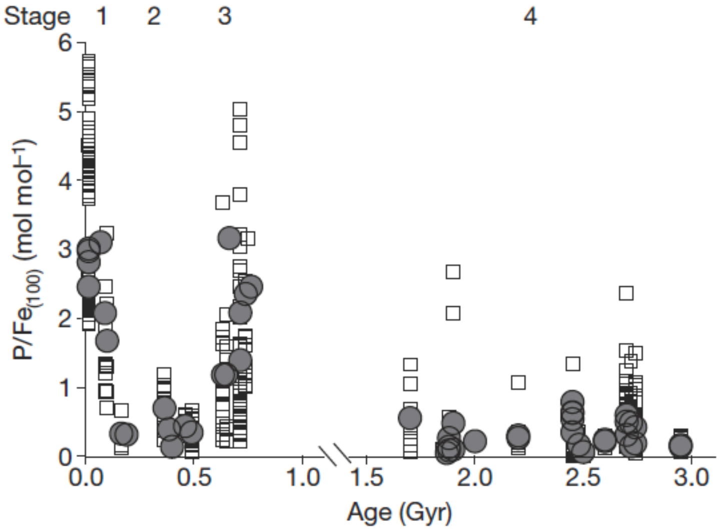

Figure 4.1. A.) P/Fe molar ratios through time in Fe oxide-rich distal hydrothermal sediments and iron formations with low amounts of siliciclastic input. Open squares are individual samples and solid circles are formation averages. The P/Fe ratio reflects the size of the marine phosphate reservoir; phosphate sorption onto ferric oxyhydroxides follows a distribution coefficient ($K_D$) relationship. The ratio is also influenced by the concentration of dissolved silica, since phosphate and silica-hydroxides compete for sorption sites on ferric oxyhydroxides oxides. Two outliers are not shown (8.6 at 90 Ma and 6.8 at 750 Ma). See SI for a box-plot view of the data.

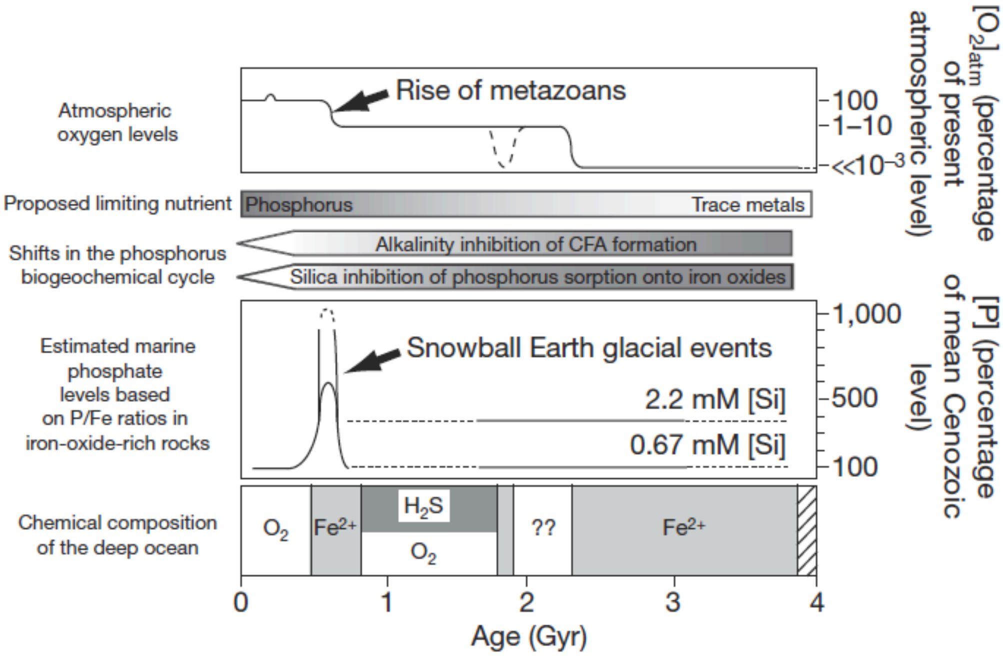

Figure 4.2. Model for the co-evolution of atmospheric and oceanic redox state and limiting nutrients for marine primary productivity. The redox model is from Canfield (2005) and Holland (2006). Phosphate concentrations are extrapolated from average P/Fe ratios for individual formations. Our compilation of P/Fe data suggests that there were elevated seawater phosphate concentrations in the Precambrian and a peak in phosphate levels associated with the Neoproterozoic Snowball Earth glaciations. This late Precambrian increase in dissolved P concentration may have stimulated high rates of organic carbon burial and a corresponding increase in atmospheric oxygen levels — paving the way for the rise of metazoans.

## Appendix: The Evolution of the Marine Phosphate Reservoir

### Sample Information

Our compiled P/Fe ratios for iron oxide-rich sediments come from new geochemical analyses and a literature survey (Appendix Table 1). We present data for sediments that contain greater than 5% Fe, with the iron predominantly in the form of oxides. We avoided sediments with a significant fine-grained siliciclastic component by selecting only those with Fe/Al ratios > 5. In addition, only samples with Fe/Mn ratios > 5 are presented to avoid samples in which phosphate might be associated with Mn oxides. Samples containing significant amounts of siderite and pyrite, as determined by XRD for this study and either XRD or petrographic work for literature values, were also excluded. Samples with visible signs of epigenetic fluid flow (e.g., extensive veining, disruption of sedimentary features, minerals cross-cutting sedimentary layers) were also avoided. We aimed to analyze iron-rich sediments where ferrous iron oxidation occurred in the marine water column; we avoided nodules and clasts that may have formed during depositional hiatuses and brine and subsurface precipitates, which may have different P/Fe ratios than typical marine plume fallout-dominated sediment. These basic filters leave two types of sediments: iron formations and distal hydrothermal sediments. There are several recent, extensive reviews of the depositional setting of iron formations (Klein, 2005; Klein and Bricker, 1977) and distal hydrothermal sediments (Grenne and Slack, 2003a, b; Slack et al., 2007). We present data from 32 iron formations and 14 distal hydrothermal units. Sample locations, ages of the deposits, and references are presented in SI Table 1.

## Extended Methods

Major element compositions were determined following previously described methods (Planavsky et al., 2009). In summary, 10 to over 100 grams of cleaned drill-core or fresh outcrop material were crushed between two plexiglass discs inside a Teflon bag using a hydraulic press. Rock chips were cleaned through several rinses with deionized water during ultrasonification. The cleaned material was powdered in an agate shatter box. In some cases, subsamples containing no significant detrital components (i.e., siliciclastic component) were selectively isolated from the crushed chips for analysis using a binocular microscope.

Sample powders were weighed in 5 mL Teflon beakers and dissolved using 2 mL of concentrated trace metal grade $HNO_3$ with 2 mL of concentrated HF. After evaporation on a hot plate at 50°C, complete dissolution and Fe oxidation were achieved by a second evaporation step using 4 mL of *aqua regia*. The dry residue was then redissolved in 4 mL of 6N HCl and 1 drop of $H_2O_2$ by heating at 40°C in a closed vessel. Organic carbon was not attacked by this procedure but was always present in only trace concentrations.

Element concentrations were determined using a Woods Hole Oceanographic Institution ThermoFinnigan *ElementII* high-resolution inductively coupled plasma mass-spectrometer (ICP-MS) with quartz spray chamber in a medium resolution mode. Instrumental sensitivity and matrix effects were corrected using an In internal standard. The analytical precision and accuracy of our measurements were checked by multiple analyses of the geostandards IF-G, BCR-1, and BHVO-1. Reproducibility was better than 95% for our analyses. Reproducibility for the literature data is estimated to be better than 90%.

## P/Fe ratios in iron oxide-rich rocks as a proxy for seawater phosphate concentrations

P/Fe ratios in modern hydrothermal plume particles scale linearly as a function of ambient dissolved phosphate concentrations [i.e., conform to a distribution coefficient ($K_D$) model] (Feely et al., 1998). Therefore, in a given solution, dissolved phosphate concentrations are equal to the P/Fe ratios in precipitated ferric oxyhydroxide divided by a distribution coefficient: $[P_D] = (1/K_D)*(P_{ads}/Fe)$ (ref. 8). Phosphate sorption appears to be independent of oxidation rate (Konhauser et al., 2007). Although phosphate and Fe(III)-oxide interactions are commonly discussed as a simple adsorption process, it appears that in modern marine systems phosphate is partially co-precipitated with Fe, possibly as a solid solution of $CaHFe(PO_4)_2$ with iron oxyhydroxides (Lilley et al., 1995). The observation that P-Fe ratios in modern ferric oxide particles can be described by a distribution coefficient relationship does not necessitate exclusively 'Langmuir type' adsorption behavior; rather it simply reflects the fact that phosphorous is sequestered into iron oxides as a function of dissolved phosphate in a predictable manner consistent with both field[9] and experimental[8] data. Despite some remaining uncertainty about the co-precipitation mechanism, the fact that a single distribution coefficient adequately describes P/Fe ratios of modern metalliferous hydrothermal particles worldwide[7] testifies to the robustness of the P/Fe proxy for local dissolved phosphorous concentrations and the relative insensitivity to other variables such as temperature, depth, Fe oxidation rate, and pH.

There is strong evidence that P/Fe ratios in hydrothermal ferric-oxide particles are invariant during sedimentation (e.g., Edmonds and German, 2004) and references therein). Therefore, differences in depositional environment (e.g., different particle setting rates) will not have a strong influence on the P/Fe ratios of Fe oxide-rich sediments. Particle growth during the initial stages of Fe oxidation will minimize the chances of significant alteration of P/Fe ratios during particle transport. During particle formation there is a rapid transformation from nanoparticulates to particles tens and even hundreds of microns in size (e.g., Edmonds and German, 2004). Settling iron oxide particles will therefore have a thin outer surface layer that may remain reactive, while a larger core will stay largely unreactive. During reductive dissolution of ferric oxides in an anoxic water column the P-Fe system is expected to behave congruently. However, this process may lower the particle P/Fe ratio if some Fe(II) is retained.

Dissolved Si can inhibit phosphate sorption to iron oxides. Iron-silica co-precipitation decreases the point of zero net charge (PZNC) of precipitating ferric oxyhydroxides (Konhauser et al., 2007; Schwertmann and Fechter, 1982), rendering them less reactive to dissolved anions. At elevated dissolved Si concentrations, P/Fe ratios still reflect ambient phosphate concentrations (i.e., conform to a distribution coefficient model) but with $K_D$

values that may decrease by an order of magnitude with varying dissolved Si concentration (Appendix Fig. 4.1). It is essential, therefore, to consider the evolution of the Si cycle when interpreting P/Fe ratios in iron oxide-rich sediments. Importantly, with the exception of silica, phosphate generally outcompetes other important marine anions for sorption sites on ferric oxides at neutral or alkaline pH. In other words, the concentration of phosphate may have a large effect on the sorption of other oxyanions to ferric oxides (e.g., sulphate or vanadate), but other oxyanions have little effect on phosphate sorption(Hawke et al., 1989; Yao and Millero, 1996,). Solution pH can have a strong effect on phosphate sorption, as the Fe oxide surface protonates with decreasing pH and the overall surface becomes more positively charged. However, at the range of pH conditions expected in marine settings, this effect is minor compared to the inhibition of phosphate sorption when dissolved Si concentrations are above ~0.5 mM. Similarly, the effect of temperature on phosphate sorption to ferric oxides is minimal relative to the effect of varying dissolved Si levels (Konhauser et al., 2007).

P/Fe ratios in modern iron oxide-rich sediments are constant or decrease during early diagenesis (on million year time scales). During burial diagenesis (pre-metamorphic conditions over time scales of tens of millions of years) P/Fe ratios in iron oxide-rich rocks do not follow a systematic, diagenetic trend. Instead, the rocks appear to record trends that can be linked with shifts in marine phosphate concentrations (e.g., Poulton and Canfield, 2006)). Available evidence suggests that microbially driven ferric iron reduction is also unlikely to significantly elevate sediment P/Fe ratios. For instance, siderite-rich intervals of the early and late Paleoproterozoic iron formations in the Transvaal and Mistassini basins, respectively, contain lower P/Fe ratios than haematite-rich horizons (Webb et al., 2003). Siderite precipitation in these iron formations was likely driven largely by diagenetic microbial iron reduction, suggesting that organic matter remineralization with Fe(III) did not result in a net increase in P/Fe ratios. Instead, the result is a decrease, making our interpretations, if anything, conservative.

Magnetite is a common component of many Archean and early Proterozoic iron formations. It has been suggested that magnetite precipitation occurred during early diagenesis. Early diagenetic magnetite formation may cause a decrease in sediment P/Fe ratios if Fe is retained without corresponding P retention during reductive ferric oxide dissolution or if magnetite formation occurs through a reaction with seawater derived Fe(II) and ferric oxides. However, a large portion of the magnetite in Precambrian iron formations appears to have formed during metamorphism. Magnetite can form at the expense of haematite during prograde metamorphism without an organic reductant[19]. If magnetite formation is linked with a carbon reductant the ratio of organic matter to iron oxides must be very low in order to retain an original haematite-magnetite mineralogy; 1g of organic carbon can convert 80g of haematite to magnetite. Under most metamorphic scenarios for iron formations P/Fe ratios should be essentially rock-buffered, and during metamorphism phosphorous typically displays similar properties as fluid-immobile components such as Ti, Zr, Hf, and Y. Metamorphism, therefore, does not inherently compromise the ability of P/Fe ratios to serve as tracers of seawater phosphate concentrations.

Given that iron will be more mobile than phosphorous during late-stage diagenesis, later-stage alteration and ore-forming processes may lower P/Fe ratios. For example, P/Fe ratios in the ore zone and altered ca. 2.5 Ga iron formation in the Hamersley Province are approximately half of those in the best-preserved samples of the same iron formation (Webb et al., 2003). Even though we have sought to avoid severely altered samples, secondary iron enrichment may be one factor (along with varying water depths of deposition and relatively short-term temporal shifts in phosphate reservoir size) causing the large range of P/Fe for some time intervals in the early Precambrian. Therefore, P/Fe ratios in iron oxide-rich rocks that suggest high Precambrian marine phosphate concentrations are unlikely to be linked to diagenetic alteration. As such, the collective evidence suggests that P/Fe ratios in ferruginous sediments can track first-order shifts in dissolved phosphorous concentrations through time if dissolved silica levels can be estimated.

### Estimates of dissolved Si concentrations

Estimates of Precambrian dissolved silica concentrations come from petrographic studies and thermodynamic considerations. Without enzymatic silica removal, the marine silica cycle was largely controlled by inorganic sedimentary reactions (Siever, 1992). Considerations regarding silica sorption on clay and zeolite minerals and the style and rate of early diagenetic silica precipitation suggest that silica concentrations were at least at saturation with respect to the silicon dioxide polymorph cristobalite (~0.67 mM) (Siever, 1992), which equates to about six times modern seawater silica levels. The lack of evidence for abundant silica precipitation in the water column or at the sediment-water interface in the Precambrian suggests that ambient seawater silica levels rarely greatly exceeded amorphous silica saturation level (~2.2 mM). There are, however, examples of replacement and pore-water silica precipitation at the sediment-water interface in the early Precambrian (Maliva et al., 2005). Therefore, locally—or more extensively but for short time periods—dissolved silica concentrations in the Precambrian likely exceeded amorphous silica saturation (Maliva et al., 2005).

Enzymatic silica removal altered the marine silica cycle dramatically. The earliest siliceous organisms are from the Cryogenian (Macdonald et al., 2010). However, Neoproterozoic biotic silica is rare; primary siliceous microfossils have so far been reported only from one formation, and they are a trace component in sedimentary rocks. Therefore, these organisms are unlikely to have had a dramatic effect on the global silica cycle in contrast to that of Phanerozoic biota. Evolution of radiolarians (siliceous protists) and siliceous sponges in the latest Neoproterozoic or early Cambrian likely decreased marine silica concentrations more appreciably[23]. However, since these organisms are heterotrophic, they would not have caused silica burial rates comparable to those of photosynthetic siliceous plankton (Racki and Cordey, 2000; Siever, 1992). Estimates of dissolved silica concentrations prior to diatom radiation, based largely on petrographic studies, range from five to ten times modern levels (Grenne and Slack, 2003b; Racki and Cordey, 2000; Siever, 1992). We have taken a conservative estimate and assumed that dissolved Si concentrations were about six times modern levels, at cristobalite saturation. This estimate is consistent with dissolved Si concentrations being buffered by silica-clay/zeolite mineral interactions. In contrast, the diatom radiation reduced dissolved marine silica concentrations dramatically. We assumed a stepped decrease in marine silica concentration associated with diatom proliferation, but there may have been a protracted expansion of diatoms from the late Jurassic through the Cretaceous. Either possibility has little impact on our first-order conclusions.

## References

Edmonds, H.N., German, C.R., 2004. Particle geochemistry in the Rainbow hydrothermal plume, Mid-Atlantic Ridge. Geochimica et Cosmochimica Acta 68, 759-772.

Feely, R.A., Trefry, J.H., Lebon, G.T., German, C.R., 1998. The relationship between P/Fe and V/Fe ratios in hydrothermal precipitates and dissolved phosphate in seawater. Geophysical Research Letters 25, 2253-2256.

Grenne, T., Slack, J.F., 2003a. Bedded jaspers of the Ordovician Lokken ophiolite, Norway: seafloor deposition and diagenetic maturation of hydrothermal plume-derived silica-iron gels. Mineralium Deposita 38, 625-639.

Grenne, T., Slack, J.F., 2003b. Paleozoic and Mesozoic silica-rich seawater: Evidence from hematitic chert (jasper) deposits. Geology 31, 319-322.

Hawke, D., Carpenter, P., Hunter, K., 1989. Competitive Adsorption of Phosphate on Goethite in Marine Electrolytes. Environmental Science and Technology 23, 197-191.

Klein, C., 2005. Some Precambrian banded iron-formations (BIFs) from around the world: Their age, geologic setting, mineralogy, metamorphism, geochemistry, and origin. American Mineralogist 90, 1473-1499.

Klein, C., Bricker, O.P., 1977. Some Aspects of Sedimentary and Diagenetic Environment of Proterozoic Banded Iron-Formation. Economic Geology 72, 1457-1470.
Konhauser, K.O., Lalonde, S.V., Amskold, L., Holland, H.D., 2007. Was there really an Archean phosphate crisis? Science 315, 1234-1234.

Lilley, M.D., Feely, R.A., Trefry, J.H., 1995. Chemical and biological transformations in hydrothermal plumes, in: S. E. Humphris, e.a. (Ed.), Seafloor Hydrothermal Systems: Physical, Chemical, Biological, and Geological. American Geophysical Union, pp. 369 – 391.

Macdonald, F.A., Cohen, P.A., Dudas, F.O., Schrag, D.P., 2010. Early Neoproterozoic scale microfossils in the Lower Tindir Group of Alaska and the Yukon Territory. Geology 38, 143-146.

Maliva, R.G., Knoll, A.H., Simonson, B.M., 2005. Secular change in the Precambrian silica cycle: Insights from chert petrology. Geological Society of America Bulletin 117, 835-845.

Planavsky, N., Rouxel, O., Bekker, A., Shapiro, R., Fralick, P., Knudsen, A., 2009. Iron-oxidizing microbial ecosystems thrived in late Paleoproterozoic redox-stratified oceans. Earth and Planetary Science Letters 286, 230-242.

Poulton, S.W., Canfield, D.E., 2006. Co-diagenesis of iron and phosphorus in hydrothermal sediments from the southern East Pacific Rise: Implications for the evaluation of paleoseawater phosphate concentrations. Geochimica et Cosmochimica Acta 70, 5883-5898.

Racki, G., Cordey, F., 2000. Radiolarian palaeoecology and radiolarites: is the present the key to the past? Earth-Science Reviews 52, 83-120.

Schwertmann, U., Fechter, H., 1982. The Point of Zero Charge of Natural and Synthetic Ferrihydrites and Its Relation to Adsorbed Silicate. Clay Minerals 17, 471-476.

Siever, R., 1992. The Silica Cycle in the Precambrian. Geochimica et Cosmochimica Acta 56, 3265-3272.

Slack, J.F., Grenne, T., Bekker, A., Rouxel, O.J., Lindberg, P.A., 2007. Suboxic deep seawater in the late Paleoproterozoic: Evidence from hematitic chert and iron formation related to seafloor-hydrothermal sulfide deposits, central Arizona, USA. Earth and Planetary Science Letters 255, 243-256.

Webb, A.D., Dickens, G.R., Olivera, N.H.S., 2003. From banded iron-formation to iron ore: geochemical and mineralogical constraints from across the Hamersley Province, Western Australia Chemical Geology 197, 215 – 251.

Yao, W., Millero, F.J., 1996,. Adsorption of phosphate on manganese dioxide in seawater. Environmental Science and Technology 30, 536-541.

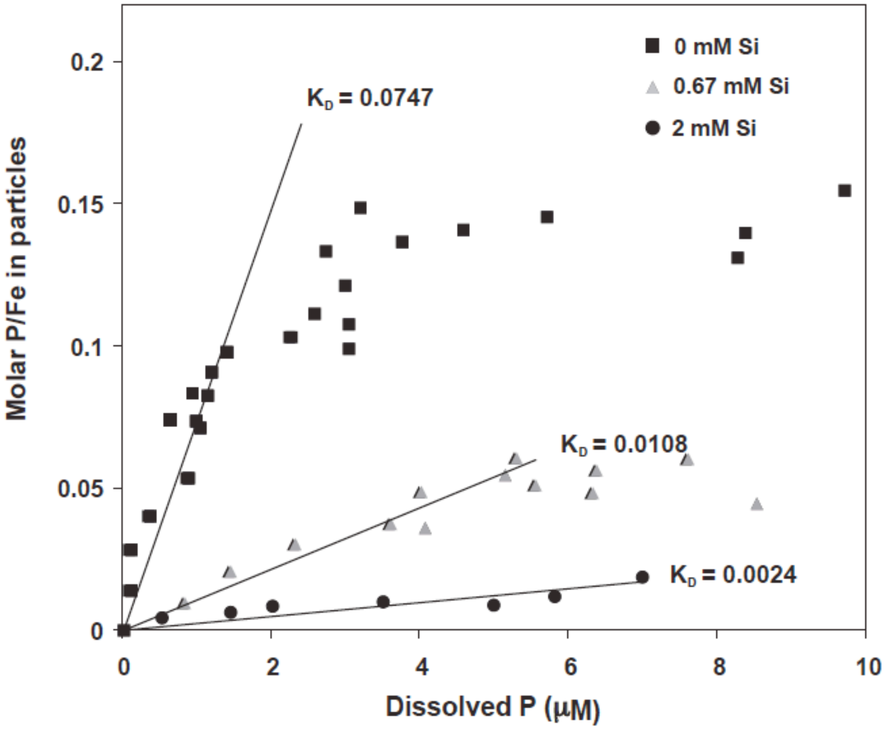

Appendix Figure 4.3. Experiments on the co-precipitation of phosphate and ferric oxides at varying Si concentrations. Experiments were performed at 25°C, at pH = 8 with 0.2 mM Fe(II). Distribution coefficients (KD) define the equilibrium concentrations for solid-phase and dissolved phosphate. It is apparent from the co-precipitation experiments that the particles incorporate decreasing amounts of phosphate with increasing dissolved silica concentrations. Modified from Konhauser and others 2007.

Appendix Table 1. Major element data for Fe oxide-rich distal hydrothermal sediments and iron formations.

| Sample | P (%) | Fe (%) | Mn (%) | Al (%) | Fe/Al | Fe/Mn | P/Fe*(100) |
|---|---|---|---|---|---|---|---|
| **0.01-0.02 Ga - Site 597, DSDP, Leg 92, SI Table 1 Ref. 1** | | | | | | | |
| **average** | **0.12** | **8.71** | **1.37** | **0.44** | **20** | **6** | **2.46** |
| 1-2, 13 | 0.20 | 9.27 | 1.31 | 0.61 | 15 | 7 | 3.83 |
| 1-2, 72 | 0.12 | 7.49 | 1.13 | 0.50 | 15 | 7 | 2.89 |
| 1-3, 13 | 0.14 | 9.89 | 1.40 | 0.54 | 18 | 7 | 2.46 |
| 1-3, 93 | 0.13 | 9.77 | 1.49 | 0.46 | 21 | 7 | 2.31 |
| 2-1, 23 | 0.12 | 9.08 | 1.31 | 0.48 | 19 | 7 | 2.42 |
| 2-1, 73 | 0.13 | 9.50 | 1.41 | 0.47 | 20 | 7 | 2.41 |
| 2-1, 133 | 0.07 | 6.24 | 1.02 | 0.29 | 22 | 6 | 2.14 |
| 2-2, 73 | 0.17 | 13.97 | 2.52 | 0.61 | 23 | 6 | 2.25 |
| 2-2, 133 | 0.07 | 6.85 | 1.32 | 0.24 | 28 | 5 | 1.95 |
| 2-5, 73 | 0.05 | 5.07 | 0.74 | 0.22 | 23 | 7 | 1.92 |
| **0.01-0.02 Ga - Site 598, DSDP, Leg 92, SI Table 1 Ref. 1** | | | | | | | |
| **average** | **0.11** | **6.75** | **1.09** | **0.36** | **24** | **6** | **2.98** |
| 1-2, 39 | 0.15 | 5.01 | 0.98 | 0.66 | 8 | 5 | 5.43 |
| 1-2, 49 | 0.17 | 6.30 | 1.17 | 0.74 | 9 | 5 | 4.89 |
| 1-2, 59 | 0.26 | 9.42 | 1.67 | 1.12 | 8 | 6 | 4.90 |
| 1-2, 69 | 0.38 | 13.22 | 2.35 | 1.75 | 8 | 6 | 5.24 |
| 1-2, 102 | 0.46 | 14.31 | 2.40 | 1.87 | 8 | 6 | 5.73 |
| 1-2, 109 | 0.42 | 13.36 | 2.19 | 1.87 | 7 | 6 | 5.68 |
| 1-2, 119 | 0.34 | 13.30 | 2.17 | 1.52 | 9 | 6 | 4.65 |
| 1-2, 129 | 0.26 | 10.59 | 1.76 | 1.15 | 9 | 6 | 4.38 |
| 1-2, 139 | 0.17 | 6.98 | 1.15 | 0.68 | 10 | 6 | 4.34 |
| 1-2, 149 | 0.12 | 4.83 | 0.81 | 0.44 | 11 | 6 | 4.44 |
| 1-3, 9 | 0.08 | 3.59 | 0.61 | 0.32 | 11 | 6 | 4.22 |
| 1-3, 19 | 0.08 | 3.42 | 0.58 | 0.29 | 12 | 6 | 4.16 |
| 1-3, 29 | 0.09 | 3.76 | 0.65 | 0.35 | 11 | 6 | 4.32 |
| 1-3, 39 | 0.12 | 5.13 | 0.87 | 0.48 | 11 | 6 | 4.04 |
| 1-3, 49 | 0.18 | 7.78 | 1.30 | 0.79 | 10 | 6 | 4.08 |
| 1-3, 59 | 0.17 | 7.86 | 1.30 | 0.78 | 10 | 6 | 3.95 |
| 1-3, 69 | 0.18 | 8.68 | 1.38 | 0.81 | 11 | 6 | 3.78 |
| 1-3,79 | 0.12 | 5.98 | 0.97 | 0.55 | 11 | 6 | 3.74 |
| 1-3, 89 | 0.10 | 4.58 | 0.73 | 0.40 | 12 | 6 | 3.78 |
| 1-3, 119 | 0.12 | 3.88 | 0.61 | 0.31 | 13 | 6 | 5.39 |
| 1-4, 29 | 0.12 | 4.59 | 0.69 | 0.34 | 14 | 7 | 4.75 |
| 1-4, 39 | 0.26 | 8.68 | 1.25 | 0.60 | 14 | 7 | 5.36 |
| 1-4,49 | 0.35 | 11.06 | 1.65 | 0.87 | 13 | 7 | 5.66 |
| 1-4, 59 | 0.22 | 7.73 | 1.15 | 0.57 | 14 | 7 | 5.18 |
| 1-4, 69 | 0.10 | 4.03 | 0.60 | 0.28 | 14 | 7 | 4.56 |
| 1-4, 89 | 0.05 | 2.27 | 0.36 | 0.16 | 14 | 6 | 4.29 |
| 1-4,99 | 0.06 | 2.39 | 0.38 | 0.17 | 14 | 6 | 4.15 |
| 1-4, 109 | 0.05 | 2.18 | 0.34 | 0.16 | 14 | 6 | 4.14 |
| 1-4, 119 | 0.05 | 2.01 | 0.32 | 0.16 | 13 | 6 | 4.40 |
| 1-4, 129 | 0.08 | 3.39 | 0.51 | 0.24 | 14 | 7 | 4.15 |
| 1-4, 139 | 0.10 | 4.56 | 0.66 | 0.32 | 14 | 7 | 4.11 |
| 1-4, 149 | 0.11 | 4.55 | 0.66 | 0.35 | 13 | 7 | 4.20 |

| | | | | | | | |
|---|---|---|---|---|---|---|---|
| 2-3, 69 | 0.06 | 4.44 | 0.62 | 0.20 | 22 | 7 | 2.56 |
| 2-3, 79 | 0.06 | 4.22 | 0.63 | 0.18 | 24 | 7 | 2.52 |
| 2-3, 89 | 0.05 | 2.89 | 0.39 | 0.15 | 19 | 7 | 3.06 |
| 2-3, 99 | 0.05 | 3.54 | 0.49 | 0.16 | 22 | 7 | 2.65 |
| 2-3, 109 | 0.06 | 4.08 | 0.60 | 0.17 | 24 | 7 | 2.52 |
| 2-3, 119 | 0.06 | 4.82 | 0.74 | 0.19 | 25 | 7 | 2.36 |
| 2-3, 129 | 0.06 | 4.54 | 0.68 | 0.19 | 24 | 7 | 2.46 |
| 2-3, 139 | 0.07 | 4.99 | 0.77 | 0.21 | 24 | 6 | 2.49 |
| 2-3, 149 | 0.07 | 5.38 | 0.83 | 0.21 | 25 | 6 | 2.45 |
| 2-4, 9 | 0.07 | 5.25 | 0.79 | 0.21 | 25 | 7 | 2.44 |
| 2-4, 19 | 0.08 | 6.14 | 0.93 | 0.25 | 25 | 7 | 2.44 |
| 2-4, 39 | 0.07 | 5.20 | 0.79 | 0.23 | 23 | 7 | 2.50 |
| 2-4, 39 | 0.07 | 4.71 | 0.69 | 0.19 | 24 | 7 | 2.56 |
| 2-4, 59 | 0.07 | 5.57 | 0.83 | 0.20 | 28 | 7 | 2.33 |
| 2-4, 69 | 0.08 | 6.45 | 0.96 | 0.24 | 27 | 7 | 2.32 |
| 2-4, 79 | 0.07 | 5.46 | 0.80 | 0.21 | 26 | 7 | 2.31 |
| 2-4, 89 | 0.08 | 5.98 | 0.89 | 0.23 | 26 | 7 | 2.32 |
| 2-4, 99 | 0.08 | 6.57 | 0.96 | 0.23 | 29 | 7 | 2.17 |
| 2-4, 109 | 0.08 | 6.24 | 0.92 | 0.23 | 27 | 7 | 2.20 |
| 2-4, 119 | 0.07 | 5.76 | 0.89 | 0.23 | 26 | 6 | 2.22 |
| 2-4, 129 | 0.07 | 5.98 | 0.90 | 0.21 | 28 | 7 | 2.14 |
| 2-4, 139 | 0.08 | 7.01 | 1.02 | 0.26 | 27 | 7 | 2.16 |
| 2-5,9 | 0.08 | 6.79 | 1.01 | 0.25 | 27 | 7 | 2.20 |
| 2-5, 19 | 0.08 | 6.54 | 0.98 | 0.24 | 27 | 7 | 2.21 |
| 2-5, 29 | 0.08 | 6.84 | 1.01 | 0.25 | 28 | 7 | 2.16 |
| 2-5, 39 | 0.10 | 8.22 | 1.18 | 0.30 | 27 | 7 | 2.28 |
| 2-5, 49 | 0.10 | 8.09 | 1.18 | 0.29 | 28 | 7 | 2.25 |
| 2-5, 59 | 0.10 | 8.15 | 1.19 | 0.30 | 27 | 7 | 2.28 |
| 2-5, 69 | 0.09 | 7.75 | 1.20 | 0.25 | 31 | 6 | 2.12 |
| 2-5, 89 | 0.10 | 7.86 | 1.15 | 0.28 | 28 | 7 | 2.23 |
| 2-5, 109 | 0.10 | 8.03 | 1.21 | 0.31 | 26 | 7 | 2.29 |
| 2-5, 130 | 0.09 | 7.06 | 1.02 | 0.24 | 29 | 7 | 2.27 |
| 2-5, 139 | 0.09 | 7.02 | 1.04 | 0.25 | 28 | 7 | 2.21 |
| 2-5, 149 | 0.09 | 7.07 | 1.07 | 0.25 | 28 | 7 | 2.27 |
| 2-6, 9 | 0.08 | 6.79 | 1.03 | 0.24 | 28 | 7 | 2.23 |
| 2-6, 19 | 0.09 | 6.87 | 1.04 | 0.23 | 30 | 7 | 2.28 |
| 2-6, 29 | 0.09 | 6.81 | 1.02 | 0.24 | 28 | 7 | 2.25 |
| 2-6, 39 | 0.08 | 6.76 | 1.01 | 0.23 | 29 | 7 | 2.13 |
| 2-6, 49 | 0.08 | 6.75 | 1.02 | 0.24 | 28 | 7 | 2.19 |
| 2-6, 59 | 0.08 | 6.74 | 1.02 | 0.24 | 28 | 7 | 2.14 |
| 2-6, 69 | 0.09 | 6.77 | 1.04 | 0.25 | 27 | 7 | 2.26 |
| 2-6, 79 | 0.08 | 6.69 | 1.04 | 0.24 | 28 | 6 | 2.24 |
| 2-6, 89 | 0.10 | 7.98 | 1.28 | 0.30 | 27 | 6 | 2.30 |
| 2-6,99 | 0.09 | 7.46 | 1.16 | 0.27 | 28 | 6 | 2.22 |
| 2-6, 119 | 0.09 | 6.99 | 1.08 | 0.26 | 27 | 6 | 2.27 |
| 2-6, 139 | 0.09 | 6.87 | 1.08 | 0.26 | 26 | 6 | 2.26 |
| 2-6, 149 | 0.09 | 6.72 | 1.07 | 0.26 | 26 | 6 | 2.33 |
| 3-1,9 | 0.13 | 10.45 | 1.74 | 0.35 | 30 | 6 | 2.24 |
| 3-1, 19 | 0.12 | 10.24 | 1.71 | 0.29 | 36 | 6 | 2.06 |

| | | | | | | | |
|---|---|---|---|---|---|---|---|
| 2-3, 69 | 0.06 | 4.44 | 0.62 | 0.20 | 22 | 7 | 2.56 |
| 2-3, 79 | 0.06 | 4.22 | 0.63 | 0.18 | 24 | 7 | 2.52 |
| 2-3, 89 | 0.05 | 2.89 | 0.39 | 0.15 | 19 | 7 | 3.06 |
| 2-3, 99 | 0.05 | 3.54 | 0.49 | 0.16 | 22 | 7 | 2.65 |
| 2-3, 109 | 0.06 | 4.08 | 0.60 | 0.17 | 24 | 7 | 2.52 |
| 2-3, 119 | 0.06 | 4.82 | 0.74 | 0.19 | 25 | 7 | 2.36 |
| 2-3, 129 | 0.06 | 4.54 | 0.68 | 0.19 | 24 | 7 | 2.46 |
| 2-3, 139 | 0.07 | 4.99 | 0.77 | 0.21 | 24 | 6 | 2.49 |
| 2-3, 149 | 0.07 | 5.38 | 0.83 | 0.21 | 25 | 6 | 2.45 |
| 2-4, 9 | 0.07 | 5.25 | 0.79 | 0.21 | 25 | 7 | 2.44 |
| 2-4, 19 | 0.08 | 6.14 | 0.93 | 0.25 | 25 | 7 | 2.44 |
| 2-4, 39 | 0.07 | 5.20 | 0.79 | 0.23 | 23 | 7 | 2.50 |
| 2-4, 39 | 0.07 | 4.71 | 0.69 | 0.19 | 24 | 7 | 2.56 |
| 2-4, 59 | 0.07 | 5.57 | 0.83 | 0.20 | 28 | 7 | 2.33 |
| 2-4, 69 | 0.08 | 6.45 | 0.96 | 0.24 | 27 | 7 | 2.32 |
| 2-4, 79 | 0.07 | 5.46 | 0.80 | 0.21 | 26 | 7 | 2.31 |
| 2-4, 89 | 0.08 | 5.98 | 0.89 | 0.23 | 26 | 7 | 2.32 |
| 2-4, 99 | 0.08 | 6.57 | 0.96 | 0.23 | 29 | 7 | 2.17 |
| 2-4, 109 | 0.08 | 6.24 | 0.92 | 0.23 | 27 | 7 | 2.20 |
| 2-4, 119 | 0.07 | 5.76 | 0.89 | 0.23 | 26 | 6 | 2.22 |
| 2-4, 129 | 0.07 | 5.98 | 0.90 | 0.21 | 28 | 7 | 2.14 |
| 2-4, 139 | 0.08 | 7.01 | 1.02 | 0.26 | 27 | 7 | 2.16 |
| 2-5,9 | 0.08 | 6.79 | 1.01 | 0.25 | 27 | 7 | 2.20 |
| 2-5, 19 | 0.08 | 6.54 | 0.98 | 0.24 | 27 | 7 | 2.21 |
| 2-5, 29 | 0.08 | 6.84 | 1.01 | 0.25 | 28 | 7 | 2.16 |
| 2-5, 39 | 0.10 | 8.22 | 1.18 | 0.30 | 27 | 7 | 2.28 |
| 2-5, 49 | 0.10 | 8.09 | 1.18 | 0.29 | 28 | 7 | 2.25 |
| 2-5, 59 | 0.10 | 8.15 | 1.19 | 0.30 | 27 | 7 | 2.28 |
| 2-5, 69 | 0.09 | 7.75 | 1.20 | 0.25 | 31 | 6 | 2.12 |
| 2-5, 89 | 0.10 | 7.86 | 1.15 | 0.28 | 28 | 7 | 2.23 |
| 2-5, 109 | 0.10 | 8.03 | 1.21 | 0.31 | 26 | 7 | 2.29 |
| 2-5, 130 | 0.09 | 7.06 | 1.02 | 0.24 | 29 | 7 | 2.27 |
| 2-5, 139 | 0.09 | 7.02 | 1.04 | 0.25 | 28 | 7 | 2.21 |
| 2-5, 149 | 0.09 | 7.07 | 1.07 | 0.25 | 28 | 7 | 2.27 |
| 2-6, 9 | 0.08 | 6.79 | 1.03 | 0.24 | 28 | 7 | 2.23 |
| 2-6, 19 | 0.09 | 6.87 | 1.04 | 0.23 | 30 | 7 | 2.28 |
| 2-6, 29 | 0.09 | 6.81 | 1.02 | 0.24 | 28 | 7 | 2.25 |
| 2-6, 39 | 0.08 | 6.76 | 1.01 | 0.23 | 29 | 7 | 2.13 |
| 2-6, 49 | 0.08 | 6.75 | 1.02 | 0.24 | 28 | 7 | 2.19 |
| 2-6, 59 | 0.08 | 6.74 | 1.02 | 0.24 | 28 | 7 | 2.14 |
| 2-6, 69 | 0.09 | 6.77 | 1.04 | 0.25 | 27 | 7 | 2.26 |
| 2-6, 79 | 0.08 | 6.69 | 1.04 | 0.24 | 28 | 6 | 2.24 |
| 2-6, 89 | 0.10 | 7.98 | 1.28 | 0.30 | 27 | 6 | 2.30 |
| 2-6,99 | 0.09 | 7.46 | 1.16 | 0.27 | 28 | 6 | 2.22 |
| 2-6, 119 | 0.09 | 6.99 | 1.08 | 0.26 | 27 | 6 | 2.27 |
| 2-6, 139 | 0.09 | 6.87 | 1.08 | 0.26 | 26 | 6 | 2.26 |
| 2-6, 149 | 0.09 | 6.72 | 1.07 | 0.26 | 26 | 6 | 2.33 |
| 3-1,9 | 0.13 | 10.45 | 1.74 | 0.35 | 30 | 6 | 2.24 |
| 3-1, 19 | 0.12 | 10.24 | 1.71 | 0.29 | 36 | 6 | 2.06 |

| | | | | | | | |
|---|---|---|---|---|---|---|---|
| 3-1,29 | 0.13 | 10.60 | 1.77 | 0.35 | 31 | 6 | 2.25 |
| 3-1,39 | 0.13 | 10.98 | 1.82 | 0.34 | 33 | 6 | 2.20 |
| 3-1,49 | 0.13 | 10.70 | 1.79 | 0.34 | 31 | 6 | 2.24 |
| 3-1,59 | 0.13 | 10.63 | 1.78 | 0.34 | 31 | 6 | 2.22 |
| 3-1,69 | 0.13 | 10.15 | 1.72 | 0.32 | 32 | 6 | 2.24 |
| 3-1,79 | 0.09 | 7.61 | 1.29 | 0.21 | 36 | 6 | 2.20 |
| 3-1,89 | 0.13 | 10.29 | 1.65 | 0.33 | 31 | 6 | 2.23 |
| 3-1,99 | 0.12 | 9.58 | 1.57 | 0.29 | 33 | 6 | 2.24 |
| 3-1,109 | 0.09 | 7.17 | 1.27 | 0.19 | 39 | 6 | 2.16 |
| 3-1,119 | 0.10 | 7.70 | 1.28 | 0.24 | 32 | 6 | 2.22 |
| 3-1,129 | 0.09 | 6.87 | 1.25 | 0.19 | 36 | 5 | 2.28 |
| 3-1,139 | 0.08 | 6.42 | 1.17 | 0.19 | 34 | 5 | 2.30 |
| 3-1,149 | 0.08 | 6.67 | 1.22 | 0.19 | 36 | 5 | 2.24 |
| 3-2,9 | 0.08 | 6.27 | 1.15 | 0.17 | 37 | 5 | 2.30 |
| 3-2, 19 | 0.08 | 6.31 | 1.15 | 0.19 | 34 | 5 | 2.34 |
| 3-2, 31 | 0.08 | 6.33 | 1.17 | 0.20 | 31 | 5 | 2.36 |
| 3-2, 39 | 0.09 | 6.38 | 1.21 | 0.20 | 31 | 5 | 2.40 |
| 3-2, 49 | 0.08 | 6.30 | 1.17 | 0.17 | 37 | 5 | 2.32 |
| 3-2, 59 | 0.08 | 6.25 | 1.15 | 0.18 | 35 | 5 | 2.31 |
| 3-2, 69 | 0.08 | 6.35 | 1.12 | 0.21 | 31 | 6 | 2.33 |
| 3-2, 79 | 0.08 | 6.46 | 1.12 | 0.19 | 33 | 6 | 2.29 |
| 3-2, 89 | 0.08 | 6.50 | 1.11 | 0.20 | 33 | 6 | 2.27 |
| 3-2, 99 | 0.08 | 6.27 | 1.16 | 0.16 | 38 | 5 | 2.16 |
| 3-2, 109 | 0.08 | 6.12 | 1.11 | 0.18 | 34 | 6 | 2.30 |
| 3-2, 119 | 0.08 | 6.25 | 1.16 | 0.20 | 32 | 5 | 2.34 |
| 3-2, 129 | 0.07 | 5.90 | 1.15 | 0.15 | 40 | 5 | 2.14 |
| **0.01 Ga Site 599 - DSDP, Leg 92, SI Table 1 Ref. 1** | | | | | | | |
| **average** | **0.06** | **3.69** | **0.55** | **0.13** | **29** | **7** | **3.01** |
| 1-2, 129 | 0.09 | 3.56 | 0.47 | 0.21 | 17 | 8 | 4.51 |
| 1-4,9 | 0.06 | 3.66 | 0.52 | 0.15 | 25 | 7 | 3.01 |
| 1-4, 29 | 0.05 | 3.24 | 0.47 | 0.10 | 32 | 7 | 2.89 |
| 1-4, 39 | 0.06 | 3.64 | 0.52 | 0.11 | 33 | 7 | 2.92 |
| 1-4, 69 | 0.05 | 3.48 | 0.54 | 0.10 | 35 | 6 | 2.69 |
| 1-4, 79 | 0.05 | 3.63 | 0.61 | 0.14 | 26 | 6 | 2.63 |
| 1-4, 89 | 0.06 | 4.61 | 0.74 | 0.12 | 39 | 6 | 2.42 |
| **0.07 Ga - Shimanto Supergroup, SI Table 1 Ref. 2** | | | | | | | |
| 2071208.00 | 0.48 | 27.82 | 0.83 | 3.39 | 8 | 34 | 3.10 |
| **0.09 Ga -Perapedhi Formation, SI Table 1 Table 1 Ref. 3,4** | | | | | | | |
| **average** | **0.44** | **37.81** | **5.11** | **1.74** | **25** | **22** | **2.08** |
| M1 | 0.53 | 38.57 | 5.44 | 1.91 | 20 | 7 | 2.47 |
| M2 | 0.30 | 40.73 | 7.07 | 1.28 | 32 | 6 | 1.31 |
| M3 | 1.79 | 37.60 | 5.26 | 1.00 | 38 | 7 | 8.60 |
| M4 | 0.32 | 42.52 | 5.62 | 1.20 | 35 | 8 | 1.35 |
| M5 | 0.27 | 40.60 | 6.03 | 1.41 | 29 | 7 | 1.20 |
| M6 | 0.29 | 40.16 | 6.66 | 1.35 | 30 | 6 | 1.29 |
| M7 | 0.39 | 37.99 | 6.87 | 1.50 | 25 | 6 | 1.86 |
| M8 | 0.27 | 40.45 | 6.45 | 1.33 | 30 | 6 | 1.21 |
| CY1 | 0.19 | 36.31 | 0.25 | 2.22 | 16 | 145 | 0.93 |
| CY3 | 0.16 | 30.44 | 5.71 | 3.04 | 10 | 5 | 0.96 |

| | | | | | | | |
|---|---|---|---|---|---|---|---|
| **0.1 Ga - Sumail ophiolite complex, SI Table 1 Ref. 5** | | | | | | | |
| **average** | **0.17** | **20.58** | **0.13** | **1.38** | **16** | **206** | **1.68** |
| 105 | 0.27 | 15.11 | 0.05 | 1.91 | 8 | 319 | 3.23 |
| 104 | 0.06 | 15.74 | 0.05 | 1.69 | 9 | 333 | 0.70 |
| 400 | 0.12 | 9.58 | 0.09 | 0.90 | 11 | 111 | 2.22 |
| 302 | 0.25 | 34.55 | 0.30 | 1.48 | 23 | 115 | 1.30 |
| 45 | 0.14 | 27.91 | 0.18 | 0.90 | 31 | 151 | 0.93 |
| **0.165 Ga - ODP-Site 801C, data this study** | | | | | | | |
| **average** | **0.02** | **10.16** | **0.01** | **0.05** | **355** | **3005** | **0.33** |
| 801C-15R1,57 | 0.01 | 4.73 | 0.01 | 0.09 | 53 | 1338 | 0.38 |
| 801C-16R3,21 | 0.03 | 13.38 | 0.01 | 0.06 | 223 | | 0.37 |
| 801C-16R3,29-32 | 0.03 | 15.13 | | 0.02 | 876 | | 0.30 |
| 801C-04R1-72 | 0.01 | 8.94 | | 0.00 | | | 0.16 |
| 801C-04R2,19 | 0.03 | 8.38 | | | | | 0.66 |
| 801C-16R3,21 | 0.01 | 12.68 | | | | | 0.12 |
| 801C-16R3,29-32 | b.d | 14.40 | 0.00 | 0.02 | 833 | 7337 | |
| 801C-22R1,7 | b.d | 9.17 | | 0.13 | 69 | | |
| **0.19 Ga - Franciscan Ophilite Complex, data this study** | | | | | | | |
| Fig27A | 0.01 | 4.63 | 0.01 | 0.06 | 78 | 340 | 0.32 |
| **0.365 Ga - Iberian Pyrite Belt, SI Table 1 Ref. 6** | | | | | | | |
| **average** | **0.03** | **7.68** | **0.28** | **0.21** | **9** | **92** | **0.70** |
| 8D | 0.03 | 5.33 | 0.13 | 0.00 | | 40 | 1.18 |
| Pe74 | 0.02 | 14.76 | 0.05 | 0.00 | | 272 | 0.24 |
| 4B | 0.03 | 14.46 | 0.06 | 0.00 | | 233 | 0.38 |
| CV3 | 0.02 | 5.52 | 1.15 | 0.00 | | 5 | 0.71 |
| 25c | 0.03 | 8.95 | 0.34 | 0.00 | | 26 | 0.62 |
| 25a.bis | 0.03 | 4.88 | 0.62 | 0.00 | | 8 | 0.97 |
| PE22 | 0.01 | 5.74 | 0.06 | 0.64 | 9 | 93 | 0.41 |
| PE64 | 0.03 | 5.80 | 0.11 | 0.58 | 10 | 53 | 0.95 |
| PE68 | 0.03 | 4.61 | 0.05 | 0.47 | 10 | 85 | 1.02 |
| 14A | 0.03 | 7.89 | 0.25 | 0.00 | | 32 | 0.60 |
| CO44 | 0.03 | 9.48 | 0.04 | 0.00 | | 245 | 0.50 |
| 26D | 0.02 | 4.80 | 0.45 | 0.86 | 6 | 11 | 0.82 |
| **0.385 Ga - Molodez cherts, data this study** | | | | | | | |
| MOL-2 | 0.02 | 9.43 | 0.01 | 0.12 | 79 | 1159 | 0.39 |
| **ca. 0.4 Ga - Alexandrinka cherts, data this study** | | | | | | | |
| Alex-1 | 0.00 | 6.12 | 0.00 | 0.05 | 117 | 11695 | 0.14 |
| **0.46 Ga - Lokken Ophilite Complex, SI Table 1 Ref. 7, data this study** | | | | | | | |
| **average** | **0.02** | **10.76** | **0.03** | **0.16** | **178** | **606** | **0.46** |
| H-3 | 0.01 | 3.13 | 0.00 | 0.00 | 783 | 882 | 0.61 |
| H-6 | 0.01 | 4.30 | 0.01 | 0.05 | 85 | 450 | 0.58 |
| L-3 | 0.02 | 10.58 | 0.01 | 0.18 | 57 | 1343 | 0.30 |
| L-4 | 0.01 | 3.44 | 0.01 | 0.04 | 84 | 460 | 0.51 |
| H-7 | b.d. | 4.63 | | | | | |
| H-17 | b.d. | 4.77 | | | | | |
| H-19 | b.d. | 22.34 | | | | | |
| **0.49 Ga - Mount Windsor Volcanic Belt, SI Table 1 ref. 8** | | | | | | | |

|  |  |  |  |  |  |  |  |
|---|---|---|---|---|---|---|---|
| S37 | 0.03 | 8.11 | 0.03 | 0.23 | 35 | 270 | 0.58 |
| S17 | 0.05 | 34.87 | 0.10 | 0.42 | 83 | 349 | 0.27 |
| S39 | 0.01 | 4.27 | 0.00 | 0.11 | 39 |  | 0.55 |
| S29 | 0.01 | 8.61 | 0.02 | 0.16 | 54 | 430 | 0.17 |
| S27 | 0.03 | 11.60 | 0.01 | 0.24 | 48 | 1160 | 0.41 |
| TH 1A | 0.01 | 9.60 | 0.01 | 0.18 | 53 | 960 | 0.25 |
| S 58 | 0.03 | 12.05 | 0.02 | 0.16 | 75 | 603 | 0.52 |
| S 60 | 0.01 | 2.96 | 0.02 | 0.19 | 16 | 148 | 0.53 |
| TB 2 | 0.01 | 9.60 | 0.02 | 0.13 | 74 | 480 | 0.16 |
| HW39 | 0.02 | 9.50 | 0.03 | 0.05 | 190 | 317 | 0.33 |
| TC9 | 0.01 | 6.69 | 0.33 | 0.01 | 744 | 20 | 0.22 |
| SS15A | 0.02 | 19.59 | 0.03 | 0.76 | 26 | 653 | 0.16 |
| SS15C | 0.01 | 25.32 | 0.03 | 2.40 | 11 | 844 | 0.06 |
| SS15D | 0.01 | 3.54 | 0.01 | 0.79 | 4 | 354 | 0.67 |
| **ca. 0.635 Ga - Puga Formation, SI Table 1 Ref. 9** |  |  |  |  |  |  |  |
| **average** | **0.16** | **37.90** | **0.04** | **3.17** | **15** | **1879** | **0.94** |
| BDQ 330/13 | 0.12 | 24.42 | 0.03 | 4.16 | 6 | 901 | 0.92 |
| BDQ 330/17 | 0.54 | 26.56 | 0.16 | 3.12 | 9 | 171 | 3.67 |
| BDQ 330/118 | 0.26 | 26.66 | 0.11 | 3.49 | 8 | 241 | 1.73 |
| BDQ 9/8C | 0.07 | 53.41 | 0.03 | 1.82 | 29 | 2028 | 0.24 |
| BDQ 9/8D | 0.13 | 43.07 | 0.01 | 1.83 | 24 | 3972 | 0.56 |
| BDQ 9/8E | 0.15 | 36.96 | 0.03 | 1.63 | 23 | 1404 | 0.75 |
| BDQ 9/8F | 0.07 | 40.51 | 0.02 | 1.49 | 27 | 2615 | 0.31 |
| 9-8A | 0.27 | 26.61 | 0.06 | 7.78 | 3 | 447 | 1.84 |
| 9-8C | 0.07 | 53.41 | 0.03 | 3.43 | 16 | 2030 | 0.24 |
| 9-8D | 0.13 | 43.07 | 0.01 | 3.45 | 12 | 3975 | 0.56 |
| 9-8E | 0.15 | 36.96 | 0.03 | 3.08 | 12 | 1405 | 0.75 |
| 9-8 F1 | 0.07 | 40.51 | 0.02 | 2.81 | 14 | 2617 | 0.31 |
| 9-8 F2 | 0.07 | 40.59 | 0.02 | 3.07 | 13 | 2622 | 0.31 |
| 9-8 G | 0.23 | 46.37 | 0.04 | 2.80 | 17 | 1198 | 0.90 |
| 9-8 H | 0.13 | 51.38 | 0.04 | 2.49 | 21 | 1277 | 0.47 |
| 9-8-I | 0.20 | 21.72 | 0.01 | 6.01 | 4 | 2338 | 1.64 |
| **ca. 0.64 Ga - Braemar member, SI Table 1 Ref. 10** |  |  |  |  |  |  |  |
| **average** | **0.33** | **41.82** | **0.08** | **1.31** | **78** | **1062** | **1.59** |
| BR8 | 0.10 | 46.70 | 0.03 | 1.55 | 30 | 1508 | 0.39 |
| BR-13 | 0.10 | 43.60 | 0.05 | 2.10 | 21 | 939 | 0.43 |
| Br-53 | 0.41 | 46.30 | 0.18 | 1.45 | 32 | 260 | 1.60 |
| BR-52 | 0.28 | 34.80 | 0.14 | 1.67 | 21 | 250 | 1.45 |
| BR-40 | 0.07 | 55.19 | 0.09 | 1.48 | 37 | 648 | 0.21 |
| BR-36 | 0.30 | 26.02 | 0.23 | 3.42 | 8 | 112 | 2.06 |
| **0.663 Ga - Siadong Formation, SI Table 1 Ref. 11** |  |  |  |  |  |  |  |
| Siadong average | 0.58 | 33.08 | 0.05 | 0.64 | 52 | 610 | 3.16 |
| **0.715 Ga - Snake River Iron Formation, SI Table 1 Ref. 12, 13** |  |  |  |  |  |  |  |
| **average** | **0.36** | **51.81** | **0.06** | **0.59** | **290** | **1791** | **1.39** |
| BS-2 | 1.08 | 40.56 | 0.03 | 0.90 | 45 | 1352 | 4.79 |
| BS-4 | 0.21 | 28.21 | 0.02 | 0.42 | 67 | 1881 | 1.37 |
| BS-6 | 0.19 | 53.72 | 0.02 | 0.21 | 254 | 2336 | 0.63 |
| BS-A-1 | 0.24 | 56.45 | 0.02 | 0.32 | 178 | 2454 | 0.77 |
| 64-GF-2-C | 0.31 | 51.76 | 0.14 | 0.05 | 978 | 370 | 1.06 |

| | | | | | | | |
|---|---|---|---|---|---|---|---|
| 64-GF12-12 | 0.32 | 46.30 | 0.05 | 0.48 | 97 | 1007 | 1.24 |
| BS-A-2 | 0.95 | 44.99 | 0.05 | 2.38 | 19 | 900 | 3.79 |
| BS-A-5 | 0.15 | 64.28 | 0.05 | 0.26 | 243 | 1286 | 0.42 |
| GROSS623-C | 0.16 | 52.91 | 0.02 | 1.01 | 53 | 2301 | 0.55 |
| BS-3-A | 0.29 | 60.32 | 0.02 | 1.01 | 60 | 4021 | 0.87 |
| BS-9-B | 0.21 | 51.06 | 0.04 | 0.11 | 482 | 1276 | 0.72 |
| BS-1 | 0.08 | 65.95 | 0.04 | 0.11 | 623 | 1649 | 0.21 |
| BS-3-B | 0.21 | 61.59 | 0.02 | 0.95 | 65 | 4106 | 0.63 |
| BS-7 | 0.06 | 24.62 | 0.04 | 0.58 | 42 | 615 | 0.42 |
| BS-8 | 0.09 | 44.98 | 0.33 | 0.11 | 425 | 136 | 0.35 |
| BS-9-A | 0.30 | 44.62 | 0.06 | 0.16 | 281 | 744 | 1.22 |
| BS-11 | 0.51 | 45.91 | 0.04 | 3.76 | 12 | 1148 | 2.02 |
| BS-A-7-A | 0.15 | 17.00 | 0.02 | 0.42 | 40 | 739 | 1.62 |
| BS-A-7-B | 0.08 | 20.49 | 0.04 | 0.37 | 55 | 512 | 0.69 |
| GROSS623-A | 0.05 | 43.23 | 0.04 | 0.32 | 136 | 1081 | 0.22 |
| GROSS623-B | 0.13 | 30.14 | 0.04 | 0.48 | 63 | 754 | 0.78 |
| 64-GF-4 | 0.05 | 28.79 | 0.17 | 1.59 | 18 | 169 | 0.33 |
| 64-GF-8 | 0.16 | 21.56 | 0.23 | 2.33 | 9 | 94 | 1.35 |
| 64-GF-9 | 0.21 | 45.64 | 0.23 | 1.54 | 30 | 198 | 0.81 |
| 64-GF-12-A | 0.06 | 18.60 | 0.05 | 0.21 | 88 | 404 | 0.59 |
| 64-GF-12-B | 0.26 | 44.06 | 0.11 | 0.21 | 208 | 401 | 1.07 |
| 64-GF-15-A | 0.43 | 35.90 | 0.10 | 0.48 | 75 | 359 | 2.17 |
| 64-GF-15-B | 0.52 | 34.02 | 0.12 | 0.42 | 80 | 284 | 2.75 |
| 64-GF-20-A | 0.04 | 30.93 | 0.02 | 0.32 | 97 | 1345 | 0.23 |
| 64-GF-20-D | 0.11 | 61.13 | 0.09 | 0.11 | 577 | 719 | 0.32 |
| 64-GF-SR-4 | 0.05 | 15.95 | 0.05 | 0.48 | 33 | 319 | 0.54 |
| 64-GF-SR-5 | 0.05 | 30.64 | 0.04 | 0.48 | 64 | 766 | 0.31 |
| 64-GF-SR-6 | 0.24 | 45.39 | 0.06 | 0.21 | 214 | 757 | 0.97 |
| 64-GF-SR-7 | 0.17 | 24.41 | 0.08 | 0.16 | 154 | 305 | 1.22 |
| 64-GF-SR-8 | 0.14 | 27.07 | 0.06 | 0.26 | 102 | 451 | 0.93 |
| 64-GF-SR-9 | 0.28 | 32.26 | 0.10 | 0.32 | 102 | 323 | 1.59 |
| Y-7-142 | 0.40 | 35.59 | 0.07 | 0.06 | 560 | 511 | 2.01 |
| Y7-152.8 | 0.21 | 23.58 | 0.00 | 0.09 | 262 | | 1.64 |
| Y5-168.7 | 0.58 | 34.53 | 0.05 | 0.63 | 55 | 637 | 3.03 |
| Y5-169.1 | 0.94 | 37.39 | 0.02 | 2.11 | 18 | 1609 | 4.55 |
| N-7-47.6 | 0.92 | 32.79 | 0.04 | 2.92 | 11 | 847 | 5.04 |
| **0.715 Ga - Tindir Formation, SI Table 1 Ref. 14** | | | | | | | |
| **average** | **0.37** | **35.30** | **0.14** | **2.16** | **18** | **489** | **2.08** |
| GY-79-25 | 0.63 | 35.54 | 0.18 | 1.99 | 18 | 200 | 3.21 |
| GY-79-56 | 0.40 | 26.54 | 0.19 | 2.93 | 9 | 137 | 2.70 |
| GY-79-109 | 0.08 | 43.82 | 0.04 | 1.55 | 28 | 1132 | 0.34 |
| **ca. 0.746 Ga - Chuos Formation, SI Table 1 Ref. 15** | | | | | | | |
| **average** | **0.47** | **35.04** | **0.09** | **1.07** | **61** | **625** | **2.35** |
| CD-1 | 0.14 | 23.98 | 0.09 | 0.42 | 57 | 258 | 1.02 |
| CD-2 | 0.13 | 22.00 | 0.05 | 0.85 | 26 | 474 | 1.04 |
| CD-3 | 0.13 | 17.59 | 0.12 | 0.40 | 44 | 142 | 1.30 |
| CD-4 | 0.25 | 38.36 | 0.10 | 0.95 | 40 | 381 | 1.17 |
| CA1/2 | 0.46 | 47.96 | 0.05 | 1.24 | 39 | 885 | 1.74 |
| CA1/3 | 0.47 | 49.46 | 0.09 | 0.67 | 74 | 532 | 1.72 |

|  |  |  |  |  |  |  |  |
|---|---|---|---|---|---|---|---|
| CA 2/5 | 0.48 | 34.28 | 0.09 | 1.96 | 17 | 403 | 2.55 |
| CA 2/6 | 0.25 | 27.42 | 0.22 | 3.38 | 8 | 127 | 1.62 |
| **ca. 0.765* Ga - Mugur Formation, SI Table 1 Ref. 16** |  |  |  |  |  |  |  |
| Mugur-average | 0.54 | 39.67 | 0.33 | 1.04 | 38 | 119 | 2.46 |
| **1.7 Ga - Jerome mining district chert, SI Table 1 Ref. 17** |  |  |  |  |  |  |  |
| **average** | **0.09** | **20.81** | **0.13** | **0.24** | **107** | **423** | **0.56** |
| JS-05-37 | 0.02 | 5.89 | 0.04 | 0.08 | 70 | 131 | 0.53 |
| JS-05-32 | 0.34 | 57.94 | 0.04 | 0.16 | 353 | 1496 | 1.05 |
| JS-05-42 | 0.01 | 4.62 | 0.03 | 0.16 | 28 | 170 | 0.51 |
| JS-05-48A-1 | 0.00 | 5.10 | 0.02 | 0.07 | 69 | 314 | 0.15 |
| JS-05-48C | 0.35 | 47.86 | 0.03 | 0.75 | 64 | 1404 | 1.33 |
| JS-05-55 | 0.01 | 5.94 | 0.14 | 0.04 | 140 | 44 | 0.27 |
| JS-05-58 | 0.02 | 5.79 | 0.44 | 0.12 | 50 | 13 | 0.68 |
| JS-05-60 | 0.01 | 3.75 | 0.16 | 0.03 | 118 | 24 | 0.42 |
| BE-05-7 | 0.02 | 50.39 | 0.23 | 0.73 | 69 | 215 | 0.06 |
| **ca. 1.88 Ga - Vulcan Iron Formation, Animikie Basin, data this study** |  |  |  |  |  |  |  |
| **average** | **0.01** | **33.14** | **0.00** | **0.28** | **131** | **7822** | **0.05** |
| Curry1 | 0.01 | 26.26 | 0.00 | 0.17 | 159 | 7811 | 0.05 |
| Curry2 | 0.01 | 40.03 | 0.01 | 0.39 | 104 | 7833 | 0.05 |
| **1.88 Ga - Biwabik Iron Formation, data this study** |  |  |  |  |  |  |  |
| **average** | **0.04** | **21.32** | **1.00** | **0.35** | **52** | **39** | **0.27** |
| 317-4 | 0.01 | 6.02 | 0.10 | 0.16 | 38 | 58 | 0.18 |
| 317-8 | 0.07 | 36.63 | 1.90 | 0.55 | 67 | 19 | 0.35 |
| 317-10 | 0.06 | 59.81 | 0.84 | 0.69 | 87 | 71 | 0.17 |
| 317-22 | 0.01 | 24.73 | 1.30 | 0.04 | 687 | 19 | 0.08 |
| 317-26 | 0.07 | 35.44 | 1.72 | 0.57 | 62 | 21 | 0.34 |
| AB-4 | 0.14 | 44.48 | 0.21 | 0.38 | 116 | 215 | 0.57 |
| AB-6 | 0.01 | 10.91 | 1.66 | 0.03 | 317 | 7 | 0.18 |
| AB-17 | 0.01 | 7.62 | 0.01 | 0.05 | 164 | 536 | 0.15 |
| AB-20 | 0.00 | 8.09 | 0.04 | 0.08 | 99 | 187 | 0.06 |
| LA-LS-1 | 0.02 | 31.59 | 0.83 | 0.36 | 87 | 38 | 0.14 |
| UT-J-2 | 0.01 | 10.70 | 1.04 | 0.05 | 232 | 10 | 0.21 |
| **1.88 Ga - Gunflint Iron formation, data this study** |  |  |  |  |  |  |  |
| **average** | **0.02** | **27.20** | **0.17** | **2.16** | **112** | **745** | **0.14** |
| DH3-27 | 0.01 | 26.38 | 0.32 | 0.12 | 218 | 84 | 0.08 |
| DH3-43 | 0.03 | 28.02 | 0.02 | 4.19 | 7 | 1406 | 0.19 |
| GF-IF-10 | 0.01 | 7.56 | 0.54 | 0.04 | 205 | 14 | 0.22 |
| GF-KF-2 | 0.00 | 3.17 | 0.06 | 0.16 | 19 | 51 | 0.23 |
| **ca. 1.88 Ga - Negaunee Iron Formation, data this study** |  |  |  |  |  |  |  |
| **average** | **0.02** | **34.22** | **0.06** | **0.16** | **213** | **569** | **0.09** |
| AB11 | 0.02 | 35.14 | 0.06 | 0.14 | 250 | 584 | 0.10 |
| DI3 | 0.01 | 33.30 | 0.06 | 0.19 | 177 | 555 | 0.08 |
| **ca. 1.9 Ga Sokoman Iron Formation, SI Ref. 18** |  |  |  |  |  |  |  |
| Labrador Trough average |  |  |  |  |  |  | 0.10 |
| **ca. 1.9 - Mistassini Basin Iron Formation, SI Table 1 Ref. 12** |  |  |  |  |  |  |  |
| 59GF127 | 0.02 | 25.07 | 0.07 | 0.95 | 26 | 358 | 0.13 |
| 59GF133I | 0.02 | 39.67 | 0.16 | 0.53 | 75 | 248 | 0.10 |
| 59GF133J | 0.02 | 20.86 | 0.93 | 0.68 | 31 | 22 | 0.15 |

|  |  |  |  |  |  |  |  |
|---|---|---|---|---|---|---|---|
| 59GF133K | 0.02 | 41.80 | 0.03 | 0.40 | 104 | 1493 | 0.09 |
| 59GF136 | 0.02 | 33.09 | 0.02 | 0.23 | 145 | 1576 | 0.10 |
| 59GF137A | 0.02 | 37.91 | 0.02 | 0.95 | 40 | 1805 | 0.10 |
| 59GF137E | 0.01 | 30.66 | 0.05 | 0.68 | 45 | 681 | 0.08 |
| 59GF138B | 0.48 | 41.72 | 0.01 | 0.17 | 246 | 3792 | 2.07 |
| 59GF138D | 0.08 | 47.98 | 0.10 | 0.20 | 239 | 505 | 0.30 |
| 59GF139A | 0.65 | 44.26 | 0.23 | 0.18 | 246 | 192 | 2.67 |
| 59GF137D | 0.04 | 28.62 | 1.59 | 1.43 | 20 | 18 | 0.25 |
| **ca. 2.0 Ga - Maru Iron Formation, SI Table 1 Ref. 18** |  |  |  |  |  |  |  |
| Maru average |  |  |  |  |  |  | 0.22 |
| **ca. 2.2 Ga - Ijil Formation, SI Table 1 Ref. 19** |  |  |  |  |  |  |  |
| **average** | **0.05** | **31.94** | **0.11** | **1.00** | **118** | **1174** | **0.27** |
| IJ-1 | 0.07 | 30.50 | 0.26 | 1.03 | 30 | 119 | 0.44 |
| IJ-2 | 0.03 | 33.32 | 0.10 | 0.26 | 126 | 331 | 0.17 |
| IJ-3 | 0.08 | 35.41 | 0.08 | 0.68 | 52 | 457 | 0.40 |
| IJ-4 | 0.02 | 30.01 | 0.20 | 3.36 | 9 | 149 | 0.10 |
| IJ-5 | 0.03 | 30.31 | 0.01 | 0.07 | 441 | 3914 | 0.21 |
| IJ-6 | 0.05 | 32.09 | 0.02 | 0.60 | 54 | 2072 | 0.29 |
| **ca. 2.2 Ga - Hotazel Formation, SI Table 1 Ref. 20, data this study** |  |  |  |  |  |  |  |
| **average** | **0.04** | **28.79** | **1.15** | **0.11** | **395** | **95** | **0.30** |
| IF-3 | 0.00 | 0.73 | 0.01 | 0.09 | 8 | 80 | 1.06 |
| Hot-39 | 0.07 | 45.08 | 0.70 | 0.26 | 171 | 65 | 0.28 |
| Hot-40 | 0.02 | 14.15 | 0.91 | 0.14 | 105 | 16 | 0.32 |
| Hot-42 | 0.04 | 39.10 | 0.34 | 0.08 | 501 | 115 | 0.16 |
| Hot-43 | 0.03 | 25.78 | 0.30 | 0.02 | 1344 | 87 | 0.20 |
| Hot-44 | 0.05 | 28.07 | 0.16 | 0.15 | 186 | 172 | 0.35 |
| Hot-45 | 0.04 | 36.37 | 0.18 | 0.06 | 620 | 200 | 0.20 |
| S-11 | 0.03 | 26.16 | 0.13 | 0.05 | 481 | 199 | 0.21 |
| S-31 | 0.03 | 35.88 | 5.89 | 0.11 | 330 | 6 | 0.13 |
| S-32 | 0.02 | 33.01 | 3.69 | 0.11 | 303 | 9 | 0.12 |
| S-35 | 0.06 | 32.38 | 0.32 | 0.11 | 298 | 102 | 0.32 |
| **2.45 Ga - Brockman Iron Formation, SI Table 1 Refs. 18, 21, data this study** |  |  |  |  |  |  |  |
| **average** | **0.03** | **39.22** | **0.03** | **0.53** | **318** | **2479** | **0.24** |
| Dales Gorge 1-average |  |  |  |  |  |  | 0.79 |
| Dales Gorge 2-average |  |  |  |  |  |  | 0.54 |
| Joffre Member-average |  |  |  |  |  |  | 0.63 |
| Groenwater Mbr-average |  |  |  |  |  |  | 0.35 |
| RM-4 | 0.09 | 12.43 | 0.01 | 0.03 | 374 | 874 | 1.35 |
| RM-5 | 0.05 | 24.62 | 0.04 | 0.07 | 362 | 683 | 0.34 |
| RM-8 | 0.11 | 41.99 | 0.30 | 0.58 | 73 | 138 | 0.48 |
| RM-7 (DD475/1) | 0.01 | 21.05 | 0.02 | 0.05 | 441 | 1353 | 0.07 |
| WIT-15 | 0.08 | 71.02 | 0.01 | 0.17 | 416 | 8232 | 0.20 |
| WIT-46 | 0.05 | 73.43 | 0.02 | 0.30 | 244 | 3596 | 0.11 |
| BIF-15-1 | 0.01 | 19.14 | 0.02 | 1.68 |  |  | 0.11 |
| BIF-15-2 | 0.01 | 25.65 | 0.02 | 1.37 |  |  | 0.09 |
| BIF-15-3 | 0.01 | 25.91 | 0.02 | 1.37 |  |  | 0.09 |
| BIF-15-4 | 0.01 | 30.37 | 0.00 |  |  |  | 0.04 |
| Avg BIF-15- | 0.01 | 24.12 | 0.01 | 1.47 |  |  | 0.07 |
| BIF-16-1 | 0.03 | 28.47 | 0.03 | 0.72 |  |  | 0.17 |

| | | | | | | | |
|---|---|---|---|---|---|---|---|
| BIF-16-2 | 0.02 | 29.19 | 0.03 | 0.87 | | | 0.13 |
| BIF-16-3 | 0.02 | 30.27 | 0.01 | | | | 0.13 |
| BIF-16-4 | 0.01 | 12.16 | 0.01 | | | | 0.21 |
| BIF-16-5 | 0.01 | 18.15 | 0.03 | | | | 0.08 |
| Avg BIF-16 | 0.02 | 23.65 | 0.02 | 0.80 | | | 0.14 |
| MP-Hem-average | 0.01 | 67.14 | 0.01 | 0.03 | | | 0.02 |
| MP-Hem-min | | 66.40 | 0.00 | 0.00 | | | |
| MP-Hem-max | 0.02 | 68.15 | 0.03 | 0.50 | | | 0.06 |
| MP-mag-average | 0.01 | 70.28 | 0.01 | 0.01 | | | 0.02 |
| MP-mag-min | | 67.22 | 0.00 | 0.00 | | | |
| MP-mag-min | 0.03 | 71.07 | 0.04 | 0.03 | | | 0.08 |
| **2.48 Ga - Kuruman Iron Formation, SI Table 1 Refs. 18, data this study** | | | | | | | |
| Kuruman-average | | | | | | | 0.32 |
| Kuruman (up shelf)-average | | | | | | | 0.20 |
| KU-9-537 | 0.10 | 52.71 | 0.01 | 0.16 | 324 | 8945 | 0.35 |
| **2.48 Ga - Westerberg iron formation, data this study** | | | | | | | |
| WIT-18-740A | 0.05 | 41.93 | 1.11 | 0.13 | 330 | 38 | 0.19 |
| **2.5 Ga - Wyoming Craton iron formations, SI Table 1 Ref. 18, data this study** | | | | | | | |
| IF-5 | 0.02 | 35.52 | 0.07 | 0.23 | 155 | 513 | 0.12 |
| Montana-average | | | | | | | 0.01 |
| **ca. 2.6 Ga - Bjornevanns Iron Formation, data this study** | | | | | | | |
| BIF-1 | 0.05 | 37.65 | 0.03 | 0.11 | 335 | 1423 | 0.22 |
| **ca. 2.6 Ga - Marra Mamba Iron Formation, SI Table 1 Ref. 22** | | | | | | | |
| **average** | **0.04** | **28.11** | **0.09** | **0.25** | **134** | **384** | **0.24** |
| DDH-270-1 | 0.03 | 20.62 | 0.12 | | | 177 | 0.30 |
| DDH-270-2 | 0.01 | 18.88 | 0.11 | 0.17 | 111 | 174 | 0.13 |
| DDH-270-3 | 0.05 | 31.52 | 0.09 | 0.23 | 138 | 339 | 0.27 |
| DDH-270-4 | 0.07 | 44.40 | 0.04 | 0.46 | 98 | 988 | 0.28 |
| DDH-270-5 | 0.03 | 25.13 | 0.11 | 0.13 | 190 | 239 | 0.23 |
| **ca. 2.7 Ga - Manjeri Iron Formation, data this study** | | | | | | | |
| **average** | **0.02** | **12.88** | **0.07** | **0.11** | **140** | **951** | **0.31** |
| B/B4 | 0.00 | 5.18 | 0.04 | 0.07 | 76 | 140 | 0.14 |
| Z04-12 | 0.03 | 15.53 | 0.00 | 0.07 | 222 | 4161 | 0.38 |
| Z04-26 | 0.04 | 12.78 | 0.01 | 0.08 | 153 | 1226 | 0.54 |
| Z04-31 | 0.03 | 21.52 | 0.15 | 0.11 | 192 | 143 | 0.24 |
| Z04-32 | 0.01 | 8.94 | 0.10 | 0.04 | 218 | 88 | 0.28 |
| BMA-1 | 0.02 | 14.03 | 0.02 | 0.20 | 70 | 829 | 0.30 |
| BMA-2 | 0.02 | 12.22 | 0.17 | 0.23 | 53 | 72 | 0.30 |
| **2.74 Ga - Temagami Iron Formation, SiI Table 1 Ref. 23, data this study** | | | | | | | |
| **average** | **0.03** | **29.48** | **0.07** | **0.35** | **322** | **2605** | **0.19** |
| FeR-3 | 0.03 | 31.00 | 0.06 | 0.04 | 714 | 507 | 0.18 |
| Fe-R-4 | 0.05 | 27.80 | 0.15 | 0.86 | 32 | 187 | 0.34 |
| IF-6 | 0.01 | 29.65 | 0.00 | 0.13 | 221 | 7123 | 0.05 |
| **ca. 2.7 Ga - Adams mine-Kirland Lake area iron formation, SI Table 1 Ref. 12** | | | | | | | |
| **average** | **0.07** | **27.42** | **0.04** | **0.27** | **184** | **1383** | **0.50** |
| 80GF833 | 0.07 | 23.18 | 0.06 | 0.21 | 109 | 374 | 0.51 |
| 80GF837 | 0.05 | 22.63 | 0.02 | 0.26 | 86 | 1509 | 0.38 |
| 80GF839A | 0.10 | 37.16 | 0.03 | 0.32 | 117 | 1199 | 0.47 |
| 80GF839B | 0.09 | 33.31 | 0.02 | 0.21 | 157 | 1448 | 0.50 |

| | | | | | | | |
|---|---|---|---|---|---|---|---|
| 80GF841 | 0.05 | 15.39 | 0.02 | 0.64 | 24 | 669 | 0.61 |
| 80GF842 | 0.07 | 27.15 | 0.02 | 0.16 | 171 | 1810 | 0.46 |
| 80GF844 | 0.02 | 5.43 | 0.04 | 0.90 | 6 | 139 | 0.58 |
| 80GF847 | 0.15 | 30.24 | 0.02 | 0.16 | 190 | 2016 | 0.88 |
| 80GF848 | 0.10 | 21.10 | 0.01 | 0.21 | 100 | 2637 | 0.86 |
| 80GF850 | 0.07 | 43.76 | 0.02 | 0.05 | 827 | 2917 | 0.31 |
| 80GF859I | 0.09 | 35.44 | 0.04 | 0.16 | 223 | 909 | 0.44 |
| 80GF859J | 0.06 | 21.04 | 0.05 | 0.16 | 133 | 457 | 0.49 |
| 80GF865 | 0.03 | 22.89 | 0.22 | 0.05 | 432 | 105 | 0.27 |
| 80GF870 | 0.10 | 39.24 | 0.02 | 0.58 | 67 | 1706 | 0.48 |
| 80GF871 | 0.10 | 33.52 | 0.02 | 0.21 | 158 | 2234 | 0.54 |
| 80GF872 | 0.09 | 38.76 | 0.03 | 0.26 | 146 | 1250 | 0.43 |
| 80GF873 | 0.05 | 32.65 | 0.02 | 0.11 | 308 | 2177 | 0.29 |
| **ca. 2.7 Ga - Bending Lake Greenstone Belt iron formation, SI Table 1 Ref. 12** | | | | | | | |
| **average** | **0.10** | **34.06** | **0.06** | **1.60** | **37** | **621** | **0.60** |
| 80GF527 | 0.12 | 30.95 | 0.03 | 0.64 | 49 | 998 | 0.69 |
| 80GF530 | 0.10 | 31.22 | 0.05 | 0.64 | 49 | 679 | 0.55 |
| 80GF531 | 0.11 | 33.67 | 0.04 | 0.48 | 71 | 863 | 0.58 |
| 80GF532 | 0.15 | 36.01 | 0.05 | 0.64 | 57 | 667 | 0.74 |
| 80GF533 | 0.12 | 45.73 | 0.06 | 0.74 | 62 | 738 | 0.46 |
| 80GF534 | 0.10 | 38.16 | 0.06 | 1.01 | 38 | 615 | 0.47 |
| 80GF535 | 0.10 | 36.88 | 0.05 | 0.58 | 63 | 683 | 0.47 |
| 80GF536 | 0.12 | 29.40 | 0.04 | 0.58 | 50 | 754 | 0.75 |
| 80GF537 | 0.08 | 32.11 | 0.07 | 2.17 | 15 | 459 | 0.44 |
| 80GF538 | 0.14 | 27.42 | 0.07 | 3.39 | 8 | 392 | 0.92 |
| 80GF539 | 0.14 | 35.40 | 0.08 | 1.75 | 20 | 460 | 0.69 |
| 80GF541 | 0.13 | 32.81 | 0.09 | 2.01 | 16 | 386 | 0.72 |
| 80GF542 | 0.12 | 35.06 | 0.09 | 1.80 | 19 | 413 | 0.61 |
| 80GF543 | 0.15 | 24.63 | 0.07 | 3.55 | 7 | 352 | 1.09 |
| 80GF544 | 0.09 | 45.22 | 0.07 | 1.32 | 34 | 646 | 0.37 |
| 80GF545 | 0.10 | 34.57 | 0.05 | 0.58 | 59 | 752 | 0.50 |
| 80GF547 | 0.17 | 12.95 | 0.05 | 5.88 | 2 | 281 | 2.37 |
| 80GF550 | 0.07 | 28.05 | 0.05 | 0.90 | 31 | 519 | 0.42 |
| 80GF551 | 0.15 | 29.01 | 0.09 | 3.23 | 9 | 341 | 0.95 |
| 80GF552 | 0.10 | 27.72 | 0.04 | 0.48 | 58 | 711 | 0.62 |
| 80GF554 | 0.17 | 24.81 | 0.08 | 4.08 | 6 | 322 | 1.24 |
| 80GF617 | 0.07 | 37.84 | 0.05 | 0.79 | 48 | 823 | 0.33 |
| 80GF618 | 0.09 | 41.45 | 0.05 | 0.69 | 60 | 901 | 0.38 |
| 80GF619 | 0.06 | 38.24 | 0.05 | 0.79 | 48 | 708 | 0.29 |
| 80GF622 | 0.08 | 38.11 | 0.04 | 0.58 | 65 | 977 | 0.37 |
| 80GF624 | 0.06 | 39.51 | 0.07 | 0.42 | 93 | 564 | 0.28 |
| 80GF625 | 0.07 | 31.02 | 0.06 | 0.32 | 98 | 500 | 0.41 |
| 80GF626 | 0.10 | 31.97 | 0.06 | 0.58 | 55 | 516 | 0.59 |
| 80GF627 | 0.10 | 36.56 | 0.05 | 0.79 | 46 | 795 | 0.50 |
| 80GF628 | 0.06 | 36.76 | 0.05 | 1.06 | 35 | 799 | 0.28 |
| 80GF630 | 0.08 | 37.06 | 0.05 | 0.64 | 58 | 806 | 0.40 |
| 80GF633 | 0.10 | 36.67 | 0.05 | 2.06 | 18 | 797 | 0.47 |
| 80GF634 | 0.10 | 29.28 | 0.05 | 2.44 | 12 | 637 | 0.59 |
| 80GF636 | 0.22 | 26.05 | 0.05 | 3.07 | 8 | 566 | 1.54 |

| | | | | | | | |
|---|---|---|---|---|---|---|---|
| 80GF637 | 0.11 | 28.19 | 0.05 | 2.86 | 10 | 522 | 0.73 |
| 80GF638 | 0.09 | 38.19 | 0.06 | 1.16 | 33 | 616 | 0.41 |
| 80GF639 | 0.14 | 23.36 | 0.05 | 3.23 | 7 | 508 | 1.04 |
| 80GF644 | 0.09 | 37.04 | 0.05 | 1.11 | 33 | 686 | 0.45 |
| 80GF645 | 0.13 | 36.48 | 0.05 | 1.59 | 23 | 676 | 0.63 |
| 80GF646 | 0.10 | 50.73 | 0.09 | 1.06 | 48 | 545 | 0.36 |
| 80GF647 | 0.14 | 30.42 | 0.08 | 3.23 | 9 | 395 | 0.85 |
| 80GF648 | 0.11 | 34.96 | 0.05 | 1.59 | 22 | 760 | 0.56 |
| 80GF649 | 0.10 | 33.10 | 0.03 | 0.48 | 69 | 1068 | 0.52 |
| 80GF650 | 0.10 | 35.44 | 0.08 | 2.49 | 14 | 460 | 0.49 |
| 80GF651 | 0.13 | 28.42 | 0.07 | 3.28 | 9 | 406 | 0.83 |
| 80GF652 | 0.11 | 40.02 | 0.05 | 0.58 | 69 | 870 | 0.49 |
| 80GF653 | 0.07 | 37.91 | 0.07 | 1.80 | 21 | 542 | 0.35 |
| 80GF654 | 0.09 | 39.27 | 0.07 | 0.69 | 57 | 561 | 0.40 |
| 80GF656 | 0.08 | 27.06 | 0.06 | 3.18 | 9 | 437 | 0.55 |
| 80GF657 | 0.06 | 37.85 | 0.05 | 0.69 | 55 | 823 | 0.29 |
| 80GF659 | 0.08 | 35.91 | 0.08 | 0.79 | 45 | 466 | 0.42 |
| 80GF661 | 0.12 | 45.11 | 0.07 | 1.11 | 41 | 644 | 0.47 |
| 80GF662 | 0.08 | 34.17 | 0.07 | 2.44 | 14 | 488 | 0.41 |
| 80GF663 | 0.07 | 37.01 | 0.08 | 0.90 | 41 | 481 | 0.32 |
| **2.72 Ga - Lake St. Joseph Greenstone belt iron formation, SI Table 1 Ref. 12** | | | | | | | |
| **average** | **0.09** | **33.77** | **0.05** | **1.80** | **41** | **702** | **0.49** |
| 70GF26A | 0.17 | 34.24 | 0.02 | 1.96 | 17 | 1902 | 0.92 |
| 70GF26B | 0.07 | 38.50 | 0.02 | 0.85 | 45 | 1925 | 0.35 |
| 70GF26C | 0.15 | 40.29 | 0.03 | 1.38 | 29 | 1612 | 0.68 |
| 80GF-400 | 0.09 | 40.61 | 0.07 | 0.53 | 77 | 580 | 0.39 |
| 80GF-401 | 0.13 | 42.53 | 0.05 | 0.26 | 161 | 925 | 0.56 |
| 80GF-402 | 0.03 | 47.18 | 0.07 | | | 674 | 0.10 |
| 80GF403 | 0.05 | 27.69 | 0.05 | 3.71 | 7 | 602 | 0.34 |
| 80GF404 | 0.08 | 39.79 | 0.05 | 0.79 | 50 | 737 | 0.38 |
| 80GF405 | 0.06 | 31.45 | 0.04 | 3.02 | 10 | 807 | 0.33 |
| 80GF406 | 0.14 | 39.82 | 0.05 | 0.48 | 84 | 737 | 0.61 |
| 80GF408 | 0.07 | 31.80 | 0.03 | 0.32 | 100 | 1026 | 0.37 |
| 80GF410 | 0.07 | 25.65 | 0.03 | 2.96 | 9 | 827 | 0.46 |
| 80GF412 | 0.06 | 30.62 | 0.04 | 1.64 | 19 | 785 | 0.33 |
| 80GF413 | 0.08 | 30.68 | 0.02 | 0.26 | 116 | 1334 | 0.49 |
| 80GF414 | 0.10 | 38.30 | 0.06 | 0.48 | 80 | 618 | 0.47 |
| 80GF415 | 0.10 | 30.91 | 0.03 | 2.33 | 13 | 997 | 0.59 |
| 80GF416 | 0.09 | 26.54 | 0.03 | 0.37 | 72 | 856 | 0.59 |
| 80GF418 | 0.05 | 34.79 | 0.05 | 0.90 | 39 | 644 | 0.27 |
| 80GF419 | 0.04 | 35.31 | 0.06 | 2.12 | 17 | 570 | 0.22 |
| 80GF420 | 0.12 | 32.94 | 0.04 | 0.42 | 78 | 845 | 0.67 |
| 80GF421 | 0.02 | 26.90 | 0.03 | 3.65 | 7 | 868 | 0.15 |
| 80GF422 | 0.04 | 39.43 | 0.07 | 0.37 | 106 | 563 | 0.18 |
| 80GF425 | 0.07 | 29.89 | 0.05 | 1.96 | 15 | 650 | 0.45 |
| 80GF426 | 0.14 | 34.80 | 0.05 | 0.37 | 94 | 645 | 0.70 |
| 80GF427 | 0.04 | 39.51 | 0.05 | 0.58 | 68 | 859 | 0.20 |
| 80GF428 | 0.13 | 36.77 | 0.05 | 0.26 | 139 | 681 | 0.62 |
| 80GF429 | 0.08 | 35.34 | 0.05 | 1.16 | 30 | 768 | 0.42 |

| | | | | | | | |
|---|---|---|---|---|---|---|---|
| 80GF430 | 0.10 | 33.52 | 0.05 | 0.85 | 40 | 729 | 0.52 |
| 80GF431 | 0.08 | 39.86 | 0.06 | 0.42 | 94 | 643 | 0.36 |
| 80GF432 | 0.09 | 37.93 | 0.05 | 0.16 | 239 | 825 | 0.44 |
| 80GF433 | 0.11 | 34.23 | 0.06 | 2.28 | 15 | 552 | 0.57 |
| 80GF434 | 0.09 | 40.16 | 0.05 | 0.58 | 69 | 873 | 0.39 |
| 80GF435 | 0.03 | 39.11 | 0.04 | 0.48 | 82 | 1003 | 0.14 |
| 80GF436 | 0.10 | 27.88 | 0.07 | 2.86 | 10 | 398 | 0.65 |
| 80GF437 | 0.06 | 16.41 | 0.04 | 3.23 | 5 | 421 | 0.62 |
| 80GF438 | 0.10 | 30.76 | 0.09 | 2.86 | 11 | 331 | 0.61 |
| 80GF441 | 0.08 | 22.58 | 0.09 | 5.35 | 4 | 243 | 0.66 |
| 80GF443 | 0.07 | 25.52 | 0.06 | 3.86 | 7 | 412 | 0.46 |
| 80GF445 | 0.12 | 27.20 | 0.06 | 2.49 | 11 | 439 | 0.81 |
| 80GF446 | 0.12 | 30.61 | 0.05 | 1.59 | 19 | 665 | 0.69 |
| 80GF447 | 0.07 | 39.83 | 0.05 | 1.22 | 33 | 866 | 0.34 |
| 80GF448 | 0.09 | 33.48 | 0.05 | 2.75 | 12 | 620 | 0.47 |
| 80GF450 | 0.11 | 35.79 | 0.04 | 0.85 | 42 | 918 | 0.57 |
| 80GF451 | 0.10 | 33.66 | 0.05 | 1.16 | 29 | 623 | 0.54 |
| 80GF452 | 0.13 | 37.76 | 0.06 | 1.01 | 38 | 609 | 0.60 |
| 80GF453 | 0.07 | 32.57 | 0.05 | 0.69 | 47 | 708 | 0.36 |
| 80GF454 | 0.10 | 33.48 | 0.03 | 1.54 | 22 | 1080 | 0.54 |
| 80GF455 | 0.08 | 25.37 | 0.04 | 3.18 | 8 | 650 | 0.56 |
| 80GF456 | 0.09 | 45.93 | 0.07 | 1.80 | 26 | 656 | 0.34 |
| 80GF457 | 0.08 | 39.75 | 0.07 | 1.64 | 24 | 568 | 0.36 |
| 80GF458 | 0.08 | 32.01 | 0.05 | 1.22 | 26 | 696 | 0.47 |
| 80GF459 | 0.15 | 34.83 | 0.05 | 3.28 | 11 | 645 | 0.79 |
| 80GF461 | 0.08 | 17.91 | 0.09 | 6.30 | 3 | 193 | 0.83 |
| 80GF462 | 0.12 | 43.29 | 0.05 | 1.22 | 36 | 802 | 0.49 |
| 80GF463 | 0.13 | 39.30 | 0.07 | 0.79 | 49 | 561 | 0.58 |
| 80GF464 | 0.10 | 38.07 | 0.08 | 1.59 | 24 | 494 | 0.48 |
| 80GF465 | 0.09 | 34.73 | 0.09 | 2.70 | 13 | 409 | 0.45 |
| 80GF466 | 0.21 | 27.95 | 0.05 | 1.80 | 16 | 608 | 1.38 |
| 80GF467 | 0.07 | 32.63 | 0.06 | 2.06 | 16 | 526 | 0.36 |
| 80GF469 | 0.07 | 22.41 | 0.05 | 3.12 | 7 | 415 | 0.56 |
| 80GF470 | 0.07 | 35.43 | 0.05 | 2.33 | 15 | 656 | 0.36 |
| 80GF471 | 0.08 | 45.16 | 0.06 | 0.85 | 53 | 728 | 0.31 |
| 80GF472 | 0.07 | 36.29 | 0.05 | 1.69 | 21 | 672 | 0.33 |
| 80GF473 | 0.10 | 25.38 | 0.05 | 1.69 | 15 | 470 | 0.68 |
| 80GF474 | 0.08 | 21.15 | 0.14 | 5.45 | 4 | 152 | 0.67 |
| 80GF475 | 0.08 | 35.02 | 0.05 | 1.27 | 28 | 649 | 0.40 |
| 80GF476 | 0.09 | 29.20 | 0.05 | 2.12 | 14 | 541 | 0.54 |
| 80GF477 | 0.07 | 41.38 | 0.06 | 1.43 | 29 | 667 | 0.29 |
| 80GF478 | 0.07 | 39.34 | 0.06 | 1.27 | 31 | 635 | 0.32 |
| 80GF479 | 0.10 | 33.65 | 0.06 | 1.06 | 32 | 543 | 0.51 |
| 80GF481 | 0.08 | 44.25 | 0.07 | 1.27 | 35 | 632 | 0.34 |
| 80GF482 | 0.17 | 41.73 | 0.05 | 1.11 | 38 | 773 | 0.72 |
| 80GF483 | 0.07 | 40.21 | 0.06 | 0.85 | 47 | 649 | 0.29 |
| 80GF484 | 0.09 | 29.27 | 0.06 | 3.23 | 9 | 472 | 0.54 |
| 80GF485 | 0.13 | 48.43 | 0.06 | 0.74 | 65 | 781 | 0.47 |
| 80GF486 | 0.08 | 21.44 | 0.06 | 4.29 | 5 | 346 | 0.70 |

|  |  |  |  |  |  |  |  |
|---|---|---|---|---|---|---|---|
| 80GF487 | 0.10 | 32.75 | 0.05 | 1.59 | 21 | 712 | 0.53 |
| 80GF488 | 0.05 | 21.97 | 0.04 | 2.44 | 9 | 563 | 0.39 |
| 80GF489 | 0.09 | 36.83 | 0.06 | 1.69 | 22 | 594 | 0.45 |
| 80GF490 | 0.06 | 32.89 | 0.06 | 1.48 | 22 | 531 | 0.33 |
| 80GF491 | 0.10 | 33.41 | 0.06 | 2.59 | 13 | 539 | 0.54 |
| 80GF492 | 0.10 | 24.17 | 0.05 | 4.08 | 6 | 448 | 0.72 |
| 80GF493 | 0.09 | 30.03 | 0.05 | 2.75 | 11 | 653 | 0.52 |
| 80GF494 | 0.07 | 20.03 | 0.05 | 4.82 | 4 | 371 | 0.67 |
| 80GF495 | 0.13 | 24.74 | 0.06 | 4.02 | 6 | 399 | 0.92 |
| 80GF496 | 0.03 | 30.93 | 0.09 | 3.49 | 9 | 333 | 0.15 |
| 80GF497 | 0.07 | 23.40 | 0.06 | 5.40 | 4 | 377 | 0.57 |
| 80GF498 | 0.09 | 23.27 | 0.04 | 2.65 | 9 | 597 | 0.68 |
| 80GF499 | 0.08 | 31.74 | 0.07 | 1.75 | 18 | 453 | 0.47 |
| 80GF501 | 0.09 | 45.25 | 0.05 | 0.48 | 95 | 984 | 0.37 |
| 80GF502 | 0.08 | 31.19 | 0.05 | 2.22 | 14 | 578 | 0.48 |
| 80GF503 | 0.07 | 34.80 | 0.05 | 0.79 | 44 | 757 | 0.36 |
| 80GF504 | 0.04 | 39.71 | 0.04 | 0.42 | 94 | 1018 | 0.20 |
| 80GF505 | 0.07 | 50.32 | 0.04 | 0.64 | 79 | 1290 | 0.27 |
| 80GF506 | 0.09 | 41.59 | 0.04 | 0.64 | 65 | 1067 | 0.40 |
| 80GF507 | 0.05 | 34.01 | 0.04 | 1.43 | 24 | 872 | 0.28 |
| 80GF508 | 0.06 | 16.40 | 0.03 | 1.27 | 13 | 529 | 0.67 |
| 80GF510 | 0.04 | 36.32 | 0.05 | 1.75 | 21 | 673 | 0.22 |
| 80GF512 | 0.10 | 39.91 | 0.04 | 0.90 | 44 | 1023 | 0.43 |
| 80GF513 | 0.14 | 38.14 | 0.05 | 0.26 | 144 | 829 | 0.66 |
| 80GF514 | 0.08 | 39.58 | 0.04 | 1.48 | 27 | 1015 | 0.38 |
| **2.72 Ga - Soudan Iron Formation, data this study** |  |  |  |  |  |  |  |
| **average** | **0.02** | **26.40** | **0.00** | **0.06** | **474** | **14017** | **0.14** |
| IF-17 | 0.02 | 21.44 | 0.00 | 0.05 | 417 | 18744 | 0.13 |
| IF-18 | 0.03 | 31.36 | 0.00 | 0.06 | 530 | 9290 | 0.15 |
| **2.74 Ga - Mary River Iron Formation, SI Table 1 Ref. 12, data this study** |  |  |  |  |  |  |  |
| **average** | **0.08** | **34.10** | **0.05** | **0.40** | **143** | **836** | **0.42** |
| JD-65-285-C11 | 0.02 | 20.98 | 0.03 | 0.13 | 161 | 683 | 0.14 |
| JD-65-C-199-3 | 0.09 | 27.05 | 0.03 | 0.31 | 87 | 893 | 0.60 |
| JD-C165A | 0.05 | 35.55 | 0.02 | 0.05 | 733 | 1741 | 0.26 |
| 81GF-525 | 0.10 | 33.93 | 0.06 | 0.21 | 160 | 571 | 0.51 |
| 81GF-526 | 0.09 | 29.14 | 0.04 | 0.74 | 39 | 728 | 0.54 |
| 81GF-527 | 0.19 | 32.35 | 0.02 | 0.21 | 153 | 1670 | 1.07 |
| 81GF-528 | 0.02 | 34.54 | 0.03 | 0.26 | 130 | 1163 | 0.09 |
| 81GF-529 |  | 39.19 | 0.04 | 0.00 |  | 979 |  |
| 81GF-530 | 0.09 | 31.89 | 0.08 | 0.37 | 86 | 398 | 0.49 |
| 81GF-531 | 0.03 | 26.50 | 0.02 | 0.11 | 250 | 1368 | 0.24 |
| 81GF-532 | 0.04 | 30.83 | 0.13 | 0.37 | 83 | 239 | 0.26 |
| 81GF-536 | 0.08 | 34.11 | 0.04 | 0.32 | 107 | 852 | 0.42 |
| 81GF-537 | 0.08 | 35.22 | 0.05 | 0.53 | 67 | 699 | 0.42 |
| 81GF-538 | 0.06 | 36.32 | 0.03 | 0.21 | 172 | 1223 | 0.30 |
| 81GF-539 | 0.07 | 31.30 | 0.05 | 0.48 | 66 | 622 | 0.40 |
| 81GF-540 | 0.05 | 30.43 | 0.03 | 0.42 | 72 | 1025 | 0.28 |
| 81GF-541 | 0.05 | 33.78 | 0.05 | 0.32 | 106 | 671 | 0.26 |
| 81GF-542 | 0.07 | 32.27 | 0.06 | 0.32 | 102 | 543 | 0.41 |

| | | | | | | | |
|---|---|---|---|---|---|---|---|
| 82GF-101A | 0.12 | 35.94 | 0.03 | 0.11 | 339 | 1210 | 0.59 |
| 82GF-101B | 0.08 | 31.16 | 0.04 | 0.21 | 147 | 778 | 0.48 |
| 82GF-102 | 0.10 | 30.75 | 0.04 | 0.05 | 581 | 768 | 0.59 |
| 82GF-103 | 0.03 | 40.73 | 0.05 | 0.48 | 85 | 809 | 0.15 |
| 82GF-105 | 0.03 | 38.68 | 0.04 | 0.32 | 122 | 966 | 0.12 |
| 82GF-106 | 0.06 | 49.87 | 0.05 | 0.69 | 72 | 990 | 0.21 |
| 82GF-108 | 0.05 | 34.08 | 0.04 | 0.26 | 129 | 851 | 0.28 |
| 82GF-109 | 0.05 | 27.63 | 0.04 | 0.32 | 87 | 690 | 0.34 |
| 82GF-110 | 0.08 | 40.22 | 0.08 | 0.42 | 95 | 502 | 0.35 |
| 82GF-111 | 0.14 | 33.33 | 0.05 | 0.48 | 70 | 662 | 0.78 |
| 82GF-114 | 0.09 | 30.41 | 0.04 | 0.37 | 82 | 760 | 0.54 |
| 82GF-118 | 0.09 | 31.32 | 0.03 | 0.37 | 85 | 1055 | 0.53 |
| 82GF-119 | 0.07 | 35.12 | 0.04 | 0.32 | 111 | 877 | 0.34 |
| 82GF-120 | 0.02 | 40.38 | 0.05 | 0.26 | 153 | 802 | 0.10 |
| 82GF-121 | 0.06 | 32.21 | 0.05 | 0.53 | 61 | 640 | 0.32 |
| 82GF-122 | 0.17 | 31.76 | 0.04 | 0.37 | 86 | 793 | 0.97 |
| 82GF-123 | 0.02 | 38.03 | 0.03 | 0.16 | 239 | 1280 | 0.08 |
| 82GF-124 | 0.06 | 32.35 | 0.06 | 0.42 | 76 | 545 | 0.34 |
| 82GF-127 | 0.02 | 35.96 | 0.05 | 0.79 | 45 | 714 | 0.11 |
| 82GF-128 | 0.18 | 34.05 | 0.11 | 0.58 | 58 | 310 | 0.97 |
| 82GF-129 | 0.07 | 28.87 | 0.13 | 1.54 | 19 | 224 | 0.41 |
| 82GF-136 | 0.20 | 34.20 | 0.05 | 0.37 | 92 | 679 | 1.04 |
| 82GF-137 | 0.29 | 34.66 | 0.08 | 0.58 | 60 | 433 | 1.50 |
| 82GF-140 | 0.08 | 36.38 | 0.03 | 0.05 | 687 | 1225 | 0.39 |
| 82GF-141 | 0.10 | 33.40 | 0.03 | | | 1125 | 0.57 |
| 82GF-142 | 0.03 | 33.59 | 0.05 | 0.42 | 79 | 667 | 0.14 |
| 82GF-143 | 0.06 | 28.18 | 0.04 | 0.69 | 41 | 704 | 0.36 |
| 82GF-144 | 0.09 | 36.22 | 0.05 | 0.79 | 46 | 719 | 0.43 |
| 82GF-145 | 0.08 | 36.93 | 0.04 | 0.26 | 140 | 923 | 0.40 |
| 82GF-146 | 0.07 | 34.93 | 0.04 | 0.16 | 220 | 873 | 0.36 |
| 82GF-151A | 0.03 | 42.78 | 0.04 | 1.27 | 34 | 1069 | 0.15 |
| 82GF-151B | 0.03 | 41.29 | 0.03 | 0.74 | 56 | 1390 | 0.13 |
| **ca. 2.95 Ga - Pongola Supergroup iron formation, SI Table 1 Ref. 24, data this study** | | | | | | | |
| **average** | **0.02** | **21.58** | **1.33** | **0.12** | **367** | **27** | **0.17** |
| P05-1 | 0.02 | 18.77 | 2.40 | 0.08 | 231 | 8 | 0.17 |
| P05-6 | 0.02 | 24.95 | 2.30 | 0.13 | 188 | 11 | 0.17 |
| P05-7 | 0.02 | 11.22 | 1.06 | 0.09 | 120 | 11 | 0.28 |
| WM42 | 0.01 | 15.53 | 0.71 | 0.07 | 226 | 22 | 0.10 |
| WM52 | 0.01 | 14.69 | 1.43 | 0.10 | 154 | 10 | 0.16 |
| WM61 | 0.02 | 56.65 | 0.26 | 0.04 | 1529 | 215 | 0.07 |
| WM62 | 0.02 | 53.43 | 1.19 | 0.35 | 151 | 45 | 0.07 |
| WM72 | 0.01 | 26.23 | 1.49 | 0.11 | 236 | 18 | 0.06 |
| WM101 | 0.01 | 18.25 | 1.85 | 0.01 | 1724 | 10 | 0.09 |
| WM102 | 0.02 | 10.63 | 1.63 | 0.28 | 39 | 7 | 0.30 |
| WM111 | 0.02 | 12.10 | 1.99 | 0.12 | 104 | 6 | 0.26 |
| WM112 | 0.01 | 12.38 | 1.23 | | | 10 | 0.19 |
| WM121 | 0.01 | 12.66 | 0.98 | | | 13 | 0.19 |
| WM122 | 0.01 | 8.39 | 0.88 | 0.03 | 264 | 10 | 0.28 |
| WM131 | 0.01 | 7.27 | 1.01 | 0.03 | 229 | 7 | 0.22 |
| WM132 | 0.01 | 10.28 | 0.27 | 0.18 | 57 | 38 | 0.15 |
| **ca. 2.95 Ga - Witwatersrand basin iron formation, data this study** | | | | | | | |
| IF-9 | 0.02 | 25.86 | 0.07 | 0.19 | 139 | 365 | 0.14 |

Appendix Table 4.2. Location, type of sedimentary deposit, and age of studied units

| Formation | Location | Setting | Iron phases | Age (Ga) | Reference discussing age constraints |
|---|---|---|---|---|---|
| Site 597, DSDP | Southeast Pacific ocean | DHS | Haematite | 0.01-0.02 | SI-Table 2 ref. 1 |
| Site 598, DSDP | Southeast Pacific ocean | DHS | Haematite | 0.01-.02 | SI-Table 2 ref. 1 |
| Site 599, DSDP | Southeast Pacific ocean | DHS | Haematite | 0.01 | SI-Table 2 ref. 1 |
| Shimanto Supergroup | Japan | DHS | Haematite | 0.07 | SI-Table 2 ref. 2 |
| Perapedhi Formation | Cyprus | DHS | Haematite | 0.09 | SI-Table 2 ref. 3 |
| Sumail ophiolite complex | Oman | DHS | Haematite | 0.10 | SI-Table 2 ref. 4 |
| ODP-Site 801C | Northwestern Pacfic | DHS | Haematite | 0.165 | SI-Table 2 ref. 5 |
| Franciscan Ophilite Complex | USA | DHS | Haematite | 0.19 | SI-Table 2 ref. 6 |
| Iberian Pyrite Belt | Spain and Portugal | DHS | Haematite, Magnetite | 0.365 | SI-Table 2 ref. 7 |
| Molodez cherts | Russia | DHS | Haematite | ca. 0.385 | SI-Table 2 ref. 8 |
| Alexandrinka cherts | Russia | DHS | Haematite | ca. 0.4 | SI-Table 2 ref. 8 |
| Lokken Ophilite Complex | Norway | DHS | Haematite | 0.46 | SI-Table 2 ref. 9 |
| Mount Windsor Volcanic Belt | Australia | DHS | Haematite | 0.49 | SI-Table 2 ref. 10 |
| Puga Formation | Brazil | R-BIF | Haematite | ca. 0.635 | SI-Table 2 ref. 11, 12 |
| Braemar member | Australia | R-BIF | Haematite | ca. 0.64 | SI-Table 2 ref. 13 |
| Siadong iron formation | China | DHS, R-BIF | Haematite | 0.663 | SI-Table 2 ref. 14 |
| Chuos Formation | Namibia | R-BIF | Haematite | ca. 0.746 | SI-Table 2 ref. 15 |
| Snake River Iron Formation | Canada | R-BIF | Haematite | 0.715 | SI-Table 2 ref. 16 |
| Tindir Iron Formation | USA | R-BIF | Haematite | 0.715 | SI-Table 2 ref. 16 |
| Mugur Formation* | Russia | R-BIF | Haematite | ca. 0.765 | SI-Table 2 ref. 17 |
| Jerome mining district chert | USA | DHS | Haematite | 1.7 | SI-Table 2 ref. 18 |
| Negaunee Iron Formation | USA | S-BIF | Haematite, Magnetite | 1.85 | SI-Table 2 ref. 19 |

| | | | | | |
|---|---|---|---|---|---|
| Vulcan Iron Formation | USA | S-BIF | Magnetite, Haematite | 1.88 | SI-Table 2 ref. 19 |
| Biwabik Iron Formation | USA | S-BIF | Haematite, Magnetite | 1.88 | SI-Table 2 ref. 19 |
| Gunflint Iron Formation | Canada | S-BIF | Haematite, Magnetite | 1.88 | SI-Table 2 ref. 19 |
| Sokoman Iron Formation | Canada | S-BIF | Haematite, Magnetite | ca. 1.9 | SI-Table 2 ref. 20 |
| Mistassini Basin Iron Formation | Canada | S-BIF | Haematite, Magnetite | ca. 1.9 | SI-Table 2 ref. 20 |
| Maru Iron Formation | Nigeria | S-BIF | Magnetite, Goethite, Haematite | ca. 2.0 | SI-Table 2 ref. 21 |
| Ijil Iron Formation | Mauritania | S-BIF | Haematite | ca. 2.0 | SI-Table 2 ref. 22 |
| Hotazel Formation | South Africa | S-BIF | Magnetite, Haematite, | ca. 2.2 | SI-Table 2 ref. 23 |
| Brockman Iron Formation | Australia | S-BIF | Magnetite, Haematite | 2.45 | SI-Table 2 ref. 24 |
| Kuruman Iron Formation | South Africa | S-BIF | Magnetite, Haematite | 2.48 | SI-Table 2 ref. 25 |
| Westerberg iron formation | South Africa | S-BIF | Haematite, Magnetite | 2.48 | SI-Table 2 ref. 25 |
| Wyoming Craton iron formations | USA | A-BIF | Haematite, Magnetite | ca. 2.5 | SI-Table 2 ref. 26 |
| Bjornevanns Iron Formation | Norway | A-BIF | Haematite, Magnetite | ca. 2.6 | SI-Table 2 ref. 27 |
| Marra Mamba Iron Formation | Australia | S-BIF | Magnetite | ca. 2.6 | SI-Table 2 ref. 28 |
| Manjeri Iron Formation | Zimbabwe | S-BIF | Magnetite, Haematite | ca. 2.7 | SI-Table 2 ref. 29 |
| Temagami Iron Formation | Canada | A-BIF | Magnetite, Haematite | ca. 2.7 | SI-Table 2 ref. 30 |
| Adams mine-Kirland Lake area iron formation | Canada | A-BIF | Magnetite, Haematite | ca. 2.7 | SI-Table 2 ref. 31 |
| Bending Lake Greenstone Belt iron formation | Canada | A-BIF | Magnetite, Haematite | ca. 2.7 | SI-Table 2 ref. 31 |
| Lake St. Joseph Greenstone belt iron formation | Canada | A-BIF | Magnetite, Haematite | ca. 2.72 | SI-Table 2 ref. 31 |
| Soudan Iron Formation | USA | A-BIF | Haematite, Magnetite | 2.72 | SI-Table 2 ref. 32 |
| Mary River Iron Formation | Canada | A-BIF | Magnetite, Haematite | 2.74 | SI-Table 2 ref. 33 |
| Pongola Supergroup iron formation | South Africa | S-BIF | Haematite, Magnetite | 2.95 | SI-Table 2 ref. 34 |
| Witwatersrand basin iron formation | South Africa | S-BIF | Haematite, Magnetite | ca. 2.95 | SI-Table 2 ref. 34 |

DHS, distal hydrothermal sediments; S-BIF, Superior type banded iron formation; R-BIF; Rapitain type banded iron formation; A-BIF, Algoma type banded iron formation

## Conclusions and Future Directions

Rare Earth Element (REE) studies have been key in shaping our view of the Earth's Early redox evolution. Redox-oriented REE studies are founded on extensive work on water column REE behavior in modern anoxic basins. In general, oxygenated marine settings show a strong negative Ce anomaly when sample REE data are normalized to shale composites ($Ce_{(SN)}$), whereas suboxic and anoxic waters lack large negative $Ce_{(SN)}$ anomalies (Byrne and Sholkovitz, 1996; German and Elderfield, 1990). Oxidation of Ce(III) greatly reduces Ce solubility resulting in preferential removal onto Mn-Fe oxyhydroxides, organic matter, and clay particles (Byrne and Sholkovitz, 1996). In contrast, suboxic and anoxic waters lack significant negative $Ce_{(SN)}$ anomalies due to reductive dissolution of settling Mn-Fe-rich particles (Byrne and Sholkovitz, 1996; German et al., 1991). Similarly, light REE depletion develops in oxygenated waters due to preferential removal of light versus heavy REEs onto Mn-Fe oxyhydroxides and other particle-reactive surfaces, and the ratio of light to heavy REEs markedly increases across redox boundaries owing to reductive dissolution of Mn-Fe oxyhydroxides (Byrne and Sholkovitz, 1996; German et al., 1991). In many basins, the $Ce_{(SN)}$ anomaly and the light to heavy REE ratio return to nearly the shale composite value across the Mn and Fe redox boundaries. In some basins, even positive $Ce_{(SN)}$ anomalies and light REE enrichment develop in anoxic and suboxic waters (Bau et al., 1997b; De Carlo and Green, 2002; Debaar et al., 1988; Schijf et al., 1995). Redox-induced shifts in REE patterns in some modern stratified basins are directly linked to Mn-cycling in the suboxic zone (De Carlo and Green, 2002; German et al., 1991).

There is no evidence for deviation from trivalent Ce behavior in many Archean and early Paleoproterozoic iron formations (Alexander et al., 2008; Bau and Dulski, 1996; Bau et al., 1997a; Bau and Moller, 1993; Frei et al., 2008; Freyer, 1976; Prakash and Devapriyan, 1996), suggesting that the water column from which ferric oxides precipitated was reducing with respect to Mn (cf. Bau and Dulski, 1996). In support of this model, a recent survey of 18 Paleoproterozoic and Archean iron formations found that bulk samples of iron formation do not display significant Ce anomalies until after atmospheric oxidation at ca. 2.3 Ga.

There also appear to be differences in trivalent REE behavior in iron formations before and after the rise of atmospheric oxygen. Archean and early Paleoproterozoic iron formations are characterized by consistently light REE depletion. This feature contrasts markedly with late Paleoproterozoic iron formations that show significant ranges in light to heavy REE ($Pr/Yb_{(SN)}$) ratios both below and above the shale composite values. The range of light to heavy REE and Y/Ho ratios in late Paleoproterozoic iron formations likely reflects varying contributions of REE + Y from Mn- and Fe-oxyhydroxide precipitation and dissolution. This interpretation implies deposition of late Paleoproterozoic (ca. 1.9 Ga) iron formations in basins having varying redox conditions, and a strong redoxcline separating the oxic upper part of the water column from the suboxic to anoxic deeper part (Planavsky et al., 2009). A similar Mn redoxcline was likely absent in Archean oceans.

Numerous studies report deviations from trivalent Ce behavior in Archean and early Paleoproterozoic iron formations (e.g., Klein and Beukes, 1989; (Kato et al., 2002; Kato et al., 1996; Kato et al., 1998; Kato et al., 2006; Khan and Naqvi, 1996; Klein and Beukes, 1989; Ohmoto et al., 2006; Spier et al., 2007). Although the significance of each reported case of negative or positive Ce anomalies in Archean rocks needs to be discussed individually, it is important to note that Ce anomalies in iron formations can arise from diagenetic alteration and analytical artifacts. Many previous REE studies are plagued by inaccurate and incomplete measurements (Bau and Dulski, 1996). For example, many REE studies that have inferred an oxidative Ce cycle were done with instrumental neutron activation analysis (INAA) methods (e.g., (Klein and Beukes, 1989), rather than with more accurate and precise inductively coupled plasma mass-spectrometry (ICP-MS), which was not widely available until the early 1990s. In addition, prior to the development of high-resolution Ge and other detectors in the 1980s, early INAA-based studies of REEs in iron formations may be problematic for Ce because of the interference of Fe on Ce in INAA data. Moreover, isotope dilution studies could not measure monoisotopic Pr (neighboring element of Ce in REE series), which made it impossible to meaningfully quantify Ce anomalies, because La displays non-conservative behavior in marine systems and the true Ce anomaly must thus be calculated using Nd and Pr data (see Bau and Dulski, 1996 for discussion). Analytical issues can also affect ICP-MS datasets. One potentially problem is that whereas Ce, the most abundant REE in calibration standards, is analyzed in an analogue detector mode, REE-poor BIFs and carbonates are analyzed in a pulse-count mode. Additionally, negative Ce anomalies were found in single samples but none of the studies documented consistent Ce anomalies for a suite of representative samples. At least some of the negative Ce anomalies, therefore, likely reflect metamorphic or recent weathering-related redistribution of REEs between metamorphic minerals and compositionally different layers, or between the soil horizon and bedrock (e.g., Braun et al., 1990; Slack et al., 2009). In this regard, it is interesting that analytically reliable bulk compositions of Archean and early Paleoproterozoic iron formations older than the rise of atmospheric oxygen at ca. 2.3 Ga do not appear to have evidence for an oxidative Ce cycle.

Stimulated by the potential of using Fe isotopes to trace biogeochemical cycling of Fe on early Earth, studies of the Fe isotope composition of iron formations have generated great interest in recent years (Beard et al., 1999; Dauphas et al., 2004; Johnson et al., 2003; Johnson et al., 2008). Experimental investigations have highlighted the importance of Fe redox cycling, mineral precipitation and dissolution, and microbial processes as factors contributing to Fe isotope compositions. Thus, it is expected that iron isotopes may provide valuable constraints on both biotic and abiotic redox processes recorded in iron formations.

A compilation of bulk rock and mineral-specific $\delta^{56}$Fe values in Archean and Paleoproterozoic BIFs is show overall variation between -2.5 and +2.7‰, which encompasses most of the natural range in iron isotope values observed to date. Although magnetite, carbonates (siderite and ankerite), and pyrite display both positive and negative $\delta^{56}$Fe values, iron oxide minerals generally show the highest $\delta^{56}$Fe values whereas carbonate minerals have subcrustal $\delta^{56}$Fe values. To date, most iron isotope studies have been done on giant 2.5 Ga deposits of the Hamersley Group (Australia) and Transvaal Supergroup (South Africa), which contain sections that have not been significantly metamorphosed (Johnson et al., 2003; Johnson et al., 2008). Other studies have focused on younger iron formations from the Animikie Basin (1.88 Ga Gunflint and Biwabik Iron formations: Planavsky et al., 2009) as well as on early Archean 3.8 Ga iron formations from Isua (Greenland) and the Nuvvuagittuq greenstone belt in northern Quebec, Canada (Dauphas, 2004, 2007). Limited data are also available on iron formations from the ca. 2.7 Ga Belingwe and Shurugwe greenstone belts, Zimbabwe (Rouxel et al., 2005; Steinhoefel et al., 2009).

The ubiquitous occurrence of magnetite and siderite in Hamersley and Transvaal iron formations with negative $\delta^{56}$Fe values down to -2.1‰ (Fig. 7) has been interpreted as evidence for bacterially-mediated Fe(III) reduction during diagenesis (Johnson et al., 2003, 2008b). In this case, $\delta^{56}$Fe values of magnetite are thought to be inherited from a ferric oxide/hydroxide precursor that formed through complete oxidation of hydrothermal $Fe^{2+}$, followed by conversion to magnetite through interaction with $Fe^{2+}$ formed by DIR. Lower $\delta^{56}$Fe values in carbonates may indicate a higher proportion of iron from DIR incorporated during diagenesis of the iron formation. In principle, partial iron oxidation in the water column may also fractionate dissolved iron in seawater toward negative $\delta^{56}$Fe values through reservoir effects, as suggested by Rouxel et al. (2005). For example, a Rayleigh fractionation mechanism involving between 50 and 80% of iron oxidation may explain both isotopically-enriched iron oxides in iron formations (up to +0.8‰) and negative $\delta^{56}$Fe values in seawater (down to -2.2‰). Regardless of the exact mechanism, it is interesting that the magnetite inventory in ca. 2.5 Ga Hamersley and Transvaal iron formations appears to have average $\delta^{56}$Fe values around 0‰ (Johnson et al., 2008b), which suggests that the iron in iron formations ultimately was derived from oceanic crust and is hydrothermal in origin; limited input of isotopically negative 'diagenetic' iron was derived from continental margin sediments as suggested for modern redox-stratified basins (Severmann et al., 2008). However, the study of Johnson et al. (2008b) focused only on mineralogically pure microlaminae and thus is likely a poor estimate for the bulk isotopic composition of iron formations.

Although early Archean iron formations from Isua, Greenland, and the Nuvvuagittuq greenstone belt in northern Quebec, Canada (e.g., Dauphas, 2004), are characterized by only positive $\delta^{56}$Fe values whereas negative $\delta^{56}$Fe values are relatively common in Late Archean iron formations, it is premature to draw robust conclusions regarding secular changes in biogeochemical cycling of iron from iron isotopes. It seems, however, that the range of iron isotope values in iron formations decrease significantly after the rise of atmospheric oxygen at ca. 2.3 Ga (Rouxel et al., 2005; Johnson et al., 2008; Planavsky et al., 2009). Based on $\delta^{56}$Fe records of iron formations and black shales, Johnson et al. (2008) argued for an emergence of DIR early in Earth's history, with a pronounced peak between ca. 2.7 Ga and 2.5 Ga coincident with the most negative $\delta^{56}$Fe values in sedimentary rocks. It was further argued that the increase in seawater $SO_4^{2-}$ by ca. 2.3 Ga may have restricted DIR in extent, due to complete titration of hydrothermal $Fe^{2+}$ to pyrite in a deep-water anoxic water column. However, it is unclear why late Paleoproterozoic (1.88 Ga) depositional systems such as in the Animikie Basin, where iron was clearly in excess of sulfate, would differ from Archean systems. In addition, a growing body of evidence suggests the development of at least local sulfidic conditions as early as 2.7 Ga (Anbar et al., 2007; Reinhard et al., 2009; Scott et al., 2011; Scott et al., 2008) contemporaneous with large negative $\delta^{56}$Fe excursions in iron formations (Rouxel et al., 2005; Johnson et al., 2008). Redox evolution is a more likely explanation for the presence of markedly negative $\delta^{56}$Fe values in Archean shales and iron formations: in an anoxic ocean, hydrothermally-derived iron could undergo partial oxidation via anoxic processes over a significant depth range, thus allowing for burial of isotopically heavy iron. This burial left behind an iron reservoir with negative iron isotope values that was buried at the latest stage in iron transport, when hydrothermal plumes crossed the chemocline between iron-rich and sulfur-rich waters and approached shallow water environments where organic matter-rich and sulfidic shales were deposited (Rouxel et al., 2005).

It is generally assumed that after ca. 1.85 Ga, sediment-hosted iron formations were not deposited for approximately 1.1 b.y. This distinctive pattern in the secular trend for iron formations has been explained by a change in the deep ocean redox state from anoxic to fully oxic (Holland, 1984) or sulfidic (Canfield, 1998) conditions. In contrast I proposed that the deep ocean was anoxic but not sulfidic, potentially with extensive suboxic conditions (Slack et al., 2007). The earlier suggestion by Holland (1984) for fully oxic deep-ocean conditions after ~1.88 Ga has fallen out of favor as multiple geochemical and geological evidence has shown that oxic environments were not as extensive in the deep ocean as those of today. An alternative model, suggesting that deep-ocean conditions were predominantly sulfidic over ~1.1 Ga of mid-Proterozoic history (e.g., Canfield, 1998), has also lost favor recently because practically all evidence for this model can be satisfied with locally developed euxinic conditions on continental shelves in oxygen minimum zones and in intracratonic basins (e.g., Slack et al., 2007; Scott et al., 2008). The emerging consensus is that the redox state of the deep ocean was variable over the time interval of ca. 1.85-0.75 Ga, but generally at a low oxidation state. The terms ‘ferruginous’ and ‘suboxic’ are not ideal for defining the redox state of the deep ocean during this period since the first was widely used for the Archean and the second has been used in different ways for modern and ancient conditions. More importantly, higher hydrothermal fluxes of metals, including Fe and Mn, should be expected if the oceans were at a low oxidation state. The record of this hydrothermal flux might be found in Fe and base metal contents of mid-Proterozoic shales and in their isotope signatures. Poulton et al. (2010) argued that euxinic shales deposited on continental margins (possibly as the equivalents of modern oxygen-minimum zones) and in intracratonic basins could have been a major sink for the hydrothermal iron flux to the mid-Proterozoic oceans, and were thus responsible for the absence or scarcity of mid-Proterozoic iron formations. At present, this suggestion has not yet been quantitatively evaluated, but it would require a higher total Fe content in average shale during this time interval. Data in Kump and Holland (1992) do show that the average Proterozoic shale has more Fe than the average Phanerozoic shale but less than the average Archean shale. It has also been proposed that a rise in seawater sulfate level after ca. 1.88 Ga led to a decrease in the flux of the hydrothermal iron—shutting off the deposition of major iron formation (Kump and Seyfried, 2005).

Although large sedimentary iron formations during the Middle Proterozoic (1.85-0.75 Ga) are indeed absent, several small iron formations and iron-rich lithologies in sedimentary rock-dominated successions are known outside of the Animikie basin. Magnetite and siderite iron formations of the Aok Formation in the Neoproterozoic Shaler Supergroup in the Duke of York and Brock Inliers of Victoria Island, northern Canada, were deposited at ca. 840 Ma before the onset of the oldest Neoproterozoic glacial events (Rainbird et al., 1994). Older examples within this age range include the ca. 1.70 Ga Freedom Formation of the Lower Baraboo Series, Wisconsin, which contains in the lower part banded ferruginous chert interlayered with sideritic and kaolinitic slate 60 to 160 m thick (Leith, 1935). Additionally, the Chuanlinggou Iron Formation on the North China craton, a classic GIF deposit, also appears to be latest Paleoproterozoic in age (ca. 1.7 Ga). Noteworthy examples of small iron deposits that formed during this time gap in shallow-water settings occur in northern Australia in the Sherwin Formation in the ca. 1.49 Ga Maiwok Subgroup of the Roper basin, Northern Territory (Abbott and

Sweet, 2000). These iron-rich units consist of oolitic ironstone and ferruginous siliciclastic rocks as much as 23 m thick (Abbott and Sweet, 2000). It is possible that these iron-rich units are linked to depostion of upwelling iron. Given current evidence, it seems likely the widespread anoxic but not sulfidic conditions were common in the mid-Proterozoic ocean.

Nutrients will exert a first order control on redox state of the ocean atmosphere system by strongly influencing organic carbon burial. Phosphorous is generally assumed to be the ultimate limiting nutrient. Phosphorous was asserted to be ultimate limiting nutrient in the Archean oceans given a high flux of iron oxides that remove phosphate (Bjerrum and Canfield, 2002). Therefore, iron formations hold the key to understanding Earth's earliest phosphorus cycle. During the Archean and Paleoproterozoic, especially during peak times of iron formation deposition, high dissolved silica concentrations could have prevented iron oxyhydroxides from being a major dissolved phosphate sink (Konhauser et al., 2007). Additionally, high levels of bicarbonate during the Precambrian (cf. Grotzinger, 1990) would have inhibited the precipitation of carbonate fluorapatite (CFA) by greatly increasing its solubility. The possibility of inhibited CFA formation is particularly important; in the modern oceans this flux accounts for the vast majority (60-80%) of phosphorus burial (e.g., (Ruttenberg and Berner, 1993). Combined, these two factors suggest relatively higher, rather than lower, dissolved phosphorus concentrations in Archean seawater with respect to the modern seawater.

If phosphorus content was not the controlling factor for Archean primary productivity, could nitrogen be the culprit? In the Archean anoxic ocean, dinitrogen was seemingly fixed by diazotrophic cyanobacteria and ammonium assimilation was also likely common (Glass et al., 2009). Both nitrogen fixation and ammonium assimilation are operated by enzymes, which are dependent on bio-essential trace metals such as Fe, V, and Mo, as metal cofactors (Glass et al., 2009). Both the V and Mo dissolved loads were generally low or negligible in early oceans (Scott et al., 2008), because under an essentially anoxic atmosphere these metals are insoluble. Thus, Mo limitation was likely in the Archean oceans due to anoxic redox conditions on land, just as iron is limiting in the modern oceans because of a predominance of the oxic water column. Iron concentrations, in contrast, were high and iron was likely utilized by diazotrophs on early Earth for nitrogen fixation and ammonium assimilation (Glass et al., 2009). Iron availability enhances nitrogen fixation and photosynthesis in modern environments; however, Fe-Mo nitrogenase is one hundred times as efficient as is the Fe-Fe nitrogenase in dinitrogen fixation (Zerkle et al., 2006). Therefore, nitrogen limitation (via trace metal co-limitation) of primary productivity was much more important than phosphorus limitation in the early oceans. There was a peak in phosphate level associated with the Neoproterozoic Snowball Earth glaciations. It is possible that at this time trace metal stress was lower. In this light it is possible this late Precambrian increase in dissolved phosphorus concentration may have stimulated high rates of organic carbon burial and a corresponding increase in atmospheric oxygen levels—paving the way for the rise of metazoans and ushering in the modern style redox conditions.

## References

Abbott, S.T., Sweet, I.P., 2000. Tectonic control on third-order sequences in a siliciclastic ramp-style basin: an example from the Roper Superbasin (Mesoproterozoic), northern Australia. Aust J Earth Sci 47, 637-657.

Alexander, B.W., Bau, M., Andersson, P., Dulski, P., 2008. Continentally-derived solutes in shallow Archean seawater: Rare earth element and Nd isotope evidence in iron formation from the 2.9 Ga Pongola Supergroup, South Africa. Geochimica et Cosmochimica Acta 72, 378-394.

Anbar, A.D., Duan, Y., Lyons, T.W., Arnold, G.L., Kendall, B., Creaser, R.A., Kaufman, A.J., Gordon, G.W., Scott, C., Garvin, J., Buick, R., 2007. A whiff of oxygen before the great oxidation event? Science. 317, 1903-1906.

Bau, M., Dulski, P., 1996. Distribution of yttrium and rare-earth elements in the Penge and Kuruman Iron-Formations, Transvaal Supergroup, South Africa. Precambrian Reasearch 79, 37-55.

Bau, M., Hohndorf, A., Dulski, P., Beukes, N.J., 1997a. Sources of rare-earth elements and iron in paleoproterozoic iron-formations from the Transvaal Supergroup, South Africa: Evidence from neodymium isotopes. Journal of Geology 105, 121-129.

Bau, M., Moller, P., 1993. Rare-Earth Element Systematics of the Chemically Precipitated Component in Early Precambrian Iron Formations and the Evolution of the Terrestrial Atmosphere-Hydrosphere-Lithosphere System. Geochimica et Cosmochimica Acta 57, 2239-2249.

Bau, M., Moller, P., Dulski, P., 1997b. Yttrium and lanthanides in eastern Mediterranean seawater and their fractionation during redox-cycling. Marine Chemistry 56, 123-131.

Beard, B.L., Johnson, C.M., Cox, L., Sun, H., Nealson, K.H., Aguilar, C., 1999. Iron isotope biosignatures. Science 285, 1889-1892.

Bjerrum, C.J., Canfield, D.E., 2002. Ocean productivity before about 1.9 Ga ago limited by phosphorus adsorption onto iron oxides. Nature 417, 159-162.

Byrne, R., Sholkovitz, E., 1996. Marine chemistry and geochemistry of the lanthanides, in: Gschneider Jr., K.A., Eyring, L. (Eds.), Handbook on the Physics and Chemistry of the Rare Earths. Elsevier, Amsterdam, pp. 497–593.

Canfield, D.E., 1998. A new model for Proterozoic ocean chemistry. Nature 396, 450-453.

Dauphas, N., van Zuilen, M., Wadhwa, M., Davis, A.M., Marty, B., Janney, P.E., 2004. Clues from iron isotope variations on the origin of early Archaean banded iron formations from Greenland. Science 306, 2077-2080.
De Carlo, E.H., Green, W.J., 2002. Rare earth elements in the water column of Lake Vanda, McMurdo Dry Valleys, Antarctica. Geochimica et Cosmochimica Acta 66, 1323-1333.

Debaar, H.J.W., German, C.R., Elderfield, H., Vangaans, P., 1988. Rare-Earth Element Distributions in Anoxic Waters of the Cariaco Trench. Geochimica et Cosmochimica Acta 52, 1203-1219.

Frei, R., Dahl, P.S., Duke, E.F., Frei, K.M., Hansen, T.R., Frandsson, M.M., Jensen, L.A., 2008. Trace element and isotopic characterization of Neoarchean and Paleoproterozoic iron formations in the Black Hills (South Dakota, USA): Assessment of chemical change during 2.9-1.9 Ga deposition bracketing the 2.4-2.2 Ga first rise of atmospheric oxygen. Precambrian Res 162, 441-474.

Freyer, B.J., 1976. Rare earth evidence in iron-formations for changing Precambrian oxidation states. Geochimica et Cosmochimica Acta 41, 361- 367.

German, C.R., Elderfield, H., 1990. Application of the Ce-anomaly as a paleoredox indicator: The ground rules. Paleoceanography 5, 823-833.

German, C.R., Holliday, B.P., Elderfield, H., 1991. Redox cycling of rare earth elements in the suboxic zone of the Black Sea. Geochimica et Cosmochimica Acta 55, 3553-3558.
Glass, J.B., Wolfe-Simon, F., Anbar, A.D., 2009. Coevolution of metal availability and nitrogen assimilation in cyanobacteria and algae. Geobiology 7, 100-123.

Johnson, C.M., Beard, B.L., Beukes, N.J., Klein, C., O'Leary, J.M., 2003. Ancient geochemical cycling in the Earth as inferred from Fe isotope studies of banded iron formations from the Transvaal Craton. Contributions to Mineralogy and Petrology 144, 523-547.

Johnson, C.M., Beard, B.L., Klein, C., Beukes, N.J., Roden, E.E., 2008. Iron isotopes constrain biologic and abiologic processes in banded iron formation genesis. Geochimica et Cosmochimica Acta 72, 151-169.

Kato, Y., Kano, T., Kunugiza, K., 2002. Negative Ce anomaly in the Indian banded iron formations: Evidence for the emergence of oxygenated deep-sea at 2.9 similar to 2.7 Ga. Resource Geology 52, 101-110.

Kato, Y., Kawakami, T., Kano, T., Kunugiza, K., Swamy, N.S., 1996. Rare-earth element geochemistry of banded iron formations and associated amphibolite from the Sargur belts, south India. Journal of Southeast Asian Earth Sciences 14, 161-164.

Kato, Y., Ohta, I., Tsunematsu, T., Watanabe, Y., Isozaki, Y., Maruyama, S., Imai, N., 1998. Rare earth element variations in mid-Archean banded iron formations: Implications for the chemistry of ocean and continent and plate tectonics. Geochimica Et Cosmochimica Acta 62, 3475-3497.

Kato, Y., Yamaguchi, K.E., Ohmoto, H., 2006. Chemical and biological evolution of early Earth: Constraints from banded iron-formations, in: Ohmoto, S.K.H. (Ed.), Rare earth elements in Precambrian banded iron formations: Secular changes of Ce and Eu anomalies and evolution of atmospheric oxygen Geological Society of America, Denver, pp. 269-289.

Khan, R.M.K., Naqvi, S.M., 1996. Geology, geochemistry and genesis of BIF of Kushtagi schist belt, Archaean Dharwar Craton, India. Mineralium Deposita 31, 123-133.

Klein, C., Beukes, N.J., 1989. Geochemistry and Sedimentology of a Facies Transition from Limestone to Iron-Formation Deposition in the Early Proterozoic Transvaal Supergroup, South-Africa. Economic Geology 84, 1733-1774.

Konhauser, K.O., Lalonde, S.V., Amskold, L., Holland, H.D., 2007. Was there really an Archean phosphate crisis? Science 315, 1234-1234.

Kump, L.R., Holland, H.D., 1992. Iron in Precambrian rocks: Implications for the global oxygen budget of the ancient Earth. Geochim Cosmochim Ac 56, 3217-3223.

Kump, L.R., Seyfried, W.E., 2005. Hydrothermal Fe fluxes during the Precambrian: Effect of low oceanic sulfate concentrations and low hydrostatic pressure on the composition of black smokers. Earth and Planetary Science Letters 235, 654-662.

Leith, A., 1935. The pre-Cambrian of the Lake Superior region, the Baraboo district, and other isolated areas in the upper Mississippi Valley. Kansas Geological Society Guide Books 9, 329–332.

Ohmoto, H., Watanabe, Y., Yamaguchi, K.E., Naraoka, H., Kakegawa, T., Haruna, M., Hayashi, K., Kato, Y., 2006. Chemical and biological evolution of early Earth: Constraints from banded iron-formations, in: Ohmoto, S.K.H. (Ed.), Evolution of the Atmosphere, Hydrosphere, and Biosphere on Early Earth: Constraints from Ore Deposits. Geological Society of America, Denver, pp. 291-331.

Planavsky, N., Rouxel, O., Bekker, A., Shapiro, R., Fralick, P., Knudsen, A., 2009. Iron-oxidizing microbial ecosystems thrived in late Paleoproterozoic redox-stratified oceans. Earth and Planetary Science Letters 286, 230-242.

Prakash, H.S.M., Devapriyan, G.V., 1996. REE enrichment in the oxide facies BIF of Chitradurga schist belt, Karnataka (vol 46, pg 202, 1995). Journal of the Geological Society of India 47, 265-265.

Rainbird, R.H., Jefferson, C.W., Hilderbrand, R.S., Worth, J.K., 1994. The Shaler Supergroup and revision of the Neoproterozoic stratigraphy in the Amundsen basin, Northwest Territories. Geological Survey of Canada Paper 94–1A, 61–70.
Reinhard, C.T., Raiswell, R., Scott, C., Anbar, A.D., Lyons, T.W., 2009. A Late Archean Sulfidic Sea Stimulated by Early Oxidative Weathering of the Continents. Science 326, 713-716.

Rouxel, O.J., Bekker, A., Edwards, K.J., 2005. Iron isotope constraints on the Archean and Paleoproterozoic ocean redox state. Science 307, 1088-1091.

Ruttenberg, K.C., Berner, R.A., 1993. Authigenic Apatite Formation and Burial in Sediments from Non-Upwelling, Continental-Margin Environments. Geochim Cosmochim Ac 57, 991-1007.

Schijf, J., de Baar, H.J.W., Millero, F.J., 1995. Vertical distributions and speciation of dissolved rare earth elements in the anoxic brines of Bannock Basin, eastern Mediterranean. Geochimica et Cosmochimica Acta 57, 1419-1432.

Scott, C., Bekker, A., Reinhard, C.R., Schnetger, B., Krapež, B., Rumble, D., Lyons, T.W., 2011. Late Archean euxinic conditions before the rise of atmospheric Geology 39, 119-122.

Scott, C., Lyons, T.W., A., B., Shen, Y., Poulton, S.W., Chu, X., Anbar, A.D., 2008. Tracing the stepwise oxygenation of the Proterozoic ocean Nature 452, 457-460.

Severmann, S., Lyons, T.W., Anbar, A., McManus, J., Gordon, G., 2008. Modern iron isotope perspective on the benthic iron shuttle and the redox evolution of ancient oceans. Geology 36, 487-490.

Slack, J.F., Grenne, T., Bekker, A., Rouxel, O.J., Lindberg, P.A., 2007. Suboxic deep seawater in the late Paleoproterozoic: Evidence from hematitic chert and iron formation related to seafloor-hydrothermal sulfide deposits, central Arizona, USA. Earth and Planetary Science Letters 255, 243-256.

Spier, C.A., de Oliveira, S.M.B., Sial, A.N., Rios, F.J., 2007. Geochemistry and genesis of the banded iron formations of the Caue Formation, Quadrilatero Ferrifero, Minas Gerais, Brazil. Precambrian Research 152, 170-206.

Steinhoefel, G., Horn, I., von Blanckenburg, F., 2009. Micro-scale tracing of Fe and Si isotope signatures in banded iron formation using femtosecond laser ablation Geochimica et Cosmochimica Acta 73, 5343-5360.

Zerkle, A.L., House, C.H., Cox, R.P., Canfield, D.E., 2006. Metal limitation of cyanobacterial N(2) fixation and implications for the Precambrian nitrogen cycle. Geobiology 4, 285-297.